# CORRELATION MEASUREMENT OF $\mathbf{\Lambda^0 \bar{\Lambda}^0}$, $\mathbf{\Lambda^0 \Lambda^0}$ AND $\mathbf{\bar{\Lambda}^0 \bar{\Lambda}^0}$ WITH THE ATLAS DETECTOR AT $\sqrt{s}$=7 TeV

by

Hok-Chuen Cheng

**A dissertation submitted in partial fulfillment
of the requirements for the degree of
Doctor of Philosophy
(Physics)
in the University of Michigan
2017**

Doctoral Committee:

      Professor Homer A. Neal, Chair
      Associate Professor Christine A. Aidala
      Professor Ratindranath Akhoury
      Professor Igor Jovanovic
      Associate Professor Junjie Zhu

Hok-Chuen Cheng

hccheng@umich.edu

ORCID iD: 0000-0002-8912-4389

# Dedication

*To my grandma, my parents,*
*and those who loved me unconditionally*

# Acknowledgements

The journey of getting a PhD in physics is not an easy one, yet it is a very rewarding one. I am enormously grateful that I always run into mentors, colleagues, and friends who are willing to give me the helping hands when I needed them the most.

Firstly, I would like to thank my supervisor, Prof. Homer Neal, for his patience and trust bestowed upon me who gave me the necessary autonomy and freedom to explore different methodologies and research topics. His sense of humor and his ability to remind me of the big picture also helped me a lot whenever I felt lost and frustrated during the course of my graduate study. Secondly, I would also like to thank Prof. Rudolf Thun (deceased) who introduced me to his down-to-earth and rigorious approach used in experimental particle physics. His thought-provoking insights will always be remembered. It was with great sadness that our group had lost a senior member who contributed tremendrous efforts to the ATLAS detector from its conception to its completion. Thirdly, I would like to thank Prof. Bing Zhou, Dr. Daniel Levin and Dr. Yusheng Wu for introducing me to the ATLAS group at Michigan, guiding me through my first few projects in the group and opening the door of experimental particle physics to me. Besides, I want to thank Prof. Jianming Qian for his wonderful collider physics class, his comments on my analysis as well as his advice on publication. In addition, I want to thank Prof. Ratindranath Akhoury and Prof. Igor

Lastly, I am truly grateful to my parents, Shui-Ki Cheng and Mei-Yu Tsang, and my deceased grandma, Yuet-Chun Lau, who loved me unconditionally and have always been supportive regardless of my ocassional insubordinations. The fact that they never had a chance to go to college due to wars and poverty constantly reminds me that higher education is a privilege and to not take things for granted. It was particularly difficult for them to let me, who is their only (grand)child, travel thousands of miles away from home to study abroad for almost seven years. I felt particularly sorry that I could not be by their side when my grandma passed away and during the difficult times of my parents. Their sacrifice for and trust on me are unimaginable. I cannot wait to bring home the trophy and share with them the happiness and glory that they long deserved.

It is the best decision I have ever made to spend the most productive years of my life working on some of the most meaningful and yet challenging problems about the Nature with some of the smartest persons on this planet, as well as traveling and living in different parts of the world experiencing different cultures and lifestyles. It is both a humbling and transformative experience. A PhD thesis is a proof that the author has acquired the ability to stand on the shoulders of all the giants throughout the history of mankind and create knowledge upon itself. It symbolizes the beginning of a brand new journey in life as a creator of knowledge!

> *For today, goodbye. For tomorrow,*
> *good luck. And forever, Go Blue!*
> — Mary Sue Coleman,
> President Emerita, University of Michigan

# TABLE OF CONTENTS

# List of Figures

xiii

# List of Tables

# List of appendices

# Abstract

This thesis summaries the measurements of correlations between $\Lambda^0\bar{\Lambda}^0$, $\Lambda^0\Lambda^0$, and $\bar{\Lambda}^0\bar{\Lambda}^0$ hyperon pairs produced inclusively at the LHC, which are useful for a better understanding of the quark-antiquark pair production and jet fragmentation and hadronization processes. The analysis is based on hyperon pairs selected using the muon and minimum bias samples collected at the ATLAS experiment from proton-proton collisions at a center-of-mass energy of 7 TeV in 2010. Excess $\Lambda^0\bar{\Lambda}^0$ are observed near the production threshold and are identified to be originated from the parton system in the string model in the Monte Carlo sample, decaying either directly or through heavy strange resonances such as $\Sigma^0$ and $\Sigma^*(1385)$. Dynamical correlations have been explored through a correlation function defined as the ratio of two-particle to single-particle densities. Positive correlation is observed for $\Lambda^0\bar{\Lambda}^0$ and anticorrelation is observed for $\Lambda^0\Lambda^0$ and $\bar{\Lambda}^0\bar{\Lambda}^0$ for $Q \in [0,2]$ GeV. The structure replicates similar correlations in $p\bar{p}$, $pp$, and $\bar{p}\bar{p}$ events in PYTHIA generator as predicted by the Lund string fragmentation model. Parameters of the "popcorn" mechanism implemented in the PYTHIA generator are tuned and are found to have little impact on the structure observed. The spin composition of the data sample is extracted using a data-driven reference sample built by event mixing. Appropriate corrections have been made to the kinematic distributions in the reference sample by kinematic weighting to make sure that the detector effects

are well modeled. A modified Pearson's $\chi^2$ test statistics is calculated for the $\cos \theta^*$ distribution to determine the best-fitted $A$-value for data. The results are consistent with zero for both like-type and unlike-type hyperon pairs in $Q \in [0, 10]$ GeV and $Q \in [1, 10]$ GeV respectively. The data statistics in the range of $Q \in [0, 1]$ GeV is currently too low for the estimation of the emitter size for Fermi-Dirac correlation.

# Introduction

This thesis presents the results of correlation measurements between $\Lambda^0\bar{\Lambda}^0$, $\Lambda^0\Lambda^0$ and $\bar{\Lambda}^0\bar{\Lambda}^0$ pairs produced inclusively in the reaction $p + p \rightarrow V_1^0 V_2^0 + X^*$ at a center-of-mass energy of 7 TeV at the LHC ATLAS detector.

The main physics goals include:

- studying the $s\bar{s}$ quark-antiquark pair production through the $\Lambda^0\bar{\Lambda}^0$ system

- testing the prediction of fragmentation and hadronization models, e.g. the Lund string model and the "popcorn" mechanism

- probing Fermi-Dirac (FD) correlation between identical fermions, i.e. $\Lambda^0\Lambda^0$ or $\bar{\Lambda}^0\bar{\Lambda}^0$ pairs

The first goal is to search for evidence that the presumed $s\bar{s}$-pairs which produce the $\Lambda^0$ and $\bar{\Lambda}^0$ are produced in unison. By using the decay channel $\Lambda^0 \rightarrow p\pi^-$ $(\bar{\Lambda}^0 \rightarrow \bar{p}\pi^+)$ in which the angular distribution of the daughter products defines the parent polarization, we look for correlation between the final state $p$ and $\bar{p}$. If indeed the $s$ and/or $\bar{s}$ pairs are produced in the same quantum process and then hadronize into $\Lambda^0$ and/or $\bar{\Lambda}^0$ and the spin information of $s$

---

$^*V$ was a generic name given to particles that decay into a pair of charged tracks and leave a V character shape in a bubble chamber. $V^0$ refers to neutral particles.

and/or $\bar{s}$ is preserved during the hadronization with $ud$ and/or $\bar{u}\bar{d}$ singlet in the constituent quark model [1], one would expect the spins of the resulting $\Lambda^0$ and $\bar{\Lambda}^0$ to be correlated and, consequently, the angles of production of the final state protons to be correlated as well. One should keep in mind that only hyperon pairs that are produced very close in space-time are of interest. Hyperon pairs with large 4-momenta difference $Q^{\dagger}$ are not expected to exhibit any correlation in their spins.

There has been considerable interest in the question of how quark/antiquark pairs are produced. Some authors have assumed that the pairs are produced with spins aligned [2, 3]. Others have advanced models with the spins antialigned [3]. Other studies suggested that there is no directional association [4]. The dramatic $\Delta\eta - \Delta\phi$ correlation between the $\Lambda^0$ and $\bar{\Lambda}^0$ reinforces the conjecture that the two particles have a common origin (Figure 0.0.1). Therefore, our tests are intended to raise the issue of spin correlation in an attempt to further examine the hypothesis of a possible simple production mechanism.

The second goal is to measure the dynamical correlations in the rapidity and momentum phase space through a correlation function $C(p_1, p_2)$ defined in Eq. (9.5.16). We look for possible enhancement or suppression of pair production of $\Lambda^0$ and/or $\bar{\Lambda}^0$ hyperons when compared to the case where the two hyperons are independently produced. A mixed data sample is used as the reference sample for the latter case. Dynamical correlations are expected for the hyperon pairs at small $Q$-value as a consequence of the baryon and antibaryon production mechanism in the string fragmentation model. $\Lambda^0\bar{\Lambda}^0$ pairs are expected to possess positive correlation while $\Lambda^0\Lambda^0$ and $\bar{\Lambda}^0\bar{\Lambda}^0$ pairs are expected to be anticorrelated. The length scale of the correlation is expected to be similar to that between other baryon/antibaryon pairs with similar rest mass, such as the case between protons and/or antiprotons, which is

---

$^{\dagger}Q$ is defined by $Q = \sqrt{-(p_1 - p_2)^2}$, where $p_1$ and $p_2$ are the 4-momenta of $\Lambda_1$ and $\Lambda_2$, respectively.
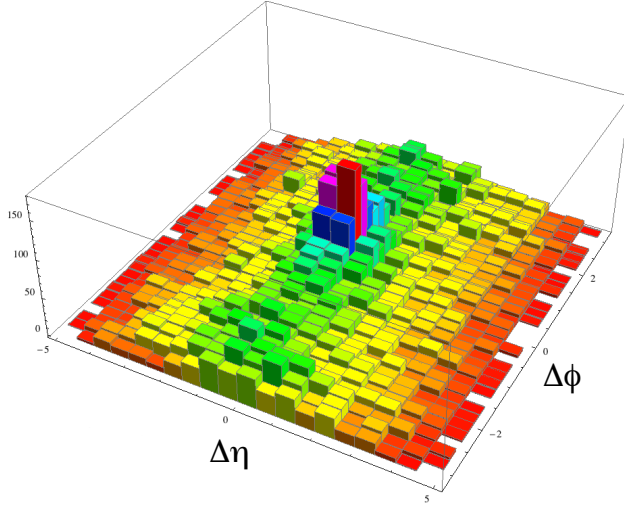
Figure 0.0.1: $\Delta\eta - \Delta\phi$ distribution for $\Lambda^0\bar{\Lambda}^0$ events. $\Delta\eta$ and $\Delta\phi$ are the relative pseudorapidity and azimuthal angle of the hyperon pairs in the lab frame which will be defined later in Section 3.2.1.

at around $Q \sim 1.5$ GeV. (Figure 6.1.1)

The third goal is to study the FD correlation arising from the antisymmetric nature of the wave function of two identical fermions. Also known as the Pauli exclusion principle (Section 1.6), identical fermions cannot share the same set of quantum numbers when they are in the vicinity of each other, which leads to the suppression of $S = 1$ state for the $\Lambda^0\Lambda^0$ or $\bar{\Lambda}^0\bar{\Lambda}^0$ system. FD correlation is therefore expected to affect the small $Q$-value region only. Previous measurements at LEP [5–7] suggested FD correlation to have an effective length scale of $Q \sim 1.5$ GeV or $R_{\Lambda\Lambda} \sim 0.15$ fm, which was later criticized by Ref. [8] that the dynamical correlations in the Monte Carlo (MC) sample used in the "double ratio" method to extract the FD emitter size $R_{\Lambda\Lambda}$ are very likely to have been underestimated, resulting in a "FD emitter size" similar to the characteristic length scale as that of the dynamical correlations predicted by the string fragmentation model. As the actual emitter size for FD effect should be comparable to the baryon size which corresponds to a $Q$-value region less

than 0.5 GeV or $R_{\Lambda\Lambda} \sim 1$ fm, it may be too small to be observed experimentally. Several other experiments measured $R_{\Lambda\Lambda}$ ranging from 0.22-0.33 fm at SELEX [4] and 0.39-4.0 fm at EXCHARM [9] to 3.13 fm at STAR [10].

The analysis presented here uses the 2010 data for which there is a lower track transverse momentum threshold, which has high impact on the reconstruction efficiency of the $V^0$ (Appendix), when compared to later runs. These measurements are important for understanding the physics behind quark-antiquark pair production and the performance of the string model in modeling the phenomenology of baryon production at the LHC energy regime. Due to limited statistics and poor modeling of the kinematic distributions of data by the MC sample, a data-driven method, namely event mixing, is used to provide a baseline reference sample to estimate the distortion in the decay angle distribution due to the detector effect.

The outline of this thesis is as follows:

- Chapter 1 gives a brief introduction to the Standard Model of particle physics with emphasis on the Quantum Chromodynamics, the jet fragmentation and hadronization models, the spin structure and properties of the $\Lambda^0$ hyperon, and the spin-statistics theorem.

- Chapter 2 describes the existing experimental techniques and results from several past measurements.

- Chapter 3 describes the LHC and the ATLAS detector with focus on the tracking system.

- Chapter 4 describes the data and MC samples used in this analysis as well as the muon and minimum bias trigger systems at the ATLAS detector.

- Chapter 5 describes the reconstruction of $V^0$ particles and the event selection for $\Lambda^0$ and $\bar{\Lambda}^0$ candidates. Signal and background modeling is discussed and signal region is defined here.

- Chapter 6 describes the dynamical correlations in terms of the correlation function and that predicted by the string model.

- Chapter 7 describes the theory, the experimental techniques, the uncertainty estimation and the results of the spin correlation measurement.

- Chapter 8 discusses the interpretations and implications of the results from the dynamcial correlation and spin correlation measurements.

- Chapter 9 summarizes and concludes the thesis and discusses the outlook for future analyses.

The Appendices discuss trigger mappings, MC study of the composition of excess hyperon pairs, effects of track $p_T$ threshold, decay angle and kinematic distributions, the relation between the two bases of decay angles, several important cross-checks and the author's other contributions at the ATLAS Collaboration.

# Chapter 1

# Theory

*Three quarks for Muster Mark!*

*Sure he hasn't got much of a bark*

*And sure any he has it's all beside the mark*

— James Joyce, *Finnegans Wake*

This chapter gives an overview of the theoretical background of the Standard Model of particle physics, with special emphasis on aspects of the Quantum Chromodynamics (QCD) related to the hadronization and fragmentation model. The $\Lambda^0$ hyperon is discussed with emphasis on its self-analyzing spin property and its spin structure. The Pauli exclusion principle, which leads to the Fermi-Dirac correlations between like-type di-hyperon pairs, will also be briefly discussed.

*Natural units*[*] are used in this thesis to simplify the formulas.

---

[*]$\hbar$ and $c$ are set to unity. As a result, energy ($mc^2$), momentum ($mc$), and mass will all appear as mass and will normally be stated in *electron-volt* (eV).

## 1.1 Background

In the late 19th century, the field of physics was thought to be settled and the atom was believed to be the fundamental building block of all types of matter. Then in 1897, J. J. Thomson discovered the electron (Table 1.1), a subatomic particle smaller than the atom that carries electric charge. With the discovery of the atomic nucleus in 1911 (Table 1.1) and the discovery of the proton in 1919 (Table 1.1) by Ernest Rutherford, it was clear that our understanding of the building blocks of our universe was far from complete. The field of particle physics was wide open.

Table 1.1: Timeline of particle physics discoveries. *Source:Wikipedia*

| Year | Discovery |
|------|-----------|
| 1897 | electron |
| 1899 | alpha and beta particle |
| 1900 | gamma ray |
| 1911 | atomic nucleus |
| 1919 | proton |
| 1932 | neutron and positron |
| 1936 | muon |
| 1947 | kaon (strange quark) and pion |
| 1955 | antiproton |
| 1956 | electron neutrino |
| 1962 | muon neutrino |
| 1974 | $J/\psi$ particle (charm quark) |
| 1977 | Upsilon particle (bottom quark) and tau lepton |
| 1979 | gluon (indirectly in three-jet events) |
| 1983 | W and Z bosons |
| 1995 | top quark |
| 2000 | tau neutrino |
| 2012 | Higgs boson |

With the founding of quantum mechanics and the advent of experimental techniques in the 20th century (Table 1.2), the number of subatomic particles discovered exploded (Table 1.1).

7

The theory of special relativity was later incorporated into quantum mechanics to conceive the so-called quantum field theory which forms the basis of the Standard Model (SM) (Section 1.2), the benchmark model in the field of particle physics nowadays that describes all the fundamental particles and their interactions with the electromagnetic, weak and strong forces. With the discovery of the Higgs boson in 2012 (Table 1.1), the Standard Model is the most successful and well-measured theory in the history of mankind.

Table 1.2: Timeline of particle physics technologies. *Source:Wikipedia*

| Year | Technology |
|------|------------|
| 1897 - 1901 | Townsend discharge |
| 1911 | cloud chamber |
| 1928 | Geiger Muller tube |
| 1934 | cyclotron |
| 1945 | synchrotron |
| 1952 | bubble chamber |
| 1968 | multiwire proportional chamber |

However, the story does not just end there. There are still unresolved problems in the Standard Model, such as the unification with the gravitational force, the origin of the neutrino mass, the origin of dark matter and dark energy and so on. Within the framework of the Standard Model, Quantum Chromodynamics, the theory that describes the interactions between quarks, antiquarks, and gluons, is a less well understood sector due to its peculiar properties, namely asymptotic freedom and confinement. Many qualitative tests are available to test the properties of QCD in the perturbative regime. Properties of the QCD in the non-perturbative regime are much harder to test due to difficulties in the calculation as perturbation theory is no longer valid. One example is the hadronization of quarks into mesons and baryons, which is studied through fragmentation models that are based on assumptions on the nature of the phenomenology of the process.

This thesis intends to give some insights into the creation mechanism of quark-antiquark pairs in the hadronization process. $\Lambda^0$ and $\bar{\Lambda}^0$ hyperons are used as handles to probe the $s$ and $\bar{s}$ spin orientation, where the $u$ and $d$ quarks form a singlet state and do not contribute to the spin content of the hyperon under the standard assumption of the Constituent Quark Model (CQM). Correlations in the momentum and spin phase space are measured and compared with model predictions and the results from past measurements.

The remaining parts of this chapter are given as follows: The Standard Model of particle physics is introduced in Section 1.2. Properties of QCD such as the running coupling, asymptotic freedom and confinement, perturbative and non-pertubative regimes of QCD are discussed in Section 1.3. Hadronization and fragmentation models such as the string model are described in Section 1.3.5, followed by a discussion on the hyperon spin structure in Section 1.5, the properties of the $\Lambda^0$ hyperon and the spin-statistics theorem in Section 1.6.

## 1.2 The Standard Model of particle physics

The Standard Model of particle physics began its inception in the 1930's when physicists discovered the fundamental building blocks of matter. It is a gauge quantum field theory which describes elementary particles and their interactions. Just like any other theories in the field of physics, the Standard Model is largely motivated by symmetries.

There are two kinds of symmetries in physics, namely global symmetries which do not depend on space-time coordinates and gauge (local) symmetry which do. Symmetries are important because of Noether's theorem [11] which states that if a system has a continuous symmetry, then there is a corresponding conserved current and hence a conserved charge. For instance, translational symmetry leads to conservation of linear momentum, rotational symmetry leads

to conservation of angular momentum and Lorentz invariance, physical laws are independent of their inertial reference frame, leads to the conservation of invariant mass.

The Standard Model unifies the electromagnetic, weak and strong nuclear forces based on the local gauge symmetries of $SU(3)_c \times SU(2)_L \times U(1)_Y$, with the $SU(3)_c$ group describes the strong force, the $SU(2)_L$ group describes the weak force and the $U(1)_Y$ group describes the electromagnetic force. The fundamental interactions are the immediate consequence of the local gauge invariance, and the excitations of these fields correspond to gauge bosons. There are a total of twelve gauge bosons: eight gluons correspond to the generators of the $SU(3)_c$, two oppositely charged $W$ bosons correspond to the generators of $SU(2)_L$, and a neutral $Z$ boson and a photon ($\gamma$), which corresponds to linear combinations of the generators of $SU(2)_L$ and $U(1)_Y$.

The particle masses are introduced via the Higgs mechanism [12–14] in which a spontaneous symmetry breaking of the electroweak group generates the masses of the weak gauge bosons and the fermions. The Higgs mechanism also predicts the existence of a massive scalar particle, the Higgs boson, which was discovered independently by the two main experiments (ATLAS and CMS) at the LHC and was reported on 4th July 2012 [15, 16].

### 1.2.1   Particle contents

The particles are categorized into fermions and bosons. Fermions are spin-half particles that make up matter. The 12 fundamental fermions can be further classified into three generations of quarks and leptons. Each generation is a heavier copy of the first one with same quantum numbers. Fermions in the heavier generation are unstable and decay promptly upon creation into lighter generation through the weak force. Matters in the nature are

therefore dominantly made of the first generation.

The left-handed fermions exist as doublets under $SU(2)_L$, while the right-handed fermions are singlets. This correspond to three generations of quark doublets and singlets

$$\begin{pmatrix} u \\ d \end{pmatrix}_L \qquad \begin{pmatrix} c \\ s \end{pmatrix}_L \qquad \begin{pmatrix} t \\ b \end{pmatrix}_L \qquad u_R \qquad d_R \qquad c_R \qquad s_R \qquad t_R \qquad b_R \tag{1.2.1}$$

where the quarks in the upper and lower row of the doublets carry electric charge of $+2/3e$ and $-1/3e$, respectively, with $e$ being the minus of the electric charge of the electron. The quark singlets carry the same charge as their doublet counterparts. The leptons also form three electroweak $SU(2)$ doublets and singlets, with the exception of neutrino that there are no[†] right-handed neutrinos or left-handed anti-neutrinos.

$$\begin{pmatrix} e \\ \nu_e^- \end{pmatrix}_L \qquad \begin{pmatrix} \mu \\ \nu_\mu^- \end{pmatrix}_L \qquad \begin{pmatrix} \tau \\ \nu_\tau^- \end{pmatrix}_L \qquad e_R^- \qquad \mu_R^- \qquad \tau_R^- \tag{1.2.2}$$

where the leptons (electron, muon, and tauon) in the upper row of the doublets and the singlets have electric charge of $-e$ and their corresponding neutrinos in the lower row of the doublets are neutral. The neutrinos are therefore directly influenced only by the weak nuclear force, which makes them notoriously difficult to detect. All 12 particles have been found with the latest discovery of the top quark by the CDF [26] and D0 [27] collaborations

---

[†]Neutrinos are assumed to be massless in the SM. However, the experimentally established phenomenon of neutrino oscillation [17–21] suggests that neutrino masses cannot be exactly zero. Their masses are believed to be obtained from mechanisms other than the Higgs mechanism, such as the Seesaw mechanism [22–25]. It predicts that neutrinos with wrong helicity to be either very heavy and/or do not participate in weak interaction (a.k.a. sterile neutrinos). They are therefore very difficult to detect experimentally.

in 1995 and tau neutrino by the DONUT [28] collaboration in 2000. (Table 1.1)

Flavor‡ can be changed through the weak interaction. Transitions between the same SU(2) doublet are most probable, even though transition between different generations can happen with much lower probabilities. Such transition probabilities can be computed using the Cabibbo-Kobayashi-Maskawa (CKM) matrix [29].
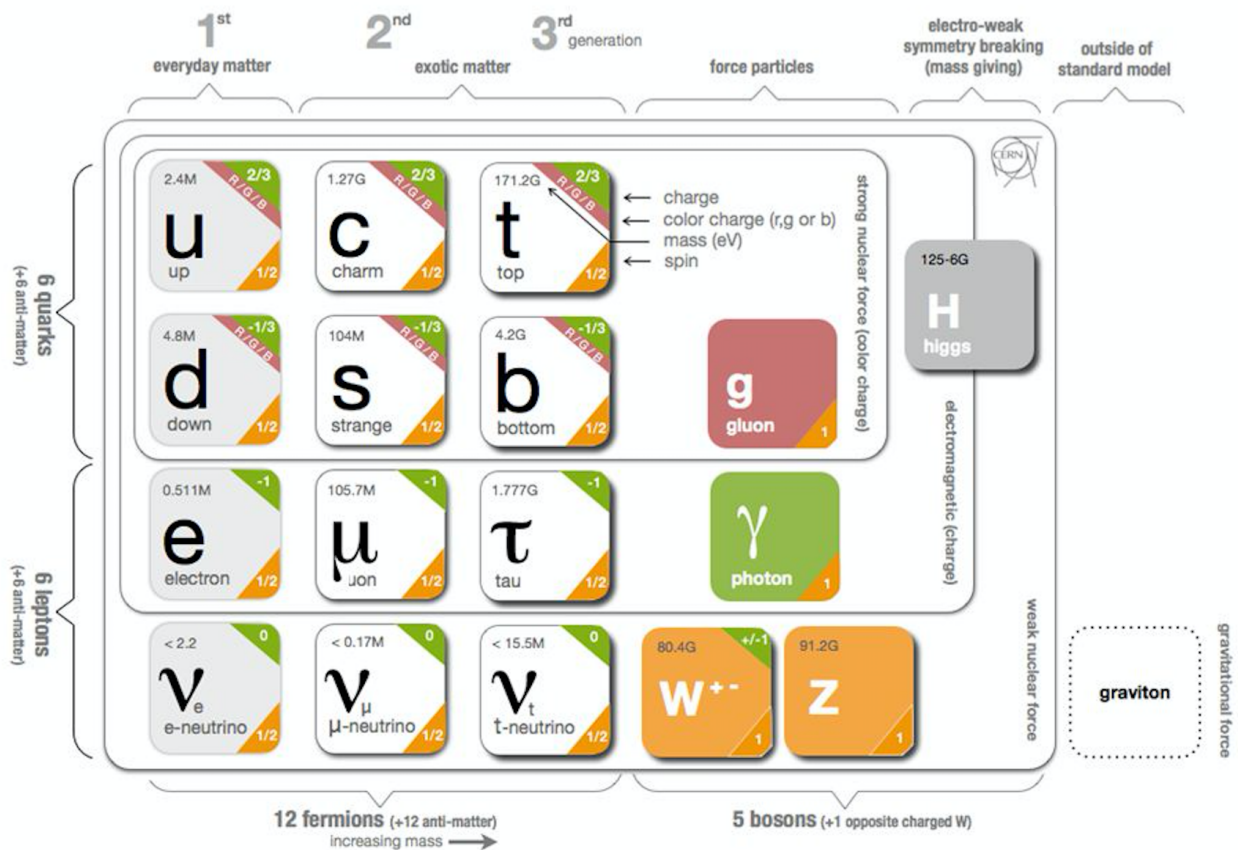


Figure 1.2.1: The Standard Model of particle physics and the hypothetical graviton in the extension of the gravitational force. *Source: CERN*

All particles in the model are massless up to this point, which is not what is measured in

---

‡Flavor refers to a species of an elementary particle. The SM contains six flavors of quarks and six flavors of leptons. They are parameterized in terms of flavor quantum numbers. For instance, strangeness $S = n_s - n_{\bar{s}}$ is related to the difference between the number of strange quarks and strange antiquarks.

nature. An attempt to give these particles mass in the Standard Model was developed in the sixties, which is called the Higgs mechanism [12–14]. A scalar Higgs field is introduced with a non-vanishing vacuum expectation value. A local symmetry is broken and some of the massless gauge fields picked up their masses. In this way the Higgs mechanism explains why the $W^+$, $W^-$ and $Z^0$ bosons are massive and the photon remains massless. The interaction of particles with the Higgs field gives them their bare mass.

## 1.3   Quantum Chromodynamics

The QCD sector defines the interactions between quarks and gluons, the dynamics of which is controlled by the QCD Lagrangian which obeys the non-Abelian $SU(3)$ symmetry as the theory of QCD is symmetric to the three color charges carried by the quarks and gluons. For the special unitary group of $SU(3)$, there are eight generators and thus eight gluon fields $G_\nu^a$ ($a = 1 \ldots 8$) are needed to represent eight spin-1 massless gluons. Quarks are triplets under $SU(3)$ and they quickly hadronize into colorless mesons and baryons after being produced due to the so-called color confinement. The gauge invariant QCD Lagrangian is defined as

$$\mathcal{L}_{\text{QCD}} = \sum_q^{u,d,s,c,t,b} \bar{\psi}_q(x)(i\gamma^\mu D_\mu - m)\psi_q(x) - \frac{1}{4}G_{\mu\nu}^a G_a^{\mu\nu} \qquad (1.3.1)$$

where $\gamma^\nu$ is the Dirac matrices of the Lorentz group, $\psi_q(x)$ is the quark field where the index $q$ runs over all six flavors of quarks and $G_{ij}^a$ is the gluon field strength tensor similar to the electromagnetic field strength tensor, $F^{\mu\nu}$, in quantum electrodynamics. It is given by

$$G_{\mu\nu}^a = \partial_\mu G_\nu^a - \partial_\nu G_\mu^a + g_3 f^{abc} G_\mu^b G_\nu^c \qquad (1.3.2)$$

13

where $g_3$ is the strong coupling and $f^{abc}$ are the structure constants of the non-Abelian $SU(3)$ gauge group in $[\lambda^a, \lambda^b] = if^{abc}\lambda^c$. The gauge part of the QCD Lagrangian $-\frac{1}{4}G^a_{\mu\nu}G^{\mu\nu}_a$ contains cubic and quartic terms in the gluon field because of the non-Abelian term in Eq. (1.3.2), which means that gluons are self-interacting and no superposition principle is at work. The covariant derivative added to preserve the gauge symmetry is defined as

$$D_\mu = \partial_\mu - ig_3 \frac{1}{2}\vec{\lambda} \cdot \vec{G}_\mu \qquad (1.3.3)$$

The interaction vertexes of the Feynman diagrams of QCD are shown in Figure 1.3.1.



(a) $\sim \sqrt{\alpha_s}$      (b) $\sim \sqrt{\alpha_s}$      (c) $\sim \alpha_s$
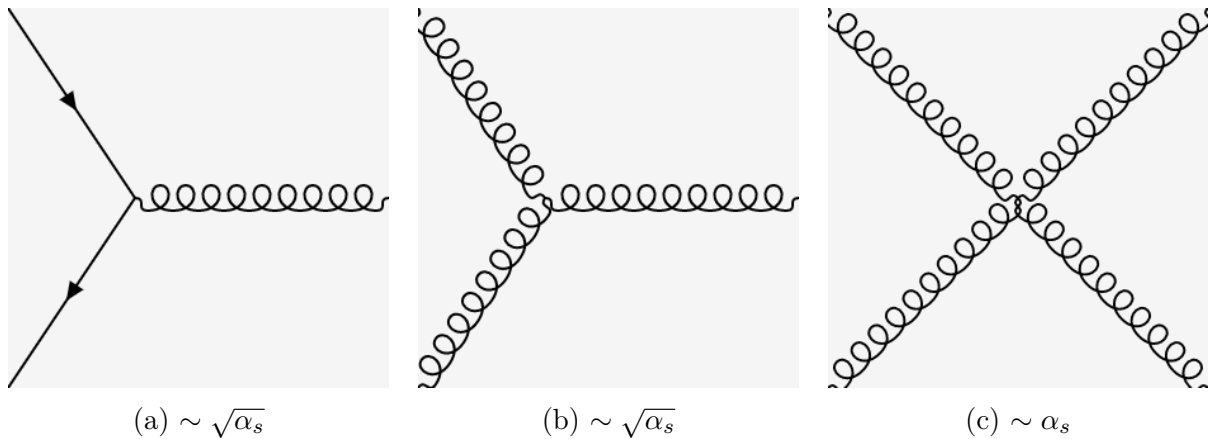
Figure 1.3.1: The interaction vertexes of the Feynman diagrams of QCD, namely (a) quark-gluon, (b) triple-gluon, and (c) quartic-gluon vertexes.

## 1.3.1 Running coupling

Interactions consist of an infinite sum of possibilities, where exchange of gluon can couple with quark loops, or extra gluons can be emitted and reabsorbed. Some of these loops make the calculation of amplitude diverge logarithmically. This divergence can be

removed by a process called renormalization. In this process, the bare coupling constant is re-parameterized to be the "measured" coupling constant. Measurement of the coupling constant includes all loops, so the final result of the sum is known.

The self-interacting gluonic vertexes in the QCD Feynman diagrams (Figure 1.3.1) introduce boson (gluon) loops in the higher order corrections such as the one-loop corrections shown in Figure 1.3.2, which interfere destructively with the fermion (quark) loop contributions. The number of fermion loops is determined by the number of flavors and the number of boson loops is determined by the number of color charges. It can later be shown that the energy scale dependence of the strong coupling constant $\alpha_s$ becomes negative when the number of flavors is smaller than a certain value and the loop corrections are dominated by the boson loops.
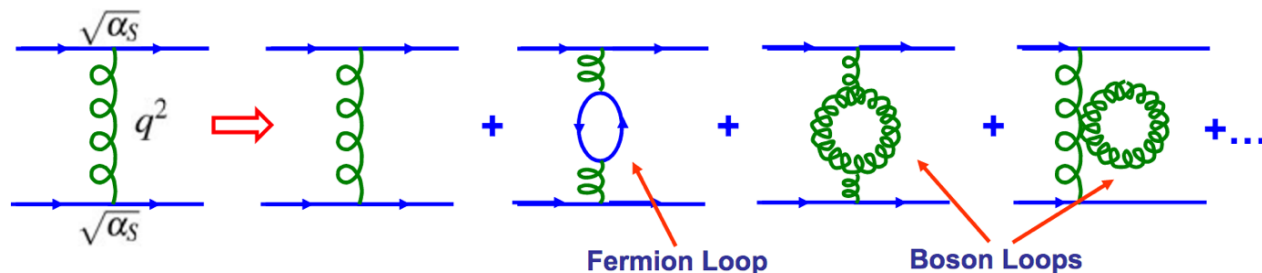


Figure 1.3.2: The QCD Feynman diagrams of a gluon propagator in a quark-quark scattering with up to one-loop (fermion and boson loops) corrections. [30]

To first order, the dependence of $\alpha_s$ on the energy of the interaction is given by:

$$\alpha_s(Q^2) = \frac{\alpha_s(\mu^2)}{1 + \frac{\alpha_s(\mu^2)}{12\pi}(33 - 2n_f)\ln(\frac{Q^2}{\mu^2})} \qquad (1.3.4)$$

where $Q^2$ is the momentum transfer for which $\alpha_2$ is calculated, $n_f$ is the number of quark flavors, and $\mu^2$ is the arbitrary value of the momentum transfer chosen for renormaliza-

15

tion. Conventionally, the energy scale $\Lambda_{qcd}^2$ at which $\alpha_s$ becomes infinite is chosen as the renormalization scale. Eq. (1.3.4) becomes

$$\alpha_s(Q^2) = \frac{12\pi}{(33 - 2n_f)\ln(\frac{Q^2}{\Lambda_{qcd}^2})} \tag{1.3.5}$$

at first order where $\Lambda_{qcd}^2 = \mu^2 exp(\frac{-12\pi}{(33-2n_f)\alpha_s(\mu^2)})$. Eq. (1.3.5) is also known as one-loop approximation.

The dependence of a coupling parameter, $g$, on the energy scale, $\mu$, of a given process is encoded in the so-called beta function, $\beta(g)$. It is defined as

$$\beta(g) = \frac{\partial g}{\partial \ln(\mu)}. \tag{1.3.6}$$

The one-loop beta function in quantum chromodynamics with $n_f$ flavors [31, 32] is

$$\beta(\alpha_s) = -(11 - \frac{2n_f}{3})\frac{\alpha_s^2}{2\pi} \tag{1.3.7}$$

written in terms of $\alpha_s = \frac{g^2}{4\pi}$.

For $n_f \leq 16$, the beta function indicates that the coupling decreases with increasing energy scale. The dependence on the number of flavors occurs because each quark flavor introduces another set of loop diagrams to the correction of the bare vertex. Currently six quark flavors are known and therefore $\alpha_s$ should become large at low momentum transfer and one can no longer rely on the perturbation theory. Conversely, the coupling increases with decreasing energy scale. A figure of the measurement of the strong coupling constant $\alpha_s$ as a function of energy scale $Q$ is shown in Figure 1.3.3.
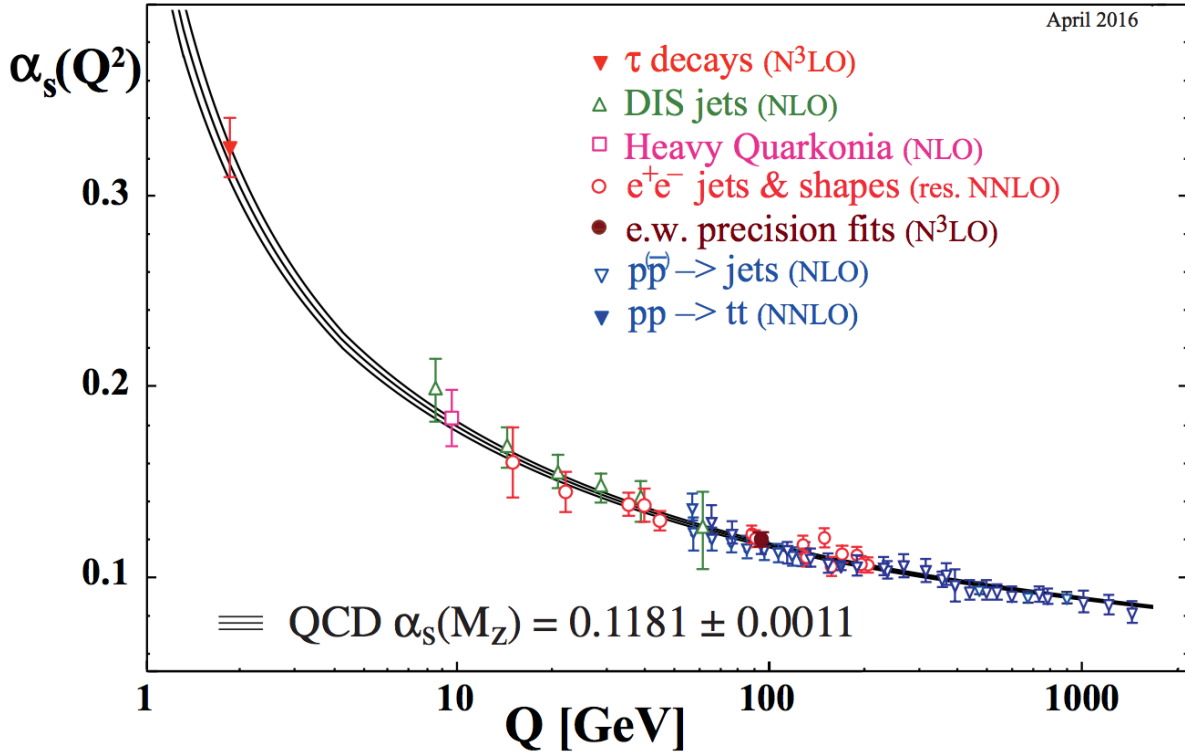
Figure 1.3.3: Summary of measurements of $\alpha_s$ as a function of the energy scale $Q$. The respective degree of QCD perturbation theory used in the extraction of $\alpha_s$ is indicated in brackets (NLO: next-to-leading order; NNLO: next-to-next-to leading order; res. NNLO: NNLO matched with resummed next-to-leading logs; N³LO: next-to-NNLO). Figure taken from Ref. [33].

## 1.3.2   Asymptotic freedom and color confinement

As a consequence of the running of the strong coupling constant $\alpha_s$, QCD enjoys two peculiar properties.

First, it is the **asymptotic freedom** which states that quarks and gluons interact very weakly in very high-energy reaction. At $E > 1$ GeV, the proton or any other hadron is a loosely bound system of quarks and gluons. The probability of emission decreases quickly with the number of emitted particles and can hence be described by the perturbation theory

of QCD. In the language of the Feynman diagram, diagrams corresponding to higher orders of $\alpha_s$ (Figure 1.3.2) can be ignored because $\alpha_s$ is much less than one in this regime.

Second, it is the **color confinement** which states that the force between quarks does not diminish as they are separated. Since the force-carrying gluons have color charge, as opposed to photons in the case of QED, a direct consequence is that the gluon field forms a narrow tube as a quark pair separates. (Figure 1.3.4) As the distance grows, it becomes energetically favorable for the color tube to break, forming a new quark-antiquark pair. (Figure 1.3.5) There are many different models describing how such quark-antiquark pairs are formed, one of the most popular one is the Lund string fragmentation model which will be discussed in detail in the next few sections.
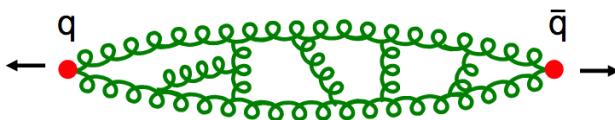


Figure 1.3.4: Color confinement of $q\bar{q}$ separation. Gluon self-interaction makes field lines attract each other and leads to the formation of color flux tube of constant energy density of about 1 GeV/fm. This color flux field is modeled as a massless relativistic string with constant tension in the Lund string model which will be described in Chapter 1.3.6. [30]

### 1.3.3   Perturbative QCD

The cross section of physics processes can be calculated by summing over contributions of all relevant Feynman diagrams. As each vertex between quarks and gluons or gluons and gluons contributes a factor of $\sqrt{\alpha_s}$ or $\alpha_s$ (Figure 1.3.1), the magnitude of the contributions of different Feynman diagrams can be grouped in powers of $\alpha_s$. Using the fact that the strong coupling constant $\alpha_s$ is small at high energy or short distance, the perturbation method can

be used to calculate the cross section of the physics process where terms of higher order of $\alpha_s$ can be neglected.

### 1.3.4  Non-perturbative QCD

Unfortunately, most physics processes involve both short- and long-distance interactions. Hence, they are not computable directly in perturbative theory for QCD. For instance, the structure of hadrons has a non-perturbative nature. Attempts to resolve this problem led to the development of the QCD factorization theorem, which separates the cross section into the process dependent perturbatively-calculable short-distance parton cross section and the universal long-distance functions. These long distance functions can be measured with global fit to experiments. They include parton distribution functions, fragmentation functions, and different kinds of form factors. The energies at which quarks combine to form hadrons, a.k.a. hadronization, are in the non-perturbative regime of QCD. Hadronization and fragmentation models are developed to explain experimental phenomena and make predictions for different measurable variables.

### 1.3.5  Models of fragmentation

As discussed in the previous few sections, the coupling constant $\alpha_s$ is a scale-dependent quantity which increases at low values of the shower evolution scale. The perturbation theory eventually becomes invalid at some point and the dynamics enter a non-perturbative phase which leads to the formation of the observed final-state hadrons. This hadronization process is currently not calculable using the available non-perturbative techniques. Jet fragmentaion and hadronization models are therefore used to make basic assumptions about the nature

of the fragmentation and hadronization process to calculate its phenomenology. They are implemented in Monte Carlo programs to create simulated events which are used to compare with data events. The performance of different fragmentation and hadronization models can then be compared and parameters in the models can be modified to improve agreement with the data. In this analysis, we mainly look at the Lund string model which is implemented in the PYTHIA event generator [34, 35]. Other common fragmentation and hadronization models include the cluster-hadronization model which is implemented in both HERWIG [36] and SHERPA [37] event generators.
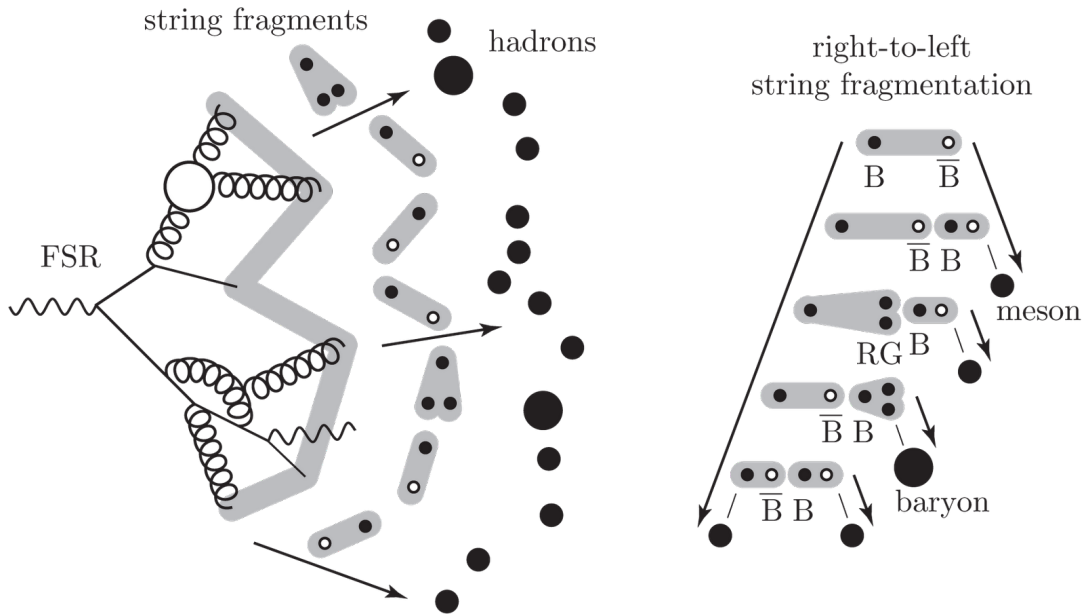


Figure 1.3.5: Hadronization of a parton shower is shown on the left. The string fragmentation of a quark-antiquark pair into a stream of mesons and baryons is shown on the right. [38]

## 1.3.6 The string model

The string fragmentation model is inspired by the observation in lattice QCD that at large distances the potential of color fields, such as that between a quark-antiquark pair, grows

linearly with distance like a string [39]. This corresponds to a distance-independent force law which is believed to be caused by the self-interacting nature of gluonic field, which collapses itself into a string or tube configuration with thickness of the order of 1 fm when the separation is much larger than this. (Figure 1.3.4)

A quark-antiquark pair is pictured as the opposite ends of a gluonic string, each carrying half of the total energy in their center-of-mass frame. As the quark and antiquark move away from each other, their kinematic energy is converted into the potential energy in the gluonic string. When the potential energy becomes the order of hadron mass, it becomes energetically favorable for the string to break at some point and pull a pair of quark-antiquark out of the vacuum. The new quark is connected to the original antiquark and the new antiquark is connected to the original quark. Two string segments then begin to stretch and break again, until all energy has been converted into the quark-antiquark pairs connected by short string segments, which can be identified as hadrons. (Figure 1.3.5) The types and momentum of hadrons formed depend on the quark-antiquark pairs produced in the string breaking. As the quark-antiquark pairs arise from string fluctuation, there is a preference of production for light quarks with low transverse momentum relative to the string axis.

Each produced hadron carries a fraction of the momentum of the original quark. The momentum of the hadron is again controlled by a fragmentation model similar to that in the Field-Feynman model [40]. The probability distribution function of the fraction of the momentum carried by the produced hadron is given by the Lund symmetric fragmentation function as shown below

$$f(z) \propto \frac{(1-z)^a}{z} \exp(-\frac{bm_\perp^2}{z}) \tag{1.3.8}$$

21

where $z$ is the fractional momentum of the parton/hadron, $a$ and $b$ are tunable parameters.

The Lund symmetric fragmentation function is motivated by the requirements of Lorentz invariance, acausality, and left-right symmetry. The Lund Area Law [41] which states that the probability to produce a set of hadrons with momentum $p_1$, $p_2$, $\cdots$, $p_n$ and total momentum $P_{tot}$ is given by

$$dP_n(\{p_j\}; P_{tot}) \propto \exp(-bA) \tag{1.3.9}$$

where $A$ is the area spanned by the color string before breakup in the 1+1 space-time diagram as shown in the shaded region in Figure 1.3.6 and $b$ is a parameter related to the density of hadronic states and the breakup properties of the string field, respectively. [41]

The probability is proportional to the size of the phase space and is exponentially suppressed by $A$. This can be understood as similar to a quantum mechanical tunneling through a potential barrier as the potential energy stored in a color string is proportional to its length in the space-time diagram. Figure 1.3.6 shows a representation of color fluctuations in the string and the production of baryon and antibaryon pairs. The dynamcial correlations in the baryon/antibaryon pair production that arise from the string breaking will be discussed in Section 6.1.

## 1.4 Hyperon spin structure

It is well known that the spin structure of proton, neutron, and other baryons is non-trivial. Since all baryons are three-quark states ($qqq$), one may build SU(3)-flavor symmetrical wave function of any member of the spin-$\frac{1}{2}$ baryon octet or spin-$\frac{3}{2}$ baryon decuplet using the lowest
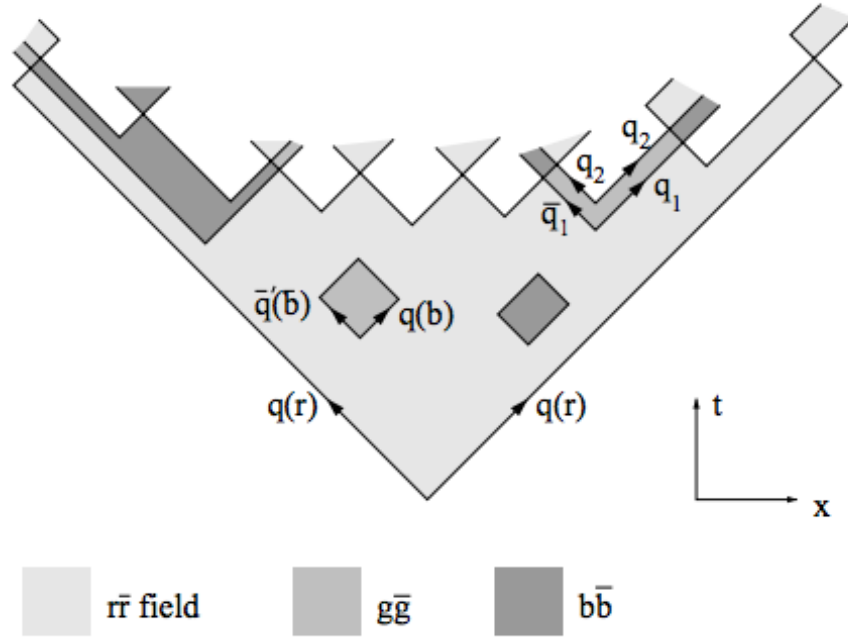
Figure 1.3.6: Representation of color fluctuations in the string. At the right-hand side we have a pair of wrongly colored pair $q_1(b)\bar{q}_1(\bar{b})$ and $q_1(g)\bar{q}_1(\bar{g})$ forming an effective diquark-antidiquark pair, yielding a pair of baryon and antibaryon, neighbors in rank. At the left-hand side, there is a production of a baryon and an antibaryon with a meson between them, arising from two breakups in a color fluctuation region. The production of baryon is suppressed when compared to that of mesons. [8]

mass flavors (u, d, and s quarks). (Figure 1.4.1)

In the naive Constituent Quark Model [1] all quarks are assumed to be in S-state and spin of a baryon is composed of the constituent quark spins. The wave function of the $\Lambda^0$ hyperon can be written as

$$|\Lambda \Uparrow\rangle = \frac{1}{\sqrt{18}} \left[ (u \uparrow d \downarrow + u \downarrow d \uparrow) - (u \downarrow d \uparrow + u \uparrow d \downarrow) \right] s \uparrow + cycl.perm. \qquad (1.4.1)$$

where $\Uparrow$ denotes that the baryon is in a pure spin state and $\uparrow$ and $\downarrow$ denote spin states of the constituent quarks. Using this wave function, the quark polarization $P_q$ in a fully polarized

23
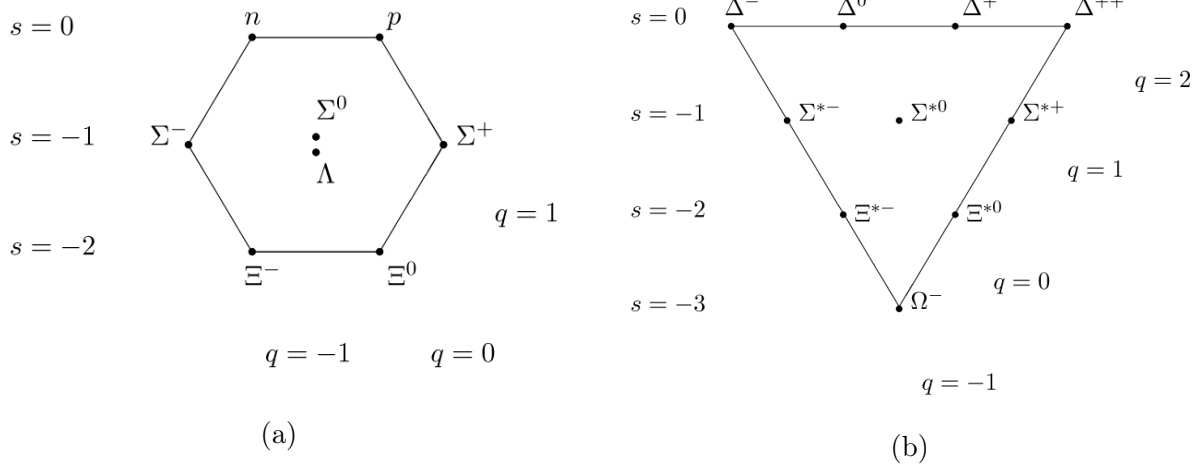
Figure 1.4.1: (a) The $S = 1/2$ ground state baryon octet and the (b) $S = 3/2$ baryon decuplet in the quark model.

baryon can be directly calculated as

$$\langle \Lambda \Uparrow | \sigma_z^{u,d} | \Lambda \Uparrow \rangle = P_{u,d} = 0 \qquad \langle \Lambda \Uparrow | \sigma_z^{s} | \Lambda \Uparrow \rangle = P_s = 1 \qquad (1.4.2)$$

According to the simple model, the spin of the $\Lambda^0$ hyperon is entirely carried by the $s$ quark, while the $ud$ pair is in a spinless (singlet) state.

One should keep in mind that such a simple model also predicts the spins in proton and neutron contributed dominantly from the $u$ and $d$ quarks. However, in late 1980's it was discovered that only a small fraction of the proton's spin, less than 30%, is carried by quarks. This is known as the "proton spin crisis" [42–45]. Testing whether the spin information in the $s$ quark is preserved during its hadronization into the $\Lambda^0$ hyperon can therefore shed light on how well such a simple model performs to model the hyperon.

# 1.5  $\Lambda^0$ hyperon

## 1.5.1  Brief history of discovery

First discovered in the October 1950 by V. D. Hopper and S. Biswas from the University of Melbourne [46], the $\Lambda^0$ hyperons were produced by cosmic rays and detected in photographic emulsions flown in a balloon at 21,000 m. They were found to live much longer than expected at about $10^{-10}$ s instead of $10^{-23}$ s. This particle was later named the lambda particle ($\Lambda^0$) and the properties that caused its long lifetime is dubbed "strangeness". That name was later inherited by one of the quarks ($s$) from which the $\Lambda^0$ particle is constructed. Some key parameters for $\Lambda^0(\bar{\Lambda}^0)$ are given in Table 1.3.

Table 1.3: Key parameters for $\Lambda^0$ hyperon. [47]

| Parameter | Value |
|---|---|
| $I\left(\ J^P\ \right)$ | $0\ \left(\frac{1}{2}^+\right)$ |
| mass [MeV] | $1115.683 \pm 0.006$ |
| mean life $[10^{-10}\text{s}]$ | $2.632 \pm 0.020$ |
| branching ratio $\mathcal{BR}\left(\Lambda^0 \to p\pi^-\right)$ [%] | $63.9 \pm 0.5$ |
| branching ratio $\mathcal{BR}\left(\Lambda^0 \to n\pi^0\right)$ [%] | $35.8 \pm 0.5$ |
| parity-violating decay parameter $\alpha_\Lambda$ for $\Lambda^0 \to p\pi^-$ | $0.642 \pm 0.013$ |

## 1.5.2  Self-analyzing properties

The $\Lambda^0(\bar{\Lambda}^0)$ hyperon, being the lightest baryon containing the $s(\bar{s})$ quark, is produced in copious amount in particle accelerators. Its long decay length and its fully-reconstructible decay channel $\Lambda^0 \to p\pi^-$ ($\bar{\Lambda}^0 \to \bar{p}\pi^+$), with a branching fraction of 63.9%, makes possible for its reconstruction as a signature displaced secondary vertex with a pair of oppositely charged tracks. The asymmetric (parity-violating) nature [48,49] of the decay, which is characterized

by the asymmetry parameter $\alpha_\Lambda$, enables the determination of its spin polarization through the angular distribution of its decay proton. As a result, $\Lambda^0$ polarization itself has been a very rich research topic. For instance, the $\Lambda^0$ polarization measured in hard scattering process in fixed target experients as shown in Figure 1.5.1 are much larger than the predictions of perturbative QCD of a few percents [50] and has been a major puzzle for the past thirty years. Recent related measurements at ATLAS include transverse polarization [51] and production [52] measurements.
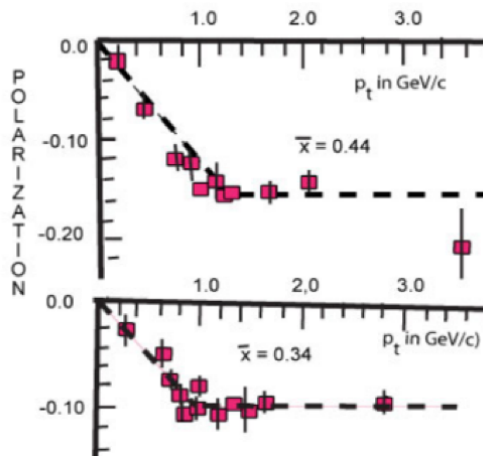


Figure 1.5.1: Dependence of the polarization in inclusive $\Lambda^0$ production in $p - p$ and $p - Be$ collisions at 400 GeV as a function of $p_T$ for two $x_F$ bins. [53]

## 1.6   Spin-statistics theorem

All particles either have integer spin (Bosons) or half-integer spin (Fermions). The spin-statistics theorem further relates the intrinsic spin of a particle to the particle statistics it obeys. The wave function of identical integer-spin particles has the same value when two particles exchange positions and is called symmetric. In contrast, the wave function of

identical half-integer spin particles changes sign when two particles are swapped and is called antisymmetric.

An immediate implication is that the wave function of identical fermions must vanish as the two particles get closer together in space-time, but there is no restriction on the number of identical bosons occupying the same quantum state. This is also known as the Pauli exclusion principle. The building blocks of matter such as protons, neutrons and electrons are fermions and can occupy space and form all kinds of macroscopic structures we see in our daily lives. Force mediators such as photons are bosons.

In Chapter 2, past experiments that attempted to measure the emitter size of fermions (e.g. $\Lambda^0$-$\Lambda^0$ and proton-proton) and bosons (e.g. kaon-kaon and pion-pion) pair production are reviewed. Suppression/enhancement of certain spin states can be probed through spin-spin correlation (identical vs nonidentical spin states) or dynamical correlation in the momentum phase space (space-time separation of particles at production) to determine the effective range of the spin-statistics (Fermi-Dirac statistics for fermions and Bose-Einstein statistics for bosons) as well as its dependence on the baryon mass.

# Chapter 2

# Past measurements and methodolgy

This chapter reviews the experimental techniques used in the measurement of correlations of di-hyperon pairs either taken from past experiments or proposed by theorists for future studies. Experimental results from several past related measurements are also reviewed with their major findings briefly discussed. The main goal is to better understand how our analysis and results may fit into the existing correlation measurement landscape and their implications on baryon/antibaryon production models.

## 2.1   Methodology

### 2.1.1   Two-particle correlation function

The Fermi-Dirac (FD), Bose-Einstein (BE) and the dynamical correlations can be studied in terms of two-particle correlation function $C_2$ defined as

$$C_2(p_1, p_2) = \frac{\rho_2(p_1, p_2)}{\rho_1(p_1)\rho_1(p_2)} \tag{2.1.1}$$

where $p_1$ and $p_2$ are the 4-momenta of particles. $\rho_2$ is a two-particle density of particles with 4-momenta $p_1$ and $p_2$ respectively. $\rho_1$ is a single-particle density for each particle. The ratio is therefore proportional to the conditional probability of creating a pair of particles with 4-momenta $p_1$ and $p_2$ with respect to an independently produced pair with the same kinematics. It can be used to look for enhancement or suppression in the pair production probability. The variables $p_1$ and $p_2$ can be replaced by other kinematic variables of interest in Eq. (2.1.1). One possible choice of parameterization of the correlation function is to use the azimuthal angle and pseudorapidity differences $\Delta\phi = \phi_1 - \phi_2$ and $\Delta\eta = \eta_1 - \eta_2$ [54]. The corresponding two-particle correlation function is defined as

$$C_2(\Delta\eta, \Delta\phi) = \frac{N_{ref}}{N_{exp}} \frac{S(\Delta\eta, \Delta\phi)}{B(\Delta\eta, \Delta\phi)}, \tag{2.1.2}$$

where

$$S(\Delta\eta, \Delta\phi) = \frac{d^2 N_{exp}}{d\Delta\eta d\Delta\phi} \tag{2.1.3}$$

and

$$B(\Delta\eta, \Delta\phi) = \frac{d^2 N_{ref}}{d\Delta\eta d\Delta\phi}. \tag{2.1.4}$$

$N_{exp}$ and $N_{ref}$ are the numbers of pairs of particles reconstructed in the experimental and reference sample. This gives a two-dimensional differential ratio and the structures at different kinematic regions such as the collinear region $(\Delta\eta, \Delta\phi) \sim (0, 0)$ and the back-to-back region $\Delta\phi \sim \pi$ can be studied.

Another common parameterization of the correlation function is to use the 4-momenta dif-

ference $Q = \sqrt{-(p_1 - p_2)^2}$ and it takes into account all possible degrees of freedom. $Q \sim 0$ implies that the two particles are essentially produced in unison. It is therefore a favorable variable to be used to probe the FD or BE correlation and the corresponding emitter radius. The correlation function is replaced by

$$C_2(Q) = \frac{N_{ref}}{N_{exp}} \cdot \frac{S(Q)}{B(Q)}. \tag{2.1.5}$$

where

$$S(Q) = \frac{dN_{exp}}{dQ} \tag{2.1.6}$$

and

$$B(Q) = \frac{dN_{ref}}{dQ}. \tag{2.1.7}$$

A reference sample free of BE or FD correlations can be defined in different ways: Monte Carlo without such kind of correlations, pairs of unlike-sign hadrons, pairs with particles from different events, or from different hemispheres (mixings) [55].

Some experiments use the so-called "double-ratio" method in which the correlation function is defined as

$$C_{d-r}(Q) = \frac{C_2^{data}(Q)}{C_2^{MC}(Q)} \tag{2.1.8}$$

where $C_2^{data}(Q)$ and $C_2^{MC}(Q)$ represent correlation functions defined in Eq. (2.1.5) for the experimental data and the MC sample.

As pointed out by Ref. [8], the major experimental challenge is to choose an appropriate reference sample such that the detector effects and the dynamical correlations are correctly modeled and the FD or BE effects can be isolated by comparing the data with the reference sample. Also, the results obtained by using the "double-ratio" method turn out to depend heavily on the modeling of the dynamical correlation in the Monte Carlo simulation. Possible tuning using nonidentical baryon pairs, such as the studies with $p\Lambda^0$ and $\bar{p}\bar{\Lambda}^0$ at the ALICE [54] and STAR [56] experiments, would be needed to make sure that the FD-free dynamical correlation is simulated correctly.

For an estimation of the production source extent of the di-hyperon pair, different parameterizations may be used. The most common one is the Goldhaber parameterization [57] which is defined as

$$C_2(Q) = N(1 + \beta e^{-R^2 Q^2}), \tag{2.1.9}$$

where $N$ is the normalization constant, $R$ is the space-time extent of the source and $\beta$ is the suppression factor.

## 2.1.2 Spin composition extraction

The spin composition of the di-hyperon system can be extracted using the proton decay angle distributions. Let us denote $y^*$ as the cosine of the angle $\theta$ between decay protons of each parent hyperon. Each proton should be transformed to its hyperon rest frame.

Taking into account $P$-violation at the $\Lambda^0$ decay from the di-hyperon system, one obtains

$$dN/dy^*|_{S=0} = N\left(1 \mp \alpha_\Lambda^2 y^*\right), \qquad dN/dy^*|_{S=1} = N\left(1 \pm \frac{\alpha_\Lambda^2}{3} y^*\right). \qquad (2.1.10)$$

where $S$ is the spin of the di-hyperon system.

For a system of two spin-$\frac{1}{2}$ fermions, the di-hyperon system can either be in $S = 0$ or $S = 1$ state, the decay angle distribution can be parameterized as the a function of the fraction of the $S = 1$ contribution $\epsilon$ as follows:

$$dN/dy^* = (1 - \epsilon)\, dN/dy^*|_{S=0} + \epsilon dN/dy^*|_{S=1} = N\left(1 + \left(\frac{4}{3}\epsilon - 1\right)\alpha_\Lambda^2 y^*\right). \qquad (2.1.11)$$

A more detailed derivation of the angular distribution of the decay (anti)protons with respect to different spin and polarization configurations and the parameterization used in this analysis can be found in Section 7.1. An alternative definition of decay angle is suggested by Ref. [3] using the decay angles of the two (anti)protons with respect to the orientation of each of their parent hyperon in the helicity frame. The two decay-angle bases are related by simple geometry as shown in Figure 9.4.19 and Eq. (9.4.15).

## 2.2   Experimental results from other experiments

A review on existing results of correlation measurement for di-hyperon pairs coming from ALICE [54] experiment at the LHC, OPAL [5], DELPHI [6], and ALEPH [7] experiments at LEP [58], NA49 [59] experiment at CERN, and EXCHARM [9] spectrometer at the Serpukhov accelerator as well as the latest results from SELEX [4] experiment (Fermilab E781) and STAR [10, 56] experiment at RHIC will be presented in the following sections.

## 2.2.1   Results from ALICE

The two-particle correlation functions were measured in $pp$ collisions at 7 TeV using data collected at the ALICE detector. [54] The analysis was carried out for pions, kaons, protons, and lambdas, for all particle/antiparticle combinations for all the pairs. The correlation function used is similar to the one defined as in Eq. (2.1.1), except that observable $Q$ is replaced by the azimuthal angle and pseudorapidity differences $\Delta\phi$ and $\Delta\eta$.
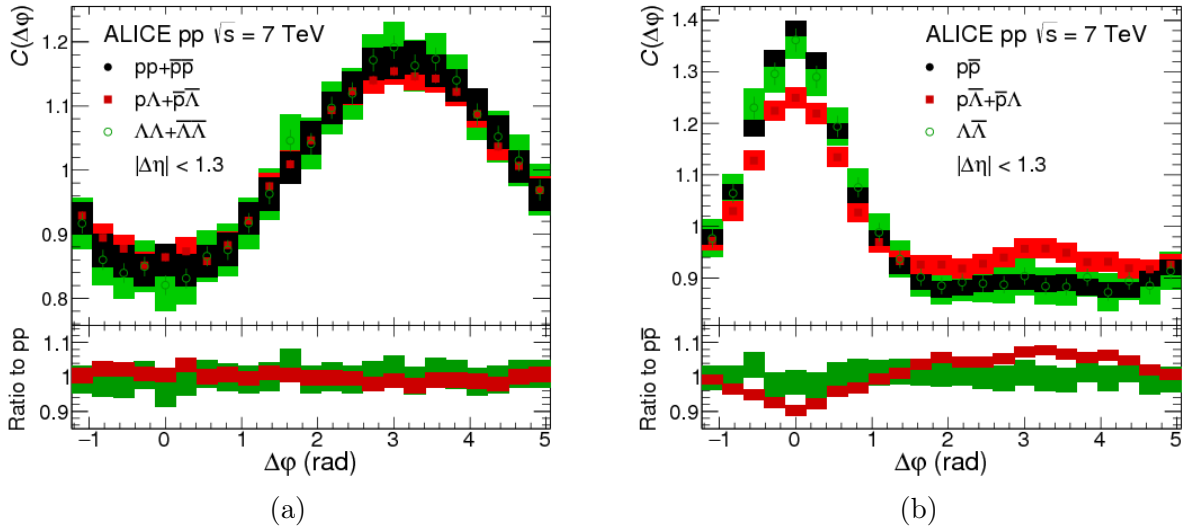


Figure 2.2.1: $\Delta\eta$ integrated projections of correlation functions for combined pairs of (a) like sign and (b) unlike sign baryon and/or antibaryon pairs as functions of $\Delta\phi$. Bottom panels shows ratios to proton/antiproton correlations. Statistical (bars) and systematic (boxes) uncertainties are plotted. [54]

A significant depletion around $(\Delta\eta, \Delta\phi) \sim (0,0)$ is observed for baryon-baryon and antibaryon-antibaryon pairs and this is not seen in baryon-antibaryon pairs. (Figure 2.2.1) The analysis is complemented by MC model calculations using PYTHIA6.4 Perugia-0, Perugia-2011, PYTHIA8, and PHOJET (v.1.12). The correlation function of the of baryons in simulations are found to be significantly different than those found in collision data. (Figure 2.2.2) While

the most surprising result is obtained for baryon-baryon (antibaryon-antibaryon) pairs where models are unable to reproduce even qualitatively the depletion which is observed experimentally, the correlations for baryon-antibaryon are qualitatively comparable between data and MC, with the simulated ones much stronger than those observed in collision data.
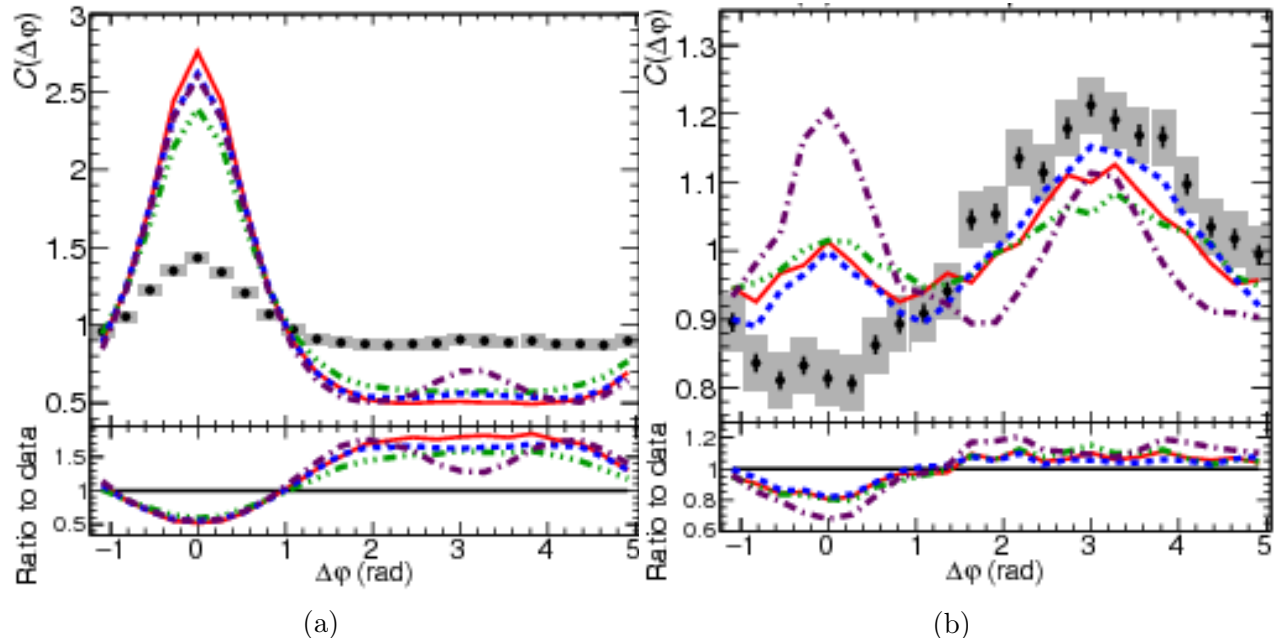


Figure 2.2.2: $\Delta\eta$ integrated projections of correlation functions for (a) $\Lambda^0\bar{\Lambda}^0$ and (b) $\Lambda^0\Lambda^0+\bar{\Lambda}^0\bar{\Lambda}^0$ events as functions of $\Delta\phi$, for ALICE data and four MC models, namely PYTHIA6 Perugia-0 (red), PYTHIA Perugia-2011 (green), PYTHIA8 Monash (blue), and PHOJET (purple). Bottom panels show ratios of MC models to ALICE data. Statistical (bars) and systematic (boxes) uncertainties are plotted. [54]

## 2.2.2 Results from LEP

The results of the correlation measurements of the three LEP experiments, OPAL [5], DELPHI [6], and ALEPH [7] are summarized in Table 2.1. The baryon-pairs are selected from $Z^0$ poles produced in $e^+e^-$ collisions at the LEP collider. The method of "double-ratio" as

described in Eq. (2.1.8) has been used to measure the momentum correlation. They all found similar results with a production radius of the order of 0.15 fm. The result is later criticized by Ref. [8] that the results depend heavily on the description of correlation in the MC, which should in principle be free of FD effects. This correlation cannot be constrained by data as it is impossible to switch off the FD effects. It is the difference between the correlation in data and the FD-free MC which is interpreted as the FD effect. Ref. [8] suggests the use of $p\Lambda$ and $\bar{p}\bar{\Lambda}$ as a tool to study the baryon-baryon correlation in hadronization in absence of FD effects.

As for the spin correlation, the LEP experiments reported FD effects which is reflected as a dominance of $S = 0$ state at small $Q$-values. The reported results as shown in Table 2.1 are consistent with those obtained from the analyses of momentum correlation. A combined fit for the $S = 1$ fraction is done as a function of $Q$ as shown in Figure 2.2.3. However, as pointed out by Ref. [8], the statistics is too limited to conclude for a reliable determination of the range of the FD effect.

Table 2.1: Experimental results for $\lambda$ and $R$ from FD correlations $C_{FD} = 1 - \lambda e^{-R^2 Q^2}$ between baryon-pairs produced in $e^+ e^-$ annihilations at the LEP collider. [8]

| | $R(fm)$ | $\lambda$ | Experiment |
|---|---|---|---|
| $\bar{p}\bar{p}$ | $0.14 \pm 0.06$ | $0.76 \pm 0.33$ | OPAL |
| | $0.11 \pm 0.01$ | $0.49 \pm 0.09$ | ALEPH |
| | $0.16 \pm 0.05$ | $0.67 \pm 0.25$ | DELPHI |
| $\Lambda^0 \Lambda^0$ | $0.11 \pm 0.02$ | $0.59 \pm 0.10$ | ALEPH |
| | $0.17 \pm 0.14$ | Spin Analysis | ALEPH |
| | $0.19^{+0.37}_{-0.07}$ | Spin Analysis | OPAL |
| | $0.11^{+0.05}_{-0.03}$ | Spin Analysis | DELPHI |
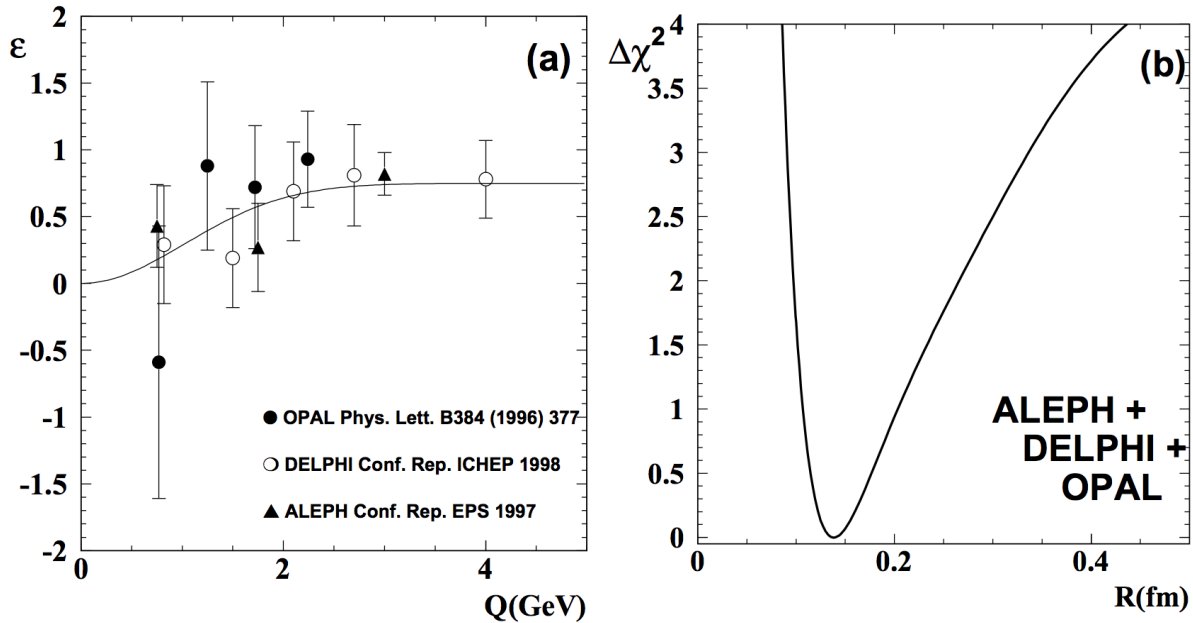
Figure 2.2.3: (a) The $S = 1$ fraction, $\epsilon$, of the $\Lambda^0\Lambda^0(\bar{\Lambda}^0\bar{\Lambda}^0)$ pairs measured as a function of $Q$ by the ALEPH, DELPHI, and OPAL collaborations. The solid line represents the results of the fit of $\epsilon(Q) = 0.75[1 - e^{-R_{\Lambda\Lambda}^2 Q^2}]$ to the data points. [58] (b) The $\Delta\chi^2 = \chi^2 - \chi^2_{min}$ dependence on $R_{\Lambda\Lambda}$. [58]

## 2.2.3 Results from SELEX (E781)

The Hanbury Brown-Twiss (HBT) interferometry of $\Lambda^0\Lambda^0$ pairs produced in $\Sigma^- A$ interactions is carried out using a $\Lambda^0\Lambda^0$ spin composition measurement with data taken by the SELEX experiment (Fermilab E781), which accumulated data during the 1996-97 fixed target run at Fermilab. The suppression of $S = 1$ state in the range of four-momenta difference $Q < 1.5$ GeV was found for $\Lambda^0\Lambda^0$ events. For $Q > 1.5$ GeV it was found to be consistent with statistical spin mixture.

For the $\Lambda^0\bar{\Lambda}^0$ system it was found to be consistent with the expectation for a statistical spin mixture. An estimation of the space-time extent of $\Lambda^0\Lambda^0$ production region gives $R = 0.31 \pm 0.11_{stat} \pm 0.04_{syst}$ fm. [4]
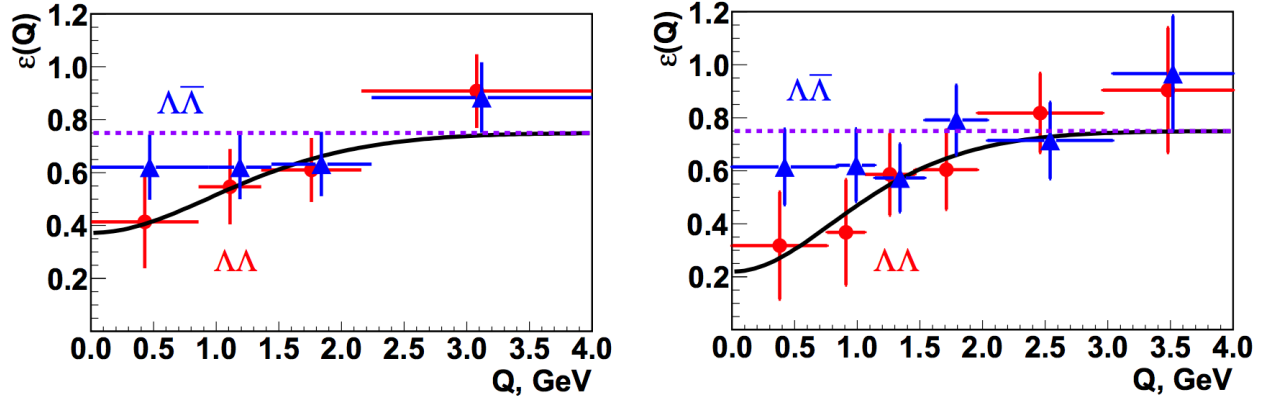
Figure 2.2.4: Spin one contribution $\epsilon(Q)$ for $\Lambda^0\Lambda^0$ (red circle) and $\Lambda^0\bar{\Lambda}^0$ (blue square) systems for different subranges selection measured at the SELEX (E781) experiment. Solid black curve represents a fit by the Goldhaber parameterization, purple dashed horizontal line represents statistical spin distribution. [4]

## 2.2.4 Results from STAR

$p\Lambda^0$ correlation is measured in $Au + Au$ collision at $\sqrt{s_{NN}} = 200$ GeV by the STAR experiment at RHIC. [56] The $p\Lambda^0$ and $\bar{p}\bar{\Lambda}^0$ interaction potentials are relatively well understood and their source sizes are inferred. As the $\bar{p}\Lambda^0$ and $p\bar{\Lambda}^0$ final state interactions (FSI) are unknown, the scattering lengths and source sizes are extracted by fitting the data from the STAR experiment with the Lednicky and Lyuboshitz analytical model. In addition to constraining baryon-antibaryon potentials, this information determines unknown $\bar{p}\Lambda^0$ and $p\bar{\Lambda}^0$ annihilation cross sections that are useful to constrain heavy-ion cascade models. The source radii $r_0$ are measured to be about 3 fm for $p\Lambda^0$ and $\bar{p}\bar{\Lambda}^0$ systems and 1.5 fm for $\bar{p}\Lambda^0$ and $p\bar{\Lambda}^0$ systems.

$\Lambda^0\Lambda^0$ correlation is measured in $Au + Au$ collision at $\sqrt{s_{NN}} = 200$ GeV by the STAR experiment at RHIC. [10] The emitter size $R_{\Lambda\Lambda}$ is measured to be 3.13 fm. Contributions from feed-down include 10% of $\Sigma^0\Lambda^0$, 5% of $\Sigma^0\Sigma^0$, and 4% of $\Xi^-\Xi^-$. Only 44% of the $\Lambda^0\Lambda^0$

are primary.
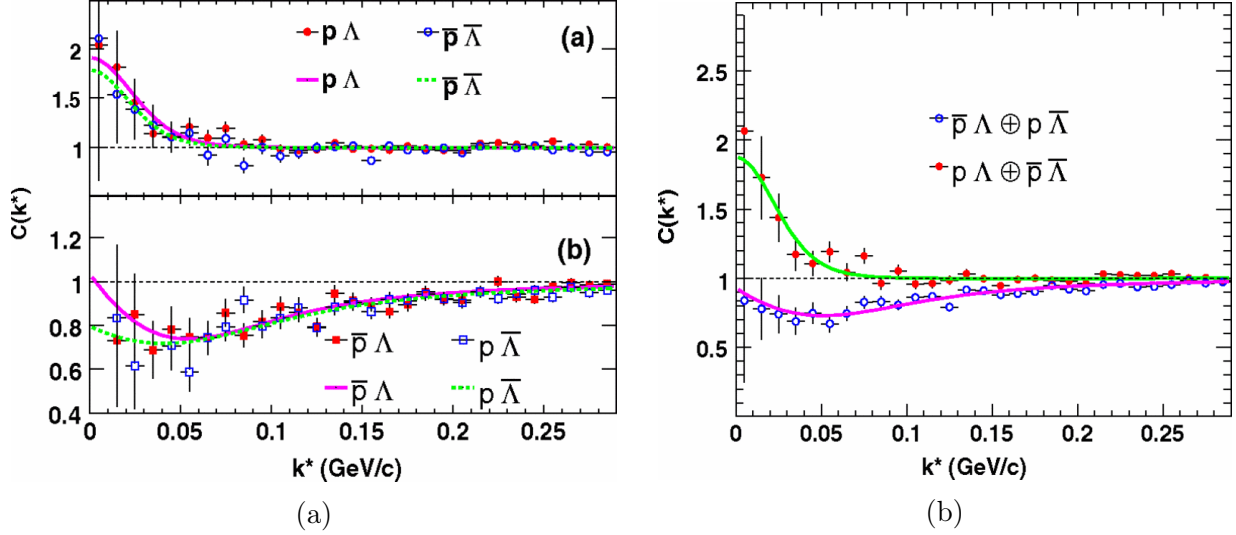


Figure 2.2.5: (a) The purity and momentum-resolution corrected correlation functions $C_{true}(k^*)$ for (a) $p\Lambda^0$, $\bar{p}\bar{\Lambda}^0$, (b) $\bar{p}\Lambda^0$, $p\bar{\Lambda}^0$ measured from the STAR experiment. Curves correspond to fits done using the Lednicky and Lyuboshitz analytical model. [56] (b) $(p\Lambda^0)\oplus(\bar{p}\bar{\Lambda}^0)$ and $(\bar{p}\Lambda^0)\oplus(p\bar{\Lambda}^0)$ combined correlation functions measured from the STAR experiment. Correlation functions are corrected for purity and momentum resolution. Curves correspond to fits done using the Lednicky and Lyuboshitz analytical model. [56]

## 2.2.5 Results from NA49

$p\Lambda^0$ correlation function is measured for the 20% most central $Pb+Pb$ reactions at 158 A GeV. [59] The fit results suggest a Gaussian source size of $R_G = 3-4$ fm which is compatible with the NA49 result on $pp$ correlations $R_G = 4.0 \pm 0.15^{+0.06}_{-0.18}$ fm.

The significance of the measured $\Lambda^0\Lambda^0$ correlation function is unfortunately limited by low statistics and does not show any clear structure. A comparison is done with theoretical expectations in an attempt to limit the range of possible parameter values. A fit is performed where $R_G$ and $\Lambda^0$ are fixed and the scattering length $f_0$, describing the strength of the

38

interaction, is varied. The fit results indicate that the correlation function would favor a relatively small $f_0$, quite independent from the assumed source size.



(a)                                                             (b)
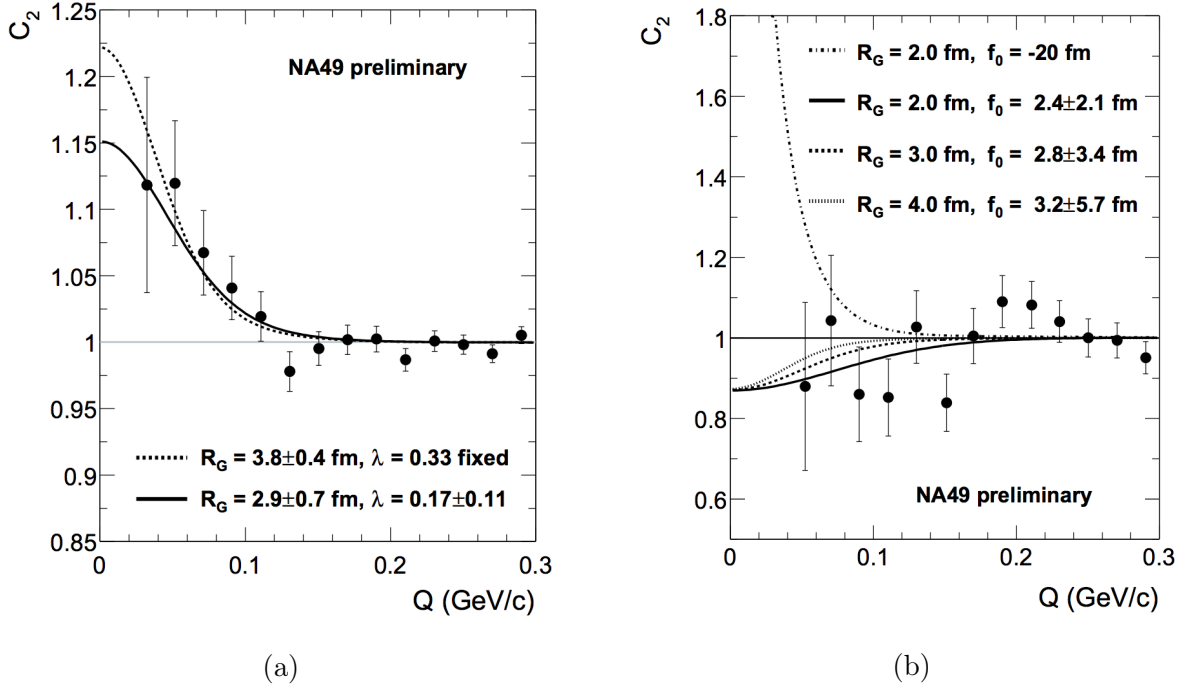
Figure 2.2.6: (a) The $\Lambda^0 p$ correlation function for the 20% most central $Pb + Pb$ reactions at 158 AGeV from the NA49 experiment. The lines represent fits of the calculated c.f. with fixed $\lambda$ parameter (dashed) and free $\lambda$ (solid). [59] (b) The $\Lambda^0 \Lambda^0$ correlation function for the 20% most central $Pb + Pb$ reactions from the NA49 experiment. The lines display the fit results of the calculated c.f. to the data for different fixed Gaussian source radii $R_G$. [59]

## 2.2.6   Results from EXCHARM

Correlation of pairs of $\Lambda^0$ hyperons, neutral kaons, and charged pions having a low relative momentum are analyzed on data obtained at the EXCHARM detector in neutron-carbon interactions at an average neutron energy of 51 GeV. [9]

$R_{\Lambda\Lambda}$ is measured ranging from $0.39 - 4.0$ fm and $\lambda$ is measured to be between -0.47 and

-0.45 using the single and double ratio methods. Correlation between charged pions and that produced in association with $K_S^0$ and $\Lambda^0$ are also measured. It is observed that the dimensions of production region decreases with increasing mass of particle under study.
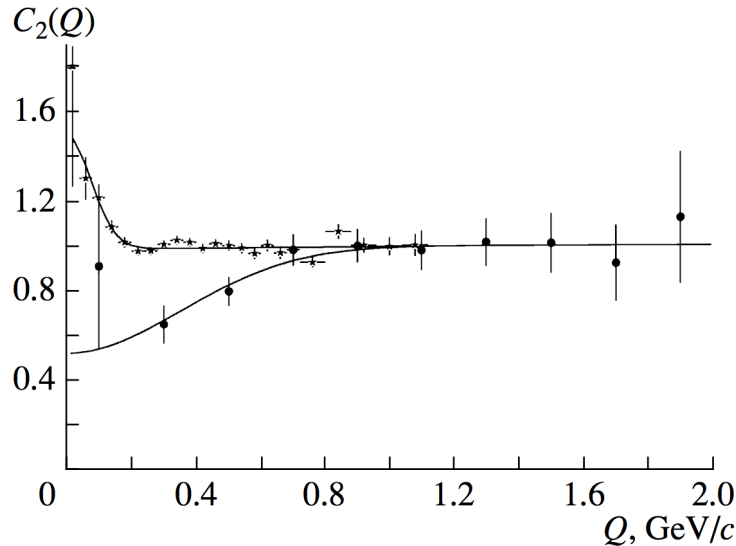


Figure 2.2.7: Correlation functions for pairs of (stars) charged pions and (closed circles) $\Lambda^0$ hyperons obtained from the EXCHARM experiment. The background distribution was obtained by the double-ratio method. The curves represent the result of approximations by a Gaussian function and a first-degree polynomial. [9]

## 2.3 Summary of past measurements and methodology

Past correlation measurements, both dynamical correlations in the momentum and angular phase space and spin analyses, of various identical or nonidentical baryon and meson pairs have been reviewed.

The measurements have been carried out at a wide variety of collisions, ranging from heavy ions to $pp$ and $e^+e^-$ collisions. Most of the correlation functions were measured as a function

of $Q$ which specifies the space-time distance between the particle pairs at production. The emitter sizes of pair productions are measured ranging from the order of 0.1 fm to 4 fm. Enhancement of production is observed for identical meson pairs such as $\pi\pi$ and $K_s^0 K_s^0$ while suppression is observed for identical fermion pairs such as $pp$ and $\Lambda^0\Lambda^0$. Cross correlation between nonidentical pairs such $p\Lambda^0$ and $\bar{p}\bar{\Lambda}^0$ are also studied to understand the dynamical correlation in baryon/antibaryon production free from FD or BE correlations. The results are limited by low statistics for the spin analyses and difficulties in finding an appropriate reference sample in the case of the "double ratio" method.

Since baryon production is among the most poorly understood aspects of the fragmentation model, having experimental measurements and constraints at a different energy regime from the past experiments is crucial to the tuning of event generators. It would be particularly interesting to test how well the string model performs at such high energy. It is hoped that with the large amount of data generated at the LHC, this analysis can be the first attempt to test if the results from the past measurements can be reproduced, possibly with lower statistical uncertainties and hopefully pave the way for more future analyses in this area at the LHC.

# Chapter 3

# Experimental setup

This chapter gives a brief overview to the LHC (Large Hadron Collider) and CERN (European Organization for Nuclear Research, formerly "*Conceil Européen pour la Recherche Nucléaire*") in Chapter 3.1 and the ATLAS detector in Chapter 3.2. More details can be found in various design concept and technical reports for the LHC [60–63] and the ATLAS detector [64–66].

## 3.1 The Large Hadron Collider

The LHC is a proton-proton collider, currently having both the highest energy and luminosity of beams in the world. (Table 3.1) It spans the Swiss-French border near the city of Geneva in Switzerland with a diameter of 27 km at a depth ranging from 50 to 175 meters underground. It was built by CERN between 1998 and 2008 and it resides in a tunnel which was formerly used to house the Large Electron-Position Collider (LEP) [67] which operated from 1989 to 2000. The collider tunnel contains two adjacent parallel beamlines that interact at four points as shown in Figure 3.1.1.
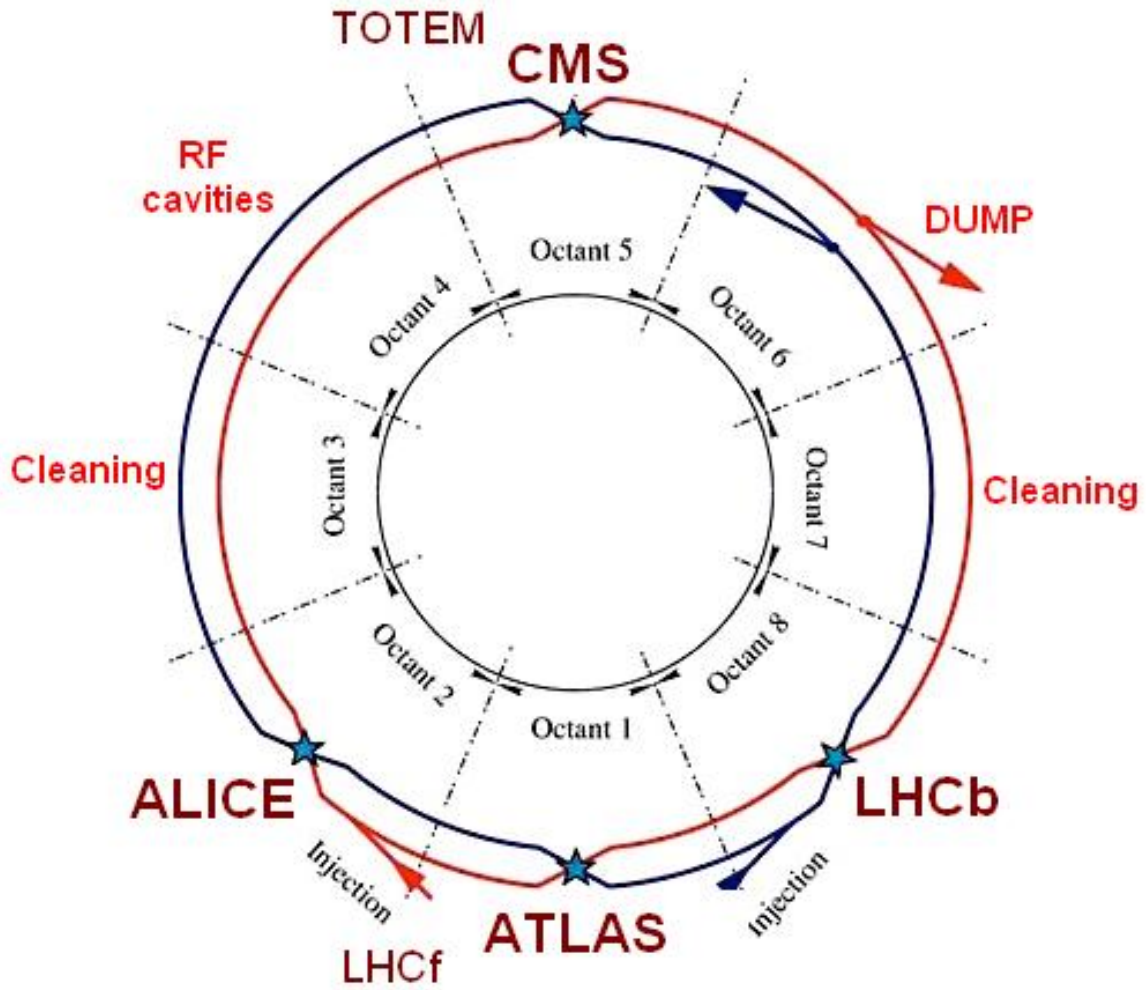
Figure 3.1.1: Eight octants and four collision points (stars) at the LHC [68].

## 3.1.1 Performance goals

The number of events per second generated in the LHC collisions is given by:

$$N_{\text{event}} = L\sigma_{\text{event}} \qquad (3.1.1)$$

where $\sigma_{\text{event}}$ is the cross section for the event under study and $L$ the machine luminosity.

The machine luminosity depends only on the beam parameters and can be written for a Gaussian beam distribution as:

$$L = \frac{N_b^2 n_b f_{\text{rev}} \gamma_r}{4\pi \epsilon_n \beta*} F \qquad (3.1.2)$$

where $N_b$ is the number of particles per bunch, $n_b$ the number of bunches per beam, $f_{\text{rev}}$ the revolution frequency, $\gamma_r$ the relativistic gamma factor, $\epsilon_n$ the normalized transverse beam emittance, $\beta*$ the beta function at the collision point, and $F$ the geometric luminosity reduction factor due to the crossing angle at the interaction point (IP)

$$F = \left(1 + \left(\frac{\theta_c \sigma_z}{2\sigma*}\right)^2\right)^{-1/2} \qquad (3.1.3)$$

$\theta_c$ is the full crossing angle at the IP, $\sigma_z$ the RMS bunch length, and $\sigma*$ the transverse RMS beam size at the IP. The above expression assumes round beams, with $\sigma_z \ll \beta$, and with equal beam parameters for both beams. The exploration of rare events in the LHC collisions therefore requires both high beam energies and high beam intensities.

The LHC has a designed center-of-mass energy ($\sqrt{s}$) of 14 TeV for proton-proton ($pp$) collisions. After a magnetic quench occurred in 2008 which damaged over 50 superconducting magnets and led to a leakage of six tonnes of helium into the tunnel [69], the LHC has only operated at reduced energies of 900 GeV in 2009, 7 TeV in 2010 and 2011, 8 TeV in 2012 and 13 TeV in 2015 and 2016. The data analyzed in this paper was collected at the ATLAS detector dated back in year 2010. The LHC is expected to resume its nominal collision center-of-mass energy of 14 TeV before or after the long shutdown 2 (LS2) in 2018-2019 [70]. The designed luminosity of the LHC at $10^{34}$ cm$^{-2}$s$^{-1}$ was first reached in June 2016 [71]. With

potential upgrades scheduled during the long shutdown 3 (LS3) in 2023-2025, the levelled luminosity in the High Luminosity configuration (HL-LHC) may be further increased by 5 to 7 folds to reach 7 to $7.5 \times 10^{34}$ cm$^{-2}$s$^{-1}$. With a performance of 300 fb$^{-1}$/year, this would allow an integrated luminosity of almost 4000 fb$^{-1}$ to be collected by 2035 [70]. Some key LHC parameters can be found in Table 3.1.

Table 3.1: Key LHC parameters [68, 72].

| Parameter | Design |
|---|---|
| Circumference [m] | 26659 |
| Dipole operating temperature [K] | 1.9 |
| Number of arcs (2450 m Long) | 8 |
| Number of straight sections (545 m long) | 8 |
| Main RF system [MHz] | 400.8 |
| Number of RF cavities per beam | 8 |
| Number of magnets | 9593 |
| Number of main dipoles | 1232 |
| Number of main quadrupoles | 392 |
| Stored energy in magnet [GJ] | 11 |
| Current in main dipole [A] | 11800 |
| Energy density of the LHC magnet [kJ/m] | 500 |
| Nominal energy, protons [TeV] | 7 |
| Minimum distance between bunches [m] | $\sim 7$ |
| Bunch spacing [ns] | 25 |
| Design luminosity [cm$^{-2}$ s$^{-1}$] | $10^{34}$† |
| No. of protons per bunch | $1.15 \times 10^{11}$ |
| No. of bunches per proton beam | 2808 |
| Stored beam energy [MJ] | 360 |
| Average crossing rate [MHz] | 31.6 |
| Number of collisions per second [million] | 600 |

† Design luminosity has been reached in June 2016 [71]

### 3.1.2 Superconducting magnets

Some 1232 dipole magnets keep the beams travel on their circular path, producing a peak magnetic field of 8.33 T required for the nominal beam energy at 7 TeV. 392 quadrupole magnets are used to keep the beam focused so as to maximize the chances of interaction at the four interaction points where the two opposite beams cross. Over 1600 superconducting magnets are installed, each typically weights over 27 tonnes. In order to produce the required magnetic field strength, copper-clad niobium-titanium has been used in the magnet which is kept at an operation temperature of 1.9 K using over 96 tonnes of superfluid helium-4, which also makes the LHC the largest cryogenic facility in the world at liquid helium temperature.

### 3.1.3 Accelerator complex

A long chain of accelerators are used to prepare protons for injection into the LHC as shown in Figure 3.1.2. Protons are obtained by stripping the orbiting electrons from hydrogen atoms. They are then inserted into the Proton Synchrotron Booster (PSB) at an energy of 50 MeV from Linac2. The booster accelerates protons to 1.4 GeV which are then fed to the Proton Synchrotron (PS) where they are further accelerated to 25 GeV. After that the beam is fed to the Super Proton Synchrotron (SPS) where protons are accelerated to 450 GeV before being transferred to the LHC, both in clockwise and anticlockwise directions, and are accelerated for 20 minutes to reach their nominal energy at 7 TeV. The beams will then circulate for many hours inside the LHC beam pipes under normal operation conditions. As a consequence of the acceleration scheme, the proton beams circulate the ring in bunches. Under nominal operation, each proton beam contains 2808 bunches, with each bunch containing about $10^{11}$ protons. These bunches are a few centimeters long and are 7.5 meters apart (25 ns bunch

spacing). A small gap in the proton beam allows the beam dump magnets have time to ramp up to full field strength.
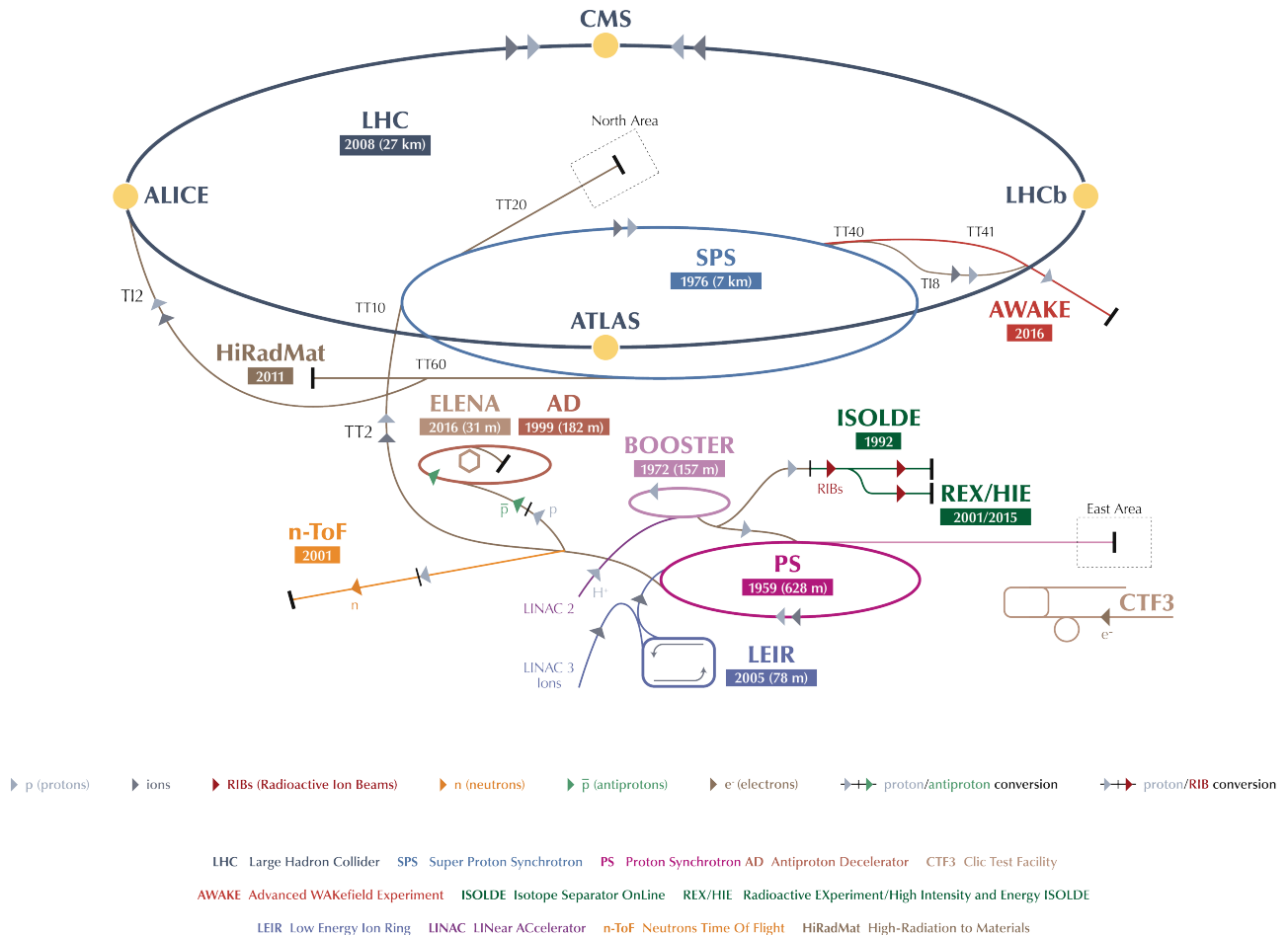


Figure 3.1.2: The CERN accelerator complex as of 2016 [73].

### 3.1.4 Detectors at LHC

There are four major experiments located at four collision points (See Figure 3.1.1) along the LHC where the beamlines of two oppositely running beams cross and beam collisions happen, they are called ALICE (**A L**arge **I**on **C**ollider **E**xperiment) [74], ATLAS (**A T**oroidal

LHC **A**pparatu**S**) [64], CMS (**C**ompact **M**uon **S**olenoid) [75], LHCb (**L**arge **H**adron **C**ollider **b**eauty) [76] respectively. Among the experiments ATLAS and CMS are the only two experiments where all-purpose detectors are installed. They are designed to measure a wide range of physics objects and processes. ALICE focuses on lead-ion collision and LHCb is a forward detector specializes in measurement of $b$-hadrons. There are three other detectors TOTEM (**TOT**al **E**lastic and diffractive cross section **M**easurement) [77], MoEDAL (**Mo**nopole and **E**xotics **D**etector **A**t the **L**HC) [78] and LHCf (**L**arge **H**adron **C**ollider **f**orward) [79] which are much smaller in size and are designed for very specific research.

## 3.2   The ATLAS experiment and detector

The ATLAS detector is an all-purpose detector designed to measure a plethora of physics objects. It has a dimension of 25 m in diameter and 44 m in length, weighing approximately 7000 tonnes - roughly twelve times the maximum takeoff weight of the Airbus A380 [80]. It consists of the following sub-detectors for the reconstruction of different physics objects: the inner detector (ID) for tracking of charged particles, the electromagnetic and hadronic calorimeters for electrons, photons, $\tau$ and jet reconstruction and the muon spectrometer (MS) for reconstruction of muons. A magnet system is installed to provide the necessary magnetic field to make momentum measurement of charged particles possible. It consists of a thin solenoid placed at the outer radius of the inner detector and three independent air core toroids placed in the muon spectrometer outside the hadronic calorimeter. A cut-away diagram of the ATLAS detector is shown in Figure 3.2.1. A high quality trigger and data acquisition system allows timely filtering and storage of useful events given the astronomically high rate of collisions and limited resources.
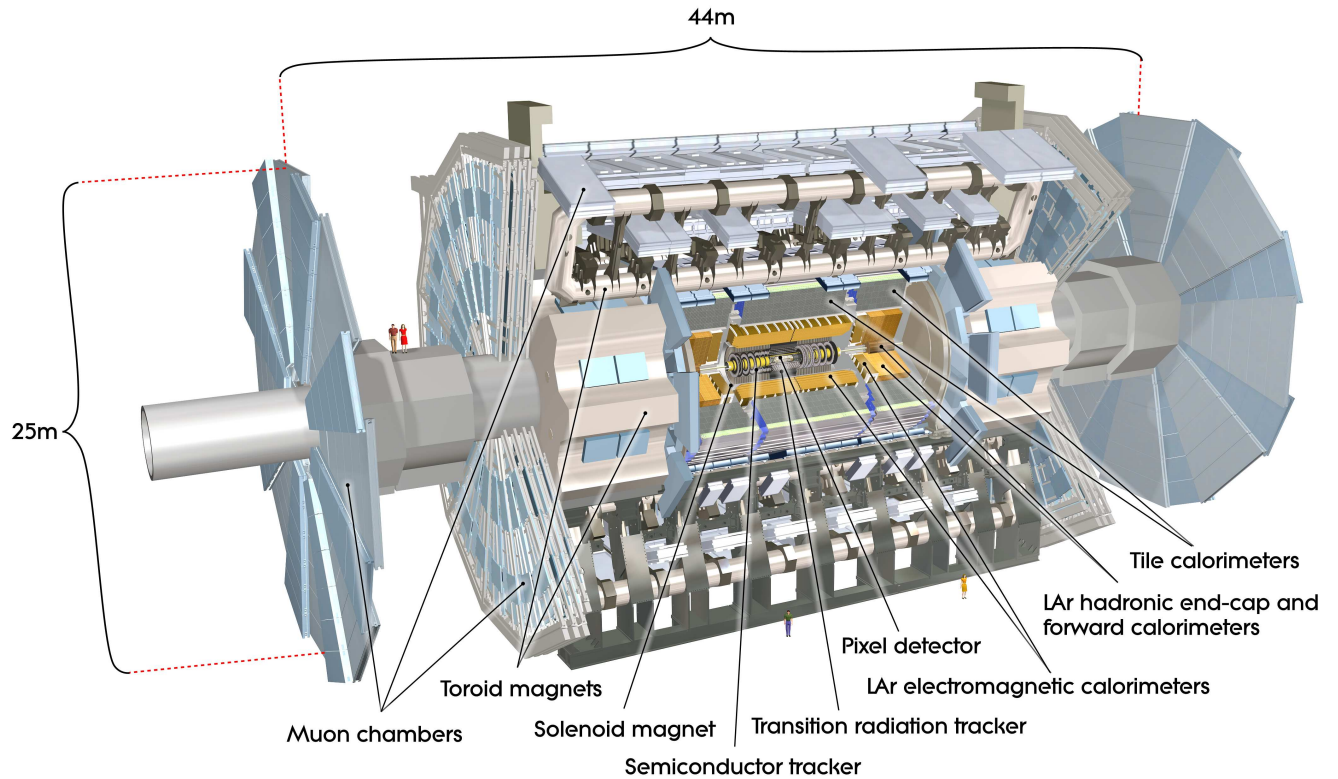
Figure 3.2.1: Cut-away view of the ATLAS detector. The dimensions of the detector are 25 m in height and 44 m in length. The overall weight of the detector is approximately 7000 tonnes. [64]

## 3.2.1 The coordinate system

The coordinate system used in ATLAS is described here as it is frequently used throughout this thesis. It is a right-handed coordinate system centered on the nominal interaction point with the $x$-axis pointing towards the center of the LHC ring, $y$-axis vertical and $z$-axis along the beam line. The half of the detector on the positive $z$-axis is referred to as the "A-side" while the other half is the "C-side". Events are often described using polar coordinates. The azimuthal angle $\phi$ is measured from the $x$-axis around the beamline and the polar angle $\theta$ is measured from the positive $z$-axis towards the $y$-axis. The rapidity is defined as

$$y = \ln \sqrt{\frac{E + p_z}{E - p_z}}. \tag{3.2.1}$$

It is preferred over $\theta$ since differences in rapidity are Lorentz invariant under boosts along the beamline ($z$-axis). For highly relativistic particle, pseudorapidity is preferred as a good approximation to rapidity as differences between $E$ and $p$ are hard to measure. It is defined as

$$\eta = -\ln \tan(\frac{\theta}{2}) \tag{3.2.2}$$

and it goes from zero at the transverse ($x$-$y$) plane to plus or minus infinity along the beamline. The distance $\Delta R$ is defined using the pseudorapidity and the azimuthal angle as $\Delta R = \sqrt{(\Delta \eta)^2 + (\Delta \phi)^2}$. The transverse momentum $p_T$, the transverse energy $E_T$ and the transverse missing energy $E_T^{miss}$ are all defined in the transverse plane. Conservation of momentum can be used in the transverse plane to calculate the transverse missing energy since we know that the initial transverse momentum is zero. In contrast, the $z$ momenta of the initial colliding partons are often unknown. It is therefore important to use quantities that are not sensitive to boosts along the $z$-axis, such as relative rapidity ($\Delta y$), relative pseudorapidity ($\Delta \eta$), distance ($\Delta R$), and the aforementioned transverse quantities.

## 3.2.2  Performance goals

The benchmark physics goals include good momentum resolution and reconstruction efficiency for charged particles in the inner detecter. A good electromagnetic calorimetry for electron and photon identification and measurement. An excellent and hermetic hadronic

calorimetry for jet measurement and accurate determination of missing transverse energy. Inner detector together with the muon spectrometer must accurately reconstruct and measure low-$p_T$ muons. The muon spectrometer must also be able to independently identify and measure high-$p_T$ muons. Lastly, a highly efficient triggering system is required to trigger on low transverse-momentum objects with sufficient background rejection, which is essential to many physics processes of interest. The general performance goals of the ATLAS detector are listed in Table 3.2.

Table 3.2: General performance goals of the ATLAS detector. For high-$p_T$ muons, the muon-spectrometer performance is independent of the inner detector system. The units for $E$ and $p_T$ are in GeV. [64]

| Detector component | Required resolution | $\eta$ coverage | |
|---|---|---|---|
| | | Measurement | Trigger |
| Tracking | $\sigma_{p_T}/p_T = 0.05\% p_T \oplus 1\%$ | $\pm 2.5$ | |
| EM calorimetry | $\sigma_E/E = 10\%/\sqrt{E} \oplus 0.7\%$ | $\pm 3.2$ | $\pm 2.5$ |
| Hadronic calorimetry (jets) | | | |
|    barrel and endcap | $\sigma_E/E = 50\%/\sqrt{E} \oplus 3\%$ | $\pm 3.2$ | $\pm 3.2$ |
|    forward | $\sigma_E/E = 100\%/\sqrt{E} \oplus 10\%$ | $3.1 < |\eta| < 4.9$ | $3.1 < |\eta| < 4.9$ |
| Muon spectrometer | $\sigma_{p_T}/p_T = 10\%$ at $p_T = 1$ TeV | $\pm 2.7$ | $\pm 2.4$ |

The following sections describe each subdetector separately, following closely the reference [64].

## 3.2.3 Inner detector

The ATLAS inner detector [81,82] is the most important sub-detector to our analysis because it is where the $\Lambda^0$ or $\bar{\Lambda}^0$ hyperon decays and then reconstructed as a secondary vertex formed by a pair of positively and negatively charged tracks.

The inner detector is contained in the cavity of the electromagnetic calorimeter (ECal). It
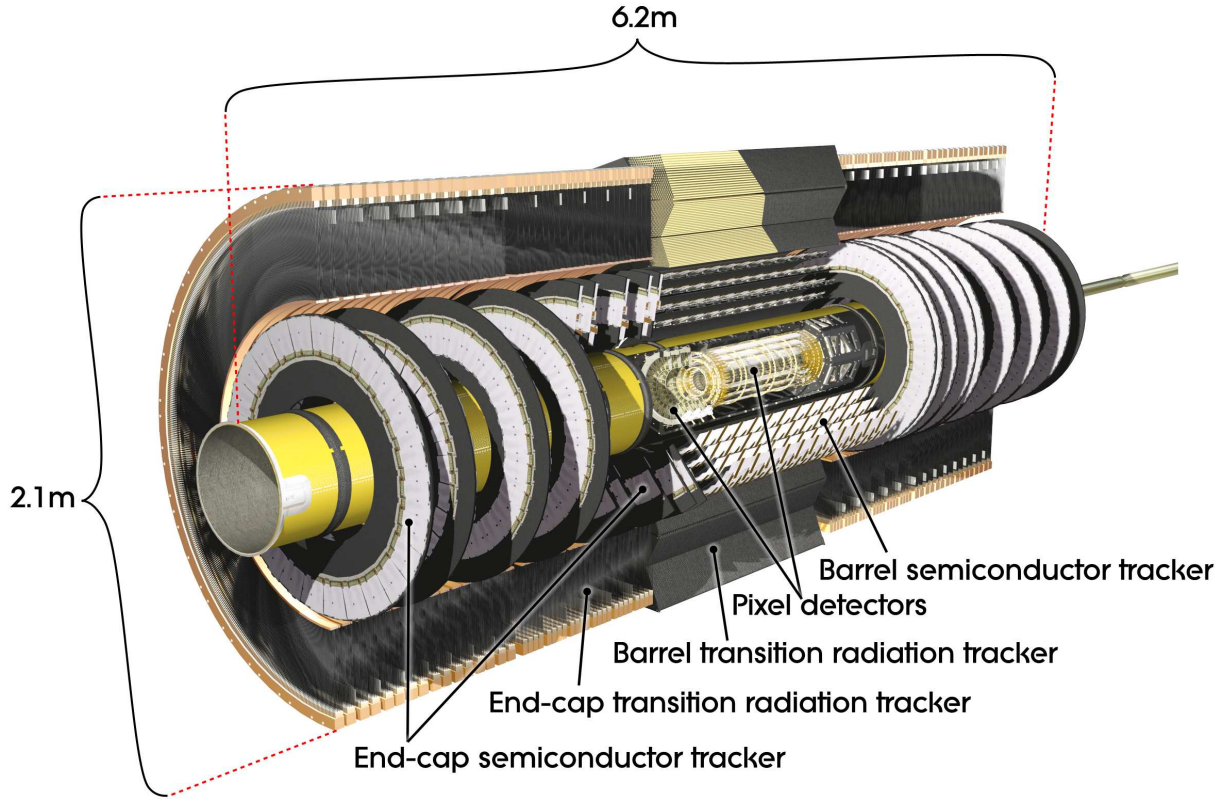
Figure 3.2.2: Cut-away view of the ATLAS inner detector. [64]

is 7 m long, with a radius of 1.15 m. It is designed for robust pattern recognition, accurate measurement of momentum, both primary and secondary vertex measurements and electron identification. It consists of high resolution silicon pixel and strip detectors in the inner part of the tracking volume and a continuous straw-tube tracking detectors with transition radiation capability in its outer part. The silicon detectors are arranged in cylindrical layers parallel to the beam axis in the barrel region and perpendicuar discs in the end-cap region. Each layer consists of a number of modules with independent read-out electronics.

- Pixel technology (Pixel) [83, 84] is used for the innermost part of the tracking system with high granularity around the interaction point for vertex reconstruction. It has

three layers in the barrel region and three layers in the end-cap discs. Digital readout allows limited measurement of charge deposited in the pixel by charged particles. It also has the finest granularity of all the ID components with over 80 million of readout channels. The spatial resolution is 10 $\mu$m in $\phi$ direction and 115 $\mu$m in $z$ direction.

- SemiConductor Tracker (SCT) [85] is made of four barrel layers and nine endcap discs on each side. It provides precise measurement of track space-points. Silicon micro-strip technology is used to minimize cost and the number of readout channels (totaled at about 6 millions). The drawback is that it measures in only one dimension per-pendicular to the strip. A two-dimensional position measurement is made possible in each module by using two silicon wafers rotated by an angle of 40 mrad. The spatial resolution of the SCT is 17 $\mu$m in $\phi$ direction and 580 $\mu$m in $z$ direction.

- Transition-Radiation Tracker (TRT) [86] is located in the outermost part of the ID. The TRT straws are laid in parallel to the beam in the barrel region and radially in the endcaps.The TRT straws are surrounded by radiator. Charged particle passing the radiator produces transition radiation proportional to its Lorentz factor $\gamma$. There are two thresholds on charge deposited in the straws - which is proportional to the intensity of a transition radiation - distinguish relativitic electrons and low-$p_T$ hadrons.

A typical track has 3 pixel layers and 8 strip layers with typically four space points. A large number of tracking points (typically 36 per track) is provided by TRT.
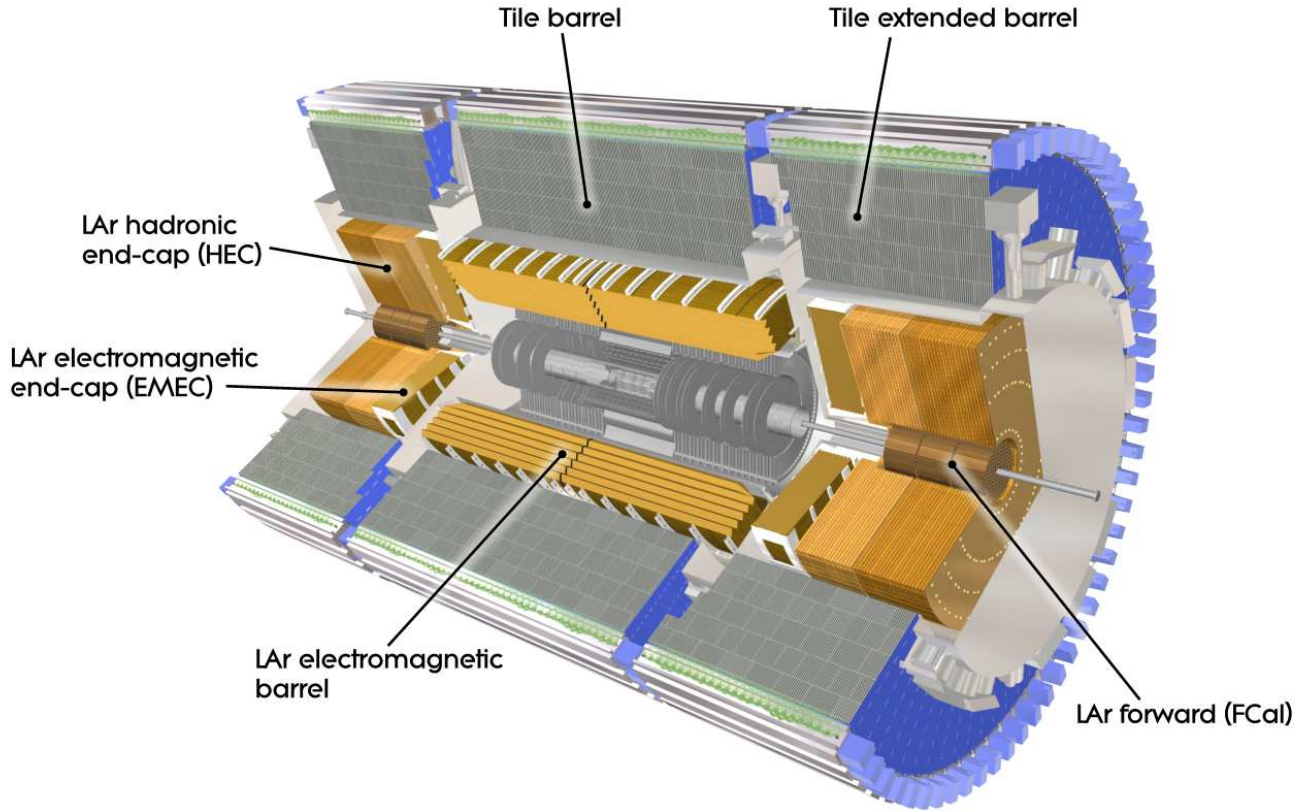
Figure 3.2.3: Cut-away view of the ATLAS calorimeter system. [64]

## 3.2.4   Calorimeters

The ATLAS calorimeters [87–89] consist of several sampling detectors with $\phi$-symmetry and full coverage over the range $|\eta| < 4.9$. Over the $\eta$ region matched to the inner detector, the fine granularity of the EM calorimeter is well suited for the precision measurement of elections, photons, $\tau$'s, hadronic jets and $E_T^{\mathrm{miss}}$. A cut-away view of the calorimeter system is available in Figure 3.2.3. Both the EM and hadronic calorimeters consist of an absorber and an active material. The absorber is usually of high density and serves for electromagnetic and hadronic shower development. The active material collects and measures the energy

deposited, which is usually a fraction of the total energy of the parent particle. Calibration is then done to calculate the energy of the parent particle. Different calorimeters are described below:

- The EM calorimeter uses liquid Argon (LAr) as the active material and lead plates as the absorber. It consists of the barrel region in $|\eta| < 1.475$ and the endcap region in $1.375 < |\eta| < 3.2$. Alternating sampling layers of 2.1 mm are filled by LAr with readout electrodes in the middle. The lead absorber plates are typically 2 mm thick, all shaped in a novel accordion geometry to allow fast response and full azimuthal coverage without dead regions. There is also a presampler layer of only LAr in $|\eta| < 1.8$ to measure the energy lost by electrons and photons to the material before the calorimeter.

- The hadronic calorimeter uses steel as the absorber and plastic scintillating plates (tiles) as the active material. It consists of the tile calorimeter in the barrel region in $|\eta| < 1.0$, the extended barrel region in $0.8 < |\eta| < 1.7$. The tiles are 3 mm thick and the total thickness of the iron plates in one period is 14 mm. Two sides of the scintillating tiles are read out by wavelength shifting fibers into two separate photomultipliers.

- The LAr hadronic endcap calorimeter uses copper as the absorber and the LAr forward calorimeter uses copper and tungsten. Both calorimeter use LAr as the active material. The LAr hadronic endcap region covers $1.5 < |\eta| < 3.2$ and the LAr forward calorimeter covers $3.1 < |\eta| < 4.9$.

The calorimeter is expected to completely contain the EM and hadronic showers to avoid any punch-through into the muon system. The total amount of material before the first active layer of the muon system in units of nuclear interaction length is shown in Figure 3.2.4.
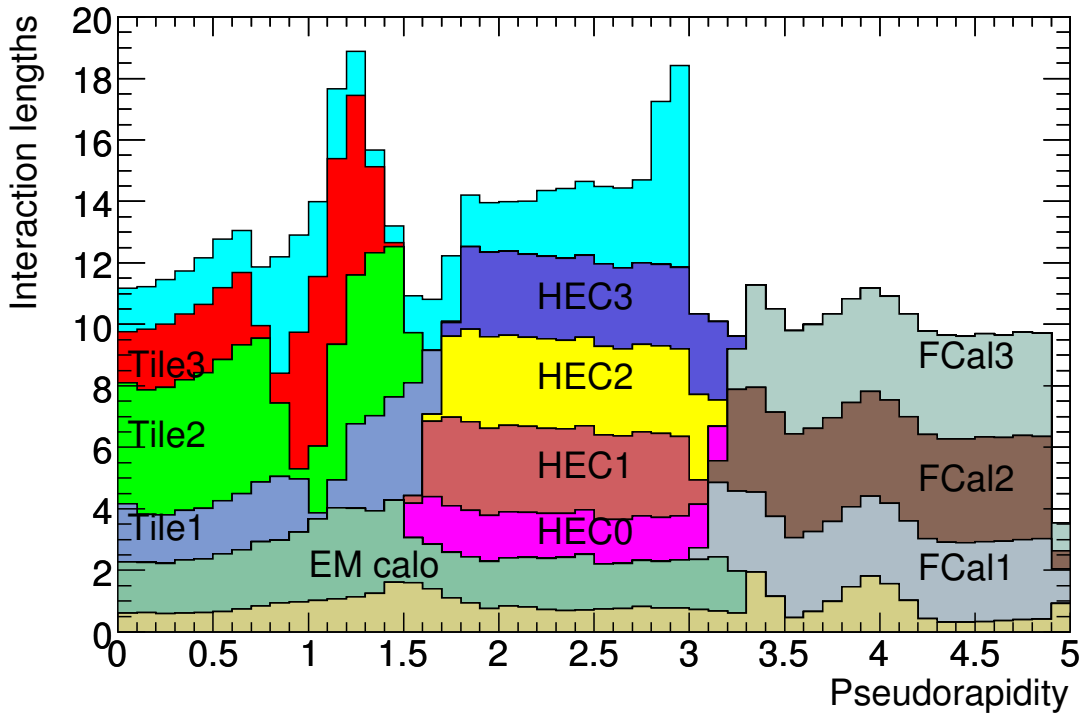
Figure 3.2.4: Cumulative amount of material, in units of interaction length, as a function of $|\eta|$, in front of the electromagnetic calorimeters, in the electromagnetic calorimeters themselves, in each hadronic compartment, and the total amount at the end of the active calorimetry. Also shown for completeness is the total amount of material in front of the first active layer of the muon spectrometer (up to $|\eta| < 3.0$). [64]

### 3.2.5   Muon spectrometer

The muon spectrometer [90] is located in the outer part of the ATLAS detector enclosing the calorimeters. It is designed to detect charged particles exiting the barrel and end-cap calorimeters and to measure their momentum precisely. It covers the pseudorapidity range $|\eta| < 2.7$ and is designed to trigger on these charged particles in the range $|\eta| < 2.4$. It has a performance goal of a standalone transverse momentum resolution of 10% for 1 TeV tracks. The measurement of momentum is based on the principle of magnetic bending of

the trajectories of charged particles by a magnetic field. The magnetic field is provided by large superconducting air-core toriod magnets in the barrel region and two smaller end-cap magnets inserted in the barrel toroid at each end and lined up with the central solenoid. The barrel toroid provides 1.5 to 5.5 Tm of bending power in the pseudorapidity range $0 < |\eta| < 1.4$ and the end-cap toroid provides 1 to 7.5 Tm in the range $1.6 < |\eta| < 2.7$. A cut-away view of the muon spectrometer is shown in 3.2.5.
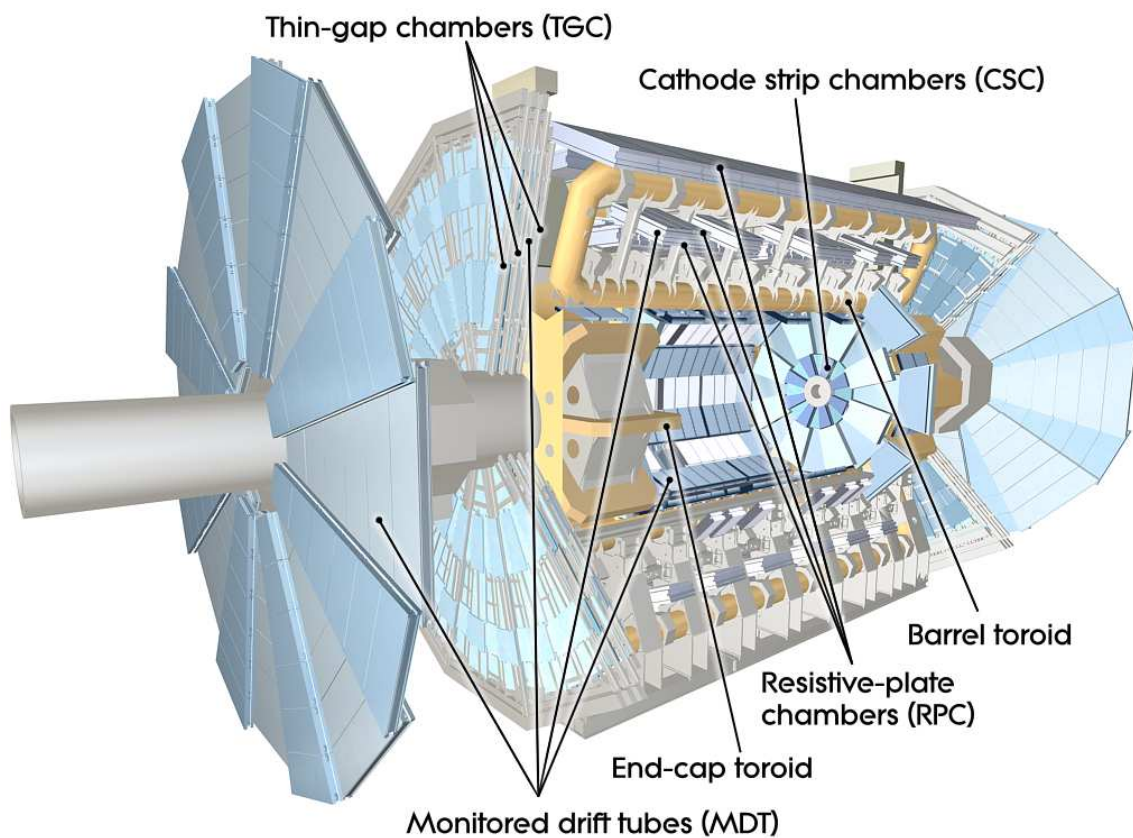


Figure 3.2.5: Cut-away view of the ATLAS muon system. [64]

Monitored Drift Tube (MDT) chamber is used for precision tracking due to its high measurement accuracy, predictability of mechanical deformations and simplicity of construction. It consists of three stations arranged as three concentric cylindrical shells around the beam

axis in the barrel region ($|\eta| < 1.0$), and four stations in the endcap region ($1.0 < |\eta| < 2.7$), arranged as four disks. The MDT is a pressurized cathode tube with a diameter of 29.970 mm, filled with 93% Argon and 7% $CO_2$ maintained at 3 bar. The central tungsten-rhenium anode wire has a diameter of 50 $\mu$m and is maintained at a potential of 3080 V. Electrons resulting from the ionization of muons passing through the pressurized gas are collected at the central wire and the drift time gives the shortest distance between the central wire and the muon tracks. The concentricity of the wire is guaranteed with respect to the tube with an accuracy of 10 $\mu$m. The average resolution is 80 $\mu$m per tube layer and 35 $\mu$m per chamber.

Cathode Strip Chambers (CSC) is used to replace the innermost disk of the MDT in the endcap region ($2.0 < |\eta| < 2.7$) due to their higher rate capability and time resolution. They are multiwire proportional gas chambers filled with 80% Argon and 20% $CO_2$, maintained at 1 bar. The chambers are segmented into small and large chambers with gold-plated tungsten-rhenium anode wires of diameter 30 $\mu$m maintained at 1900 V, oriented in the radial direction. The cathode strips are segmented and are oriented both parallel and orthogonal to the anode wires. They allow both coordinates to be measured from the induced-charge distribution with a spatial resolution of the chamber is 60 $\mu$m per CSC plane and a time resolution of 7 ns. The CSCs have a maximum drift time of about 20 ns, compared to about 700 ns for the MDT chambers.

Two types of fast tracking chambers are installed to deliver track information for triggering within a few nanosecond after the passage of the particle. They are the Resistive Plate Chambers (RPC) in the barrel region ($|\eta| < 1.05$) and the Thin Gap Chambers (TGC) in the endcap region ($1.05 < |\eta| < 2.4$). The design goal is the keep a reliable beam-crossing identification with over 99% probability.

In the barrel region, RPCs are used due to good spatial and time resolution as well as

adequate rate capability. A RPC has no wires, which simplifies its construction and makes chambers less sensitive to small deviations from planarity if appropriate spacers are used to keep the gap width constant. Being located in the comparatively homogeneous field of the barrel toroid and having sufficient spacing between the three trigger layers, RPCs give sufficient trigger selectivity even with moderate channel count, i.e. spatial resolution. They have a spatial resolution of 10mm in both $z$ and $\phi$ directions per chamber and a time resolution of 1.5 ns.

In the endcap region, TGCs have been selected: they operate on the same principle as multi-wire proportional chambers, and they provide good time resolution and high rate capability. Their spatial resolution is mainly determined by the readout channel granularity, which can be adjusted to the needs by wire ganging. TGCs have demonstrated a high level of reliability and robustness in previous experiments. They have a spatial resolution of 2 - 6 mm in $R$ and 2 - 7 mm in $\phi$ directions per chamber and a time resolution of 4 ns.

## 3.2.6   Magnet system

This section gives a brief description of the magnetic system [91], which consists of a central solenoid and three toroids (one barrel and two end-caps). A diagram of the magnet windings and tile calorimeter steel of the ATLAS magnet system is shown in Figure 3.2.6.

The ATLAS detector uses a superconducting magnet system to bend charged particles and to measure their momenta. This bending is due to the Lorentz force and is proportional to the velocity of the particle. It is perpendicular to both the velocity of the particle and the direction of the magnetic field. Since particles produced at the LHC energy are traveling at very close to the speed of light, the forces acting on particles of different momenta are

roughly equal. As a consequence, high-momentum particles get deflected very slightly, while low-momentum particles curve significantly. The amount of curvature of the track of a particle can therefore be used to determine its momentum. For a three-point measurement, the relative momentum resolution degrades linearly with transverse momentum, improves linearly with increasing magnetic field and quadratically with radial extension of detector.

The magnet system is arranged such that the Central Solenoid (CS) [92] provides the Inner Detector with magnetic field, surrounded by a system of three large air-core toroids generating the magnetic field for the muon spectrometer. The CS extends over a length of 5.3 m and has a bore of 2.4 m. The two End-Cap Toroids (ECT) [93] are inserted into the Barrel Toroid (BT) [94] at each end and line up with the CS. The BT consists of eight very large air-core superconducting barrel loops. They have a length of 5 m, an outer diameter of 10.7 m and an inner bore of 1.65 m. The overall dimensions of the magnet system are 26 m in length and 20 m in diameter and it stores a total of 1.6 GJ of energy.

The CS provides a central field of 2 T with a peak magnetic field of 2.6 T at the superconductor itself. Its near uniform direction and strength allow very accurate measurement to be made. Particles with momenta below about 400 MeV will be curved so strongly that they will loop forever in the field and most likely not measured. The BT and ECT have peak magnetic fields on the superconductor at 3.9 and 4.1 T respectively. The BT provides 2 to 6 Tm and the ECT contributes with 4 to 8 Tm in the 0.0 - 1.3 and 1.6 - 2.7 pseudorapidity ranges respectively. The bending power is lower in the transition regions where the two magnets overlap $(1.3 < |\eta| < 1.6)$.

The magnets are cooled by forced flow of helium at 4.5 K through tubes welded on the casting of the windings. The CS is cooled via a dewar coupled to the refrigerator. The BE and ECT have cold helium pumps to guarantee cooling by forced helium flow. A central

refrigeration plant located in the side cavern supplies the cooling power and the services are distributed among the four magnets. Electrically all torioid coils are connected in series, they have a 21 kA power supply and are equipped with control systems for fast and slow energy dumps. The CS is energized by an 8 kA power supply. A quench protection system is used to safety dissipate the stored energy without overheating the coil windings.
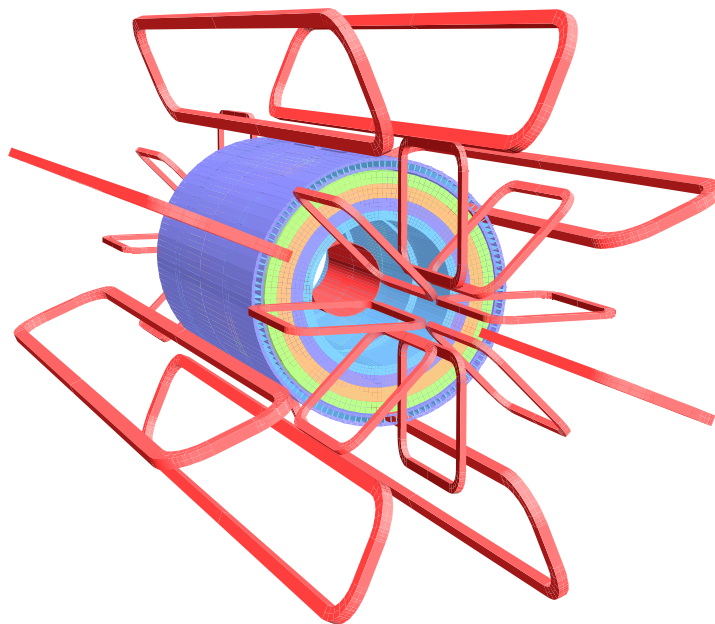


Figure 3.2.6: Geometry of magnet windings and tile calorimeter steel. The eight barrel toroid coils, with the end-cap coils interleaved are visible. The solenoid winding lies inside the calorimeter volume. The tile calorimeter is modelled by four layers with different magnetic properties, plus an outside return yoke. For the sake of clarity the forward shielding disk is not displayed. [64]

### 3.2.7 Trigger and data acquisition systems

In order to cope with large volumes of data within nanosecond timescales, the 'trigger' system is designed to select interesting events quickly and efficiently. Roughly one billion events per

second occur within the ATLAS detector at LHC design intensity. It is technically impossible to store all the data for all events. It is therefore necessary to develop a strategy to reject uninteresting events and retain only the interesting ones. This is done in three successive stages carried out by the trigger system [95]. They include a hardware-based Level-1 (L1) trigger and a two-stage High Level Trigger (HLT) consisting of the Level-2 (L2) and the event filter (EF) triggers. Each trigger level refines the decision made at the previous level and applies additional selection criteria. A schematics of the trigger and data acquisition system in 2012 (Run 1) is shown in Figure 3.2.7.
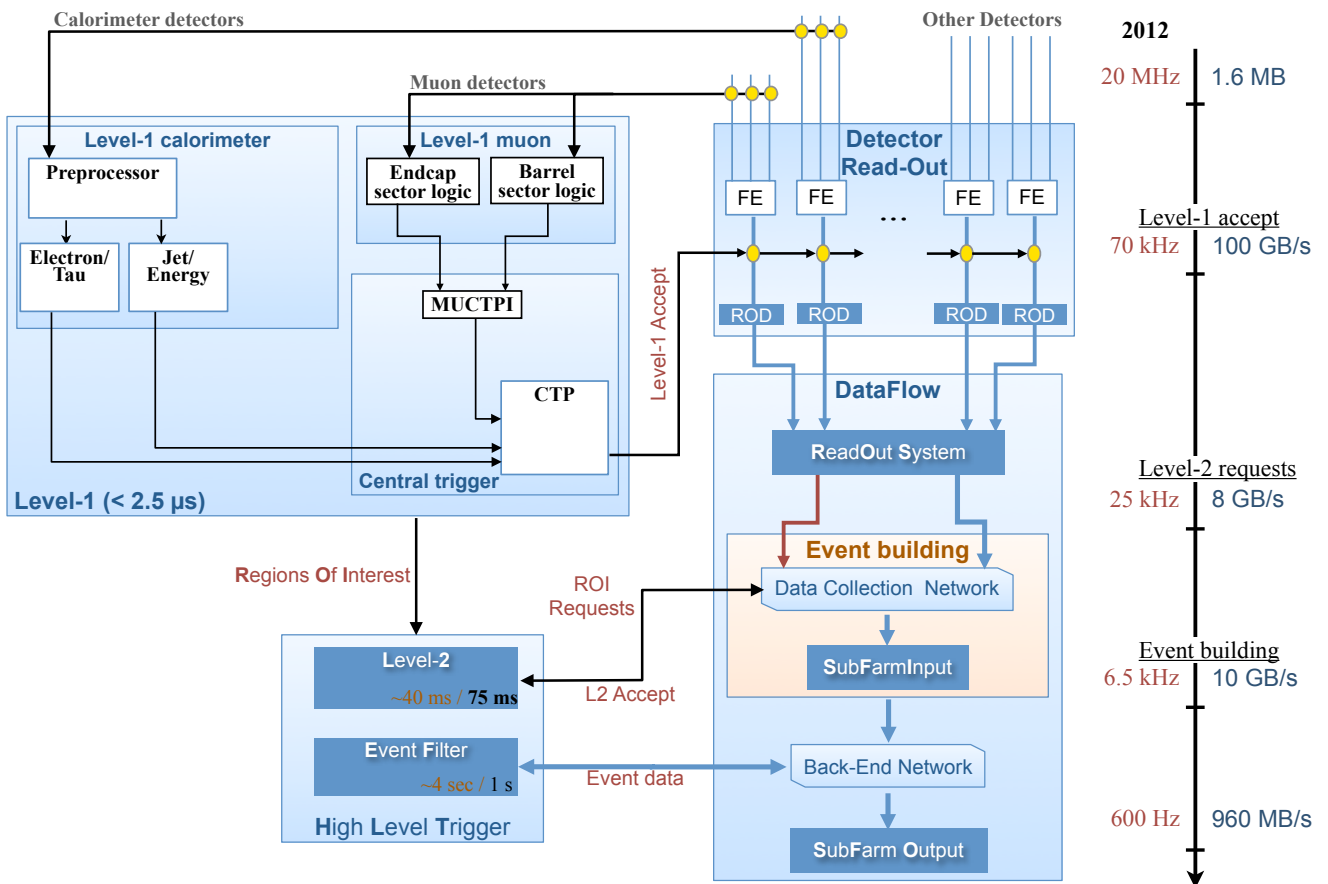


Figure 3.2.7: Block diagram of the ATLAS trigger and data acquisition systems in 2012 (Run 1). [96]

The L1 trigger [97] reduces the event rate from 40 MHz to 75 kHz within a time frame of 2.5 microseconds. It uses reduced-granularity information from a subset of detectors for different objects. The muon triggers consist of the RPC and TGC, which are triggered by high-$p_T$ muons. Muon tracks are found by measuring hits in one plane and then searching for additional hits in nearby planes along pre-determined patterns. The calorimeter trigger receives 7,200 analog signals from the electromagnetic and hadronic calorimeters, which are a sum of several calorimeter cells and are of reduced granularity. Specialized hardware is used to search for patterns as expected for electrons, photons, $\tau$-leptons and jets. The L1 calorimeter system can also calculate the amount of missing energy in an event. For each object found by the L1 systems, a 'region of interest' (RoI) is identified. Analog signals from the interacting particles are processed by the front-end electronics and are digitized and stored in the Level-1 buffer. The data waits in these buffers until the decision from the L1 trigger is made. The identified objects are sent to a central trigger processor where up to 128 different criteria are stored. If the event passes one of the stored criteria, a so-called L1 accept is sent to the detector which signals the front-end hardware to send the data to the Readout Drivers (RODs), otherwise the data is removed from the L1 buffer.

The L2 trigger reduces the event rate to below 3.5 kHz within 10 milliseconds. It is seeded by the regions of interest and it runs more complex lepton, photon and jet identification algroithms using information from the tracking detectors, the muon spectrometer and the full granularity information from the calorimeters. If the event passes one of the 256 different L2 event criteria, the full detector information is sent to the event filter system, where a final selection is carried out.

The EF trigger reduces the event rate to 200 Hz within one second. It uses offline analysis procedures on fully-built events using commercial computers. Over 17,000 computing cores

are used in L2 and event filter systems. If the event is selected, the data is transferred to permanent storage at the CERN computing center for offline analysis, otherwise the event is deleted from the RODs.
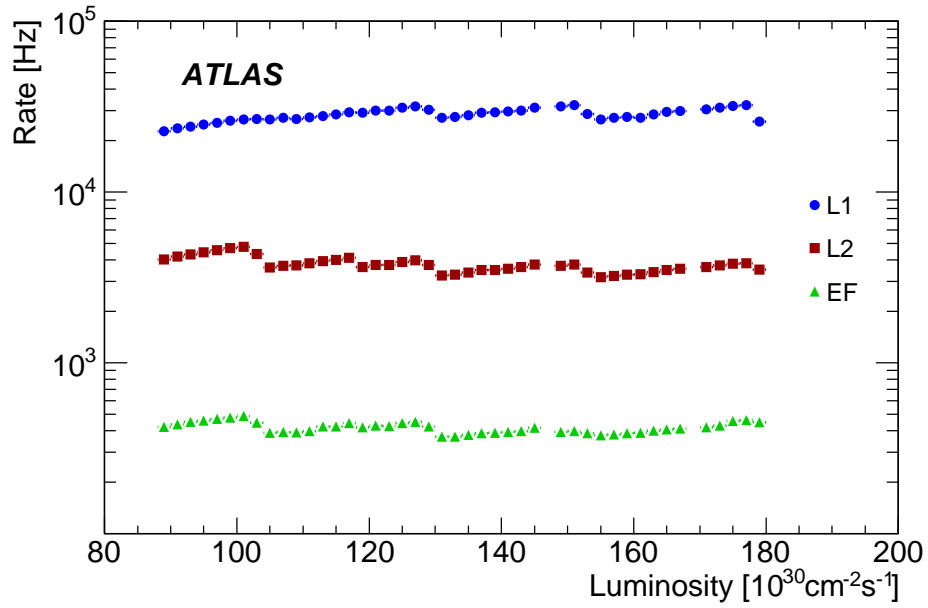


Figure 3.2.8: Total output trigger rates as a function of instantaneous luminosity in a sample run from period I for each trigger level in 2010. [98]
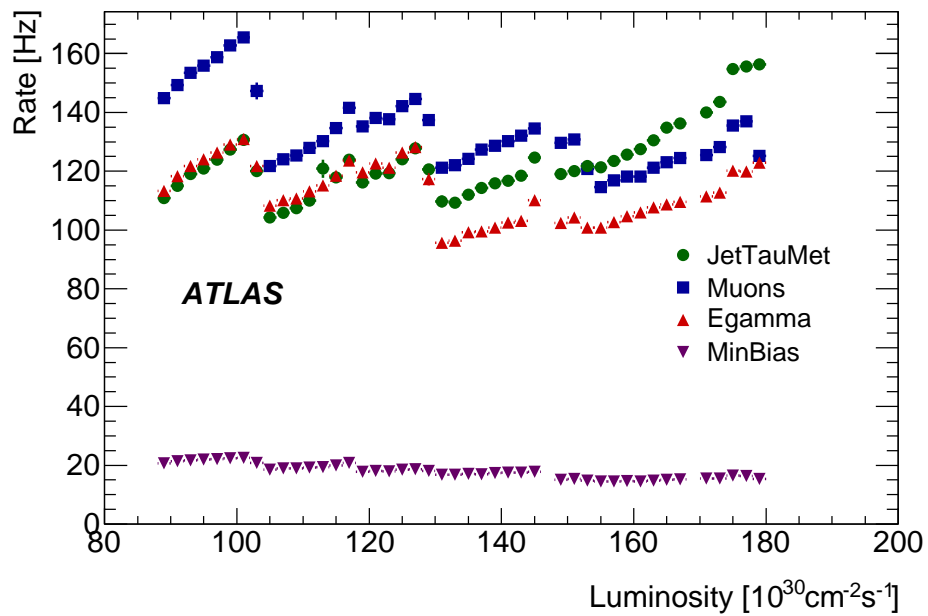
Figure 3.2.9: Total output trigger rates as a function of instantaneous luminosity in a sample run from period I for each stream in 2010. B-jet triggers are included in the JetTauEtmiss stream and B-physics triggers are included in the muon stream. [98]

# Chapter 4

# Data and simulation samples

This chapter describes the minimum bias and the muon stream data samples, the mixed data sample, and the Monte Carlo sample used in this analysis. The muon and minimum bias trigger systems at ATLAS are also described in detail.

## 4.1 Data sample

The data set used in this analysis was recorded by ATLAS in 2010 of proton-proton collisions provided by the LHC at the center-of-mass energy of 7 TeV. The integrated luminosity for each period in 2010 running is shown in Table 4.1 and Figure 4.0.1. The periods A-H add up to an integrated luminosity of 22.12 pb$^{-1}$.

Ideally, the minimum bias stream sample should be used to reduce biases introduced by the triggers. However, due to relatively low statistics of the sample, the muon stream sample, which is the data stream with the highest statistics, is used in the full analysis of the spin correlation extraction and systematic uncertainties estimation. The results of analysis using
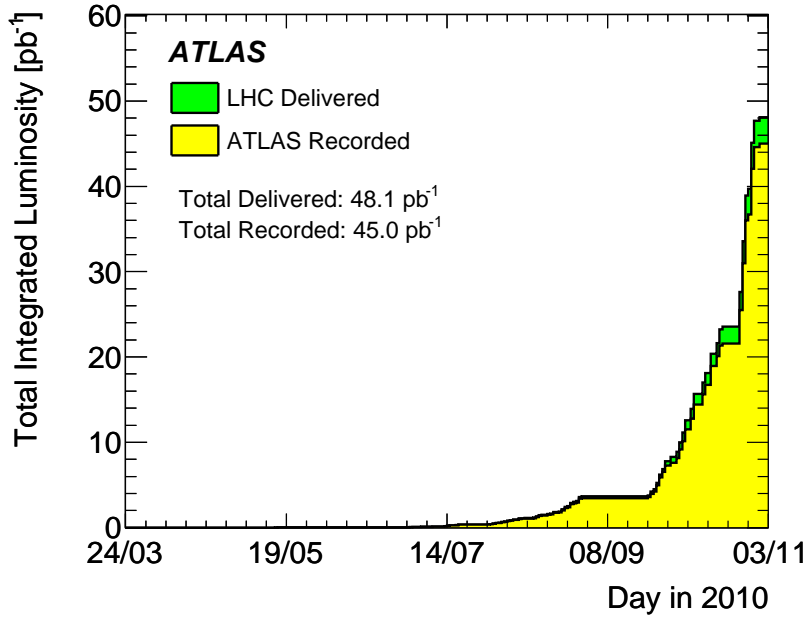
Figure 4.0.1: Profile with respect to time of the cumulative luminosity recorded by ATLAS during stable beams in $\sqrt{s} = 7$ TeV $pp$ collisions in 2010. [98]

Table 4.1: Data-taking periods for proton-proton runs in 2010 [98].

| Period | $\int \mathcal{L}[\mathrm{pb}^{-1}]$ | Max. $\mathcal{L}[\mathrm{cm}^{-2}\mathrm{s}^{-1}]$ |
|--------|-----------------|------------------|
| A | $0.4 \times 10^{-3}$ | $2.5 \times 10^{27}$ |
| B | $9.0 \times 10^{-3}$ | $6.8 \times 10^{28}$ |
| C | $9.5 \times 10^{-3}$ | $2.4 \times 10^{29}$ |
| D | 0.3 | $1.6 \times 10^{30}$ |
| E | 1.4 | $3.9 \times 10^{30}$ |
| F | 2.0 | $1.0 \times 10^{31}$ |
| G | 9.1 | $7.1 \times 10^{31}$ |
| H | 9.3 | $1.5 \times 10^{32}$ |
| I | 23.0 | $2.1 \times 10^{32}$ |

the minimum bias sample with limited statistics is then used to compare with the muon sample results to make sure no large discrepancy between the two samples.

A Good Runs List (GRL)* is used to ensure the detector conditions and data quality match

---

*data10_7TeV.periodAllYear_DetStatus-v21-pro05_CoolRunQuery-00-04-00_Tracking.xml

the standard approved by the ATLAS data quality group. Only luminosity blocks selected in the GRL is used for event selection in the analysis. The trigger selection has been removed to maximize the data statistics. Trigger mappings as shown in Figures 9.0.4 and 9.0.5 are created for the minimum bias and muon streams separately to determine the trigger distributions and hence the dominant triggers in each data stream.

### 4.1.1 Muons stream sample

The periods A1-D6 in `physics_MuonswBeam`[†] stream contain about 53M events and the periods E1-H2 in `physics_Muons`[‡] stream contain about 131M events have been used in the muon stream sample.

### 4.1.2 Minimum Bias stream sample

The periods A-H in `physics_MinBias`[§] stream contains about 167M events have been used in the minimum bias stream sample.

## 4.2 Triggers

### 4.2.1 Muon triggers

Muons are triggered in the ATLAS experiment within a rapidity range of $|\eta| < 2.4$. This region is segmented into the endcap region ($|\eta| > 1.05$) and barrel region ($|\eta| < 1.05$). The

---

[†]data10_7TeV.period[A-D].physics_MuonswBeam.PhysCont.AOD.repro05_v02/
[‡]data10_7TeV.period[E-H].physics_Muons.PhysCont.AOD.repro05_v02/
[§]data10_7TeV.period[A-H].physics_MinBias.PhysCont.AOD.repro05_v02/

barrel region of the MS includes RPCs to provide fast trigger signals and MDTs for precision hits in the $\eta$ coordinate. The endcap region is equipped with TGCs for the trigger signals and MDTs for precision hits. CSCs are also installed in $2 < |\eta| < 2.4$ to reduce the background sensitivity in this region.

At L1, muons are selected using hit information from the RPC and TGC detectors. A coincidence is formed from $\eta$ and $\phi$ projections of hits in different layers of the muon stations. Muon candidates are then passed on to the high level trigger which encompasses a fast algorithm stage (L2) and the event filter. At L2 the candidate from L1 is refined including the data of the precision muon detectors and other detector elements. The L2 MS only algorithm has access to the data in the RoI defined by the L1 candidate. The momentum and track parameters of the muon candidate are refined by fast fitting algorithms and Look-up-tables (LUTs).

A pattern recognition algorithm selects hits from the MDT based on a region identified by the L1. A track fit is performed using the MDT drift times, and a $p_T$ measurement is assigned from LUTs. Additionally, the L2 muon combined algorithm uses the ID tracks to combine the muon candidate reconstructed with data from the MS with tracks from the ID to refine the track parameter resolution. The combination allows to reject muons from in-flight decays of light mesons and from cosmic radiation.

A third algorithm, the L2 isolated muon algorithm, combines MS information, ID tracks and calorimetric information to find isolated muon candidates. The algorithm is seeded by the L2 muon combined algorithm and evaluates the electromagnetic and hadronic energy deposits as measured by the calorimeters in cones centered around the muon direction. For the muon selection two different concentric cones are defined: An internal cone chosen to contain the energy deposited by the muon itself, and an external cone, containing energy
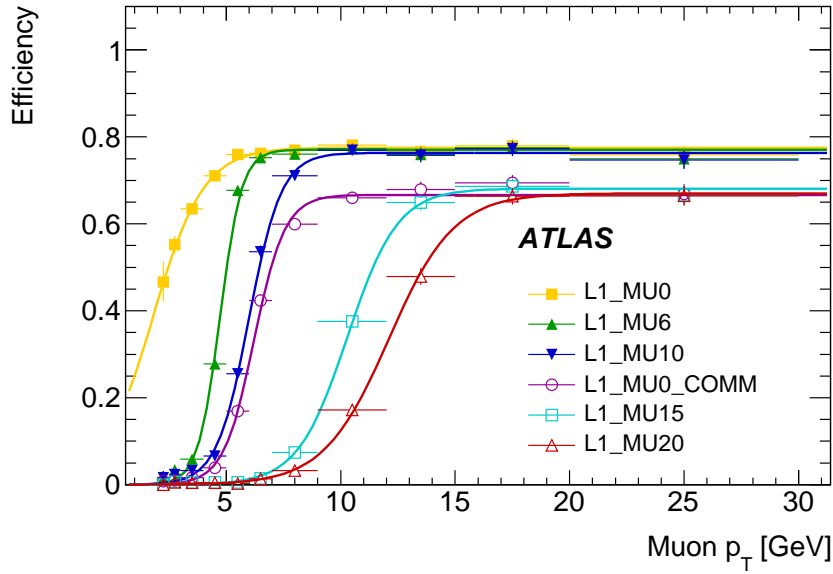
Figure 4.2.1: L1 RPC trigger efficiency for combined muons reconstructed offline. A Fermi function is fitted to the measurements for each trigger. Statistical uncertainties are represented by vertical bars. [98]
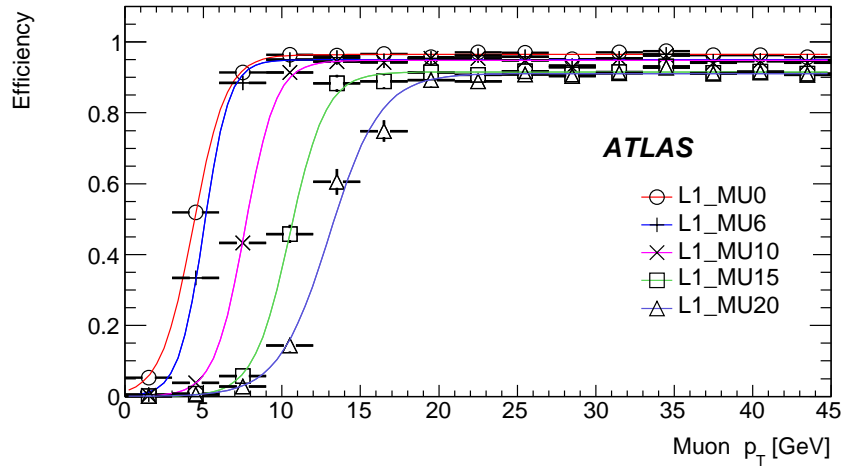


Figure 4.2.2: L1 TGC trigger efficiency for combined muons reconstructed offline. A Fermi function is fitted to the measurements for each trigger. Statistical uncertainties are represented by vertical bars. [98]

from detector noise and other particles.

At the EF level the full event data are accessible. The muon reconstruction starts from the RoI identified by L1 and L2, reconstructing segments and tracks from the trigger and precision chambers. The track is then extrapolated to the interaction region to form a muon candidate using data only from the MS, resulting in the EF MS only trigger. Similar to the L2 algorithms the muon candidate is combined with an ID track to form a EF muon combined candidate. This "outside-in" strategy is complemented by a second algorithm which starts with ID tracks and extrapolates to the muon detectors to form EF muon inside-out candidates. All three EF algorithms rely on offline tools to reconstruct muons online in the trigger.

This section is mainly adapted from Ref. [99].

## 4.2.2 Minimum Bias triggers

The Minimum Bias (MB) trigger [100] is used to select inelastic collisions while avoiding biasing the sample. As its name suggests, some bias is present due to various reasons, such as minimum energy thresholds or limited geometrical acceptance of the trigger. The ATLAS experiment uses two complementary minimum bias triggers, working at different trigger levels.

The MBTS (Minimum Bias Trigger Scintillator) [101] is one of the triggers that have been used in the very early phase of the data taking in order to select Minimum Bias events generated in the proton-proton collisions. The MBTS detector is formed by two disks installed at $|z| = 3.56$ m between the Inner Detector and the Liquid Argon calorimeter in the forward region covering the rapidity range $2.09 < |\eta| < 3.84$. Each disk consists of 16, 2-cm

71

polystyrene-based scintillator counters. The single disk is separated into an inner and an outer ring organized into 8 independent $\phi$ sectors. Light emitted by each scintillator segment is collected by wavelength-shifting optical fibers and guided to a photomultiplier tube (PMT). The PMT signal is read out by the Tile Calorimeter electronics. The MBTS signals, after being shaped and amplified, are fed into leading edge discriminators and sent as 25 ns pulses to the Central Trigger Processor (CTP). The MBTS multiplicity is then calculated for each side independently and with such information three L1 trigger items are formed: `L1_MBTS_1`, `L1_MBTS_2` and `L1_MBTS_1_1`. They require a signal from the electrostatic beam pick-up devices (BPTX), and the first also at least one MBTS hit, the second also at least two MBTS hit and the third also at least one MBTS hit per side respectively. This trigger is highly efficient in selecting inelastic proton-proton collisions.
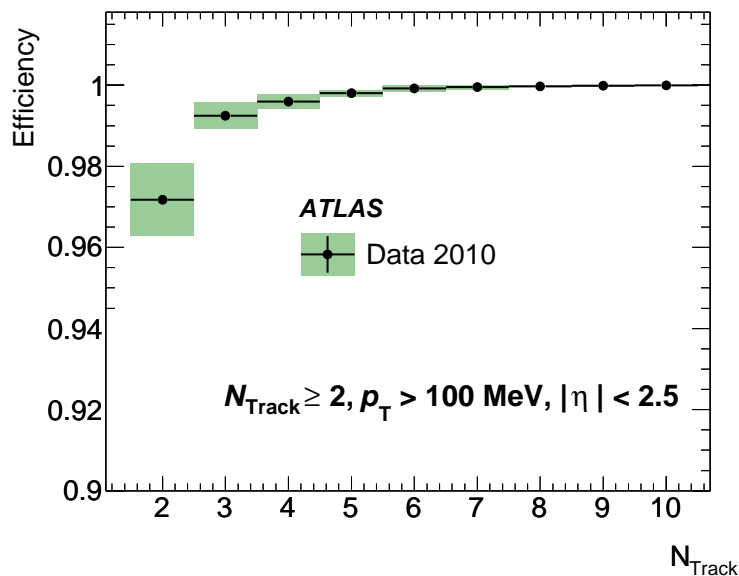


Figure 4.2.3: The `L1_MBTS_1` trigger efficiency for inelastic $pp$ collisions at $\sqrt{s} = 7$ TeV in 2010. The shaded areas represent the statistical and systematic uncertainties added in quadrature. The statistical uncertainty is negligible compared to the systematic uncertainty. [98]

The second is the ID based MB trigger mbSpTrk (control trigger) [102]. It is a supporting trigger designed to be a minimally biased trigger which can be used to measure the trigger efficiencies of the other MB triggers. It uses central tracking detectors to perform inelastic event selection on randomly seeded filled bunches to avoid any selection bias. The trigger mbSpTrk uses the ID Pixel and SCT detectors. It covers the complete ID tracking region up to $|\eta| < 2.5$. The alogrithms detect central detector activity by forming space-points in both Pixel and SCT in the L2 trigger. Track reconstruction is then performed on the whole event at the EF trigger. Both triggers are essential to cover the whole of the particle kinematic spectra.

Other MB triggers include LUCID (LUminosity Cherenkov Integrating Detector) [103, 104], ZDC (Zero Degree Calorimeter) [105] and BCM (Beam Conditions Monitor) [106]. They are forward detectors that can also be used to trigger MB events and expand the pseudorapidity coverage from $5.61 < |\eta| < 5.93$ (LUCID) to $|\eta| > 8.3$ (ZDC).

## 4.3   Mixed data sample

Mixed samples are created by mixing single $\Lambda^0/\bar{\Lambda}^0$ candidates selected from odd and even events. It is used as the reference sample in the correlation function in the dynamcial correlation measurement and is used to build the templates in the spin correlation extraction.

## 4.4   Monte Carlo sample

A sample of 20M minimum bias events was generated with PYTHIA 6.421 [34] using the ATLAS minimum bias tune (AMBT1) [107] and MRST2007LO [108] parton distribution

functions. The GEANT4 package [109] is used to simulate the propagation of generated particles through the detector [110]. GEANT4 also handles decays of long-lived unstable particles, such as pions, kaons and $\Lambda^0$ hyperons. It decays $\Lambda^0$ and $\bar{\Lambda}^0$ with a uniform angular distribution, which corresponds to zero polarization and correlation. Mixed samples are created in a similar manner as the data. Since the MC sample has a somewhat different kinematic distributions when compared to the data sample as shown in Figure 6.4.1 and limited statistics, it has been used only for systematic uncertainty estimation. The mixed data sample is used as the reference sample in the spin correlation extraction.

# Chapter 5

# Reconstruction and candidate selection

This chapter discusses the reconstruction of long-lived 2-prong decay candidates in the inner tracker and the selection of $\Lambda^0$ and $\bar{\Lambda}^0$ candidates, followed by the modeling of signal and background components of the invariant mass distribution and the definition of signal and background regions.

## 5.1 Reconstruction

Long-lived 2-prong decay candidates ($V^0$'s) are reconstructed using the standard ATLAS $V^0$ finder package in default setting. It is designed to reconstruct decays $V^0 \rightarrow f^+ f^-$, where $f^\pm$ are charged tracks. Transition Radiation Tracker (TRT) can be used to identify electrons, however its capacity of identifying $p/\pi/K$ is limited and is not used in this analysis. Track pairs with opposite charge are used as input tracks in the `InDetV0Finder` package. A three-dimensional vertex fitting is first carried out without any mass or pointing constraint. It tries to intersect circles that are $(R, \phi)$ projections of the helical trajectories of the two tracks. If the circles intersect, the intersection with smaller $z$ difference between the two

helices extrapolated to the intersection is chosen. If the circles do not intersect, the vertex approximation is taken as the point of closest approach of the two circles. If the unconstrained fit satisfies a number of condition, mass constrained fits, assuming $\Lambda^0$, $\bar{\Lambda}^0$, $K_S^0$ and $\gamma$ hypotheses, are performed. The invariant mass of the $V^0$ candidate is calculated under $\Lambda^0 \to p\pi^-$, $\bar{\Lambda}^0 \to \bar{p}\pi^+$, $K_S^0 \to \pi^+\pi^-$ and $\gamma \to e^+e^-$ hypotheses. For example, $\Lambda^0 \to p\pi^-$ hypothesis means proton mass is assigned to the positive track and pion mass is assigned to the negative track. The data is reconstructed with the requirement on the track transverse momentum, $p_T^{trk} > 50$ MeV. The reconstructed mass resolution for $\Lambda^0$ and $\bar{\Lambda}^0$ is about 3.5 MeV (Tables 5.2 and 5.3) and a mass window of roughly 5 times the resolution is used in the mass constrained fit (Figure 5.3.1).

## 5.2   Candidate selection

The $\Lambda^0$ and $\bar{\Lambda}^0$ candidate selection has largely been inherited from a previous analysis on the measurement of transverse polarization of $\Lambda^0$ and $\bar{\Lambda}^0$ hyperons from Refs. [51, 111]. An outline of the strategy used is listed below:

- $\Lambda^0$ and $\bar{\Lambda}^0$ candidates are reconstructed using the standard ATLAS $V^0$ reconstruction tool as described in Section 5.1

- Additional cuts are applied to improve the quality of reconstructed $\Lambda^0/\bar{\Lambda}^0$ candidates and reduce background

- Cuts on the mass hypothesis for $K_s \to \pi^+\pi^-$ and $\gamma \to e^+e^-$ are applied to get rid of candidates misidentified as $\Lambda^0/\bar{\Lambda}^0$ candidates to further reduce the background

76

- Events with at least one pair of $\Lambda^0 \bar{\Lambda}^0$ , $\Lambda^0 \Lambda^0$ or $\bar{\Lambda}^0 \bar{\Lambda}^0$ are saved. Decay angles in the helicity frame for the selected $\Lambda^0/\bar{\Lambda}^0$ candidates are calculated

- For single $V^0$ sample, events with at least one $\Lambda^0$ or one $\bar{\Lambda}^0$ are saved. $\Lambda^0$ and $\bar{\Lambda}^0$ selected from different events are joined to produce the mixed data sample which is used as the reference sample in the correlation measurement

The details of $V^0$ selection are listed below:

- Reconstructed invariant mass $m_{p\pi}$ falls between 1100 and 1135 MeV

- Vertex $\chi^2$ probability $> 0.05$ (To ensure quality of reconstructed secondary vertex)

- Number of pixel and SCT hits $> 3$ for each reconstructed track (To ensure quality of reconstructed tracks that formed the secondary vertex)

- Fraction of high threshold TRT hits $< 0.14$ (To remove electron background)

- $\gamma$ removal: $m_{ee} < 75$ MeV (To remove photon conversion background)

- $K_S^0$ removal: $480 < m_{\pi\pi} < 515$ MeV (To remove $K_S^0$ background)

- $\Lambda^0$ decay length $L_{xy} > 15$ mm (To reduce secondary vertex formed by combinatoric tracks)

- Significance of $\Lambda^0$ decay length $\sigma_{L_{xy}} > 15$ (To remove secondary vertex formed by combinatoric tracks)

- Significance of the shortest distance between the refitted track of $V^0$ and the primary vertex $a_0/\sigma_{a_0} < 3$ (To select candidates originating from the primary vertex)

- For $V^0$ pairs selected from the same event, any pair sharing any reconstructed track is removed (To remove candidates reconstructed using overlapped tracks)

The determination of the values of the selection cuts are done using signal and background MC sample shown in Figure 5.2.3.
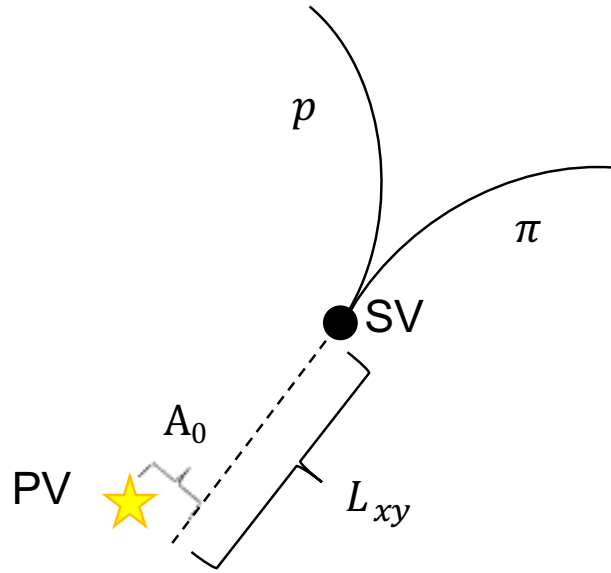


Figure 5.2.1: Decay topology of a $\Lambda^0$ candidate. PV and SV denote the primary vertex and secondary vertex respectively. $A_0$ is the three-dimensional distance between the refitted track (dashed line) and the primary vertex. $L_{xy}$ is the transverse distance between the primary vertex and the secondary vertex. The secondary vertex is reconstructed using a pair of oppositely charged tracks labeled $p$ and $\pi$ curving in opposite directions inside a magnetic field perpendicular to the transverse plane along the beam line in the inner tracker.
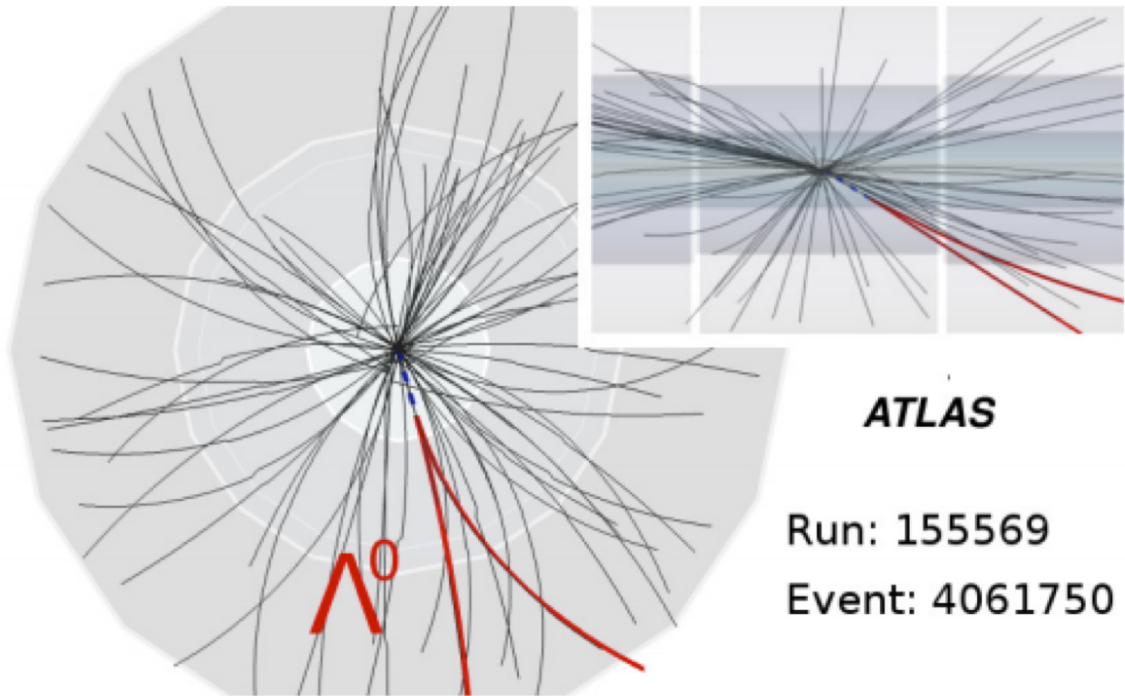
Figure 5.2.2: Event display of a $\Lambda^0 \to p\pi$ decay in the inner tracker in $xy$ and $zR$ projections. Highlighted tracks in red are the vertex-refitted tracks for proton and pion candidates. The blue-dashed track is the vertex-refitted track for the $\Lambda^0$ candidate. The three concentric rings represent 3 sub-detectors of the inner tracker: pixel, semiconductor tracker, and transition radiation tracker. [111]
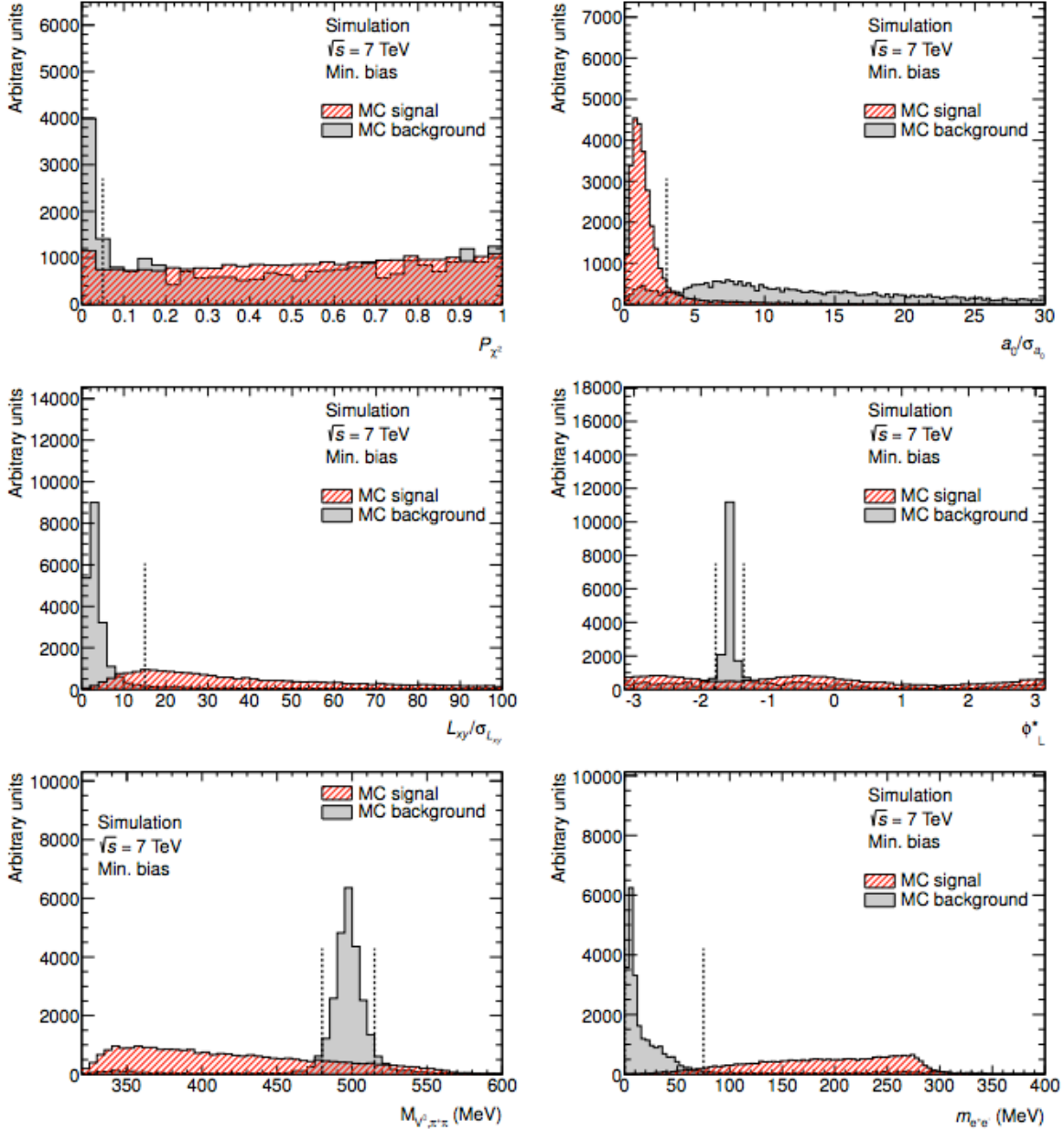
Figure 5.2.3: Distributions of selection variables for signal and background candidates in the minimum bias MC sample. All plots show candidates after the final selection and are normalized to the same area. The cumulative $\chi^2$ probability of the vertex fit $P_{\chi^2}$ (top-left), the $\Lambda^0$ impact parameter significance $a_0/\sigma_{a_0}$ (top-right), the transverse decay distance significance $L_{xy}/\sigma_{L_{xy}}$ (middle-left), the angle between the $\Lambda^0$ production and decay planes $\phi^*$ (middle-right), the invariant mass under $K_S^0$ mass hypothesis (bottom-left) and the $\gamma$ hypothesis (bottom-right) are shown. Cuts are indicated by dashed lines. [111]

At least one $\Lambda^0$ and one $\bar{\Lambda}^0$ are required in each $\Lambda^0\bar{\Lambda}^0$ event. For like-type events, at least two of the same type candidates have to be present in the same event. All possible combinations of $V^0$ are paired up for unlike-type events with multiple $\Lambda^0$ or $\bar{\Lambda}^0$ candidates and for like-type events with more than two candidates. The selection yields for data and MC samples and their corresponding mixed samples are shown in Table 5.1.

Table 5.1: Selection results for $\Lambda^0\bar{\Lambda}^0$ , $\Lambda^0\Lambda^0$ and $\bar{\Lambda}^0\bar{\Lambda}^0$ pairs selected from the same event in data (Data sample), from different events in data (Mixed data sample), from the same event in MC (MC sample) and from different events in the MC (Mixed MC sample).

| Type of hyperon pairs | | $\Lambda^0\bar{\Lambda}^0$ | $\Lambda^0\Lambda^0$ | $\bar{\Lambda}^0\bar{\Lambda}^0$ |
|---|---|---|---|---|
| Data sample | (minbias) | 53,561 | 25,551 | 20,127 |
| | (muon) | 295,202 | 140,232 | 113,596 |
| Mixed data sample | (minbias) | 595,869 | 671,355 | 594,813 |
| | (muon) | 2,534,826 | 2,823,627 | 2,527,252 |
| MC sample | | 2,679 | 1,005 | 673 |
| Mixed MC sample | | 54,460 | 67,182 | 53,439 |

## 5.3   Signal and background modeling

The invariant mass distribution of the $\Lambda^0$ or $\bar{\Lambda}^0$ candidates in the range $[1100, 1135]$ MeV are fitted with a 2-component PDF as $\mathcal{M}(m) = N_{sig}\mathcal{M}_{sig}(m) + N_{bkg}\mathcal{M}_{bkg}(m)$ where $\mathcal{M}_{sig}(m)$ and $\mathcal{M}_{bkg}(m)$ denote the normalized signal and background components respectively. $N_{sig}$ and $N_{bkg}$ are the signal and background yields. The signal component can be expressed as

$$\mathcal{M}_{sig}(m) = f_1\mathcal{G}(m - m_\Lambda, \sigma_1^L, \sigma_1^R) + (1 - f_1)\mathcal{G}(m - m_\Lambda, \sigma_2^L, \sigma_2^R) \qquad (5.3.1)$$

where $\mathcal{G}(m - m_\Lambda, \sigma^L, \sigma^R)$ is an asymmetric Gaussian function with mean $m_\Lambda$, left width $\sigma^L$ and right width $\sigma^R$, $f_1$ is the fractional contribution of the first Gaussian function. The

background component is modeled by a linear function as

$$\mathcal{M}_{bkg}(m) = \frac{1}{\Delta m}\left[1 + c_0(m - m_c)\right] \tag{5.3.2}$$

where $\Delta m = m_{high} - m_{low}$ is the width of the mass window being fitted, $m_{high}$ and $m_{low}$ are the upper and lower bounds of the fit, $m_c$ is the mid-value of the mass window and $c_0$ is the fit parameter of the linear polynomial function. The invariant mass resolution is calculated as the square-root of the variance of the signal component as

$$\sigma_m = \sqrt{\frac{1}{2}\left[f_1\left((\sigma_1^L)^2 + (\sigma_1^R)^2\right) + (1 - f_1)\left((\sigma_2^L)^2 + (\sigma_2^R)^2\right)\right]}. \tag{5.3.3}$$

The double asymmetric Gaussian function is used to account for the peak asymmetry caused by the track reconstruction inefficiency for low $p_T$ tracks, i.e. protons and pions.

## 5.4   2D signal region

The invariant mass peak of each hyperon as shown in Figure 5.4.1 is fitted with a double asymmetric Gaussian signal component $\mathcal{M}_{sig}(m)$ and a linear polynomial background component $\mathcal{M}_{bkg}(m)$ (Section 5.3 and Figure 5.3.1) with the RooFit package [112]. A 2D PDF is built by multiplying the two 1D PDFs

$$\mathcal{M}(m_1, m_2) = N_{sig}\mathcal{M}_{sig}(m_1)\mathcal{M}_{sig}(m_2) + N_{bkg}\mathcal{M}_{bkg}(m_1)\mathcal{M}_{bkg}(m_2) \tag{5.4.1}$$

The signal yield $N_{sig}$ and background yield $N_{bkg}$ are allowed to flow in the extended maximum
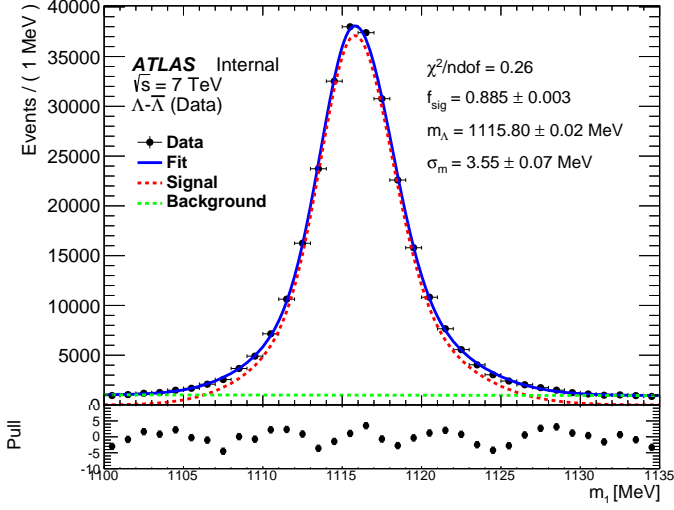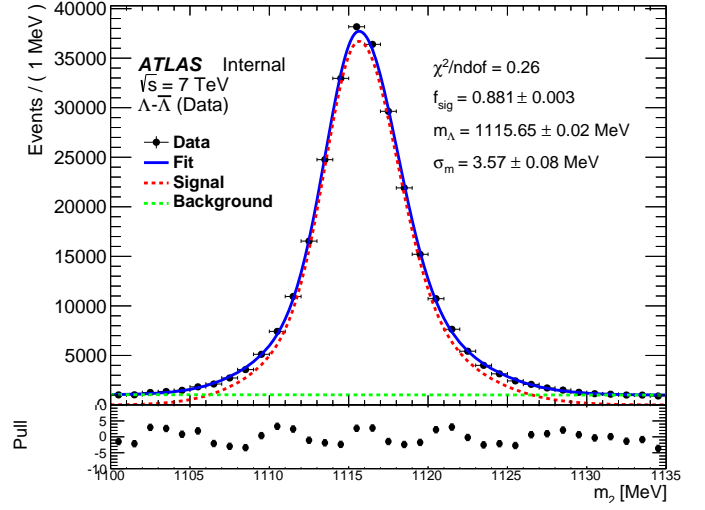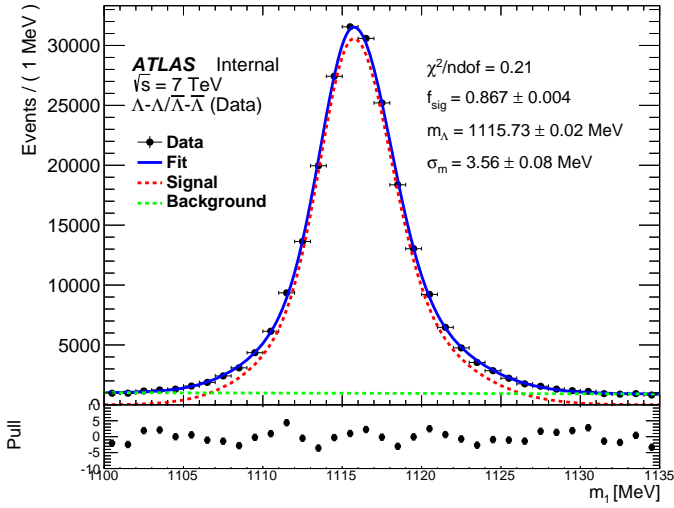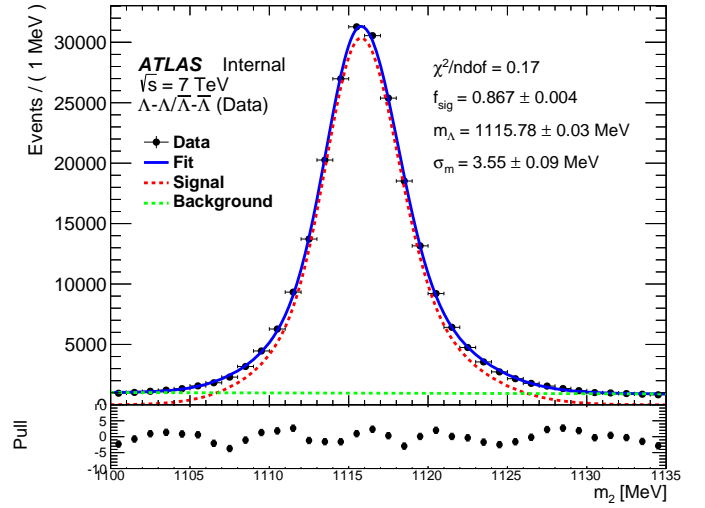
Figure 5.3.1: Hyperon invariant mass spectrum of (a) $\Lambda_1$ ($\Lambda^0\bar{\Lambda}^0$), (b) $\Lambda_2$ ($\Lambda^0\bar{\Lambda}^0$), (c) $\Lambda_1$ ($\Lambda^0\Lambda^0+\bar{\Lambda}^0\bar{\Lambda}^0$) and (d) $\Lambda_2$ ($\Lambda^0\Lambda^0+\bar{\Lambda}^0\bar{\Lambda}^0$) fitted with a double asymmetric Gaussian signal function (Eq. (5.3.1)) and a linear polynomial background function (Eq. (5.3.2)) using the RooFit package [112]. The fit results are expressed in terms of the signal fraction $f_{sig} = N_{sig}/(N_{sig} + N_{bkg})$, the position of mass peak $m_\Lambda$ and the mass resolution $\sigma_m$ as shown in the figures.

likelihood fit while the shape of the signal and background components are fixed. The signal fraction in a bin centered at $(m_1, m_2)$ can be calculated as follows

$$f_{sig}(m_1, m_2) = \frac{\int_{m_1-\Delta}^{m_1+\Delta} dm_1' \int_{m_2-\Delta}^{m_2+\Delta} dm_2' N_{sig} \mathcal{M}_{sig}(m_1') \mathcal{M}_{sig}(m_2')}{\int_{m_1-\Delta}^{m_1+\Delta} dm_1' \int_{m_2-\Delta}^{m_2+\Delta} dm_2' \mathcal{M}(m_1', m_2')} \quad (5.4.2)$$

where $2\Delta$ is the bin size. The resulting 2D signal fraction plots are shown in Figure 5.4.3.

The signal region is determined by varying the lower bound $m_{low}$ and upper bound $m_{high}$ of the mass range of the 2D mass window and maximizing the signal significance $S = N_{sig}/\sqrt{N_{bkg}}$ in the region. A 2D scanning is done by varying $m_{high}$ and $m_{low}$ each at a step size of 1 MeV in the mass range [1100, 1135] MeV with $m_{low} < m_{high}$. The signal region that maximizes the signal significance was found to be [1112, 1120] MeV for both $\Lambda_1$ and $\Lambda_2$ for all four types of events. The signal fractions $f_{sig}$, as defined in Eq. (5.4.2), in all the signal regions are above 98% for all four types of events. The results of the scanning is shown in Tables 5.4 and 5.5.

Table 5.2: Summary of the fit results for the invariant mass peaks for all four types of events for the muon stream sample.

| Event type | $\Lambda^0\bar{\Lambda}^0$ | $\Lambda^0\Lambda^0 + \bar{\Lambda}^0\bar{\Lambda}^0$ | $\Lambda^0\Lambda^0$ | $\bar{\Lambda}^0\bar{\Lambda}^0$ |
|---|---|---|---|---|
| Signal fraction $f_{sig}$ [%] | $88.1 \pm 0.3$ | $86.1 \pm 0.3$ | $86.6 \pm 0.4$ | $85.4 \pm 0.4$ |
| $\Lambda_1$ invariant mass $m_{\Lambda_1}$ [MeV] | $1115.80 \pm 0.02$ | $1115.73 \pm 0.02$ | $1115.76 \pm 0.03$ | $1115.69 \pm 0.03$ |
| $\Lambda_2$ invariant mass $m_{\Lambda_2}$ [MeV] | $1115.65 \pm 0.02$ | $1115.78 \pm 0.03$ | $1115.79 \pm 0.04$ | $1115.76 \pm 0.04$ |
| $\Lambda_1$ mass resolution $\sigma_{m_{\Lambda_1}}$ [MeV] | $3.55 \pm 0.07$ | $3.56 \pm 0.08$ | $3.57 \pm 0.11$ | $3.55 \pm 0.13$ |
| $\Lambda_2$ mass resolution $\sigma_{m_{\Lambda_2}}$ [MeV] | $3.57 \pm 0.08$ | $3.55 \pm 0.09$ | $3.55 \pm 0.11$ | $3.56 \pm 0.14$ |

Table 5.3: Summary of the fit results for the invariant mass peaks for all four types of events for the minimum bias stream sample.

| Event type | $\Lambda^0\bar{\Lambda}^0$ | $\Lambda^0\Lambda^0 + \bar{\Lambda}^0\bar{\Lambda}^0$ | $\Lambda^0\Lambda^0$ | $\bar{\Lambda}^0\bar{\Lambda}^0$ |
|---|---|---|---|---|
| Signal fraction $f_{sig}$ [%] | $89.3 \pm 0.6$ | $88.2 \pm 0.6$ | $89.0 \pm 0.9$ | $87.4 \pm 1.0$ |
| $\Lambda_1$ invariant mass $m_{\Lambda_1}$ [MeV] | $1115.82 \pm 0.06$ | $1115.70 \pm 0.06$ | $1115.76 \pm 0.09$ | $1115.66 \pm 0.08$ |
| $\Lambda_2$ invariant mass $m_{\Lambda_2}$ [MeV] | $1115.67 \pm 0.05$ | $1115.76 \pm 0.06$ | $1115.81 \pm 0.09$ | $1115.71 \pm 0.08$ |
| $\Lambda_1$ mass resolution $\sigma_{m_{\Lambda_1}}$ [MeV] | $3.56 \pm 0.16$ | $3.50 \pm 0.18$ | $3.56 \pm 0.30$ | $3.46 \pm 0.25$ |
| $\Lambda_2$ mass resolution $\sigma_{m_{\Lambda_2}}$ [MeV] | $3.55 \pm 0.19$ | $3.63 \pm 0.21$ | $3.67 \pm 0.31$ | $3.58 \pm 0.29$ |
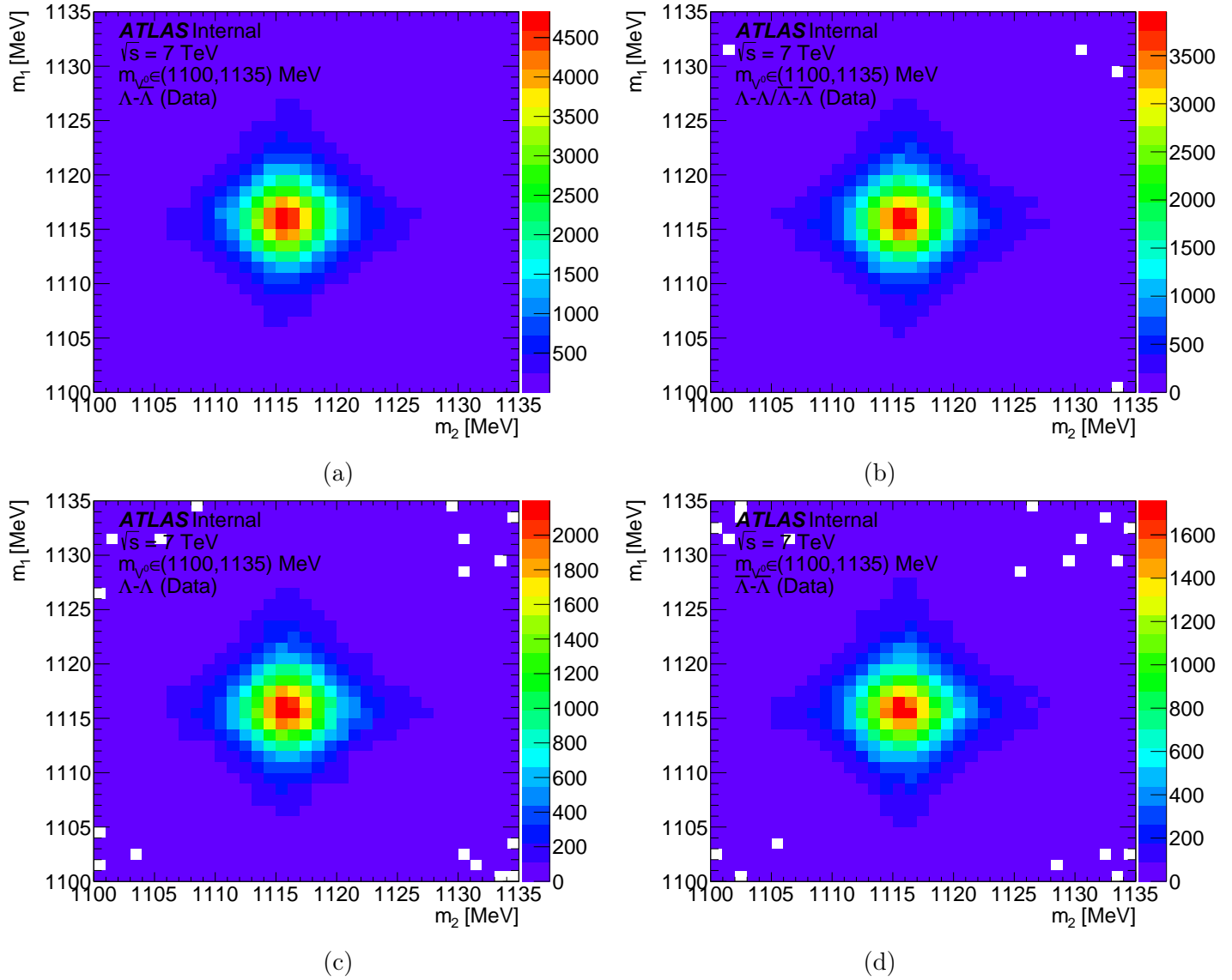
Figure 5.4.1: Uncorrected 2D distributions of hyperon invariant masses ($m_1$ vs $m_2$) for (a) $\Lambda^0\bar{\Lambda}^0$, (b) $\Lambda^0\Lambda^0 + \bar{\Lambda}^0\bar{\Lambda}^0$, (c) $\Lambda^0\Lambda^0$, and (d) $\bar{\Lambda}^0\bar{\Lambda}^0$ events in the mass range [1100,1135] MeV.
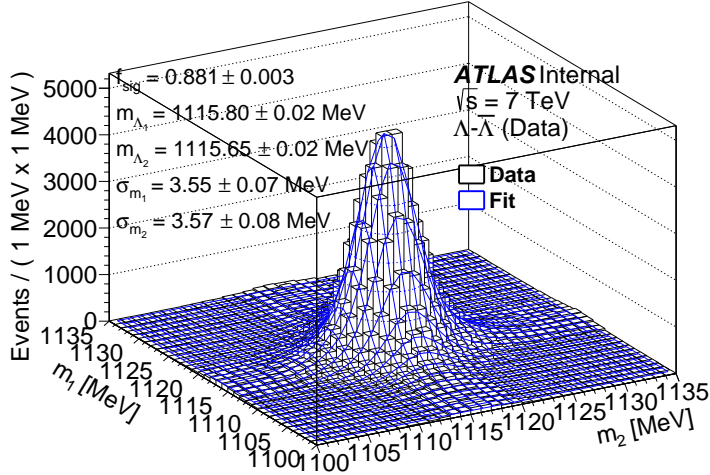
(a)
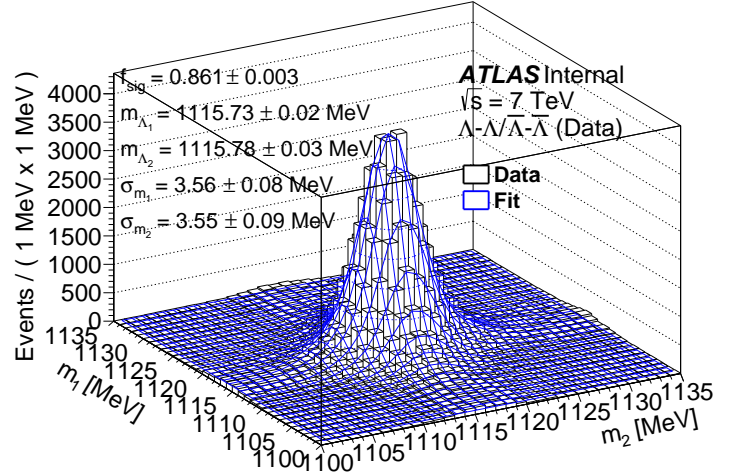
(b)
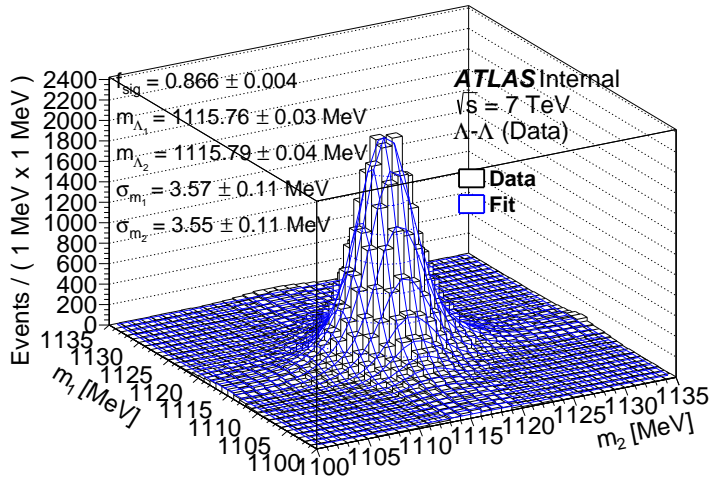
(c)
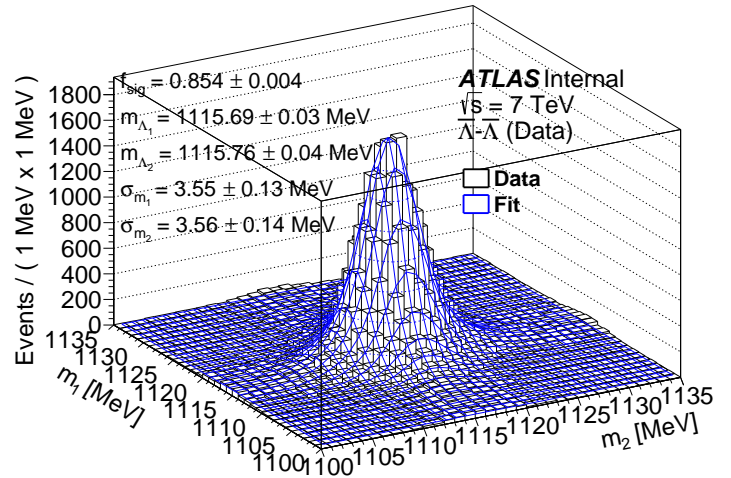
(d)

Figure 5.4.2: 2D distributions of hyperon invariant masses ($m_1$ vs $m_2$) overlaid with fit model $\mathcal{M}(m_1, m_2)$ as defined by Eq. (5.4.1) for (a) $\Lambda^0\bar{\Lambda}^0$, (b) $\Lambda^0\Lambda^0 + \bar{\Lambda}^0\bar{\Lambda}^0$, (c) $\Lambda^0\Lambda^0$, and (d) $\bar{\Lambda}^0\bar{\Lambda}^0$ events in the mass range [1100,1135] MeV. The results are expressed in terms of the signal fraction $f_{sig}$, the position of $\Lambda_1$ mass peak for $m_1$, the position of $\Lambda_2$ mass peak $m_2$, the width of $\Lambda_1$ mass peak $\sigma_{m_1}$ and the width of $\Lambda_2$ mass peak $\sigma_{m_2}$.

87
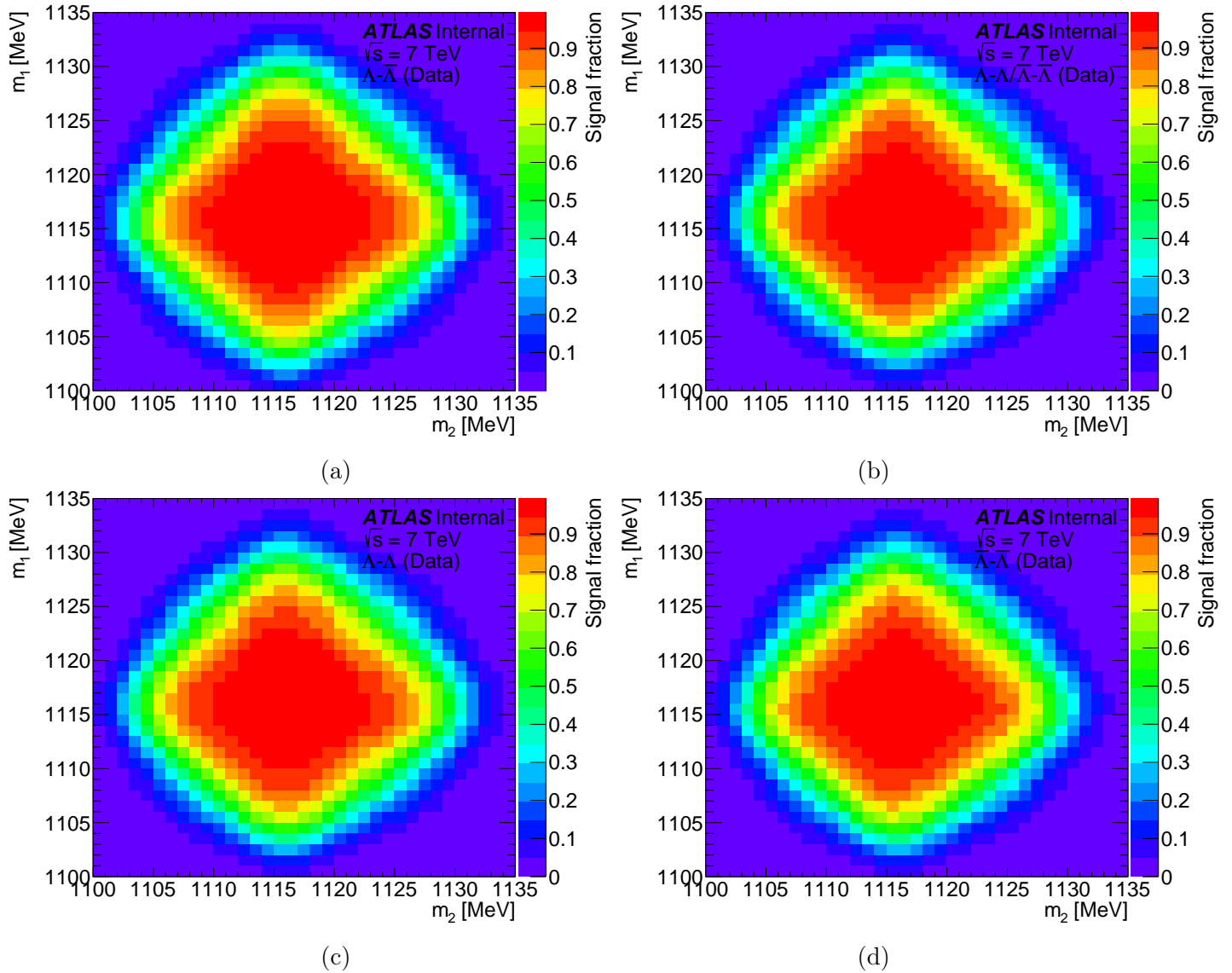
Figure 5.4.3: The signal fraction $f_{sig}$, calculated using the signal component and background component of the fit model $\mathcal{M}(m_1, m_2)$ in Eq. (5.4.2), as a function of invariant masses $m_1$ and $m_2$ for (a) $\Lambda^0\bar{\Lambda}^0$, (b) $\Lambda^0\Lambda^0 + \bar{\Lambda}^0\bar{\Lambda}^0$, (c) $\Lambda^0\Lambda^0$, and (d) $\bar{\Lambda}^0\bar{\Lambda}^0$ events using bin size of 1 MeV in the mass range [1100,1135] MeV. The area with high signal fraction is slightly skewed to the high mass region as a result of the track reconstruction inefficiency.

Table 5.4: Summary of the fit results for the signal regions that give the maximum signal significance for all four types of events using the muon sample. The fit results for the full mass range are also shown here for comparison. The fit results are expressed in terms of the signal yield $N_{sig}$, the background yield $N_{bkg}$, and the signal fraction $f_{sig}$.

| Event type | $\Lambda^0\bar{\Lambda}^0$ | $\Lambda^0\Lambda^0 + \bar{\Lambda}^0\bar{\Lambda}^0$ | $\Lambda^0\Lambda^0$ | $\bar{\Lambda}^0\bar{\Lambda}^0$ |
|---|---|---|---|---|
| Signal region $[m_{high}, m_{low}]$ [MeV] | [1112, 1120] | [1112, 1120] | [1112, 1120] | [1112, 1120] |
| Signal yield $N_{sig}$ | 162990 | 133653 | 74374 | 59275 |
| Background yield $N_{bkg}$ | 1881 | 1861 | 988 | 872 |
| Signal fraction $f_{sig}$ [%] | 98.85 | 98.63 | 98.68 | 98.55 |
| Full range $[m_{high}, m_{low}]$ [MeV] | [1100, 1135] | [1100, 1135] | [1100, 1135] | [1100, 1135] |
| Signal yield $N_{sig}$ | 264729 | 218529 | 121502 | 97036 |
| Background yield $N_{bkg}$ | 35852 | 35284 | 18723 | 16553 |
| Signal fraction $f_{sig}$ [%] | 88.07 | 86.10 | 86.65 | 85.43 |

Table 5.5: Summary of the fit results for the signal regions that give the maximum signal significance for all four types of events using the minimum bias sample. The fit results for the full mass range are also shown here for comparison. The fit results are expressed in terms of the signal yield $N_{sig}$, the background yield $N_{bkg}$, and the signal fraction $f_{sig}$.

| Event type | $\Lambda^0\bar{\Lambda}^0$ | $\Lambda^0\Lambda^0 + \bar{\Lambda}^0\bar{\Lambda}^0$ | $\Lambda^0\Lambda^0$ | $\bar{\Lambda}^0\bar{\Lambda}^0$ |
|---|---|---|---|---|
| Signal region $[m_{high}, m_{low}]$ [MeV] | [1112, 1120] | [1112, 1120] | [1112, 1120] | [1112, 1120] |
| Signal yield $N_{sig}$ | 28809 | 23988 | 13411 | 10539 |
| Background yield $N_{bkg}$ | 330 | 339 | 187 | 131 |
| Signal fraction $f_{sig}$ [%] | 98.87 | 98.61 | 98.62 | 98.77 |
| Full range $[m_{high}, m_{low}]$ [MeV] | [1100, 1135] | [1100, 1135] | [1100, 1135] | [1100, 1135] |
| Signal yield $N_{sig}$ | 47244 | 39177 | 21973 | 17623 |
| Background yield $N_{bkg}$ | 6315 | 6499 | 3577 | 2503 |
| Signal fraction $f_{sig}$ [%] | 88.21 | 85.77 | 86.00 | 87.57 |

# Chapter 6

# Dynamical correlations

This chapter discusses the dynamical correlations of the hyperon-pairs in the rapidity and momentum phase space as measured in the data and that predicted in the string fragmentation model in PYTHIA event generator.

## 6.1 Predictions of the string model

As discussed in Section 1.3.6, baryon-antibaryon pairs can be produced when the string breaks by the production of diquark-antidiquark pair in the string model. This mechanism produces strongly correlated baryon-antibaryon pairs which share two quarks with flavors in common. This correlation is stronger than observed and this is because the diquarks can be produced in a stepwise manner with mesons $(M)$ pop up in between the diquarks. This is also known as the "popcorn" mechanism and results in baryon and antibaryon pairs further apart in rapidity and momentum space. A baryon-antibaryon pairs $(B\bar{B})$ are often produced from a single diquark-antidiquark breakup as baryon production is suppressed when compared to meson production. The baryon and antibaryon pairs are produced as neighbors and not

far from each other in the momentum space. In contrast, two baryons (antibaryons) are necessarily produced from two different $B\bar{B}$ pairs and must be separated by at least one antibaryon (baryon), often with one or more mesons. As a result, the string model predicts positive correlation for $\Lambda^0\bar{\Lambda}^0$ pairs and anticorrelation for $\Lambda^0\Lambda^0$ or $\bar{\Lambda}^0\bar{\Lambda}^0$ pairs [8].
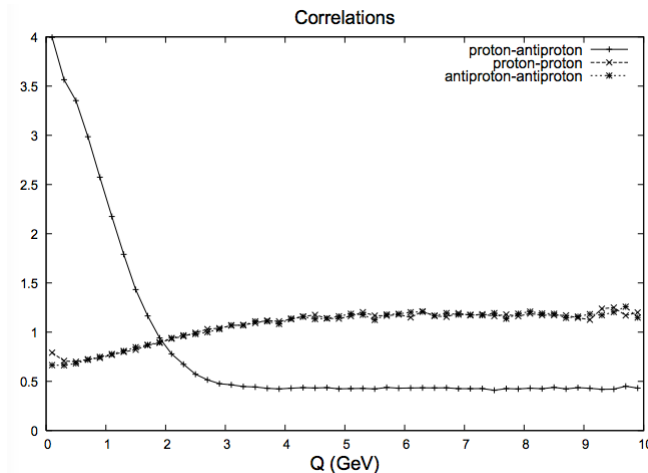


Figure 6.1.1: The correlation function $C_2(Q)$ plotted as a function of $Q$ for PYTHIA simulation sample for $pp$- ($\times$), $\bar{p}\bar{p}$- (*), and $p\bar{p}$-pairs ($+$) from 0 to 10 GeV. [8]

A similar behavior can be found between proton-antiproton, proton-proton and antiproton-antiproton produced in PYTHIA generator as shown in Figure 6.1.1, adapted from Ref. [8].

## 6.2 Dynamical correlations in data and MC samples

The correlation function defined in Section 2.1.1 is calculated as a function of $Q$, $\Delta\phi_{12}$, and $\cos\Delta\phi_{12}$ for unlike-type ($\Lambda^0\bar{\Lambda}^0$) and like-type ($\Lambda^0\Lambda^0+\bar{\Lambda}^0\bar{\Lambda}^0$) events.

$\Lambda^0\bar{\Lambda}^0$ events have shown very strong positive correlation for $Q < 2$ GeV for both minimum bias and muon sample while $\Lambda^0\Lambda^0+\bar{\Lambda}^0\bar{\Lambda}^0$ events have shown some small anticorrelation as $Q$ gets close to zero as shown in Figure 6.2.1. The data is overlaid with minimum bias

91

MC sample for both type of hyperon pairs in Figure 6.2.2. The positive correlation is overestimated in the MC sample for $\Lambda^0\bar{\Lambda}^0$ events and the anticorrelation is consistent between data and MC samples except the first bin which shows two standard deviations from zero and has a rather large statistical uncertainty. It is shown that the measured correlation function distributions are very similar to those for proton/antiproton created by PYTHIA event generator as shown in Figure 6.1.1.

Figure 6.2.3 shows the correlation functions for minimum bias and muon samples as functions of $\Delta\phi_{12}$ in the domain of $[-1, 2\pi - 1)$ to better illustrate the peak near zero. Figure 6.2.4 shows the correlation functions of minimum bias and muon data samples overlaid with that of MC sample. The results are similar to that obtained from the ALICE experiment as shown in Figure 2.2.1.

Figure 6.2.5 shows the same correlation functions for minimum bias and muon samples as functions of of $\cos\Delta\phi_{12}$. Figure 6.2.6 shows the correlation function of data overlaid with that of MC sample for comparison. The positive correlation in the MC sample near $\cos\Delta\phi_{12} = 1$ is again overestimated for the $\Lambda^0\bar{\Lambda}^0$ events. Small enhancement is observed at $\cos\Delta\phi_{12} \sim -1$ where the hyperon pairs are produced nearly back-to-back for both $\Lambda^0\bar{\Lambda}^0$ and $\Lambda^0\Lambda^0 + \bar{\Lambda}^0\bar{\Lambda}^0$ cases.

The $\Lambda^0\bar{\Lambda}^0$ events in the muon sample has slightly stronger positive correlation when compared to that in the minimum bias sample for $Q$ and $\Delta\phi_{12}$ near zero as shown in Figure (a) of 6.2.1, 6.2.3, and 6.2.5. The small difference may be caused by the difference in efficiency as hyperon pairs in the muon sample has slightly higher combined transverse momentum than those in minimum bias sample.
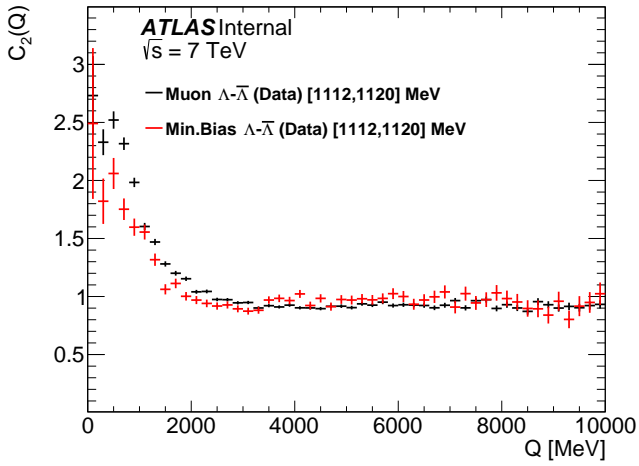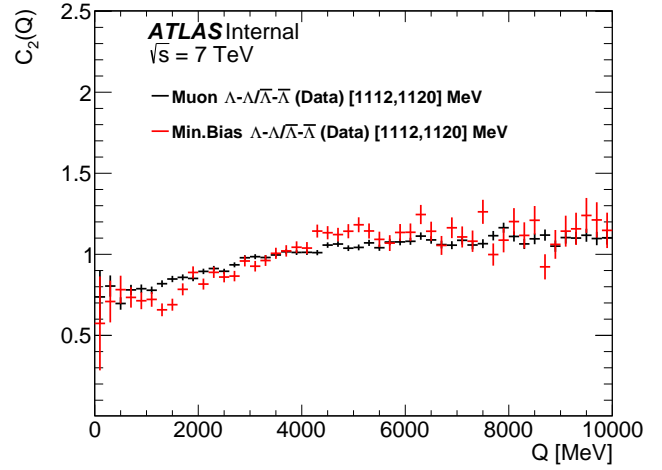
Figure 6.2.1: The correlation function $C_2(Q)$ plotted as a function of $Q$ for (a) $\Lambda^0\bar{\Lambda}^0$ and (b) $\Lambda^0\Lambda^0+\bar{\Lambda}^0\bar{\Lambda}^0$ pairs in muon (black) and minimum bias (red) data samples.
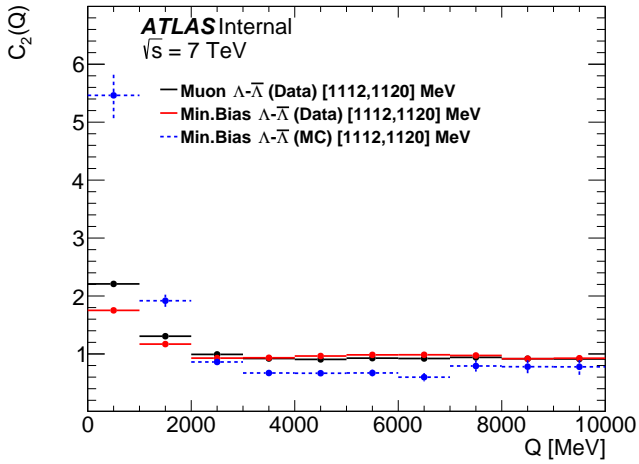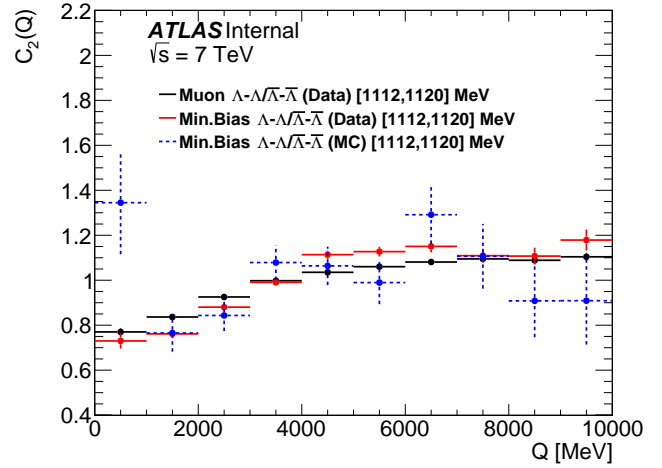


Figure 6.2.2: The correlation function $C_2(Q)$ plotted as a function of $Q$ for (a) $\Lambda^0\bar{\Lambda}^0$ and (b) $\Lambda^0\Lambda^0+\bar{\Lambda}^0\bar{\Lambda}^0$ pairs in muon data (black), minimum bias data (red), and minimum bias MC (blue dashed) sample. 1 GeV bin size has been used to accommodate the low statistics in MC sample.
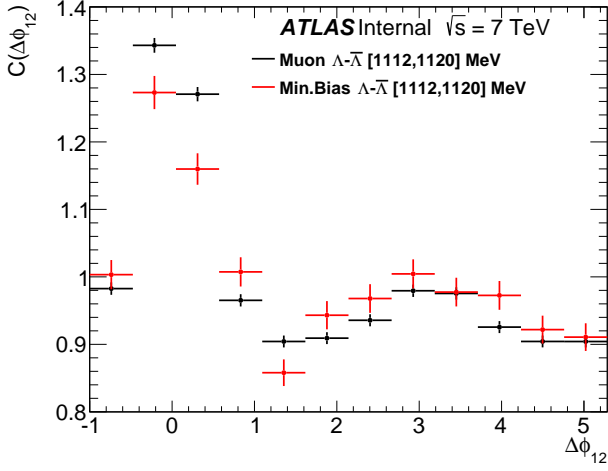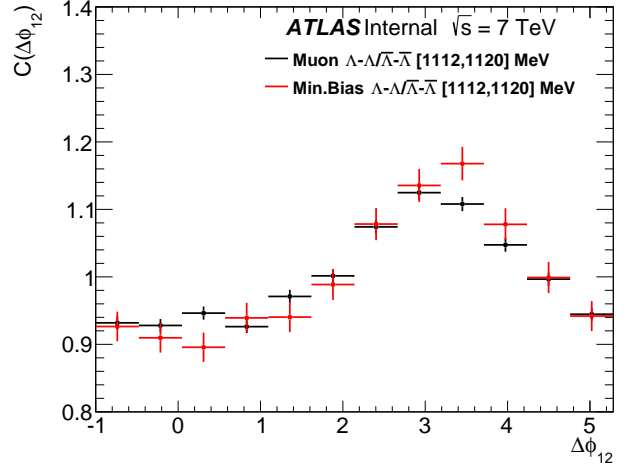
(a)　　　　　　　　　　　　　　　(b)

Figure 6.2.3: The $\Delta\eta$ integrated projections of the correlation function $C(\Delta\phi_{12})$ for (a) unlike-type and (b) like-type hyperon pairs for $\Delta\phi_{12} \in [-1, 2\pi - 1)$ where $\Delta\phi_{12} = \phi_1 - \phi_2$ is the difference in azimuthal angles of the two hyperons in the lab frame for muon (black) and minimum bias (red) data samples.
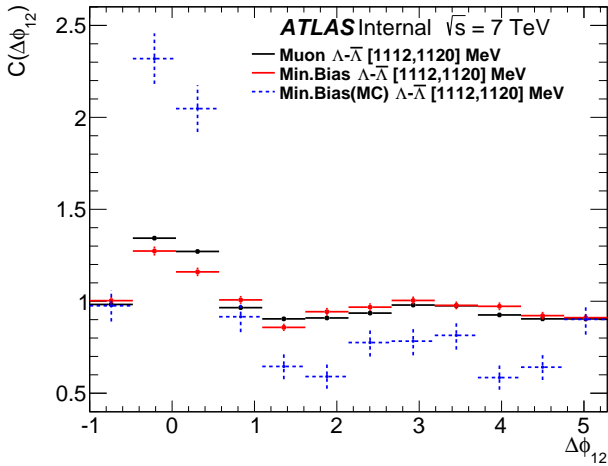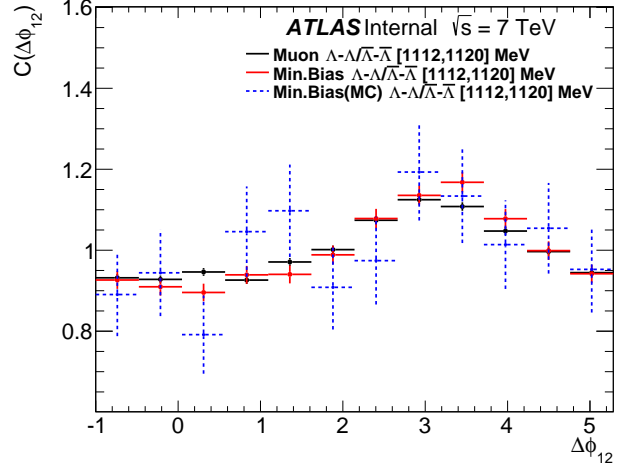


(a)　　　　　　　　　　　　　　　(b)

Figure 6.2.4: The $\Delta\eta$ integrated projections of correlation function $C(\Delta\phi_{12})$ for (a) unlike-type and (b) like-type hyperon pairs for $\Delta\phi_{12} \in [-1, 2\pi - 1)$ where $\Delta\phi_{12} = \phi_1 - \phi_2$ is the difference in azimuthal angles of the two hyperons in the lab frame for muon data (black), minimum bias data (red), and minimum bias MC (blue) samples.
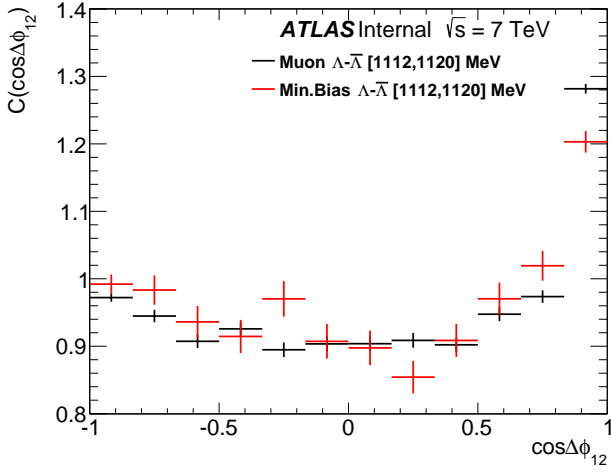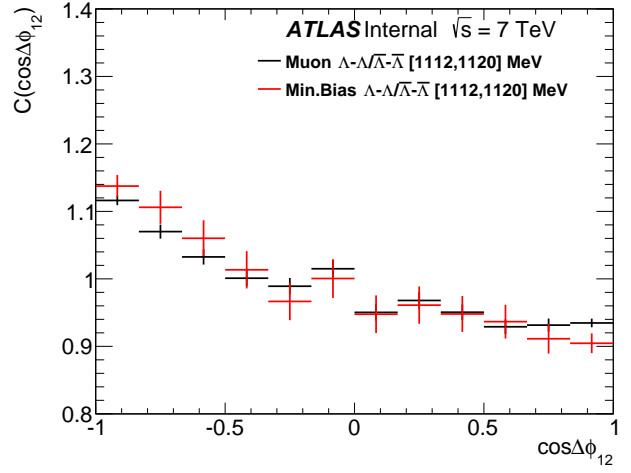
(a)  (b)

Figure 6.2.5: The cosine of the $\Delta\eta$ integrated projections of the correlation function $C(\cos\Delta\phi_{12})$ for (a) unlike-type and (b) like-type hyperon pairs for $\cos\Delta\phi_{12} \in [-1,1]$ where $\Delta\phi_{12} = \phi_1 - \phi_2$ is the difference in azimuthal angles of the two hyperons in the lab frame for muon (black) and minimum bias (red) data samples.
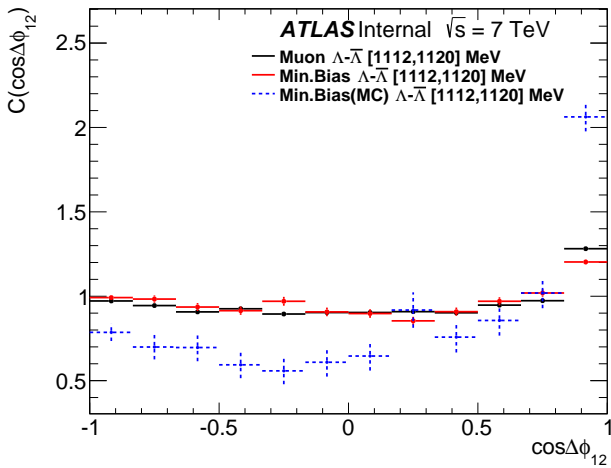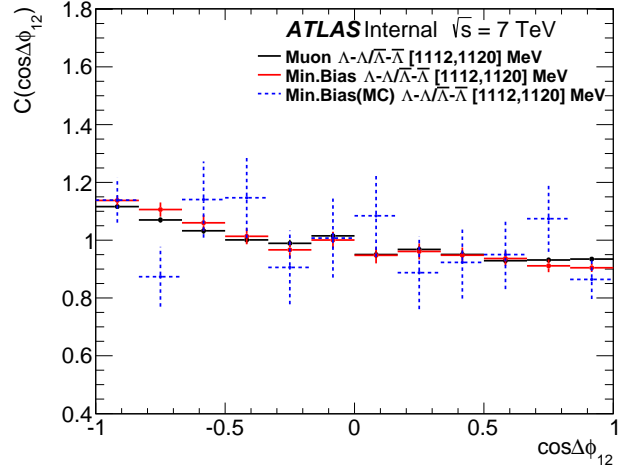


(a)  (b)

Figure 6.2.6: The cosine of the $\Delta\eta$ integrated projections of the correlation function $C(\cos\Delta\phi_{12})$ for (a) unlike-type and (b) like-type hyperon pairs for $\cos\Delta\phi_{12} \in [-1,1]$ where $\Delta\phi_{12} = \phi_1 - \phi_2$ is the difference in azimuthal angles of the two hyperons in the lab frame for muon data (black), minimum bias data (red), and minimum bias MC (blue) samples.

95

## 6.3 "Popcorn" mechanism

The "popcorn" mechanism in the string model allows a set of mesons to be produced in between the baryon and antibaryon and thus helps to regulate the momentum correlation of the produced baryon and antibaryon pairs. Currently, only the simplest scenario is implemented in the PYTHIA generator wherein at most one intermediate meson may be produced. The "popcorn" mechanism is controlled by three parameters in the `StringFlav` class, namely `StringFlav:popcornRate`, `StringFlav:popcornSpair`, and `StringFlav:popcornSmeson`, and they have the following functions [34, 35]:

- `StringFlav:popcornRate` gives the relative rates of $B\ \bar{B}$ and $B\ M\ \bar{B}$ production and roughly as $\mathrm{Prob}(B\ M\ \bar{B})\ /\ (\mathrm{Prob}(B\ \bar{B}) + \mathrm{Prob}(B\ M\ \bar{B})) = $ `popcornRate` $/\ (0.5 + $ `popcornRate`$)$. (default = 0.5; minimum = 0.0; maximum = 2.0)

- `StringFlav:popcornSpair` gives extra suppression for having an $s\bar{s}$ pair shared between $B$ and $\bar{B}$ in a $B\ M\ \bar{B}$ configuration. (default = 1.0; minimum = 0.0; maximum = 1.0)

- `StringFlav:popcornSmeson` gives extra suppression for having a strange meson $M$ in a $B\ M\ \bar{B}$ configuration. (default = 0.5; minimum = 0.0; maximum = 1.0)

The differential cross section ratio for data in the signal region (SR) and the full mass window at reconstucted level is overlaid with the "popcorn" parameters at default PYTHIA setting at generator level in Figure 6.3.1. It is discovered that the distribution of the data events in the SR and that of the MC sample agrees surprisingly well with each other. The differential cross section ratio as a function of $Q$ under different popcorn settings are shown in Figure 6.3.2. It

is shown that the distribution is quite insensitive to different popcorn settings. This suggests that the "popcorn" mechanism affects baryon-antibaryon and baryon-baryon/antibaryon-antibaryon production at roughly the same rate for all values of $Q$. Further studies can be done using different tunings and results from different fragmentation and hadronization models such as the cluster-hadronization model to see if the shape of the differential cross section ratio as a function of $Q$ is unique to baryon/antibaryon production in the string model regardless of the suppression from meson production.



(a)                                                          (b)
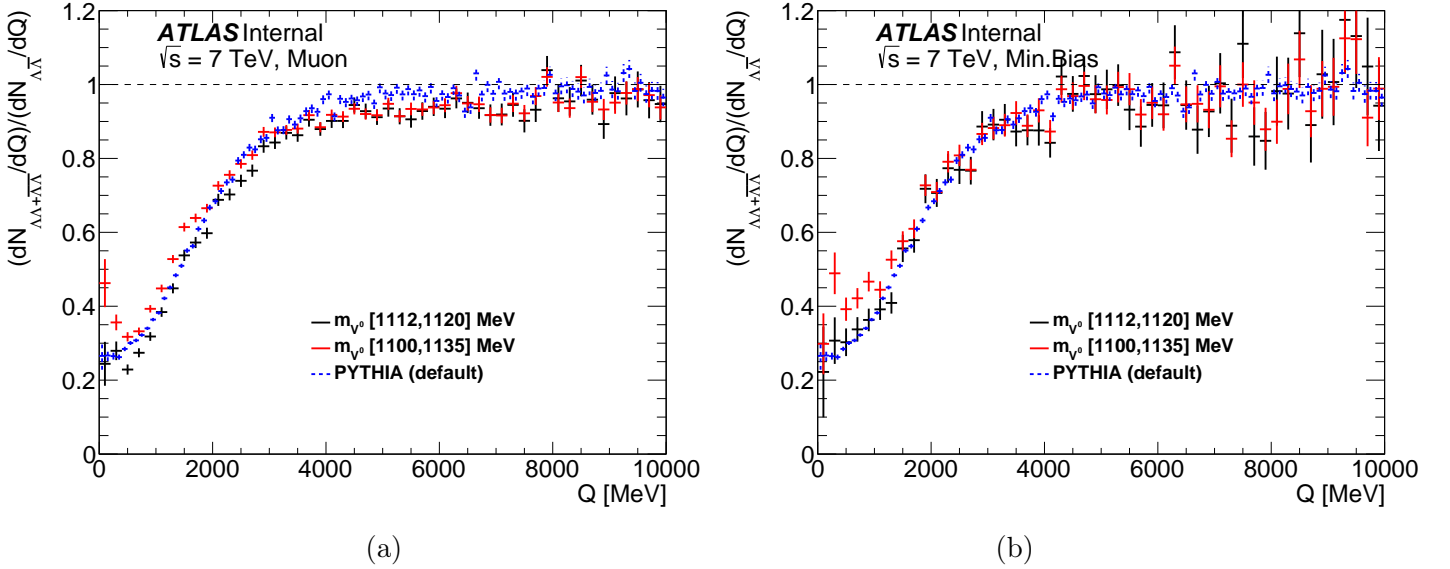
Figure 6.3.1: Differential cross section ratio of $\Lambda^0\Lambda^0 + \bar{\Lambda}^0\bar{\Lambda}^0$ to $\Lambda^0\bar{\Lambda}^0$ events as a function of $Q$ for (a) muon and (b) minimum bias stream data samples with signal mass window [1112,1120] MeV (black) and full mass window (red) overlaid with PYTHIA simulation sample (blue dashed) at default setting at generator level.
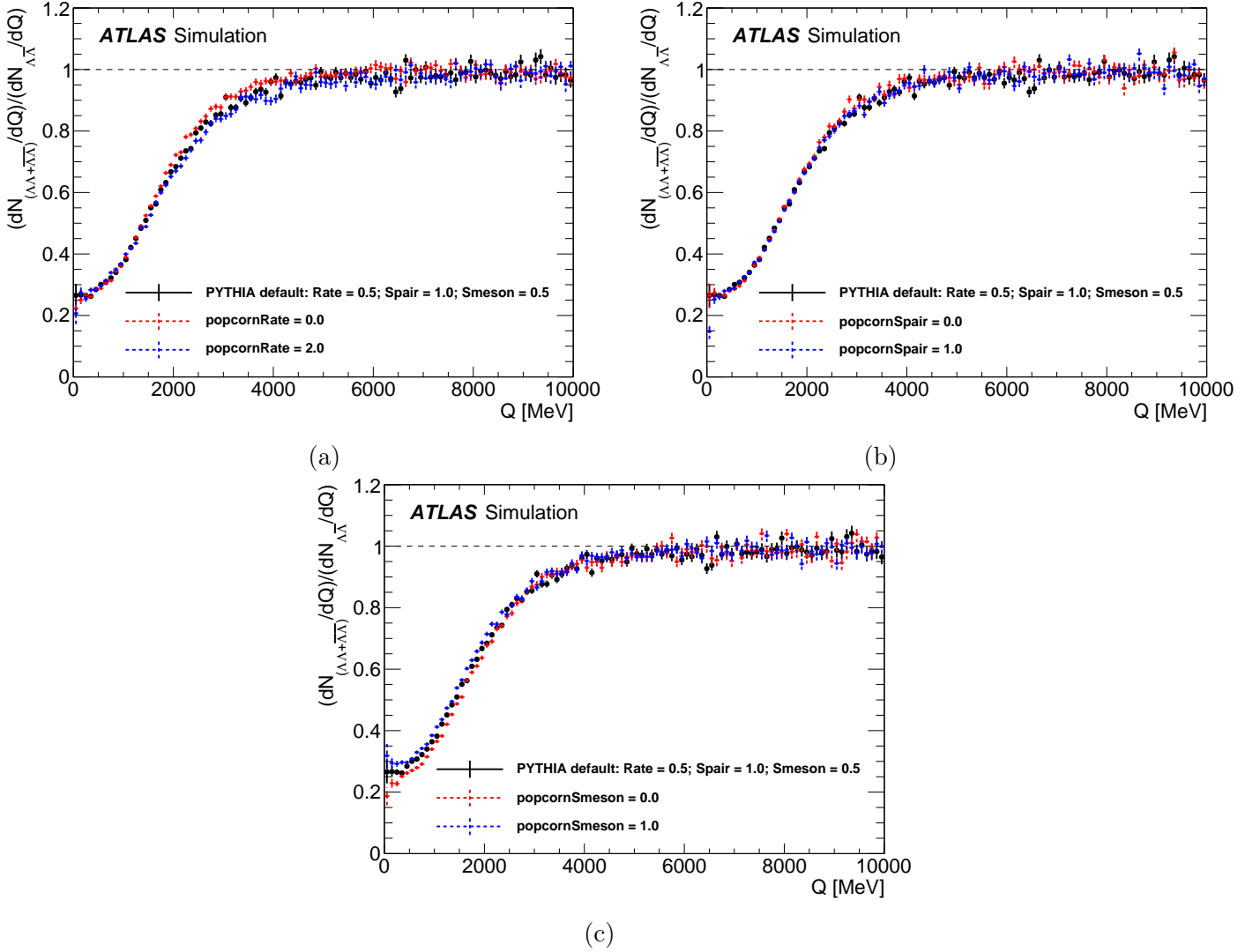
Figure 6.3.2: Differential cross section ratio of $\Lambda^0\Lambda^0 + \bar{\Lambda}^0\bar{\Lambda}^0$ to $\Lambda^0\bar{\Lambda}^0$ events as a function of $Q$ for MC sample with different popcorn settings with (a) `popcornRate`, (b) `popcornSpair`, and (c) `popcornSmeson` set at default (black), minimum (red), and maximum (blue) values in the PYTHIA event generator. The shape of the differential cross section ratio is measured to be quite stable with respect to different popcorn settings.

## 6.4 Excess of $\Lambda^0\bar{\Lambda}^0$ events near the $(\Lambda\Lambda)$ threshold

The $\Lambda^0\Lambda^0$ and $\bar{\Lambda}^0\bar{\Lambda}^0$ events are combined to form the like-type sample and its result is used to compare with the unlike-type sample. Figure 6.4.2 shows that there are excess $\Lambda^0\bar{\Lambda}^0$ events near the $(\Lambda\Lambda)$ threshold up to 4-5 GeV. The excess events also have slightly higher average combined $p_T$ and smaller opening angle $\Delta R$ than the like-type events. It is therefore useful to study the PYTHIA generator [34, 35] to understand the origin of the hyperon pairs in the region where the excess events are observed. One should however keep in mind that the MC sample does overestimate the excess events (Figure 6.4.1) and many baryon resonances are missing due to unknown branching fractions [34]. The composition of the excess events in the MC sample is discussed in Section 6.5 and are found to be originated from hyperon pairs sharing common ancestors, decaying either directly or through feed-down from some heavier hyperons such as $\Sigma^{0\dagger}$ and $\Sigma^*(1385)^\ddagger$.

Comparisons of the kinematic distributions between the like-type and unlike-type events are shown in Figure 6.4.2. It is shown that at large invariant mass $m_{\Lambda_1+\Lambda_2}$ or opening angle $\Delta R$ regions the two types of events agree very well. This is expected as the two hyperons would in such case be produced independently at a large distance and hence with little correlation, regardless of whether they are of the same type or opposite types.

---

$^\dagger \Sigma^0 \to \Lambda^0 + \gamma$ BR $= 100\%$ [47]
$^\ddagger \Sigma^{*0/\pm} \to \Lambda^0 + \pi^{0/\pm}$ BR $= (87.0\pm1.5)\%$ [47]
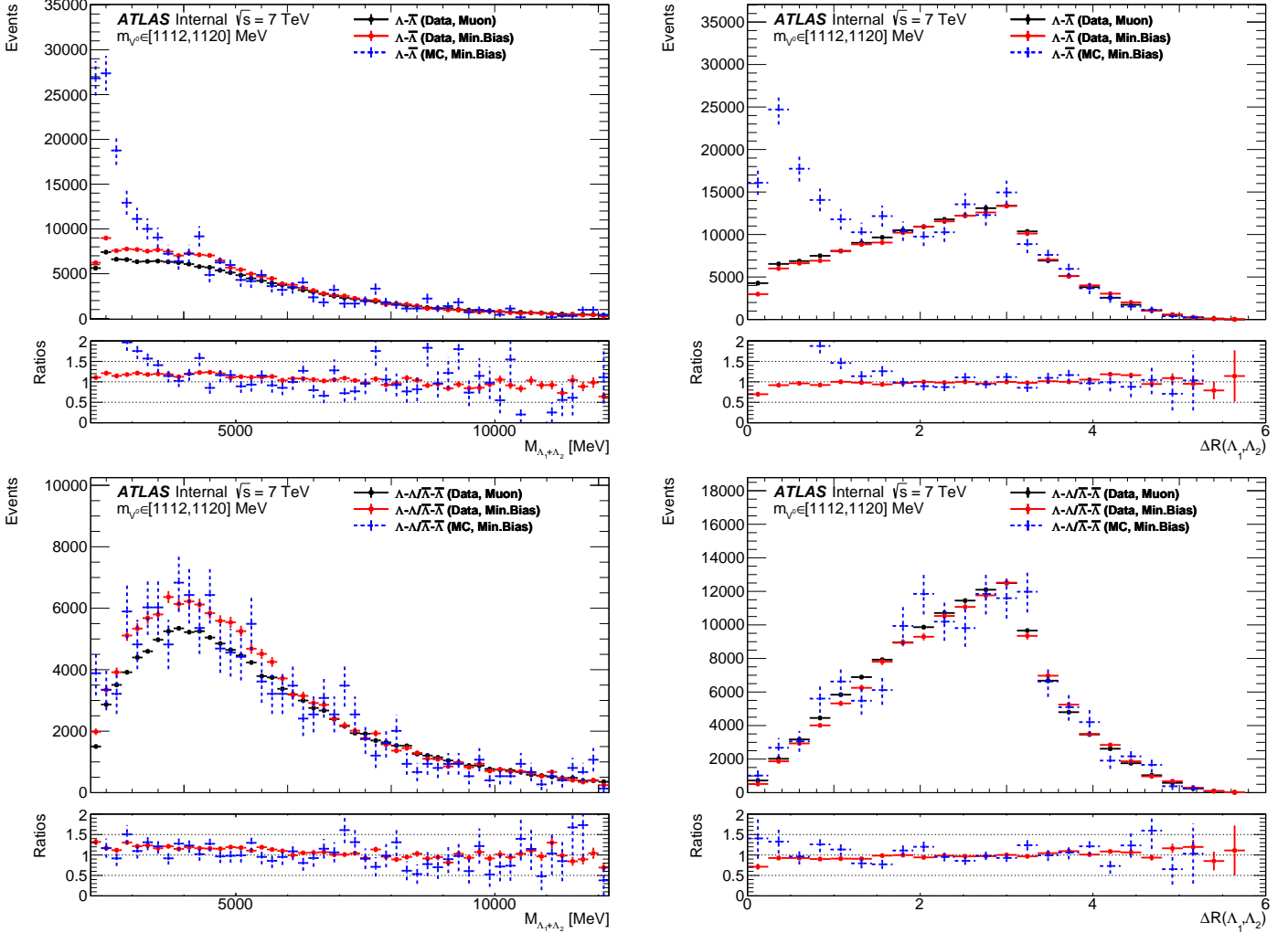
Figure 6.4.1: Invariant mass $m_{\Lambda_1+\Lambda_2}$ (left, normalized in [6200, 12200] MeV) and opening angle $\Delta R$ (right, normalized in [2.4, 6.0]) distributions for $\Lambda^0\bar{\Lambda}^0$ (upper) and $\Lambda^0\Lambda^0+\bar{\Lambda}^0\bar{\Lambda}^0$ (lower) pairs in muon data (black) and minimum bias data (red), and minimum bias MC (blue) samples. The excess $\Lambda^0\bar{\Lambda}^0$ events near $(\Lambda\Lambda)$ threshold are overestimated in MC sample.
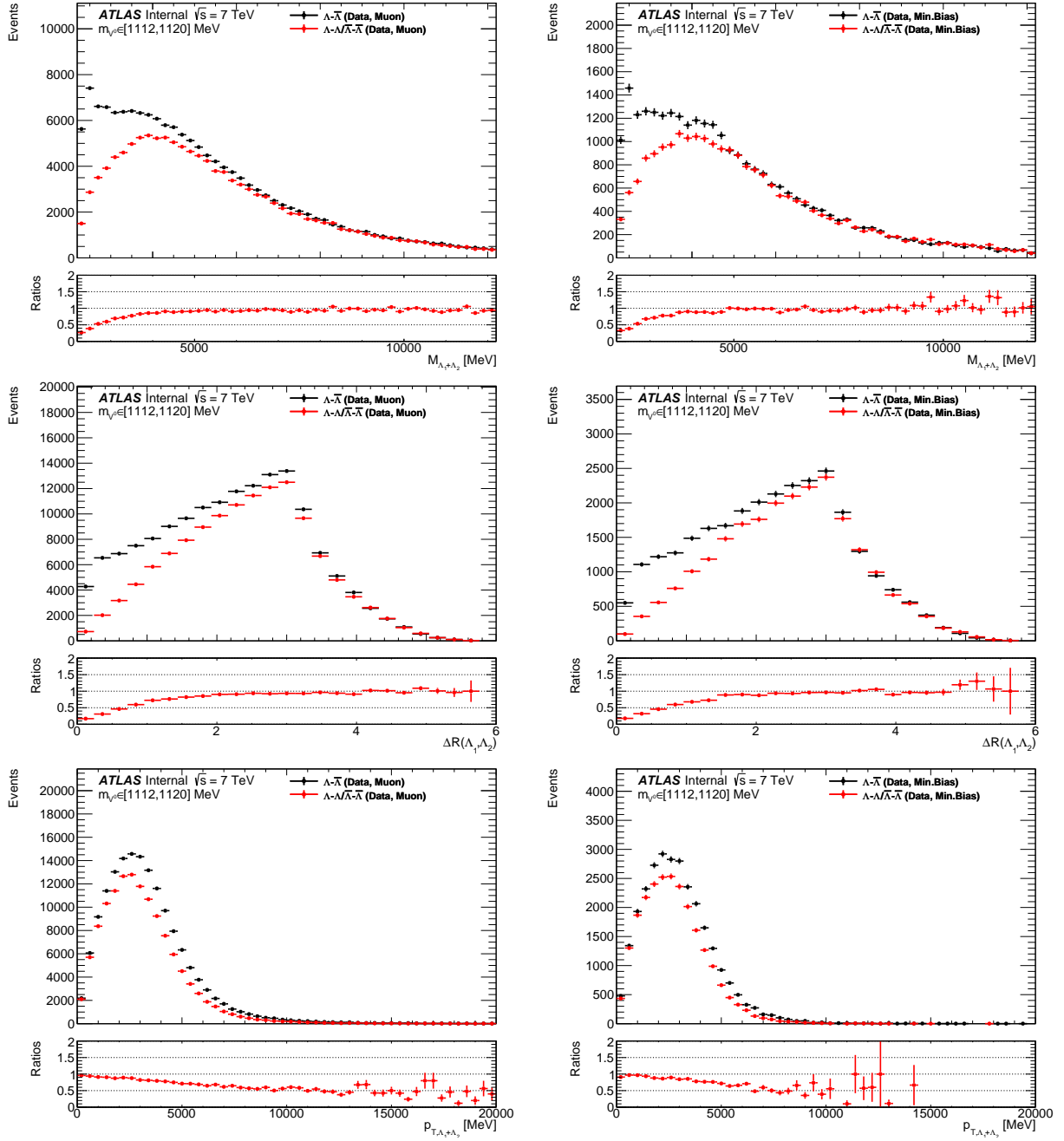
Figure 6.4.2: Invariant mass $m_{\Lambda_1 + \Lambda_2}$ (upper), opening angle $\Delta R$ (middle) and transverse momentum $p_{T,\Lambda_1 + \Lambda_2}$ (lower) distributions for unlike-type ($\Lambda^0 \bar{\Lambda}^0$) (black) and like-type ($\Lambda^0 \Lambda^0 + \bar{\Lambda}^0 \bar{\Lambda}^0$) (red) events at reconstructed level for muon (left) and minimum bias (right) data samples. An excess of unlike-type over like-type events is observed near the ($\Lambda\Lambda$) threshold. The excess events also have slightly higher average combined $p_{T,\Lambda_1 + \Lambda_2}$ than the like-type events.

101

## 6.5   Composition of $\Lambda^0\bar{\Lambda}^0$ peak from MC studies

As discussed in Section 6.4, the $\Lambda^0\bar{\Lambda}^0$ peak near the $(\Lambda\Lambda)$ threshold is overestimated by the MC sample as can be shown in Figure 6.4.1. It is therefore very tempting to understand where those $\Lambda^0\bar{\Lambda}^0$ pairs are originated in the PYTHIA generator. 5000 events at generator level have been analyzed using the MC sample[†]. No selection cut has been applied except the selection for $\Lambda^0$ and $\bar{\Lambda}^0$. The events are classified into four categories:

- Direct common ancestor (Black): Hyperon pairs share direct production vertex

- One intermediate state (Red): Either one of the hyperon decayed from the shared production vertex through an intermediate state

- Two intermediate states (Blue): Both hyperons decayed from the shared production vertex through an intermediate state

- More intermediate states (Green): Other unclassified events with more intermediate states
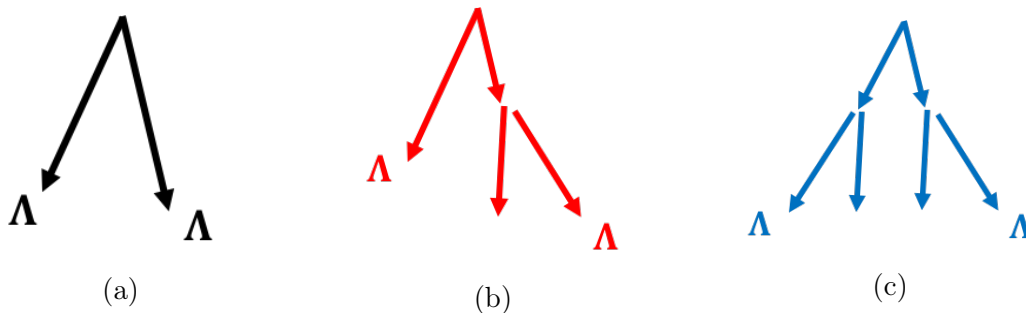


Figure 6.5.1: Classification of ancestor types of hyperon pairs with a (a) direct common ancester, (b) one intermediate state, and (c) two intermediate states.

---

[†]mc10_7TeV.105001.pythia_minbias.evgen.EVNT.e577_tid153938_00

The decay topologies of the first three ancestor types for hyperon pairs sharing a common production vertex are shown in Figure 6.5.1. It is shown that the excess events near the $(\Lambda\Lambda)$ threshold and in the small $\Delta R$ region are originated from hyperon pairs produced from a shared production vertex, either directly or with both or one of the hyperons decayed through an intermediate state as shown in Figure 6.5.2.

Further studies revealed that all events with common ancestor in the first three categories descended from a common production vertex identified as string (PDG ID = 92) in the PYTHIA generator which represents the parton system in the string fragmentation model [34,35]. Most of the intermediate states are identified as either string or $\Sigma$ resonances such as $\Sigma^0$, $\Sigma^{*0}(1385)$, and $\Sigma^{*\pm}(1385)$ as shown in Figure 6.5.3. $\Sigma^0$, which decays into $\Lambda^0$ and photon $\gamma$ with 100% branching fraction, and $\Sigma^{*0}$, which decays into $\Lambda^0$ and $\pi^0$ with a branching fraction of 88%, cannot be reconstructed as photon and $\pi^0$ do not leave a track in the inner tracker and are too soft to reach the calorimeter. Attempts to reconstruct and veto the $\Sigma^{*\pm}(1385)$ using the decay channel $\Sigma^{*\pm} \to \Lambda^0 \pi^\pm$ in our data sample have been made by a undergraduate as a summer project[‡][§]. Mass hypothesis is done on the refitted track of $\Lambda^0$ or $\bar{\Lambda}^0$ candidates and each of the associated tracks in each event. The pion mass is assigned to the track and the combined invariant mass $m_{\Lambda\pi}$ of the $\Lambda^0$ or $\bar{\Lambda}^0$ candidate and the "pion" track is required to be close to the $\Sigma$ resonance mass. The attempt was not very successful due to the very short lifetime ($\tau \sim 10^{-23}$) of $\Sigma$ which results in a production vertex very close to the primary vertex and a large number of background associated tracks ($N_{track} \sim 100$) coming from the same primary vertex. (Figure 6.5.4) The track multiplicity was reduced from an average of around 100 down to around 20 after additional selection cuts, such as

---

[‡]http://cds.cern.ch/record/1748073
[§]https://indico.cern.ch/event/309212/contributions/1681322/attachments/590939/813416/thirdPresentation.pdf

opening angle $\Delta R(\Lambda, \pi)$ and $p_{T,\Lambda\pi}$, based on MC studies with $\Sigma$ signal and background are applied, but the number of tracks are still too high for the $\Sigma^*(1385)$ fed-down removal to work without removing a large proportion ($\sim 90\%$) of the $\Lambda^0$ or $\bar{\Lambda}^0$ candidates. Selection of $\Sigma^*(1385)$ by training Boosted Decision Trees (BDT) on MC signal and background events will be attempted before submitting for final publication if time allows.



(a)

(b)
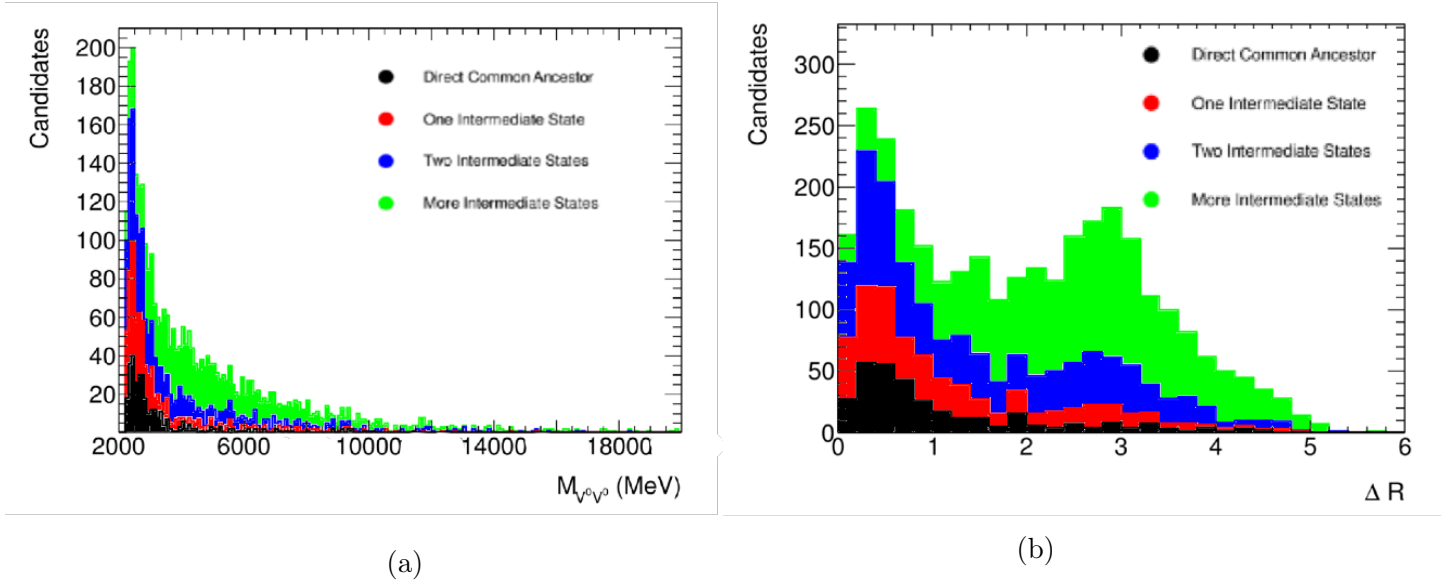
Figure 6.5.2: Stacked distributions of (a) invariant mass $m_{\Lambda\Lambda}$ and (b) opening angle $\Delta R$ for the $\Lambda^0\bar{\Lambda}^0$ events which share direct (black), one intermediate state (red), two intermediate states (blue), and other unclassified events (green). It is shown that the excess events near the ($\Lambda\Lambda$) threshold and in the small $\Delta R$ region are originated from hyperon pairs produced from a shared production vertex, either directly or with both or one of the hyperons decayed through an intermediate state.
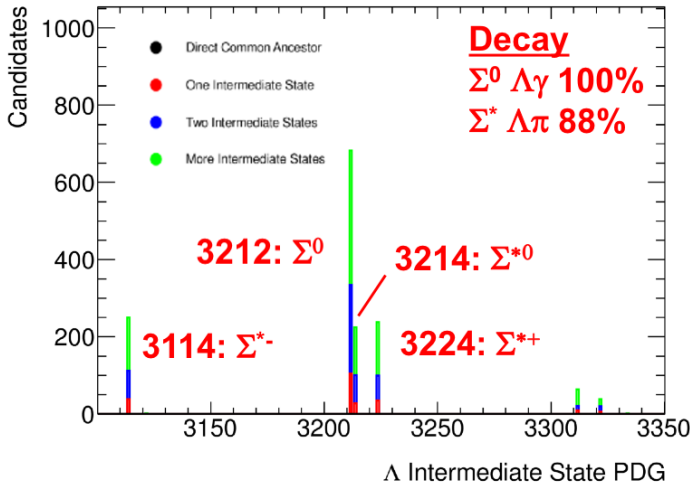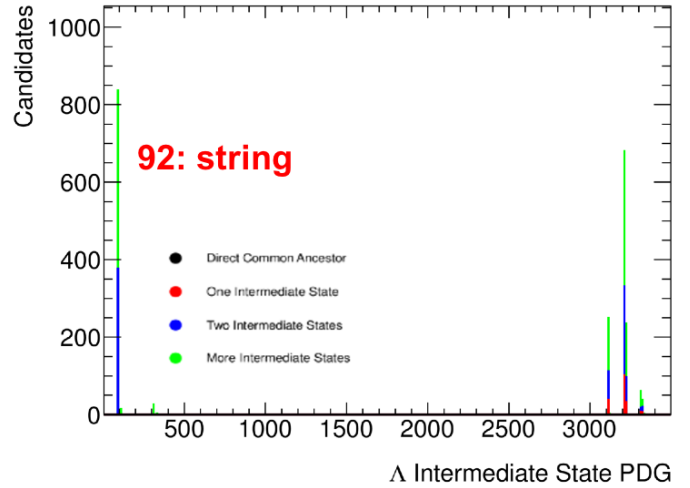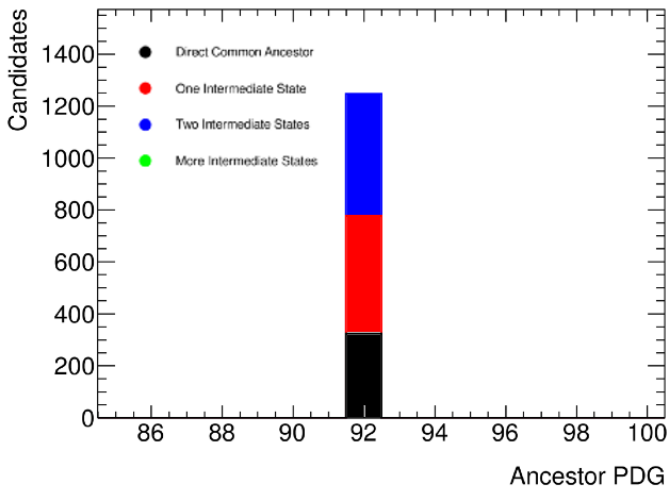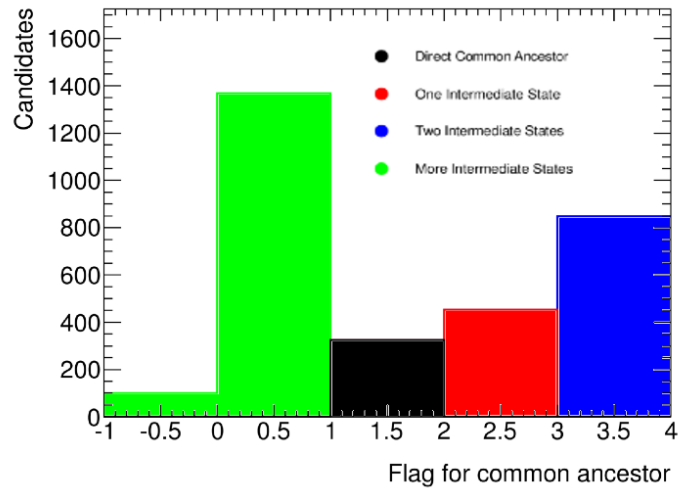
Figure 6.5.3: PDG IDs of (a) & (b) the intermediate states and (c) the common ancestor of the $\Lambda^0 \bar{\Lambda}^0$ events which share direct parent (black), with one intermediate state (red), with two intermediate states (blue), and other unclassified events (green). (d) Number of events for each category of events. It is shown that the majority of the intermediate states are either string or $\Sigma^0/\Sigma^*(1385)$ resonances. All the events with common ancestor in the first three categories descended from string.

105
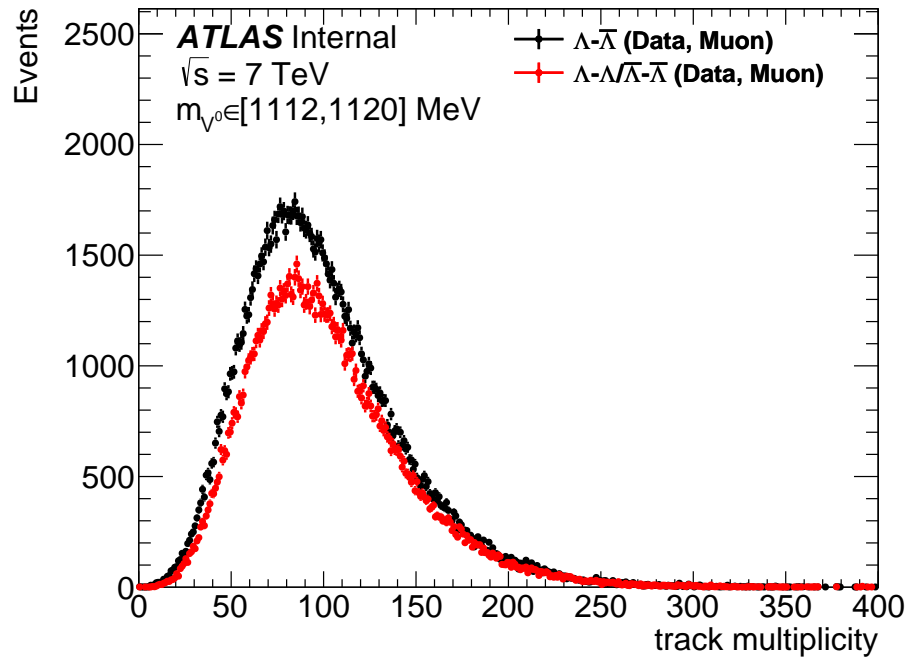
Figure 6.5.4: Distribution of track multiplicity for $\Lambda^0\bar{\Lambda}^0$ and $\Lambda^0\Lambda^0+\bar{\Lambda}^0\bar{\Lambda}^0$ events for the muon sample. The track multiplicity distribution is peaked around 80 for both type of events.

# Chapter 7

# Extraction of spin correlation

This chapter describes the measurement strategy and details of the extraction of the spin correlation, the estimation of statistical and systematic uncertainties, and a summary of the results.

## 7.1 Spin correlation and decay angles

One way of studying the correlation is to determine the spin composition of the system , and the spin composition can be studied indirectly through the correlation between the decay protons of the di-hyperon state as described below.

The normalized angular distribution at the decay $\Lambda^0 \rightarrow p + \pi^-$ takes the form:

$$\frac{dw(\mathbf{n})}{d\Omega_{\mathbf{n}}} = \frac{1}{4\pi}(1 + \alpha_\Lambda \mathbf{P}_\Lambda \mathbf{n}) \tag{7.1.1}$$

where $\mathbf{P}_\Lambda$ is the polarization vector of the $\Lambda^0$ particle, $\mathbf{n}$ is the unit vector along the direction of proton momentum in the rest frame of the $\Lambda^0$ particle, $\alpha_\Lambda = 0.642 \pm 0.013$ is the decay

asymmetry parameter for $\Lambda^0$ [47].

Now we consider the double angular distribution of flight direction of the decay protons of two $\Lambda^0$ decay into the channel $\Lambda^0 \rightarrow p + \pi^-$, normalized by unity. It is described by the following formula:

$$\frac{d^2w(\mathbf{n}_1, \mathbf{n}_2)}{d\Omega_{\mathbf{n}_1}d\Omega_{\mathbf{n}_1}} = \frac{1}{16\pi^2}[1 + \alpha_\Lambda \mathbf{P}_1 \mathbf{n}_1 + \alpha_\Lambda \mathbf{P}_2 \mathbf{n}_2 + \alpha_\Lambda^2 \sum_{i=1}^{3}\sum_{k=1}^{3} T_{ik} n_{1i} n_{2k}] \qquad (7.1.2)$$

where $\mathbf{P}_1$ and $\mathbf{P}_2$ are the polarization vectors of the first and second $\Lambda^0$ particle, $T_{ik}$ are the correlation tensor components, $\mathbf{n}_1$ and $\mathbf{n}_2$ are the unit vectors along the direction of first and second proton momentum in the rest frame of their respective parent $\Lambda^0$ particles.

The angular correlation, integrated over all angles except the angle between the vectors $\mathbf{n}_1$ and $\mathbf{n}_2$ can be described by the formula:

$$\frac{dw(\cos\theta^*)}{d\cos\theta^*} = \frac{1}{2}(1 + \frac{1}{3}\alpha_\Lambda^2 T \cos\theta^*) = \frac{1}{2}(1 + A\alpha_\Lambda^2 \cos\theta^*) \qquad (7.1.3)$$

where $A = (N_{aligned} - N_{antialigned})/N_{total}$ is the spin correlation parameter that we extract from data in this analysis, the correlation tensor $T = W_t - 3W_s$ can be expressed in terms of the relative fractions of the singlet state $W_s$ and triplet state $W_t$, and it does not depend on the polarization vectors.

Due to CP-invariance, the coefficients of P-odd angular asymmetry for the decay $\Lambda^0 \rightarrow p + \pi^-$ and $\bar{\Lambda}^0 \rightarrow \bar{p} + \pi^+$ have equal magnitude and opposite signs: $\alpha_{\bar{\Lambda}} = - \alpha_\Lambda = $ -0.642. The angular correlation for $\Lambda^0 \bar{\Lambda}^0$ pairs decay becomes:

$$\frac{dw(\cos\theta^*)}{d\cos\theta^*} = \frac{1}{2}(1 - \frac{1}{3}\alpha_\Lambda^2 T \cos\theta^*) = \frac{1}{2}(1 - A\alpha_\Lambda^2 \cos\theta^*) \qquad (7.1.4)$$

108
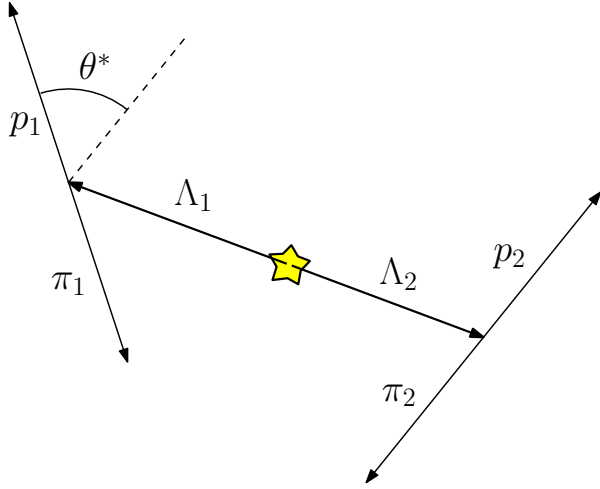
Figure 7.1.1: Definition of decay angle $\theta^*$ which is the angle between the flight directions of $p_1$ and $p_2$ in the rest frame of their respective parents $\Lambda_1$ and $\Lambda_2$ in their common center-of-mass frame.
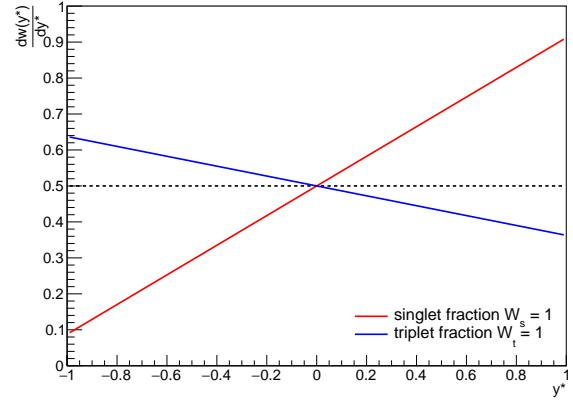


Figure 7.1.2: Distributions of $y^*$ $(\cos\theta^*)$ at true level for pure singlet and triplet states for $\Lambda^0\,\bar{\Lambda}^0$ events. For like-type events, the slopes become the negative of the $\Lambda^0\,\bar{\Lambda}^0$ case with the same absolute values.

The derivation of the angular correlation $\cos\theta^*$ here is mainly adapted from Ref. [113]. $\cos\theta^*$ and $y^*$ will be used interchangeably from now on. The goal of this analysis is to extract the variable $A$ in Eqs. (7.1.3) and (7.1.4) as a function of $Q$, where $Q$ is the relative 4-momentum of the hyperon pair as defined earlier.

By measuring the slope of the $\cos\theta^*$ distribution as shown in Figure 7.1.2, the value of $A$ in Eqs. (7.1.3) and (7.1.4) can be extracted from data. A finite spin correlation due to the spin alignment of the initial state is expected only in the very small $Q$-value region [3] while FD correlation between the like pairs is expected to have a suppression of $S = 1$ state in a $Q$-value region less than 0.5 GeV [8–10].

109

## 7.2 Experimental considerations

The direction of the spin alignment of the hyperon pairs can be inferred from the asymmetric angular distribution of the decay particles, namely the decay proton(antiproton) for $\Lambda^0(\bar{\Lambda}^0)$. Unfortunately, the detector, the track reconstruction inefficiency in particular, can distort the angular distributions. An appropriate reference sample is therefore needed to model the distortion of the angular distribution in absence of any spin correlation. As discussed before, the MC sample has very limited statistics and its kinematic distributions are very different from data (Figure 6.4.1), the mixed data sample is used as the reference sample for the estimation of the effect of the track reconstruction inefficiency of the data sample.

The following factors have been taken into consideration to justify the use of data-driven mixed sample as the appropriate reference sample for spin correlation extraction

- Hyperon pairs selected from odd and even events will have uncorrelated angular distribution in the absence of detector effect

- Detector effects depend solely on the kinematics of the hyperon but not on its origin of production after the hyperon is produced

- Each hyperon is reconstructed independently in the data sample and the interference between the reconstruction of multiple hyperons in the same event can be neglected

- The angular distribution is well reconstructed enough to be used to inject spin correlation to the mixed sample to create the templates

More details of the methodology will be discussed in the following few sections.

## 7.3 Weighting of reference sample

From Figure 6.2.1, the mixed data sample has dynamical correlations somewhat different from that of the data sample, especially for $\Lambda^0\bar{\Lambda}^0$ events. The reference sample is therefore weighted to improve agreement with the data sample (kinematic weighting) and to allow assignment of different spin correlation to the hyperon pairs (correlation weighting). As $\Lambda^0$ and $\bar{\Lambda}^0$ hyperons have different reconstruction efficiency and kinematic distribution, separate corrections have to be made for each type of hyperon pairs. The weighting consists of a two-step process:

1. Correlation weighting is performed by weighting the mixed data sample by a factor of $(1 \pm A\alpha_\Lambda^2 \cos\theta^*)$ for different input $A$-values.

2. Kinematic weighting is then performed independently in each $Q$ bin.

In step one, the true decay angle $\cos\theta^{*true}$ should ideally be used for injecting the spin correlation. However, such decay angle is not available in the data-driven reference sample. As a result, the reconstructed decay angle $\cos\theta^{*reco}$ (which will be referred to as $\cos\theta^*$ from now on) is used for correlation weighting instead.

In step two, the following kinematic variables have been used:

- Opening angle between $\Lambda_1$ and $\Lambda_2$: $\Delta R(\Lambda_1, \Lambda_2)$

- Invariant mass of $\Lambda_1$, $\Lambda_2$ and the hyperon pairs: $m_{\Lambda_1}$, $m_{\Lambda_2}$ and $m_{\Lambda_1+\Lambda_2}$

- Transverse momentum of $\Lambda_1$, $\Lambda_2$ and the hyperon pairs: $p_{T,\Lambda_1}$, $p_{T,\Lambda_2}$ and $p_{T,\Lambda_1+\Lambda_2}$

- Pseudorapidity of $\Lambda_1$, $\Lambda_2$ and the hyperon pairs: $\eta_{\Lambda_1}$, $\eta_{\Lambda_2}$ and $\eta_{\Lambda_1+\Lambda_2}$

111

Iterative weighting has been used to make sure all kinematic variables agree between the data sample and the reference sample. At each iteration, each event in the reference sample is assigned a weight such that the distribution of the current kinematic variable agrees between the data sample and the reference sample. The weight is then updated in the next iteration for the next variable. The iteration continues until the weights of the events become stable. The kinematic distributions before and after kinematic weighting are shown in Figures 9.3.13, 9.3.14, 9.3.17, 9.3.18, 9.3.17, and 9.3.18.

After some careful studies, it is found that the kinematic distribution and the angular correlation are slightly correlated. Weighting the aforementioned kinematic variables may distort the angular correlation. As the mixed data sample and the data sample have very similar kinematic distributions in most of the phase space except in the small $Q$-value range for $\Lambda^0\bar{\Lambda}^0$ events where the data events have significantly higher combined transverse momentum $p_{T,\Lambda_1+\Lambda_2}$ and smaller opening angle $\Delta R(\Lambda_1, \Lambda_2)$, the systematic uncertainty due to kinematic weighting is treated naively by repeating the analysis without kinematic weighting and taking the difference between the new value and the baseline values as the uncertainty.

## 7.4   Minimum $\chi^2$ method

After performing the correlation and kinematic weightings as discussed in the previous section, the modified Pearson's $\chi^2$ test statistic for comparing usual and weighted histograms as described in Ref. [114] is calculated to quantify the compatibility of the $\cos\theta^*$ distribution between each pair of data and template. Each template is weighted to a different $A$-value, as shown in Figure 7.4.1 for both like-type and unlike-type events in the range $0 < Q < 1$ GeV as an example. The best-fitted $A$-value of data is determined by minimizing the value of $\chi^2$

and the uncertainty is estimated by the variation of $A$ at $\chi^2_{min}+1$ as shown in Figure 7.4.1 (b) and (d). The extracted $A$-values are plotted with the corresponding statistical uncertainties as a function of $Q$ in Figure 7.8.1.
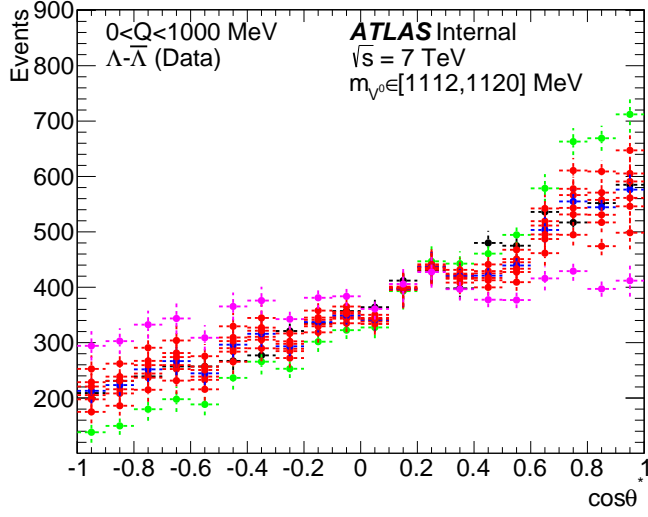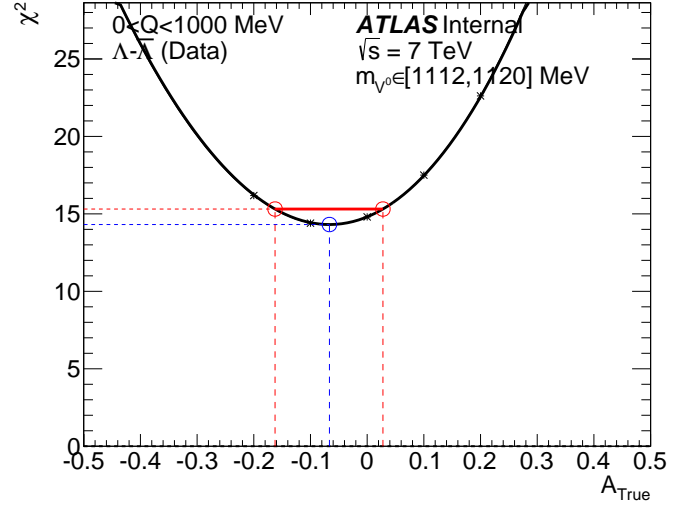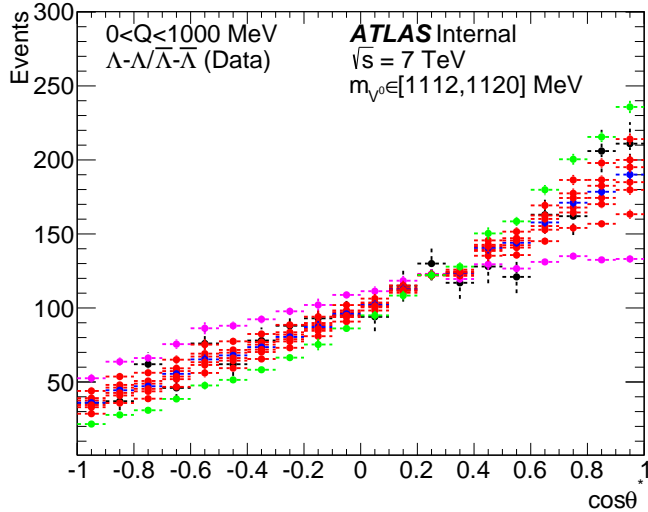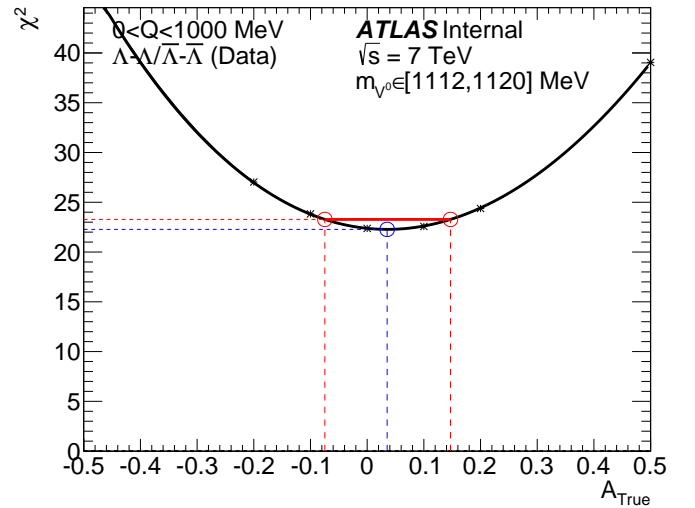
Figure 7.4.1: Reconstructed $\cos\theta^*$ distribution for (a) $\Lambda^0\bar{\Lambda}^0$ and (c) $\Lambda^0\Lambda^0+\bar{\Lambda}^0\bar{\Lambda}^0$ events in the range $0 < Q < 1$ GeV in the signal region. Black: data; blue: template with $A = 0$; green/magenta: template weighted to $A = +1$ or $-1$; red: templates weighted to $A$ values of $\pm 0.1, \pm 0.2$ and $\pm 0.5$. $\chi^2$ vs $A_{\text{True}}$ distribution for (b) $\Lambda^0\bar{\Lambda}^0$ and (d) $\Lambda^0\Lambda^0+\bar{\Lambda}^0\bar{\Lambda}^0$ events in the range $0 < Q < 1$ GeV in the signal region. The extracted $A$-value is determined by the minimum value of $\chi^2$ as indicated by blue dashed lines. The uncertainty of $A$ is estimated by the variation of $A$ at $\chi^2_{min} + 1$ as indicated by red dashed and solid lines.

## 7.5 Statistical uncertainties

Statistical uncertainties can be reduced by increasing the sample size of data. The method of minimum $\chi^2$ is used to determine the best-fitted $A$-value for data. The statistical uncertainty is estimated at the variation of $A$ at $\chi^2_{min} + 1$, as shown in Figures 7.4.1b and 7.4.1d. The statistical uncertainty of the extracted $A$-values are plotted as a function of $Q$ are shown in Figure 7.8.1.

## 7.6 Systematic uncertainties

The systematic uncertainties are estimated by varying different aspects of the analysis and measuring how each affects the measured values of the spin correlation. The main contribution of systematic uncertainties are kinematic weighting, binning and template statistics. The uncertainties are assumed to be uncorrelated and are added in quadrature to obtain a total systematic uncertainty. All uncertainties are treated symmetrically except the uncertainty due to kinematic weighting. The systematic uncertainties considered are described in the following subsections.

### 7.6.1 Kinematic weighting

The difference between $A$-values measured with and without kinematic weighting is treated as the systematic uncertainty.

Kinematic weighting can change the input spin correlation $A_{\text{True}}$ of the template if there is correlation between $A_{\text{True}}$ and the kinematic variables that were used in the weighting

process. The templates may not correspond to injected $A$-values after kinematic weighting. To estimate the effect of kinematic weighting, the analysis is repeated without the kinematic weighting in which case the templates correspond to the injected $A$-values but may have kinematics different from the data. The difference in kinematics between the data and the templates are assumed to be caused by the difference in $A$-value and the difference in detector effects is neglected. The extracted alternative $A$-values are then compared to the default results and the difference is treated as the systematic uncertainty. This is the dominating systematic uncertainty in the first bin ($0 < Q < 1$ GeV) for all four types of events due to the strikingly different kinematics between the data and templates for $\Lambda^0\bar{\Lambda}^0$ and low template statistics in general. (Figure 7.6.1) This is a very conservative estimation of the uncertainty due to kinematic weighting. Nonetheless, this uncertainty is relatively small in the range $1 < Q < 10$ GeV where the kinematics of the data and the mixed data sample are very similar.

## 7.6.2   Binning

The effect of re-binning the $\cos\theta^*$ distribution has been studied. The analysis is repeated with 2-times finer and coarser binning of the $\cos\theta^*$ distribution. The new results are compared to the baseline result and the difference in each case is calculated. The larger of the two is treated as the systematic uncertainty.

## 7.6.3   Template statistics

Limited statistics of the data-driven template projects into the precision with which the $A$-value extracted by the minimum $\chi^2$ method. To estimate the effect of the limited statistics of
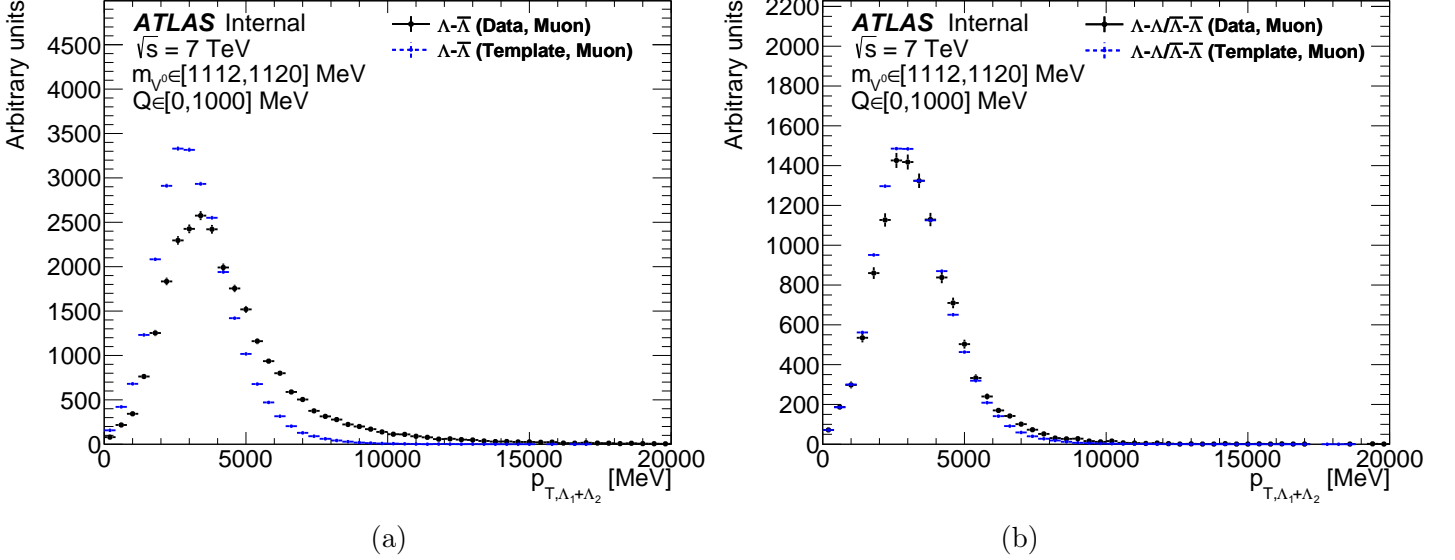
Figure 7.6.1: $p_{T,\Lambda_1+\Lambda_2}$ distributions for (a) $\Lambda^0\bar{\Lambda}^0$ and (b) $\Lambda^0\Lambda^0+\bar{\Lambda}^0\bar{\Lambda}^0$ events in the first bin $(0 < Q < 1$ GeV) for data and template samples before kinematic weighting. The $\Lambda^0\bar{\Lambda}^0$ data events have a higher average combined $p_T$ than the mixed sample events before kinematic weighting. The large discrepancy in the $p_T$ spectrum led to a huge systematic uncertainty due to kinematic weighting and is shown in the first bin in Figure 7.8.1b. $\Lambda^0\Lambda^0+\bar{\Lambda}^0\bar{\Lambda}^0$ events in data and template samples have similar $p_{T,\Lambda_1+\Lambda_2}$ distributions and correspond to a much smaller systematic uncertainty as shown in Figure 7.8.1a.

the data-driven template, the template is split into 4 statistically independent sub-samples. A measurement is then performed with each sub-sample on the data and the differences to the baseline result is calculated. The uncertainty is estimated as a standard deviation of the obtained differences scaled down by a factor of $\sqrt{3}$, to account for the fact that each sub-sample has 4-times less events than the original one.

### 7.6.4    Background

The $A$-values and the signal fractions $f_{sig}$ are measured separately in the signal region $[1112, 1120]$ MeV and sidebands $[1100, 1107] \bigcup [1125, 1135]$ MeV and the $A$-values are re-

117

calculated in each bin taken into account the contribution from background.

Let $f_{\mathrm{SR}}$ and $f_{\mathrm{BG}}$ be the signal fractions measured in the SR and BG regions, $A_{\mathrm{SR}}$ and $A_{\mathrm{BG}}$ be the spin correlations measured in the signal and background regions and $A_{\mathrm{sig}}$ and $A_{\mathrm{bkg}}$ be the spin correlations of the signal and background events. $A_{\mathrm{sig}}$ and $A_{\mathrm{bkg}}$ can be expressed as follow

$$A_{\mathrm{SR}} = f_{\mathrm{SR}} A_{\mathrm{sig}} + (1 - f_{\mathrm{SR}}) A_{\mathrm{bkg}} \tag{7.6.1}$$

and

$$A_{\mathrm{BG}} = f_{\mathrm{BG}} A_{\mathrm{sig}} + (1 - f_{\mathrm{BG}}) A_{\mathrm{bkg}}. \tag{7.6.2}$$

From (7.6.1) $\times (1 - f_{\mathrm{BG}})$ - (7.6.2) $\times (1 - f_{\mathrm{SR}})$, we have

$$A_{\mathrm{sig}} = \frac{1}{f_{\mathrm{SR}} - f_{\mathrm{BG}}} \left[ (1 - f_{\mathrm{BG}}) A_{\mathrm{SR}} - (1 - f_{\mathrm{SR}}) A_{\mathrm{BG}} \right] \tag{7.6.3}$$

$A_{\mathrm{sig}}$ is computed by Eq. (7.6.3) and is compared to the default results computed using events in the signal region without background subtraction. The difference between the alternative and the default values is treated as the systematic uncertainty.

The spin correlation in the BG region is assumed to be constant. In principle, such assumption can be relaxed by splitting the BG region into sidebands and corners if enough statistics is available in the BG region and the signal purity in the SR region is low. However, since the signal purity in the SR region is above 98%, such higher-order effect is neglected.

## 7.6.5  Width of signal region

The width of the signal region is varied up and down by 2 MeV. The difference between the alternative value and the default value is calculated in each case. The larger difference is taken as the systematic uncertainty.

## 7.6.6  Event migration

The measured $A$ values are plotted as a function of reconstructed $Q$ while the results should be interpreted as a function of true $Q$. Using the MC sample, the fraction of events migrated from neighboring bins to the bin of interest is calculated. The MC sample has been weighted kinematically to the data. Migration matrices of reconstructed $Q$ versus true $Q$, normalized in true $Q$ bins, are shown in Figure 7.6.2. The diagonal terms represent events in which the true $Q$ is reconstructed in the same bin while the off-diagonal terms correspond to the true $Q$ that is distorted as it is reconstructed. A corrected $A'$ value for the true $Q$ bin is calculated as the following weighted average

$$A'_i = \sum_j m_{ij} A_j \tag{7.6.4}$$

where $A'_i$ is the corrected spin correlation for $i$-th bin in true $Q$, $A_j$ is the original spin correlation for the $j$-th bin in reconstructed $Q$, $m_{ij}$ is the $j$-th term in the $i$-th column in the migration matrix as shown in Figure 7.6.2. The systematic uncertainties due to event migration is calculated by measuring the difference between the baseline results $A$ and the weighted average $A'$ in each bin.
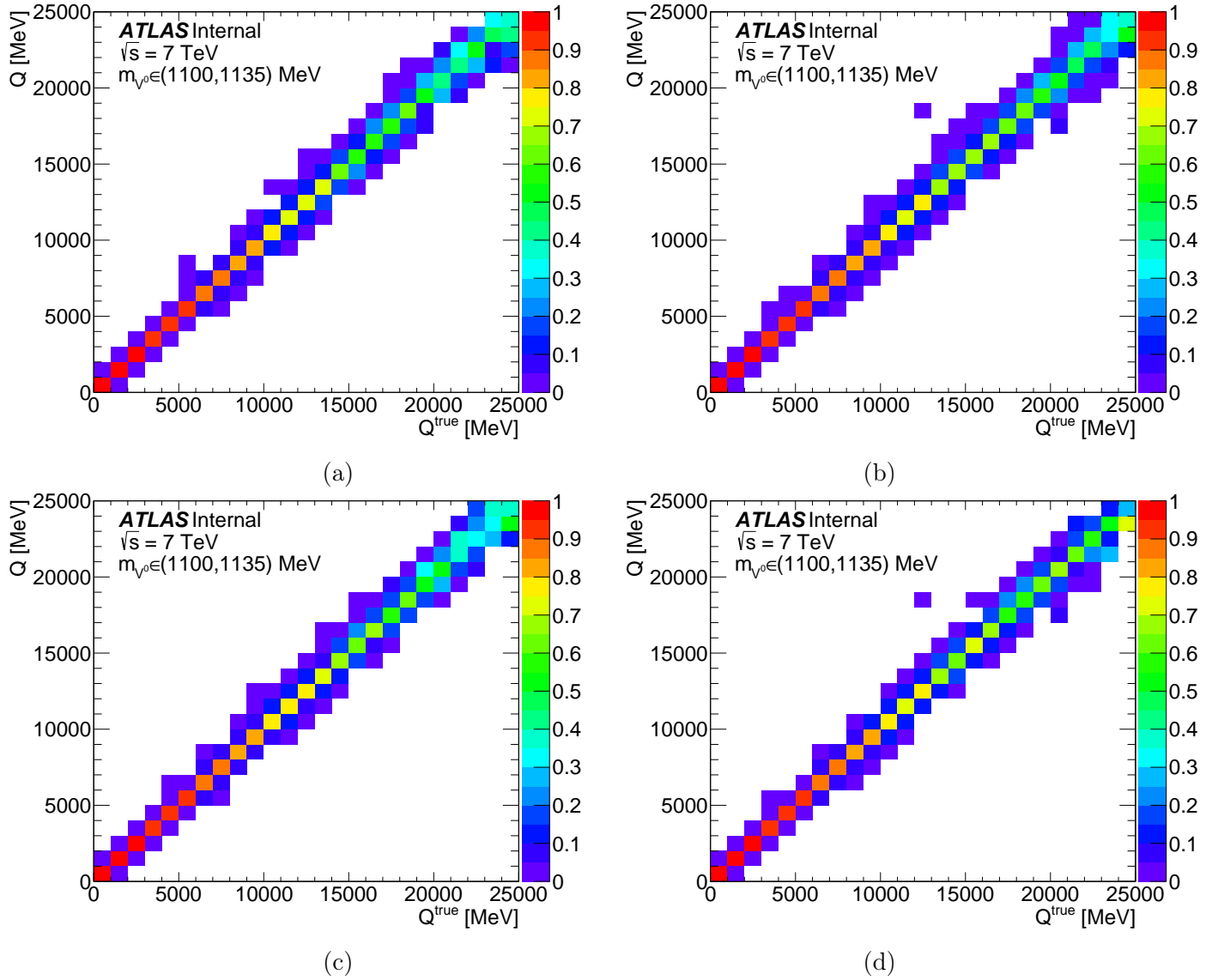
Figure 7.6.2: Migration matrices of reconstructed $Q$ versus true $Q$ normalized in bins of true $Q$ for (a) $\Lambda^0\bar{\Lambda}^0$, (b) $\Lambda^0\Lambda^0+\bar{\Lambda}^0\bar{\Lambda}^0$, (c) $\Lambda^0\Lambda^0$, and (d) $\bar{\Lambda}^0\bar{\Lambda}^0$ events.

## 7.6.7 Decay angle resolution

The mixed MC sample is weighted to the mixed data sample and $\cos\theta^{*true}$ is used for correlation weighting instead of $\cos\theta^{*reco}$.

In the correlation weighting, a non-zero spin correlation is introduced to the uncorrelated template by assigning a weight of $w(\cos\theta^*) = (1 \pm \alpha_\Lambda^2 \cos\theta^*)$ to each event in the sample. In the ideal case, the true decay angles $\cos\theta^{*true}$ should be used in the correlation weighting process. However, owing to the limited statistics of the full-simulated MC sample, an uncorrelated data-driven template has been used as a benchmark to extract the spin correlation from data. As only the reconstructed decay angles are available in the data-driven template, they are used to weight the template to introduce non-zero spin correlations. This is not ideal because the finite resolution of the decay angle reconstruction would smear the true decay angle and get reflected in the distribution of the reconstructed angle. This is shown by the resolution matrices of reconstructed decay angle $\cos\theta^{*reco}$ versus true decay angle $\cos\theta^{*true}$ in Figure 7.6.3.

A template weighted by the true decay angle $\cos\theta^{*true}$ will therefore produce a reconstructed decay angle distribution with a smaller $A$-value due to the smearing effect of the finite detector resolution when compared to one weighted by reconstructed decay angle. The $A$-value extracted using templates weighted by the true decay angle will be larger for the same reconstructed decay angle distribution in data. To estimate the uncertainties caused by such effect, an uncorrelated mixed MC sample is first weighted to have the same kinematic distribution and the decay angle distribution as the data. Then, two lists of templates are produced by weighting to different $A$-values using the true decay angle and the reconstructed decay angle. The $A$-value of the data is extracted as a function of $Q$ using the two list of templates and the difference between these two results is treated as the systematic uncertainties. The systematic uncertainties due to decay angle resolution are found to be negligible when compared to other uncertainties.
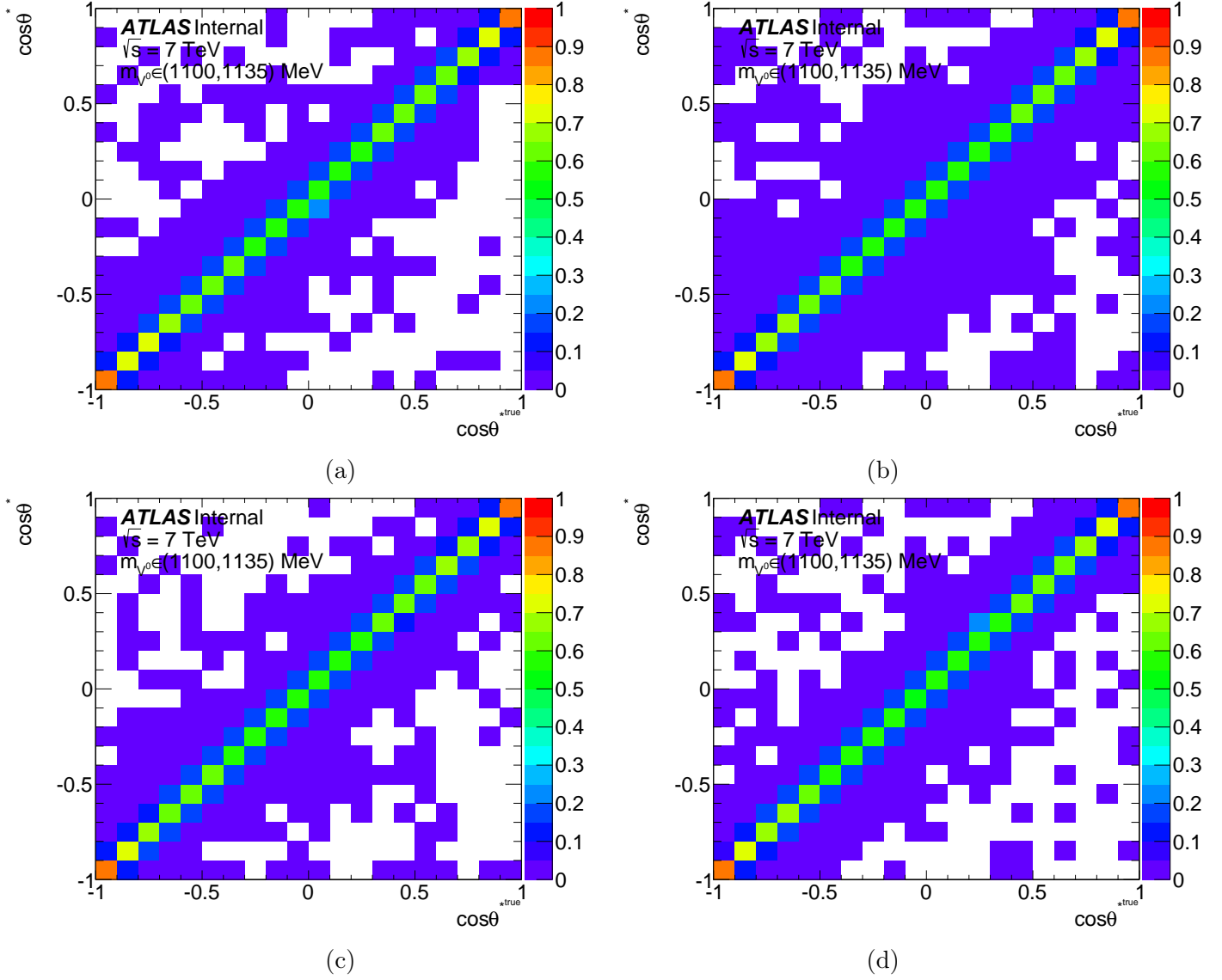
Figure 7.6.3: Resolution matrices for decay angle $\cos\theta^*$ $(y^*)$ normalized in bins of true $\cos\theta^*$ $(y^*)$ for (a) $\Lambda^0\bar{\Lambda}^0$, (b) $\Lambda^0\Lambda^0+\bar{\Lambda}^0\bar{\Lambda}^0$, (c) $\Lambda^0\Lambda^0$, and (d) $\bar{\Lambda}^0\bar{\Lambda}^0$ events.

## 7.6.8 Uncertainty of $\alpha$ parameter

The decay parameter $\alpha_\Lambda$ of $\Lambda^0$ is measured to be $0.642 \pm 0.013$ [47]. The corresponding systematic uncertainty propagated to the measurement of $A$ is estimated by repeating the

measurement with $\alpha_\Lambda$ varied up and down by 0.013. The difference between the new result and the baseline result is calculated in each case. The larger of the two values is treated as the systematic uncertainty. Such uncertainties are found to be negligible when compared to other uncertainties.

## 7.7 Summary of uncertainties estimation

The total systematic uncertainties of the spin correlation parameter are found to be less than 0.1 for most of the $Q$ range with the exception of the first bin where $0 < Q < 1$ GeV. For the like-type events, the total systematic uncertainty is around 0.2 in the first bin. For the unlike-type events, the total systematic uncertainty is around 0.6 and is mainly due to the systematic uncertainty of kinematic weighting. The breakdowns of the sources of systematic uncertainties in bins of $Q$ are shown in Tables 7.1, 7.2, 7.3, and 7.4*. The dominant systematic uncertainty, uncertainty of kinematic weighting, is treated asymmetrically to avoid misleading the reader of the actual range of the uncertainty. The uncertainty is included in the calculation of the total uncertainty in either the upside or the downside depending on whether the uncertainty is positive or negative respectively. The asymmetric total systematic uncertainties are listed in Tables 7.5 and 7.6.

---

*The number of digits here is only for illustration purposes for some uncertainties of particularly small values. For the actual number of significance figures of the total uncertainties, readers should refer to Tables 7.5 and 7.6.

Table 7.1: Summary of systematic uncertainties for $\Lambda^0\bar{\Lambda}^0$ events in the range $0 < Q < 10$ GeV. The systematic uncertainties in each bin are assumed to be uncorrelated and are added in quadrature to compute the total uncertainty. The uncertainties are broken down as follows: 1. Kinematic weighting 2. Template statistics 3. Binning 4. Width of signal region 5. Background 6. Event migration 7. Decay angle resolution 8. Uncertainty of $\alpha$ parameter

| $Q$ [GeV] | 1 | 2 | 3 | 4 | 5 | 6 | 7 | 8 | Total |
|---|---|---|---|---|---|---|---|---|---|
| 0-1 | 0.62340 | 0.07705 | 0.02553 | 0.03060 | -0.00280 | -0.00126 | 0.00275 | 0.00143 | 0.62942 |
| 1-2 | 0.00296 | 0.02534 | 0.00429 | 0.00104 | -0.00037 | 0.00208 | -0.00063 | 0.00053 | 0.02599 |
| 2-3 | -0.08520 | 0.00952 | 0.00167 | 0.00516 | 0.00040 | -0.00188 | 0.00053 | 0.00201 | 0.08594 |
| 3-4 | -0.03703 | 0.01148 | 0.00540 | 0.00261 | -0.00169 | 0.00064 | -0.00084 | 0.00009 | 0.03928 |
| 4-5 | -0.00661 | 0.01177 | 0.00731 | 0.00773 | -0.00052 | -0.00070 | 0.00027 | 0.00050 | 0.01722 |
| 5-6 | -0.00659 | 0.00958 | 0.00274 | 0.00854 | 0.00278 | 0.00448 | -0.00096 | 0.00156 | 0.01571 |
| 6-7 | -0.00595 | 0.01477 | 0.00534 | 0.00305 | -0.00230 | -0.00250 | -0.00226 | 0.00103 | 0.01758 |
| 7-8 | -0.00760 | 0.01872 | 0.00582 | 0.00598 | -0.00103 | 0.00001 | 0.00055 | 0.00160 | 0.02195 |
| 8-9 | -0.00013 | 0.01111 | 0.00266 | 0.01207 | -0.00036 | -0.00089 | -0.00104 | 0.00234 | 0.01684 |
| 9-10 | -0.02451 | 0.02549 | 0.00518 | 0.01117 | 0.00208 | -0.00756 | 0.00147 | 0.00341 | 0.03843 |

Table 7.2: Summary of systematic uncertainties for $\Lambda^0\Lambda^0 + \bar{\Lambda}^0\bar{\Lambda}^0$ events in the range $0 < Q < 10$ GeV. The systematic uncertainties in each bin are assumed to be uncorrelated and are added in quadrature to compute the total uncertainty. The uncertainties are broken down as follows: 1. Kinematic weighting 2. Template statistics 3. Binning 4. Width of signal region 5. Background 6. Event migration 7. Decay angle resolution 8. Uncertainty of $\alpha$ parameter

| $Q$ [GeV] | 1 | 2 | 3 | 4 | 5 | 6 | 7 | 8 | Total |
|---|---|---|---|---|---|---|---|---|---|
| 0-1 | -0.20046 | 0.03267 | 0.04350 | 0.01707 | -0.00064 | 0.00226 | 0.00531 | 0.00019 | 0.20849 |
| 1-2 | -0.03274 | 0.00402 | 0.00289 | 0.00929 | -0.00525 | 0.00082 | 0.00019 | 0.00194 | 0.03485 |
| 2-3 | 0.02605 | 0.00346 | 0.00472 | 0.00703 | -0.00057 | -0.00324 | 0.00017 | 0.00440 | 0.02816 |
| 3-4 | -0.00473 | 0.00597 | 0.00190 | 0.00319 | -0.00006 | 0.00354 | 0.00063 | 0.00044 | 0.00922 |
| 4-5 | -0.00584 | 0.00965 | 0.00328 | 0.00221 | -0.00176 | -0.00507 | 0.00057 | 0.00209 | 0.01328 |
| 5-6 | -0.00492 | 0.00432 | 0.00229 | 0.00071 | -0.00008 | 0.00610 | 0.00158 | 0.00168 | 0.00955 |
| 6-7 | -0.00287 | 0.00706 | 0.00268 | 0.00618 | 0.00035 | -0.00744 | 0.00054 | 0.00019 | 0.01262 |
| 7-8 | -0.00657 | 0.01658 | 0.00201 | 0.01042 | 0.00301 | 0.00527 | 0.00037 | 0.00308 | 0.02185 |
| 8-9 | -0.00556 | 0.01327 | 0.00133 | 0.00580 | -0.00021 | 0.00668 | 0.00030 | 0.00339 | 0.01728 |
| 9-10 | -0.00885 | 0.02582 | 0.00631 | 0.00469 | -0.00516 | -0.00901 | -0.00040 | 0.00061 | 0.03025 |

Table 7.3: Summary of systematic uncertainties for $\Lambda^0\Lambda^0$ events in the range $0 < Q < 10$ GeV. The systematic uncertainties in each bin are assumed to be uncorrelated and are added in quadrature to compute the total uncertainty. The uncertainties are broken down as follows: 1. Kinematic weighting 2. Template statistics 3. Binning 4. Width of signal region 5. Background 6. Event migration 7. Decay angle resolution 8. Uncertainty of $\alpha$ parameter

| $Q$ [GeV] | 1 | 2 | 3 | 4 | 5 | 6 | 7 | 8 | Total |
|---|---|---|---|---|---|---|---|---|---|
| 0-1 | -0.12839 | 0.01107 | 0.07503 | 0.02277 | -0.00112 | -0.00421 | 0.00987 | 0.00457 | 0.15130 |
| 1-2 | -0.02586 | 0.00376 | 0.01095 | 0.02020 | -0.00347 | 0.00281 | 0.00017 | 0.00098 | 0.03509 |
| 2-3 | 0.01547 | 0.00767 | 0.00513 | 0.00345 | -0.00058 | -0.00482 | 0.00039 | 0.00510 | 0.01964 |
| 3-4 | -0.01143 | 0.00806 | 0.00300 | 0.00396 | 0.00027 | 0.00569 | 0.00011 | 0.00124 | 0.01595 |
| 4-5 | -0.00501 | 0.01353 | 0.00609 | 0.00379 | -0.00033 | -0.00527 | 0.00054 | 0.00173 | 0.01705 |
| 5-6 | -0.00426 | 0.00525 | 0.00644 | 0.00781 | -0.00124 | 0.00622 | 0.00232 | 0.00142 | 0.01399 |
| 6-7 | -0.01354 | 0.01102 | 0.00485 | 0.00724 | -0.00123 | -0.00616 | 0.00065 | 0.00123 | 0.02055 |
| 7-8 | -0.00581 | 0.01456 | 0.00693 | 0.01177 | 0.00113 | 0.00785 | 0.00317 | 0.00057 | 0.02248 |
| 8-9 | -0.00972 | 0.01272 | 0.00216 | 0.00564 | -0.00096 | -0.01370 | 0.00285 | 0.00252 | 0.02227 |
| 9-10 | -0.00523 | 0.04971 | 0.00699 | 0.00631 | -0.00287 | 0.01331 | 0.00568 | 0.00221 | 0.05301 |

Table 7.4: Summary of systematic uncertainties for $\bar{\Lambda}^0\bar{\Lambda}^0$ events in the range $0 < Q < 10$ GeV. The systematic uncertainties in each bin are assumed to be uncorrelated and are added in quadrature to compute the total uncertainty. The uncertainties are broken down as follows: 1. Kinematic weighting 2. Template statistics 3. Binning 4. Width of signal region 5. Background 6. Event migration 7. Decay angle resolution 8. Uncertainty of $\alpha$ parameter

| $Q$ [GeV] | 1 | 2 | 3 | 4 | 5 | 6 | 7 | 8 | Total |
|---|---|---|---|---|---|---|---|---|---|
| 0-1 | -0.14019 | 0.04258 | 0.01826 | 0.04086 | 0.00014 | 0.00250 | -0.01992 | 0.00203 | 0.15452 |
| 1-2 | -0.03012 | 0.00472 | 0.00476 | 0.00592 | -0.00737 | -0.00027 | -0.00128 | 0.00315 | 0.03245 |
| 2-3 | 0.03906 | 0.00460 | 0.00615 | 0.01118 | -0.00056 | -0.00088 | -0.00024 | 0.00332 | 0.04149 |
| 3-4 | -0.00300 | 0.00530 | 0.00573 | 0.00543 | -0.00044 | 0.00112 | 0.00213 | 0.00218 | 0.01049 |
| 4-5 | -0.00915 | 0.01178 | 0.00055 | 0.00435 | -0.00275 | -0.00477 | 0.00083 | 0.00256 | 0.01671 |
| 5-6 | -0.00350 | 0.01023 | 0.00409 | 0.00909 | 0.00145 | 0.00576 | -0.00042 | 0.00204 | 0.01599 |
| 6-7 | 0.00592 | 0.01115 | 0.00816 | 0.00423 | 0.00225 | -0.00970 | 0.00138 | 0.00082 | 0.01859 |
| 7-8 | -0.01358 | 0.02425 | 0.00344 | 0.00869 | 0.00463 | -0.00083 | -0.00342 | 0.00618 | 0.03053 |
| 8-9 | -0.03977 | 0.01165 | 0.00645 | 0.00609 | 0.00186 | 0.04422 | 0.00103 | 0.01099 | 0.06227 |
| 9-10 | -0.02637 | 0.02404 | 0.00877 | 0.01176 | -0.00984 | -0.03872 | 0.01082 | 0.00333 | 0.05669 |

## 7.8 Results

### 7.8.1 Spin correlation $A$ vs $Q$ for muon sample using 1 GeV bin size for the muon sample with both statistical and systematic uncertainties

The spin correlation $A$ in the helicity frame as defined in Eqs. (7.1.3) and (7.1.4) has been extracted as a function of $Q$ with 1 GeV bin size for the muon sample. The total uncertainty, which is the quadrature sum of the statistical and systematic uncertainties as described in Section 7.7, is calculated independently for each $Q$ bin. All the systematic uncertainties are treated symmetrically except that due to kinematic weighting. The results are summarized in Figure 7.8.1 as well as in Tables 7.5 and 7.6.
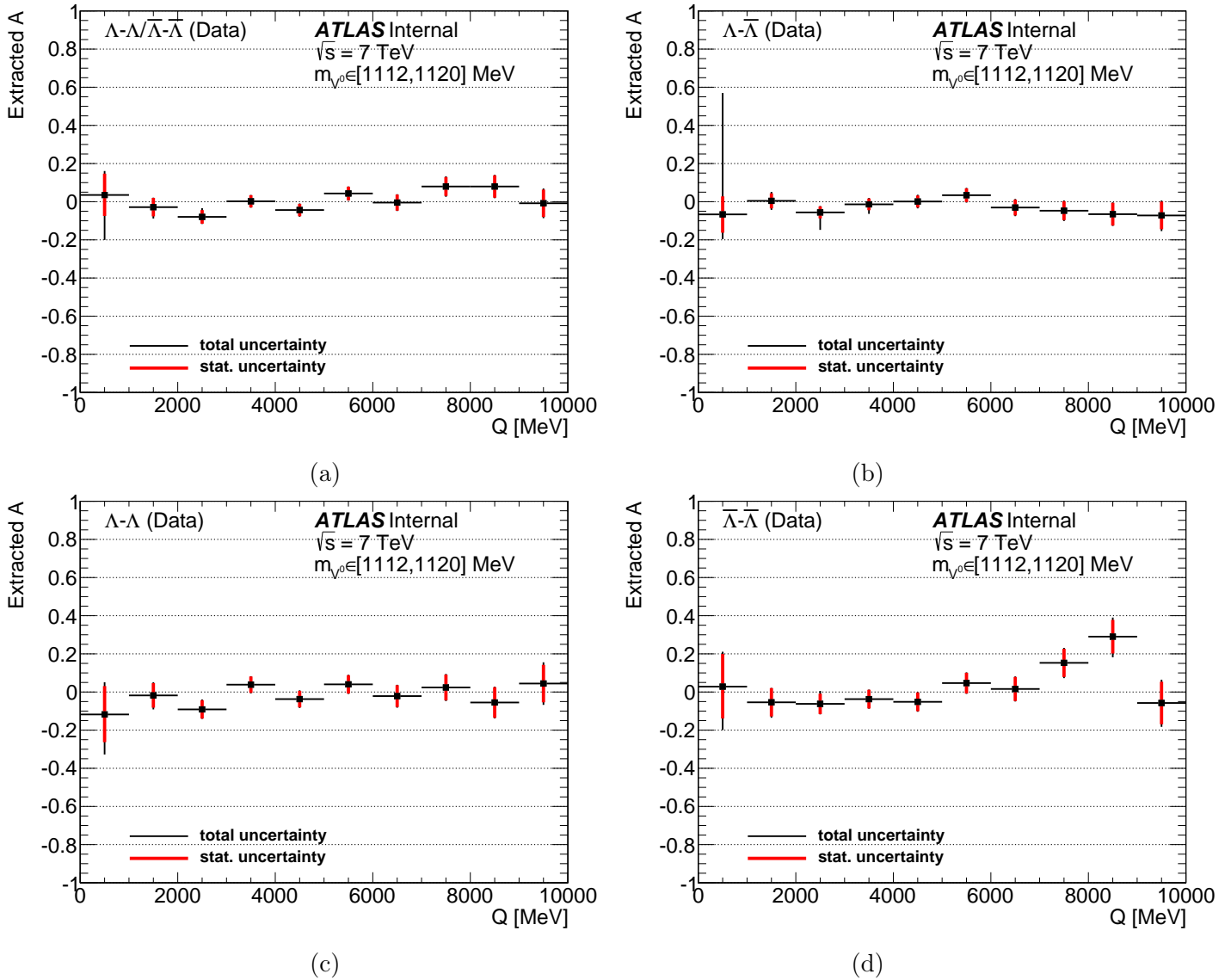
Figure 7.8.1: Extracted spin correlation $A$ in the helicity frame as a function of $Q$ for (a) like-type, (b) unlike-type, (c) $\Lambda^0\Lambda^0$, and (d) $\bar{\Lambda}^0\bar{\Lambda}^0$ events for $0 < Q < 10$ GeV using the minimum $\chi^2$ method. The statistical uncertainties indicate variation of $A$ at $\chi^2_{min} + 1$, as described in Figure 7.4.1b. The total uncertainties are calculated by adding the statistical and systematic uncertainties in quadrature.

127

Table 7.5: Extracted spin correlation $A$ in the helicity frame as a function of $Q$ for unlike-type ($\Lambda^0\bar{\Lambda}^0$) and like-type ($\Lambda^0\Lambda^0+\bar{\Lambda}^0\bar{\Lambda}^0$) events.

| $Q$ [GeV] | $A$ for $\Lambda^0\bar{\Lambda}^0$ | $A$ for $\Lambda^0\Lambda^0+\bar{\Lambda}^0\bar{\Lambda}^0$ |
|---|---|---|
| 0-1 | $-0.026^{+0.089}_{-0.090}$ (stat) $^{+0.629}_{-0.087}$ (syst) | $-0.012^{+0.107}_{-0.105}$ (stat) $^{+0.057}_{-0.208}$ (syst) |
| 1-2 | $0.015 \pm 0.038$ (stat) $^{+0.026}_{-0.026}$ (syst) | $-0.045 \pm 0.048$ (stat) $^{+0.012}_{-0.035}$ (syst) |
| 2-3 | $-0.047 \pm 0.031$ (stat) $^{+0.011}_{-0.086}$ (syst) | $-0.096 \pm 0.036$ (stat) $^{+0.028}_{-0.011}$ (syst) |
| 3-4 | $-0.006 \pm 0.030$ (stat) $^{+0.013}_{-0.039}$ (syst) | $-0.006 \pm 0.032$ (stat) $^{+0.008}_{-0.009}$ (syst) |
| 4-5 | $0.009 \pm 0.032$ (stat) $^{+0.016}_{-0.017}$ (syst) | $-0.045 \pm 0.032$ (stat) $^{+0.012}_{-0.013}$ (syst) |
| 5-6 | $0.034 \pm 0.035$ (stat) $^{+0.014}_{-0.016}$ (syst) | $0.042 \pm 0.036$ (stat) $^{+0.008}_{-0.010}$ (syst) |
| 6-7 | $-0.027 \pm 0.041$ (stat) $^{+0.017}_{-0.018}$ (syst) | $-0.002 \pm 0.042$ (stat) $^{+0.012}_{-0.013}$ (syst) |
| 7-8 | $-0.041 \pm 0.049$ (stat) $^{+0.021}_{-0.022}$ (syst) | $0.075 \pm 0.049$ (stat) $^{+0.021}_{-0.022}$ (syst) |
| 8-9 | $-0.058 \pm 0.058$ (stat) $\pm 0.017$ (syst) | $0.082 \pm 0.058$ (stat) $^{+0.016}_{-0.017}$ (syst) |
| 9-10 | $-0.082^{+0.071}_{-0.070}$ (stat) $^{+0.030}_{-0.038}$ (syst) | $-0.012^{+0.071}_{-0.072}$ (stat) $^{+0.029}_{-0.030}$ (syst) |

Table 7.6: Extracted spin correlation $A$ in the helicity frame as a function of $Q$ for $\Lambda^0\Lambda^0$ and $\bar{\Lambda}^0\bar{\Lambda}^0$ events.

| $Q$ [GeV] | $A$ for $\Lambda^0\Lambda^0$ | $A$ for $\bar{\Lambda}^0\bar{\Lambda}^0$ |
|---|---|---|
| 0-1 | $-0.114^{+0.138}_{-0.135}$ (stat) $^{+0.080}_{-0.151}$ (syst) | $0.033^{+0.163}_{-0.160}$ (stat) $^{+0.065}_{-0.154}$ (syst) |
| 1-2 | $-0.024 \pm 0.063$ (stat) $^{+0.024}_{-0.035}$ (syst) | $-0.073 \pm 0.073$ (stat) $^{+0.012}_{-0.032}$ (syst) |
| 2-3 | $-0.111 \pm 0.048$ (stat) $^{+0.020}_{-0.012}$ (syst) | $-0.071 \pm 0.053$ (stat) $^{+0.041}_{-0.014}$ (syst) |
| 3-4 | $0.032 \pm 0.043$ (stat) $^{+0.011}_{-0.016}$ (syst) | $-0.046 \pm 0.049$ (stat) $\pm 0.010$ (syst) |
| 4-5 | $-0.037 \pm 0.043$ (stat) $^{+0.016}_{-0.017}$ (syst) | $-0.056 \pm 0.049$ (stat) $^{+0.014}_{-0.017}$ (syst) |
| 5-6 | $0.036 \pm 0.048$ (stat) $^{+0.013}_{-0.014}$ (syst) | $0.051 \pm 0.054$ (stat) $\pm 0.016$ (syst) |
| 6-7 | $-0.027 \pm 0.057$ (stat) $^{+0.015}_{-0.021}$ (syst) | $0.022 \pm 0.062$ (stat) $^{+0.019}_{-0.018}$ (syst) |
| 7-8 | $0.015 \pm 0.066$ (stat) $\pm 0.022$ (syst) | $0.148^{+0.072}_{-0.073}$ (stat) $^{+0.027}_{-0.030}$ (syst) |
| 8-9 | $-0.057 \pm 0.079$ (stat) $^{+0.020}_{-0.022}$ (syst) | $0.261 \pm 0.086$ (stat) $^{+0.048}_{-0.062}$ (syst) |
| 9-10 | $0.054^{+0.094}_{-0.095}$ (stat) $\pm 0.053$ (syst) | $-0.076 \pm 0.109$ (stat) $^{+0.050}_{-0.057}$ (syst) |

## 7.8.2 Spin correlation $A$ vs $Q$ for minimum bias sample using 1 GeV bin size
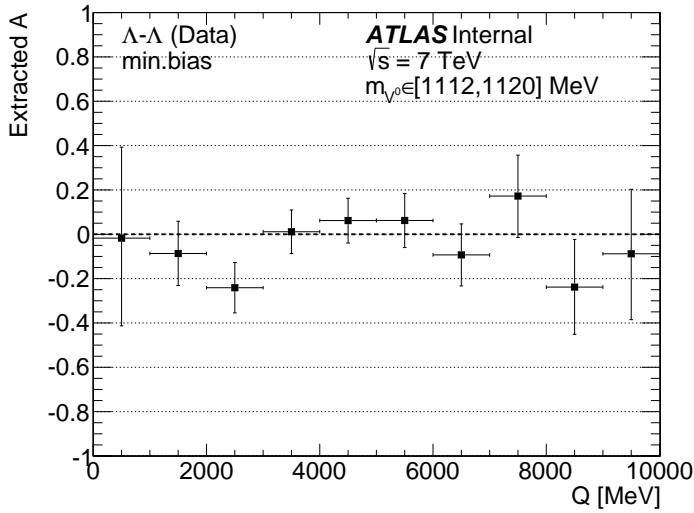
The spin correlation $A$ in the helicity frame as defined in Eqs. (7.1.3) and (7.1.4) has been extracted as a function of $Q$ with 1 GeV bin size for minimum bias sample as shown in Figure 7.8.2.
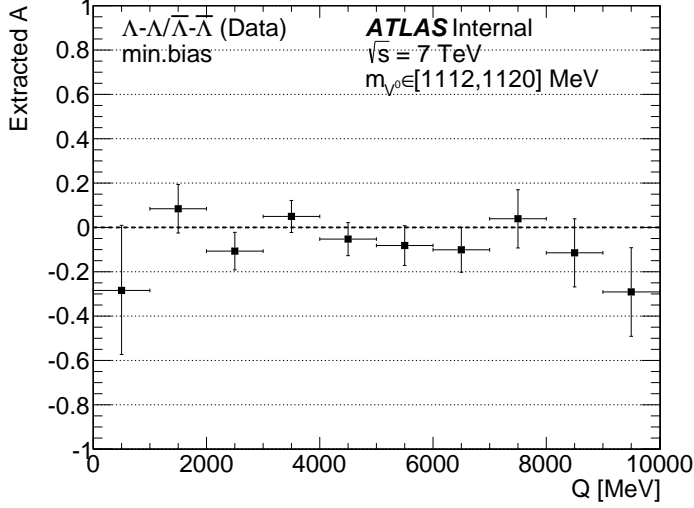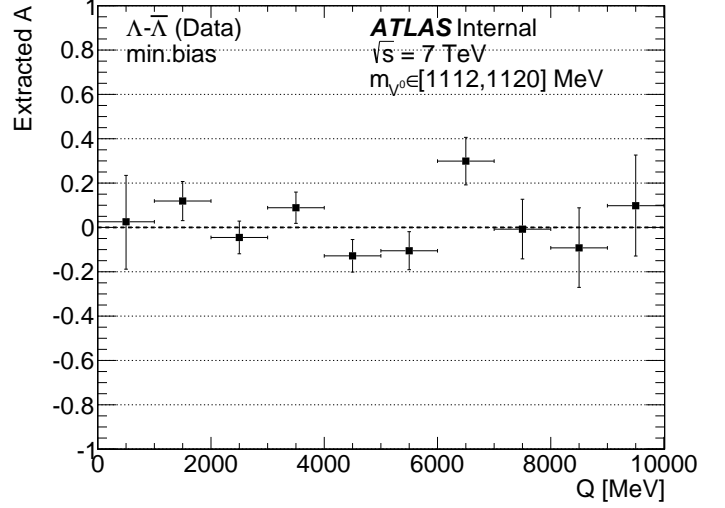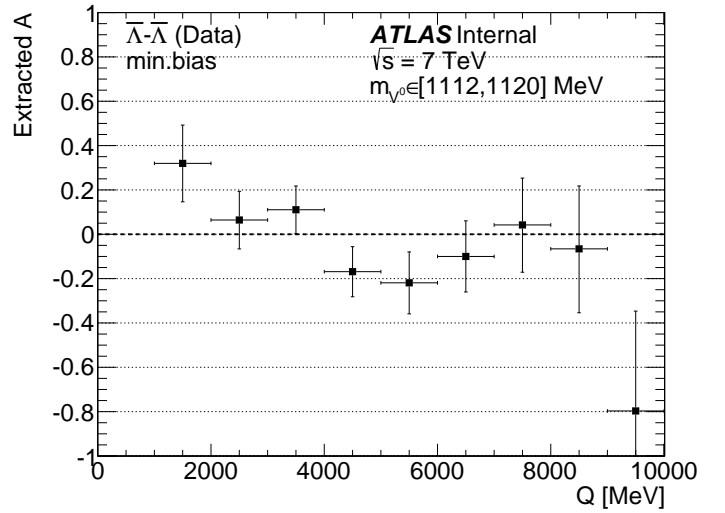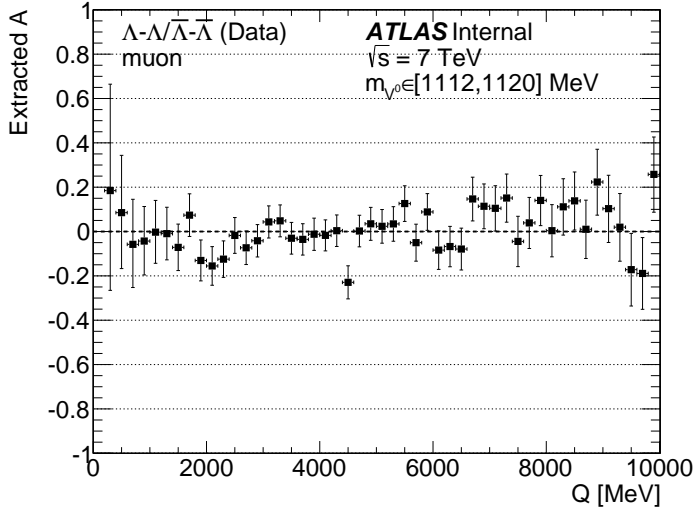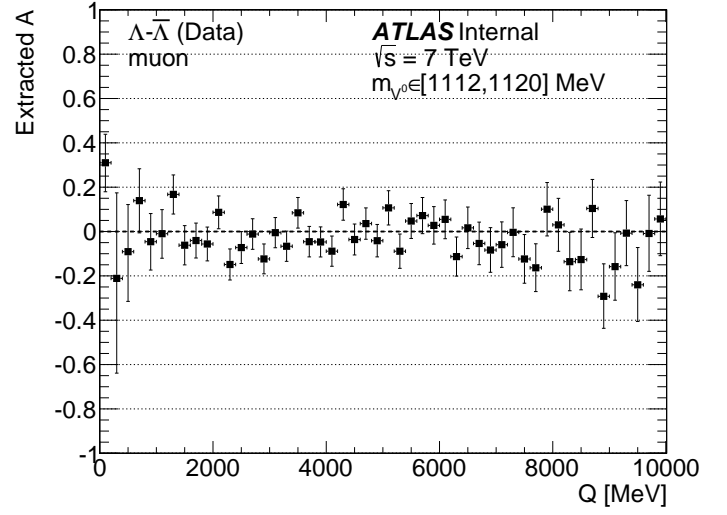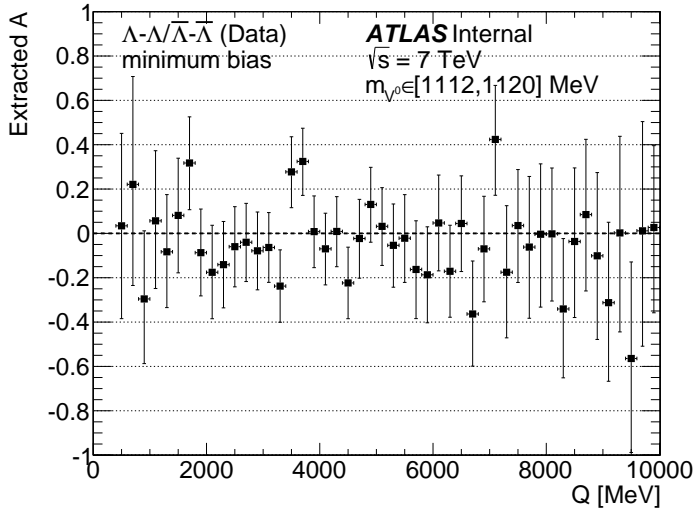
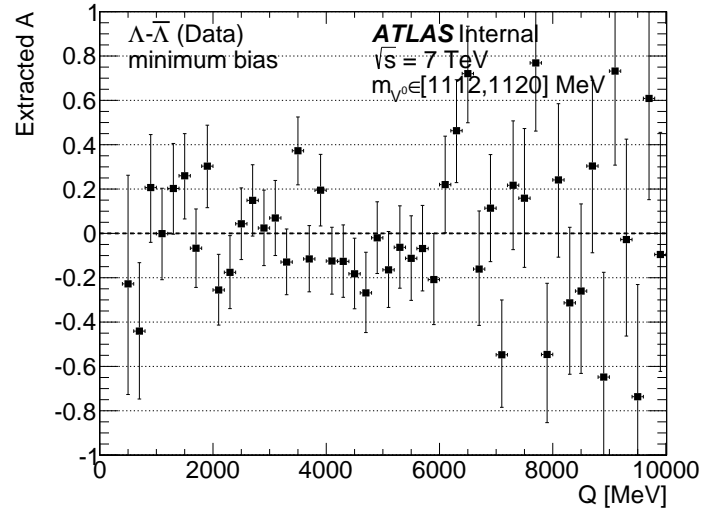Figure 7.8.2: Extracted spin correlation $A$ in the helicity frame as a function of $Q$ for (a) like-type, (b) unlike-type, (c) $\Lambda^0\Lambda^0$, and (d) $\bar{\Lambda}^0\bar{\Lambda}^0$ events for $0 < Q < 10$ GeV using the minimum $\chi^2$ method. The statistical uncertainties indicate variation of $A$ at $\chi^2_{min} + 1$, as described in Figure 7.4.1b. Only statistical uncertainties are shown here. The first bin in Figure (d) is missing due to low statistics.

130

### 7.8.3 Spin correlation $A$ vs $Q$ for muon and minimum bias sample using 200 MeV bin size

The spin correlation $A$ in the helicity frame as defined in Eqs. (7.1.3) and (7.1.4) has been extracted as a function of $Q$ with 200 MeV bin size for muon and minimum bias sample as shown in Figure 7.8.3.
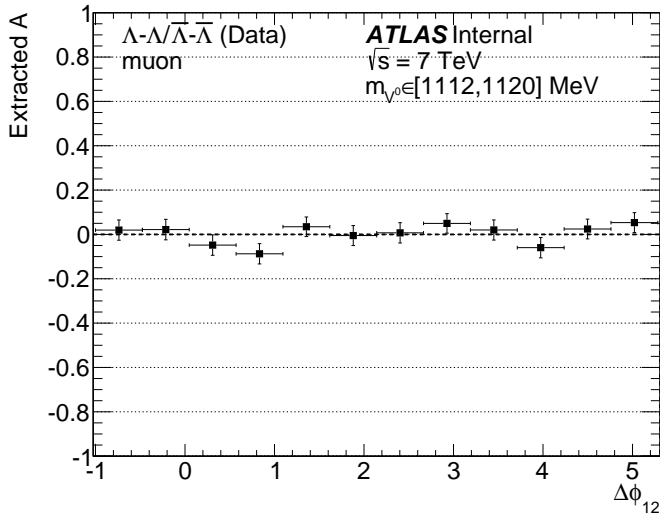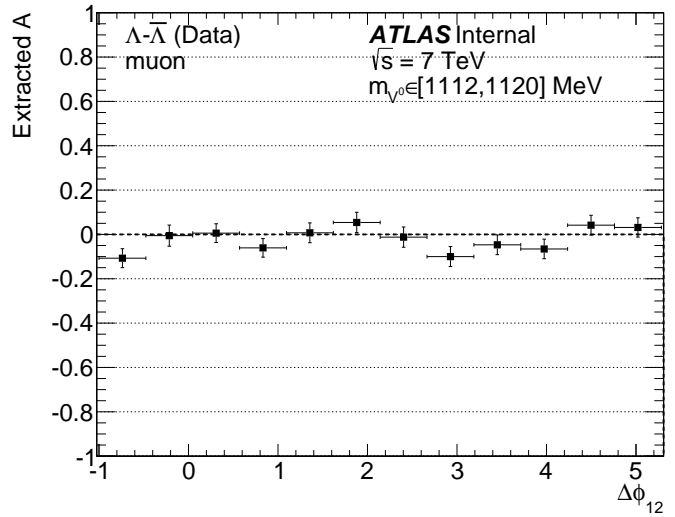
(a)

(b)

(c)

(d)

Figure 7.8.3: Extracted spin correlation $A$ in the helicity frame as a function of $Q$ for (a) like-type for muon sample, (b) unlike-type for muon sample, (c) like-type for minimum bias sample, and (d) unlike-type for minimum bias sample for $0 < Q < 10$ GeV using the minimum $\chi^2$ method with 200 MeV bin size. The statistical uncertainties indicate variation of $A$ at $\chi^2_{min} + 1$, as described in Figure 7.4.1b. Only statistical uncertainties are shown here. The first bin in Figures (a) and the first two bins in Figures (c) & (d) are missing due to low statistics.

## 7.8.4  Spin correlation $A$ vs $\Delta\phi_{12}$ for muon and minimum bias sample
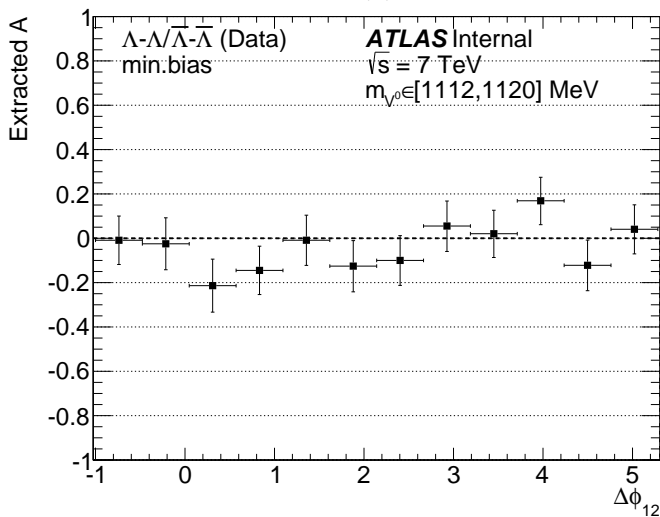
The spin correlation $A$ in the helicity frame as defined in Eqs. (7.1.3) and (7.1.4) has been extracted in terms of the $A$ parameter as a function of $\Delta\phi_{12}$ for muon and minimum bias sample as shown in Figure 7.8.4.
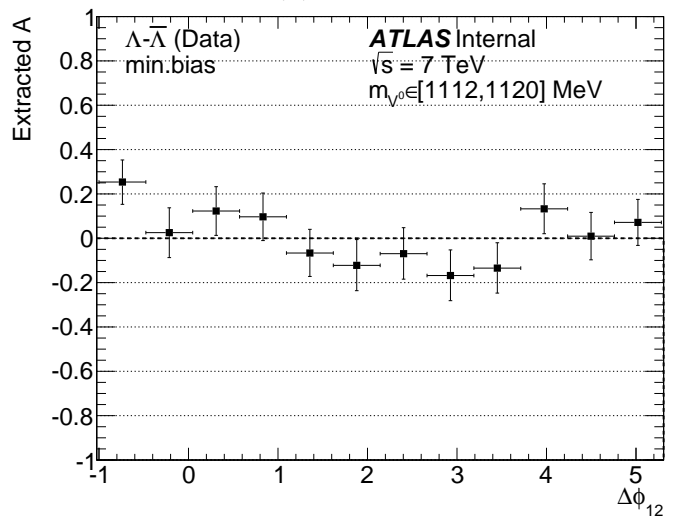
Figure 7.8.4: Extracted spin correlation $A$ in the helicity frame as a function of $Q$ for (a) like-type for muon sample, (b) unlike-type for muon sample, (c) like-type for minimum bias sample, and (d) unlike-type for minimum bias sample for $\Delta\phi_{12} \in [-1, 2\pi - 1)$ using the minimum $\chi^2$ method. The statistical uncertainties indicate variation of $A$ at $\chi^2_{min} + 1$, as described in Figure 7.4.1b. Only statistical uncertainties are shown here.

# Chapter 8

# Discussion

This chapter discusses the interpretations and implications of the results from the dynamcial correlation and spin correlation measurements.

It is demonstrated that the dynamical correlations measured in both the muon and minimum bias sample are qualitatively consistent with the predictions of the string model, with $\Lambda^0\bar{\Lambda}^0$ being positively correlated and $\Lambda^0\Lambda^0+\bar{\Lambda}^0\bar{\Lambda}^0$ being anticorrelated at small $Q$ and $\Delta\phi$ close to zero. The similarity of such dynamical correlations between $\Lambda^0/\bar{\Lambda}^0$ particle and proton/antiproton may suggest that this dynamical correlation is a universal characteristic for baryon/antibaryon production in the string model.

The MC study in Section 6.5 suggested that the excess $\Lambda^0\bar{\Lambda}^0$ events originated from the parton system in the string fragmentation model, and the excess of $\Lambda^0\bar{\Lambda}^0$ events observed in the muon and minimum bias samples can therefore be interpreted as hints for $s\bar{s}$ production from the string model at the LHC energy regime.

The MC study in Section 6.5 also showed that a significant proportion of the excess $\Lambda^0\bar{\Lambda}^0$

135

decayed from feed-down from heavier hyperon resonances such as $\Sigma^{0\dagger}$ and $\Sigma^*(1385)^\ddagger$. The spin correlation originated from the $s\bar{s}$ that arose from the string breaking in the string fragmentation model could be diluted through the feed-down and results in a spin correlation value too small to be significant enough to be measured. This is especially true in the small $Q$ region where correlation is expected to appear and data statistics is limited.

The spin correlation is measured to be consistent with zero for both $\Lambda^0\bar{\Lambda}^0$ and $\Lambda^0\Lambda^0+\bar{\Lambda}^0\bar{\Lambda}^0$ events for $Q \in [1, 10]$ GeV and $Q \in [0, 10]$ GeV respectively in the muon and minimum bias samples. The spin correlation extracted as a function of $\Delta\phi$ is also measured to be consistent with zero, including the region near zero where dynamcial correlation is the strongest.

In the context of the string model, a $s\bar{s}$-pair cannot be produced at exactly the same space-time point and they are produced with some spacial separation [115]. In such a case, the $s\bar{s}$ system would be created with some finite angular momentum $\vec{L}$ in the transverse direction as shown in Figure 8.0.1. In order to cancel this angular momentum, the sum of the spin angular momentum of the $s$ and $\bar{s}$ must be transverse to the direction of motion of the $s$ and $\bar{s}$ in the center-of-mass frame. The magnitude of the spin angular momentum of a $s\bar{s}$-pair must be equal to $|\vec{L}|$ and opposite in direction in order to keep the total angular momentum conserved, that is to be the same as before a $s\bar{s}$-pair was created, at zero. The longitudinal component of the spin correlation would therefore have be close to zero which is consistent with the negative results of our spin correlation measurement.

Last but not least, there is also a possibility that the assumption of the Constituent Quark Model is not valid and the spin contribution of other baryon components such as gluons and sea quarks destroyed the spin information carried by the $s(\bar{s})$ quark during its hadronization

---

$\dagger\Sigma^0 \to \Lambda^0 + \gamma$ BR $= 100\%$ [47]
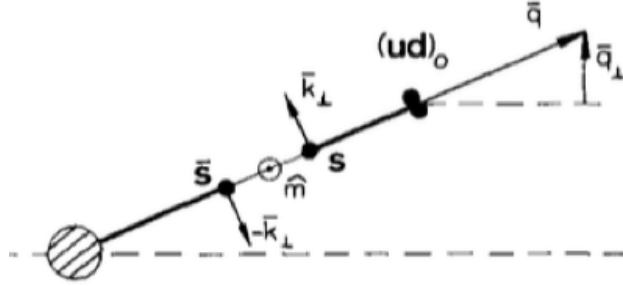$\ddagger\Sigma^{*0/\pm} \to \Lambda^0 + \pi^{0/\pm}$ BR $= (87.0\pm1.5)\%$ [47]

Figure 8.0.1: A spin-zero ud-diquark is scattered with transverse momentum $\vec{q}_\perp$. An $s\bar{s}$-pair is created from the color field with an angular momentum $\vec{L} = \vec{q} \times \vec{k}_\perp$ in the direction of $\hat{m}$ where $|\vec{q}|$ is the distance between the $s$ and $\bar{s}$ quarks. [115]

into the $\Lambda^0(\bar{\Lambda}^0)$ hyperon. This interpretation would disprove the assumption made in Ref. [3] that the $\Lambda^0(\bar{\Lambda}^0)$ hyperon retains the spin information in the $s(\bar{s})$ quark. This should not be too surprising since the same model failed to explain the origin of spin in proton [42–45], which is nothing but a lighter cousin of the $\Lambda^0$ hyperon.

All in all, there are several possible explanations for the spin correlation to be either diluted or destroyed in the fragmentation and hadronization processes and our negative results are consistent with these scenarios.

# Chapter 9

# Conclusion and outlook

## 9.1  Conclusion

The results of the correlation measurements for the unlike-type ($\Lambda^0\bar{\Lambda}^0$), like-type ($\Lambda^0\Lambda^0+\bar{\Lambda}^0\bar{\Lambda}^0$), $\Lambda^0\Lambda^0$, and $\bar{\Lambda}^0\bar{\Lambda}^0$ events using data with a center-of-mass energy of 7 TeV collected in 2010 at the ATLAS detector are presented here.

The spin correlation is extracted using the minimum $\chi^2$ method with data-driven templates created by mixing uncorrelated hyperon pairs from odd and even events. Nine templates are created with injected $A$-values ranging from -1 to 1. The templates are weighted to have the same kinematic distributions as the data sample to ensure identical detector effects in data and templates. The spin correlation is then extracted by interpolating the $\chi^2$-values. The injected $A$-value that minimizes the $\chi^2$-value is determined to be the $A$-value of the data sample and it is measured as a function of $Q$ from 0 to 10 GeV using a bin size of 1 GeV as shown in Figure 7.8.1. The total uncertainty is less than 0.1 and is dominated by the statistical uncertainty everywhere except for $Q$ less than 1 GeV. The extracted correlation is consistent with zero with occasional statistical fluctuations in the large $Q$ region where data

138

statistics is limited. The total uncertainty in the first $Q$ bin is dominated by the systematic uncertainty due to kinematic weighting. The huge uncertainty for $\Lambda^0\bar{\Lambda}^0$ events in the first bin is caused by the strong momentum correlation in data, which is destroyed in the event mixing in order to create the templates.

The dynamical correlation between $\Lambda^0\bar{\Lambda}^0$, $\Lambda^0\Lambda^0$, and $\bar{\Lambda}^0\bar{\Lambda}^0$ events have been extracted using the differential cross section ratio between the data sample and the mixed sample as a function of $Q$, $\Delta\phi$, and $\cos\Delta\phi$. Positive correlation has been observed for $\Lambda^0\bar{\Lambda}^0$ events and anticorrelation for $\Lambda^0\Lambda^0$ and $\bar{\Lambda}^0\bar{\Lambda}^0$ events for $Q \in [0, 2]$ GeV. A similar structure is also observed for proton and antiproton production in PYTHIA generator and is known to be the consequence of string breaking in the Lund string model for baryon and antibaryon production. Parameters controlling the "popcorn" mechanism have been modified. The differential cross section ratio of $\Lambda^0\bar{\Lambda}^0$ to $\Lambda^0\Lambda^0+\bar{\Lambda}^0\bar{\Lambda}^0$ is not very sensitive to the "popcorn" parameters. It is suggested in Ref. [8] that the splitting function which determines the fractional momentum assigned to each meson produced during the string breaking in the string model can affect the dynamical correlations in baryon and antibaryon production. An overestimation of the excess of unlike-type events over the like-type events near the ($\Lambda\Lambda$) threshold by the Monte Carlo sample suggests that certain parameters in the PYTHIA generator may require further tuning, especially those related to strange baryon and meson production.

The FD correlation is expected to cause a suppression of $S = 1$ state in $Q \in [0, 0.5]$ GeV and additional suppression of correlation function on top of the anticorrelation created by the string model for $\Lambda^0\Lambda^0$ and $\bar{\Lambda}^0\bar{\Lambda}^0$ events. The kinematic region is both statistically limited and dynamically challenging to find an appropriate reference sample for correlation measurement. No additional anticorrelation in $Q \in [0, 0.5]$ GeV is significant enough to allow

for a meaningful FD emitter size estimation.

## 9.2 Outlook

This thesis has demonstrated that measurements of correlations between the $\Lambda^0$ and/or $\bar{\Lambda}^0$ hyperon pairs are feasible at the ATLAS detector. In order to probe the $Q \in [0, 0.5]$ GeV regime where the FD effects are expected to be effective, more data statistics will be needed for future analyses to extract the FD correlation between $\Lambda^0\Lambda^0$ and $\bar{\Lambda}^0\bar{\Lambda}^0$ events. However, the track $p_T$ threshold has been raised from 100 MeV in 2010 to 400 MeV in 2011 and may be further increased to 500 MeV in future runs. As a consequence, the reconstruction efficiency of the hyperons and the decay angles at ATLAS will be dampened. (Table 9.1) It is hoped that with more detector upgrades, the track reconstruction efficiency will be improved to partially compensate for the increased track $p_T$ threshold.

Given the significant overestimation of the excess $\Lambda^0\bar{\Lambda}^0$ events, future tuning will be needed to modify the momentum correlation of $\Lambda^0\bar{\Lambda}^0$ production in the string fragmentation model in the event generators. Since $s\bar{s}$ produced in the string model hadronize into a family of strange baryons and mesons, a systematic study of the whole family of strange baryons and mesons will be needed to constrain the parameters in string model as implemented in the MC event generators.

The dynamical correlation in proton-proton correlation has shown some dependence on the $a$ and $b$ parameters in the Lund symmetric fragmentation function as defined in Eq. (1.3.8). (Figure 9.2.1) Further studies may be carried out to check if the $a$ and $b$ parameters in the Lund symmetric fragmentation function also affects the strange baryon and meson production and the correlation between pair-produced strange baryons and mesons.

These parameters are handled by the parameters `StringZ:aLund` and `StringZ:bLund` in the `StringZ` class in the PYTHIA event generator* [34, 35]. The $a$ and $b$ parameters in principle can carry different values for different flavors but the option is only given for strange quarks and diquarks in the PYTHIA event generator. They are controlled by the parameters `StringZ:aExtraSQuark` and `StringZ:aExtraSDiquark`. Therefore, the correlation for strange quarks and diquarks production can be tuned independently relative to the light quarks.
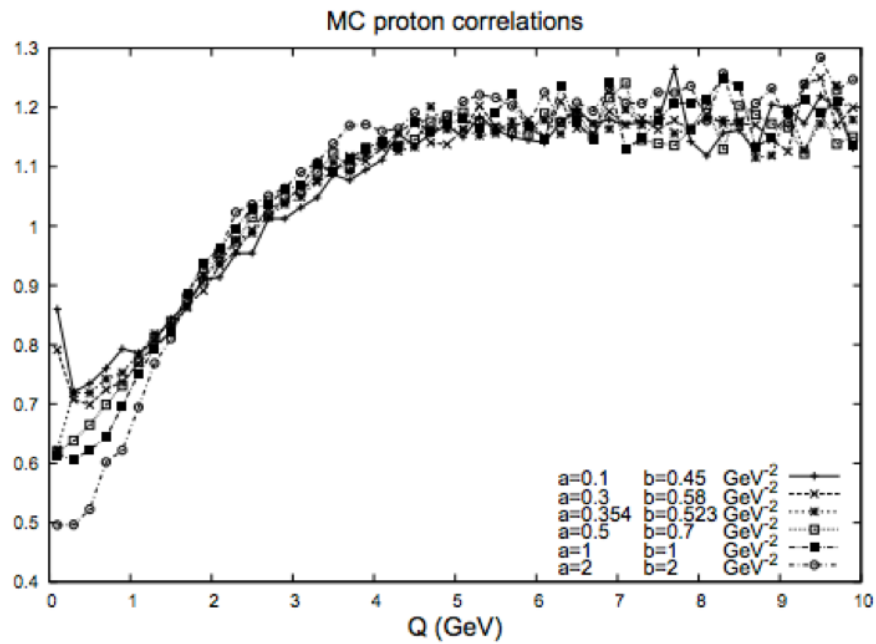


Figure 9.2.1: *pp* correlation for different parameter settings in the Lund symmetric fragmentation function as defined in Eq. (1.3.8). Larger $a$ and $b$ values correspond to stronger correlation and a deeper dip in the small $Q$ region for the correlation function. [8]

Another useful cross-check would be to look at the dynamcial correlation between the hyperon pairs under different fragmentation and hadronization models such as the cluster

---

*http://home.thep.lu.se/ torbjorn/pythia82html/Fragmentation.html

model and the UCLA model. The cluster-hadronization model is implemented in both HERWIG [36] and SHERPA [37] event generators. We can then see if the structures observed in the correlation function and the differential cross section ratio are truly unique to the string model.

The data-driven method used to extract the spin composition is limited by the fact that the dynamical correlations between the hyperon pairs are destroyed in the event mixing, which results in a very large systematic uncertainty in $Q \in [0, 1]$ GeV in the spin correlation for $\Lambda^0 \bar{\Lambda}^0$ events. The $p\Lambda^0$ and $\bar{p}\bar{\Lambda}^0$ correlations may be used to model the dynamical correlation free of FD effects for the reference sample used in the correlation measurement, e.g. measurements at STAR. (Figure 2.2.5) Such correlation measurements should in principle have more data statistics as the production cross section should be proportional to single proton/antiproton/$\Lambda^0$/$\bar{\Lambda}^0$ production cross section instead of pair production. (Figure 9.2.2)
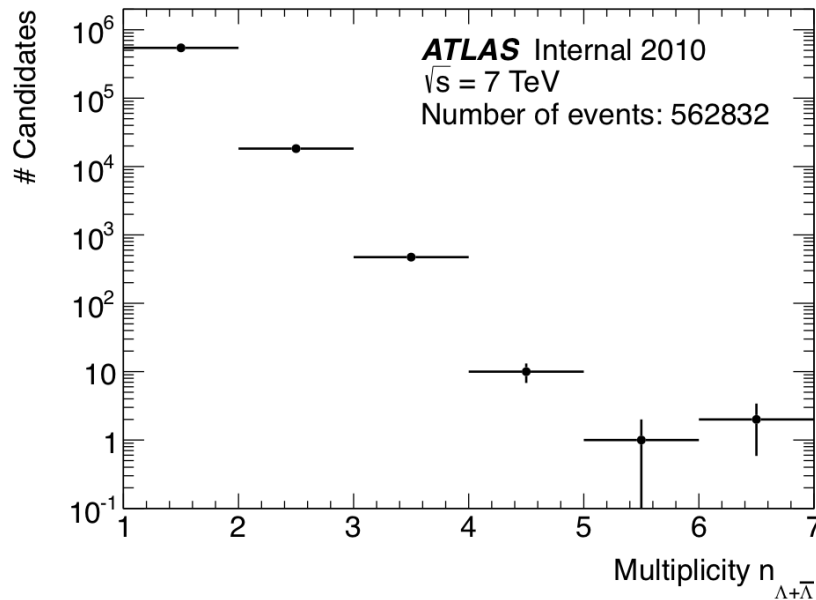


Figure 9.2.2: Multiplicity of $V^0$ ($\Lambda^0$ or $\bar{\Lambda}^0$) candidates reconstructed in events selected from the muon sample.

It has to be pointed out that the dynamical correlation is calculated as the differential cross section ratio at reconstructed level. It is under the assumption that the reconstruction efficiency and acceptance of $\Lambda^0$ and $\bar{\Lambda}^0$ are roughly the same to first order approximation (Figure 9.2.3) and the reconstruction efficiency and acceptance of the data sample and the mixed data sample in each $Q$ bin are similar. The reconstruction efficiency and acceptance can be corrected either by a bin-by-bin correction factor method or by unfolding with a response matrix created using the true level information in the MC sample. This work can be done in the subsequence analyses as cross check for the dynamical correlation measurement and the two methods may be used independently as cross checks. Since the reconstruction efficiency and acceptance depends strongly on the track $p_T$ threshold, a large difference in the kinematic distributions will result in a large diffence in the reconstruction efficiency and acceptance. We expect this correction to affect the region where the kinematic distributions of the data sample and the mixed data sample are very different the most, namely $\Lambda^0\bar{\Lambda}^0$ events in the range $0 < Q < 1$ GeV. In addtion, the small discrepancy between the results of the muon and minimum bias samples might be caused by the efficiency and acceptance difference and the discrepancy may disappear after corrections are made.

It is also highly motivated to measure the transverse spin correlation as depicted in the string breaking picture in Figure 8.0.1. The only complication is that for hyperon pairs of interest with very small $Q$ value, the pair would be almost collinear in the lab frame. As the transverse direction is defined as the cross product of the directional vectors of the hyperons, it may be difficult to reconstruct due to the finite resolution of the reconstructed directional vector of the refitted track of each hyperon. MC studies using the true level information would be needed to verify that the transverse directional vector is well reconstructed and the measurement is made in the actual transverse direction.

In addition, it is suggested that the analysis can be repeated with trigger selection using the dominant triggers as shown in Figures 9.0.4 and 9.0.5 in order to improve the reproducibility of the results. All the cross-checks and updates to be carried out in the future should be documented in the ATLAS internal note[†] unless otherwise specified.

---

[†]`https://cds.cern.ch/record/2239393/`
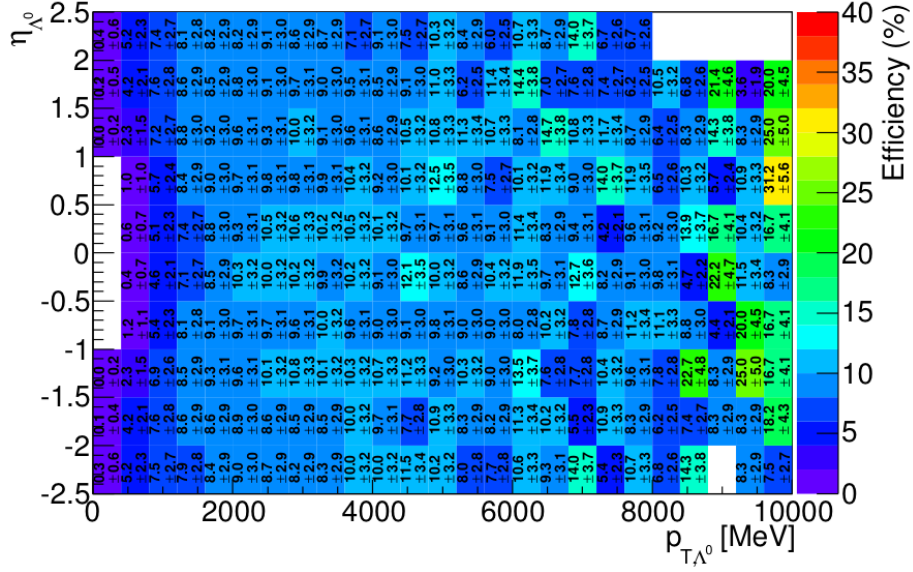
(a)
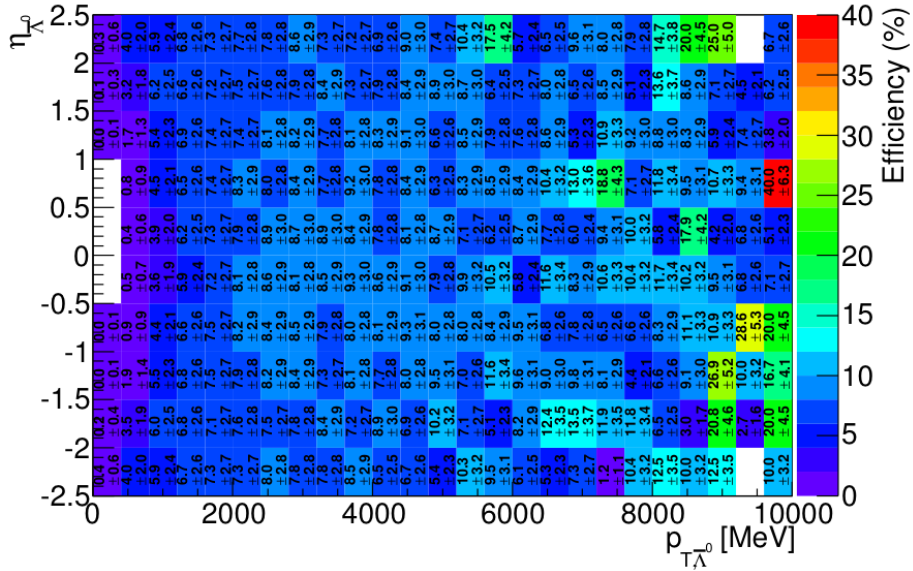


(b)

Figure 9.2.3: Efficiency maps of (a) $\Lambda^0$ and (b) $\bar{\Lambda}^0$ as functions of pseudorapidity $\eta$ and transverse momentum $p_T$ of the hyperon. $\Lambda^0$ has slightly higher reconstruction efficiency than $\bar{\Lambda}^0$ due to the difference in the interaction cross section between proton and antiproton with the detector material as pointed out in Ref. [111]. More statistics is needed to create a more reliable efficiency map for data correction purpose.

145

# Appendices

# Appendix A
# Trigger mappings

This appendix describes the trigger distributions for the muon and the minimum bias stream samples after trigger selection is disabled in the event selection process.



Figure 9.0.4: Trigger mapping for the muon data stream created using the $\Lambda^0\bar{\Lambda}^0$ selection. The dominant triggers include `EF_mu6`, `EF_mu10` and `EF_mu4_j20_matched`. The trigger mappings using the $\Lambda^0\Lambda^0$ and $\bar{\Lambda}^0\bar{\Lambda}^0$ selections are found to be similar to that using the $\Lambda^0\bar{\Lambda}^0$ selection and are not shown here.

Figure 9.0.5: Trigger mappings for the minimum bias data stream created using the $\Lambda^0\bar{\Lambda}^0$ selection. The dominant triggers include EF_L1ItemStreamer_L1_MBTS_1, EF_mbMbts_1, EF_mbMbts_1_NoCut_Time, EF_mbSpTrkMh_MB2 and EF_mb_M1_eff. The trigger mappings using the $\Lambda^0\Lambda^0$ and $\bar{\Lambda}^0\bar{\Lambda}^0$ selections are found to be similar to that using the $\Lambda^0\bar{\Lambda}^0$ selection and are not shown here.

# Appendix B
# Effects of track $p_T$ threshold

The effects of the track transverse momentum $p_T$ threshold are studied in this appendix.

The kinematics of the daughter proton and pion in the center-of-mass frame of the $\Lambda^0$ hyperon pair is fully determined by their respective rest masses and their decay angles $\theta_1$, $\phi_1$, $\theta_2$, and $\phi_2$ as shown in Figure 9.4.19. As a consequence, the kinematics of the daughters in the lab frame is fully determined by the 4-vector of the hyperon pair in the lab frame.

Considering a 1-to-2 particle decay, the 4-momenta of the particles are related by $P = p_1 + p_2$ where $P = (M, \vec{0})$. By writing $p_2 = P - p_1$, we obtain

$$p_2^2 = (P - p_1)^2 = P^2 - 2P \cdot p_1 + p_1^2 \tag{9.1.1}$$

$$m_2^2 = M^2 - 2ME_1 + m_1^2 \Rightarrow E_1 = \frac{M^2 + m_1^2 - m_2^2}{2M} \tag{9.1.2}$$

$$E_2 = M - E_1 \Rightarrow E_2 = \frac{M^2 + m_2^2 - m_1^2}{2M} \tag{9.1.3}$$

From $p_1 = \sqrt{E_1^2 - m_1^2}$ and $p_2 = \sqrt{E_2^2 - m_2^2}$, where $p_1 = |\vec{p_1}|$ and $p_2 = |\vec{p_2}|$, we have

$$p_1 = \frac{\sqrt{(M^2 + m_1^2 - m_2^2) - 4M^2 m_1^2}}{2M} \tag{9.1.4}$$

and

$$p_2 = \frac{\sqrt{(M^2 + m_2^2 - m_1^2) - 4M^2 m_2^2}}{2M} \qquad (9.1.5)$$

Typical values of the hyperon transverse momentum $p_T$ in the lab frame obtained from our data are then substituted into Eqs. (9.1.4) and (9.1.5) for the two extreme cases where the proton is either aligned or antialigned with the parent hyperon in the center-of-mass frame. For $p_\Lambda = 0.4$ GeV in the lab frame and $\theta_p \sim 0$, we have $\cos\theta_p \sim 1$, $\sin\theta_p \sim 0$

$$p_p \sim \sqrt{1.128} \times 0.418 = 0.614 \text{ GeV} \qquad (9.1.6)$$

and

$$p_\pi \sim \sqrt{1.128} \times 0.042 = 0.045 \text{ GeV} \qquad (9.1.7)$$

For $\theta_p \sim \pi$, we have $\cos\theta_p \sim -1$, $\sin\theta_p \sim 0$

$$p_p \sim \sqrt{1.128} \times 0.218 = 0.232 \text{ GeV} \qquad (9.1.8)$$

and

$$p_\pi \sim \sqrt{1.128} \times 0.158 = 0.167 \text{ GeV} \qquad (9.1.9)$$

For $p_\Lambda = 1.2$ GeV in the lab frame and $\theta_p \sim 0$, we have $\cos\theta_p \sim 1$, $\sin\theta_p \sim 0$

$$p_p \sim \sqrt{2.158} \times 0.79 = 1.16 \text{ GeV} \qquad (9.1.10)$$

and

$$p_\pi \sim \sqrt{2.158} \times 0.026 = 0.038 \text{ GeV} \tag{9.1.11}$$

For $\theta_p \sim \pi$, we have $\cos\theta_p \sim -1$, $\sin\theta_p \sim 0$

$$p_p \sim \sqrt{2.158} \times 0.58 = 0.87 \text{ GeV} \tag{9.1.12}$$

and

$$p_\pi \sim \sqrt{2.158} \times 0.226 = 0.33 \text{ GeV} \tag{9.1.13}$$
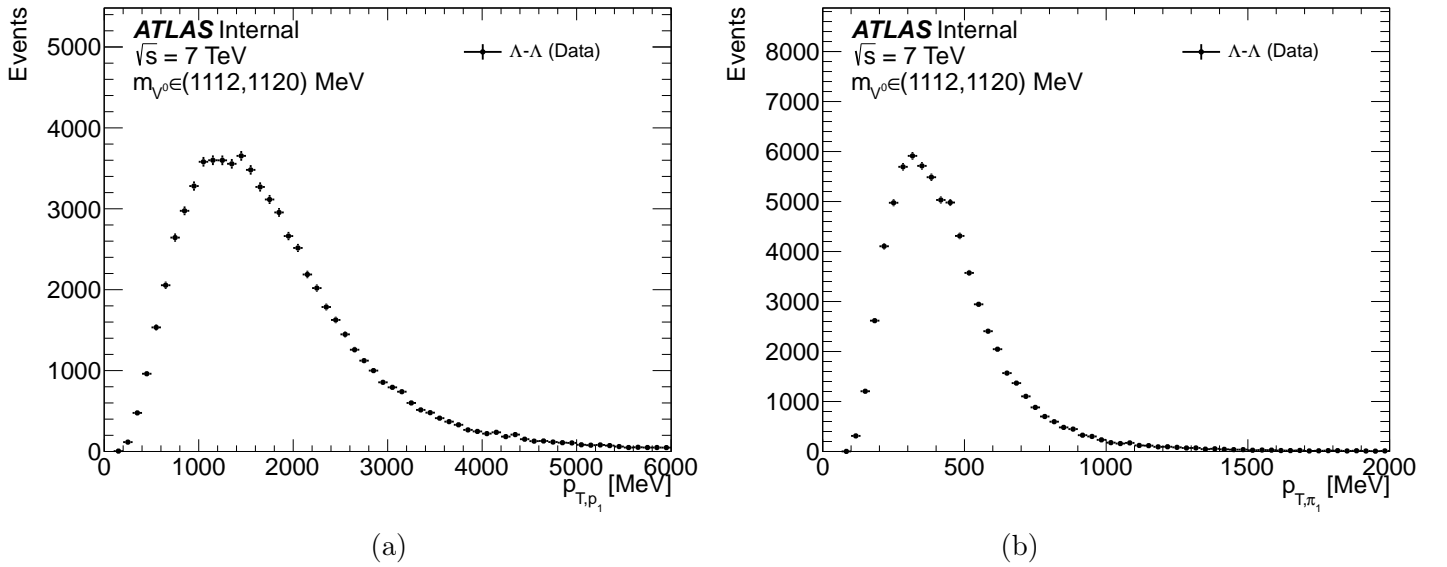


Figure 9.1.6: Reconstructed transverse momentum $p_T$ distributions for (a) proton and (b) pion in the lab frame.

In all cases, it is shown that the pion tends to carry much less momentum than the proton in the lab frame. In the case where the proton aligns with the parent hyperon, the pion

has momentum much lower than the track $p_T$ threshold which is at about 100 MeV. (Figure 9.1.8) In Figure 9.1.6, the reconstructed transverse momenta of the proton and pion peak at about 1.1 GeV and 0.3 GeV respectively, which agree quite well with our rough estimations. Figures 9.2.11 and 9.2.12 show depletion of events in the positive quadrant of the decay angle distributions for $\cos\theta_1$ and $\cos\theta_2$, which correspond to the case in which the proton aligns with the parent hyperon and the pion has a very low transverse momentum. The $\cos\theta^*$ distributions in Figures 9.2.9 and 9.2.10 are affected less by the track $p_T$ threshold as the angle between the two decay protons is used and is typically averaged over the full range of $\theta_1$ and $\theta_2$.
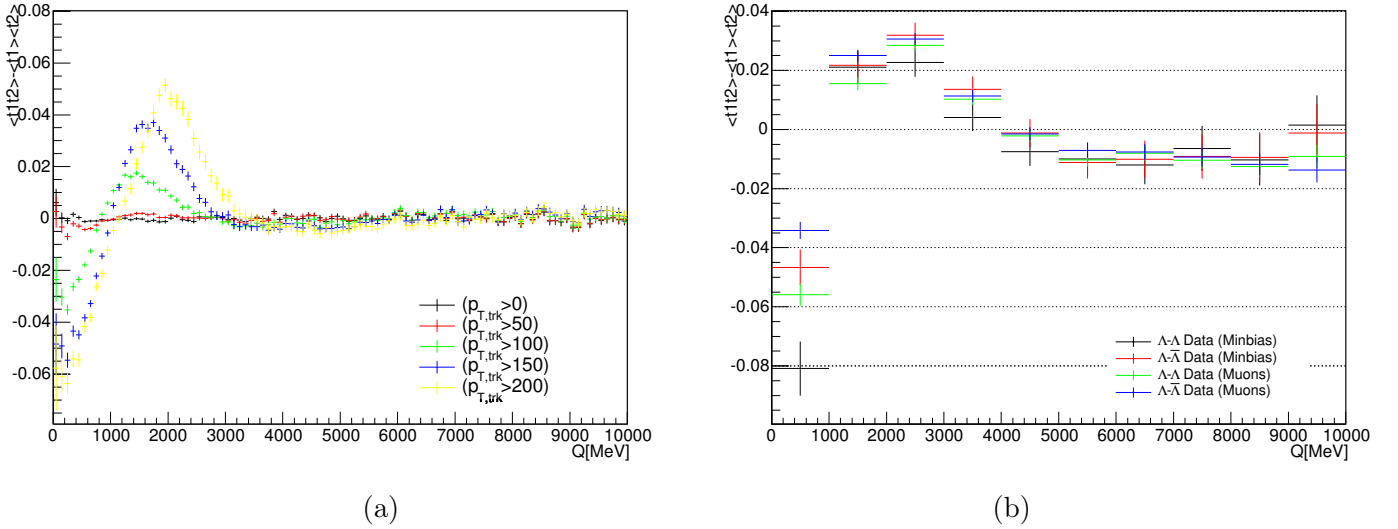


Figure 9.1.7: (a) Correlation parameter vs $Q$ for transverse momentum $p_T$ thresholds at 0, 50, 100, 150, and 200 MeV for the toy MC sample. (b) Correlation parameter vs $Q$ for minimum bias and muon data samples.

A toy MC sample at generator level is used to study the effect of different track $p_T$ thresholds. A simplified correlation parameter $C(\cos\theta_1, \cos\theta_2) = \langle \cos\theta_1 \cos\theta_2 \rangle - \langle \cos\theta_1 \rangle \langle \cos\theta_2 \rangle$ is plotted for track $p_T$ thresholds at 0, 50, 100, 150, and 200 MeV in Figure 9.1.7 (a). The

results for minimum bias and muon data samples are shown in Figure 9.1.7 (b). The shape of the data sample correlation parameter curve is the result of a gradual turn-on of the track reconstruction efficiency as a function of track $p_T$ as shown in Figure 9.1.8. As a consequence, naively calculating the correlation parameter measures the correlation due to the track $p_T$ threshold. A more sophisticated analysis scheme is needed to isolate the decay angle correlation due to actual spin correlation from that due to the detector effects.



(a)                                                   (b)
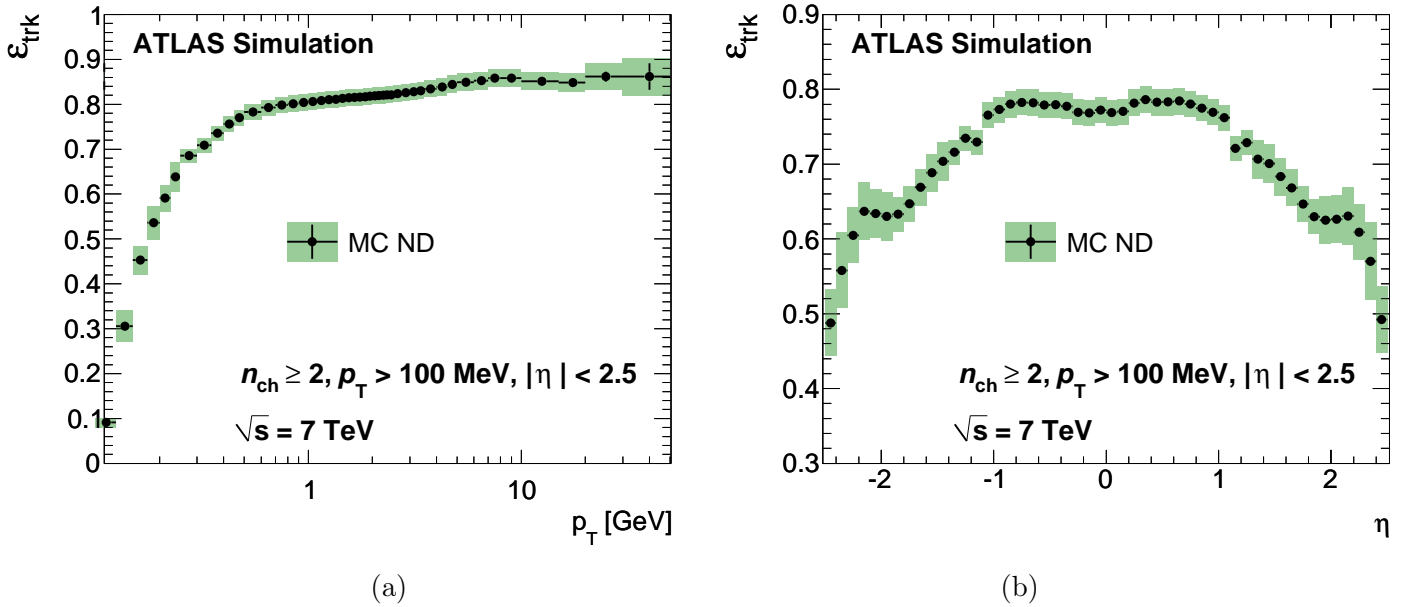
Figure 9.1.8: Track reconstruction efficiency $\epsilon_{\mathrm{trk}}$ as a function of (a) transverse momentum $p_T$ and (b) pseudorapidity $\eta$. [116]

The track $p_T$ threshold has been increased from 100 MeV in 2010 to 400 MeV in 2011. It may be further increased to 500 MeV in future runs. The estimated reduction of event yields has been calculated by applying $p_T$ cuts at 400 MeV and 500 MeV to the 2010 muon and minimum data samples. About 17-23% and 5-9% of the events remain respectively when the track $p_T$ threshold is set to 400 MeV and 500 MeV. The selection results are shown in Table 9.1.

153

Table 9.1: Selection results for $\Lambda^0\bar{\Lambda}^0$, $\Lambda^0\Lambda^0$, and $\bar{\Lambda}^0\bar{\Lambda}^0$ pairs for track $p_T$ threshold in 2010 default settings, 400 MeV, and 500 MeV for minimum bias and muon data samples. The percentages in the bracket indicate the proportion of events left after applying the new track $p_T$ thresholds at 400 MeV and 500 MeV relative to the selection yields using the 2010 default settings.

| Data stream | Track $p_T$ threshold | Type of hyperon pairs | | |
|---|---|---|---|---|
| | | $\Lambda^0\bar{\Lambda}^0$ | $\Lambda^0\Lambda^0$ | $\bar{\Lambda}^0\bar{\Lambda}^0$ |
| Minimum bias | Default in 2010 | 53,561 (100%) | 25,551 (100%) | 20,127 (100%) |
| | 400 MeV | 10,020 (18.7%) | 4,385 (17.2%) | 3,760 (18.7%) |
| | 500 MeV | 3,212 (6.0%) | 1,332 (5.2%) | 1,150 (5.7%) |
| Muon | Default in 2010 | 295,202 (100%) | 140,232 (100%) | 113,596 (100%) |
| | 400 MeV | 69,575 (23.6%) | 29,734 (21.2%) | 25,309 (22.3%) |
| | 500 MeV | 27,262 (9.2%) | 11,109 (7.9%) | 9,583 (8.4%) |

# Appendix C
# Decay angle distributions
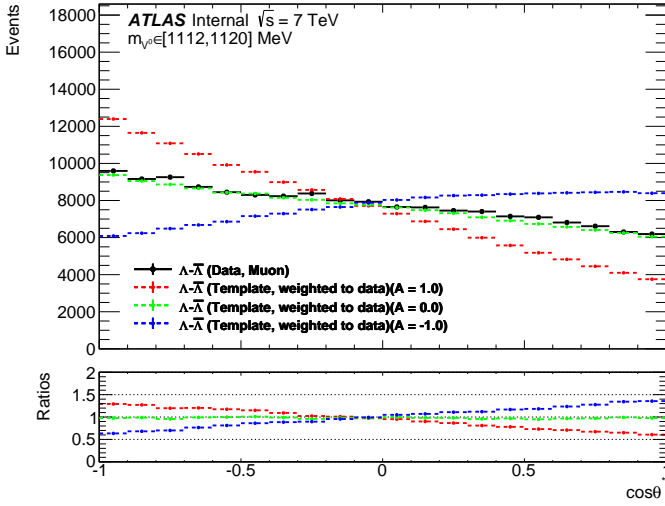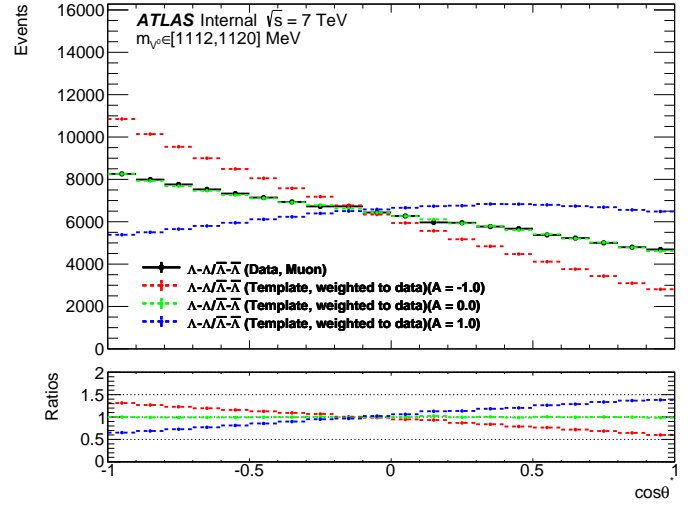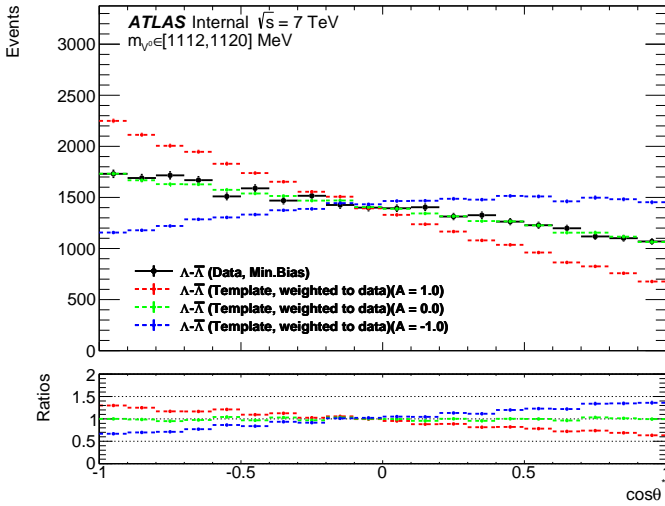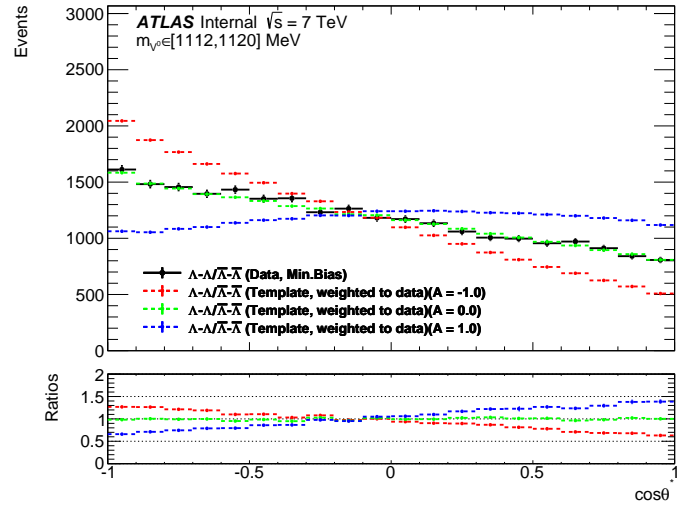
Figure 9.2.9: Distribution of $\cos\theta^*$ for data overlaid with three templates weighted to $A = -1$, 0, and 1 for $\Lambda^0\bar{\Lambda}^0$ (left) and $\Lambda^0\Lambda^0 + \bar{\Lambda}^0\bar{\Lambda}^0$ (right) in muon (top) and minimum bias (bottom) data samples. Template-to-data ratio is shown in the ratio plot in the bottom.
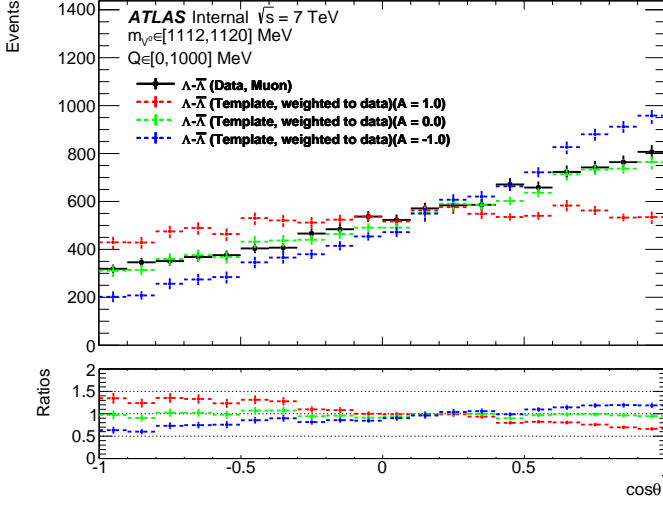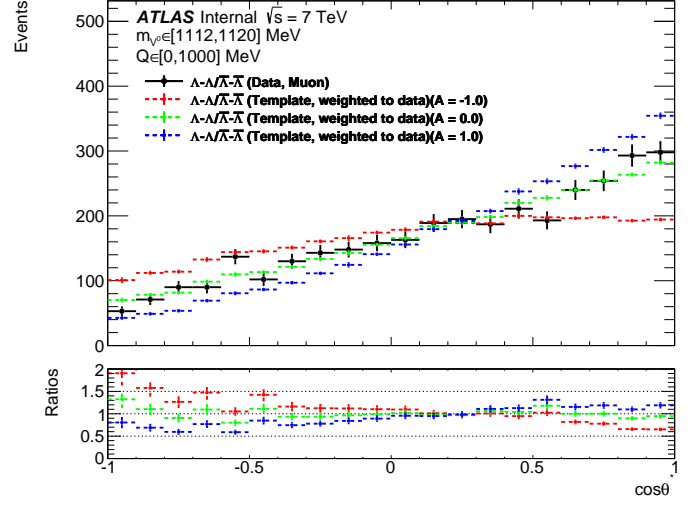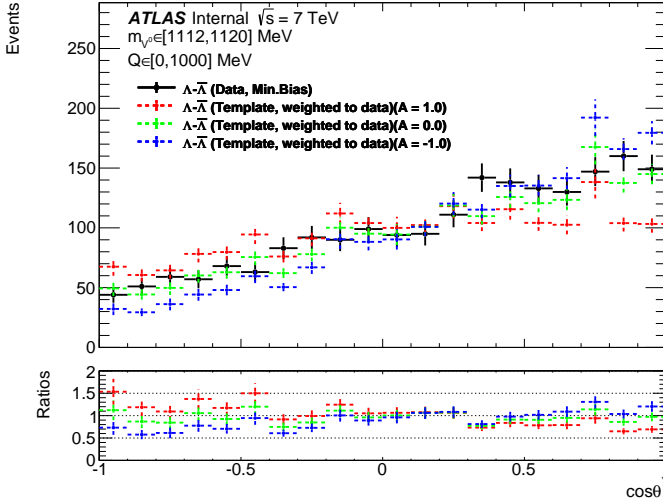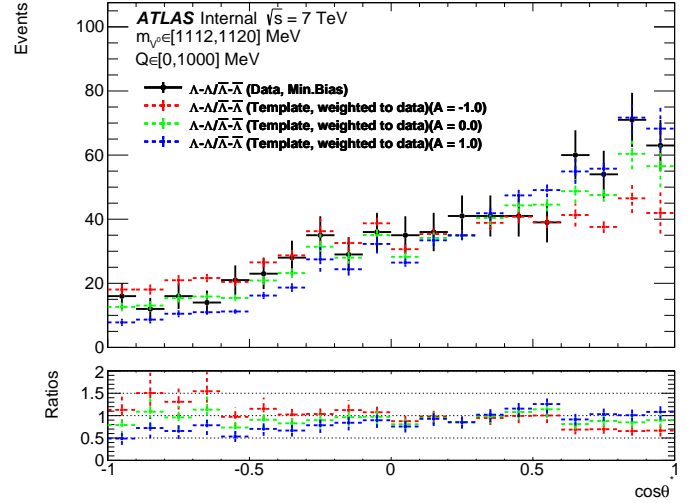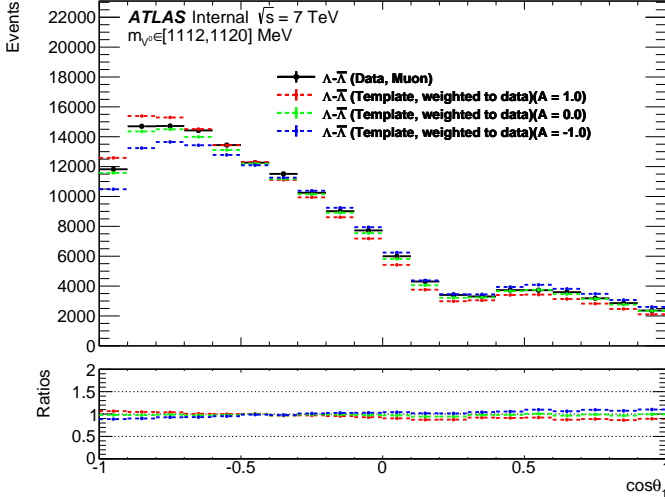
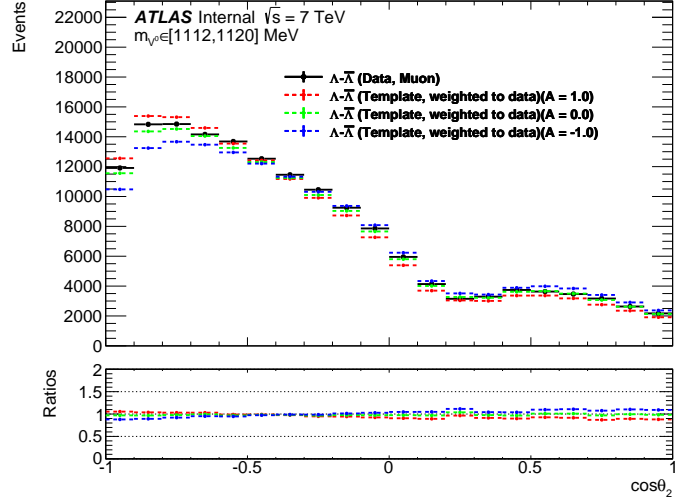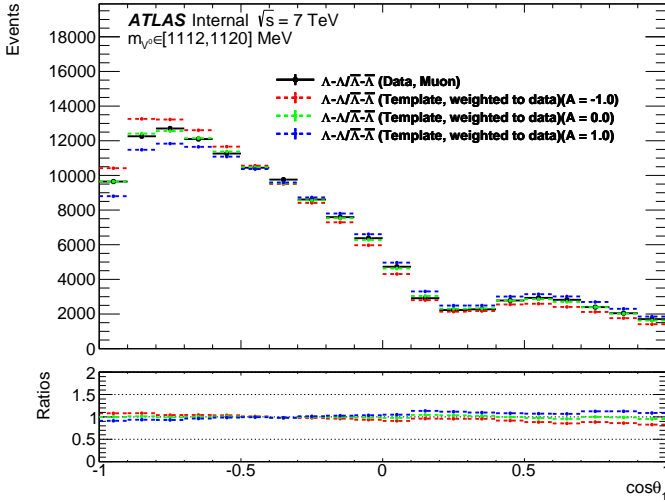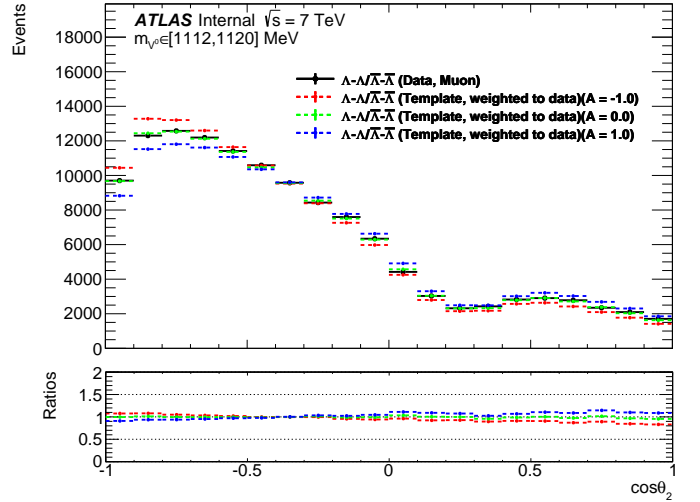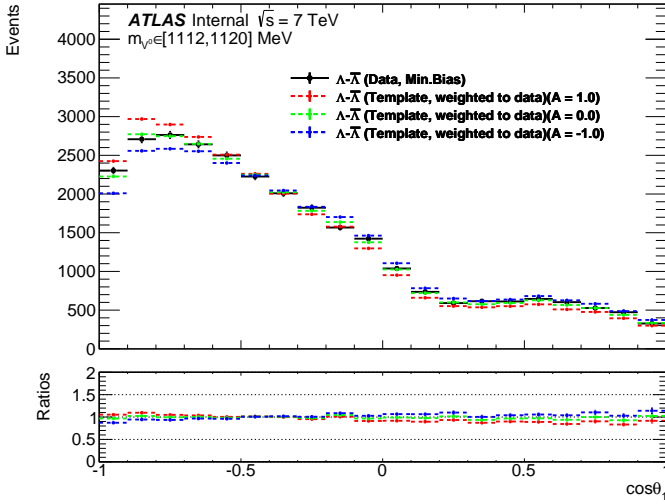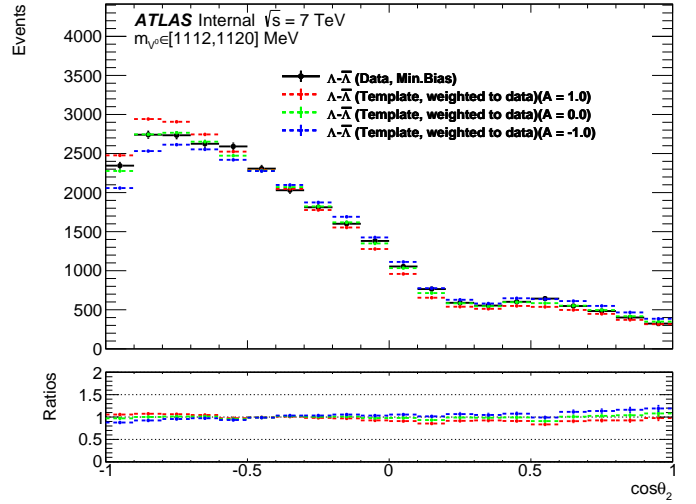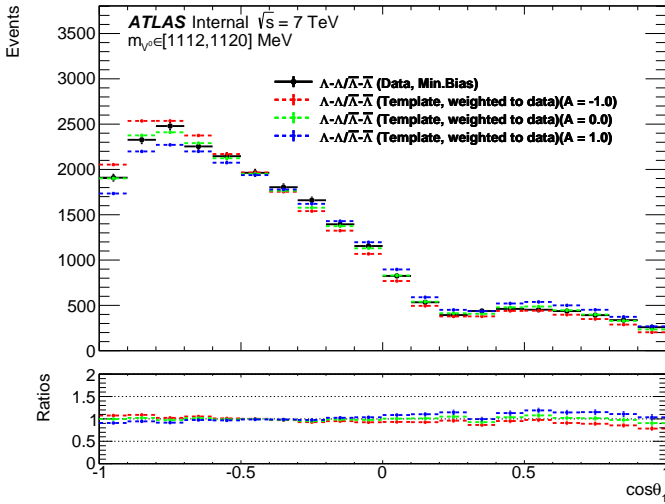Figure 9.2.10: Distribution of $\cos\theta^*$ for $Q \in [0, 1000]$ MeV for data overlaid with three templates weighted to $A = -1$, 0, and 1 for $\Lambda^0\bar{\Lambda}^0$ (left) and $\Lambda^0\Lambda^0 + \bar{\Lambda}^0\bar{\Lambda}^0$ (right) in muon (top) and minimum bias (bottom) data samples. Template-to-data ratio is shown in the ratio plot in the bottom.

Figure 9.2.11: Distributions of $\cos\theta_1$ (left) and $\cos\theta_2$ (right) for muon data sample overlaid with three templates weighted to $A = -1$, 0, and 1 for $\Lambda^0\bar{\Lambda}^0$ (top) and $\Lambda^0\Lambda^0 + \bar{\Lambda}^0\bar{\Lambda}^0$ (bottom) events. Template-to-data ratio is shown in the ratio plot in the bottom.
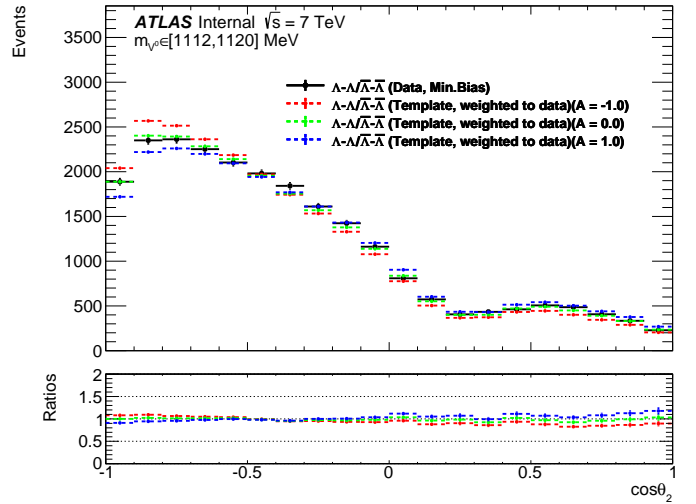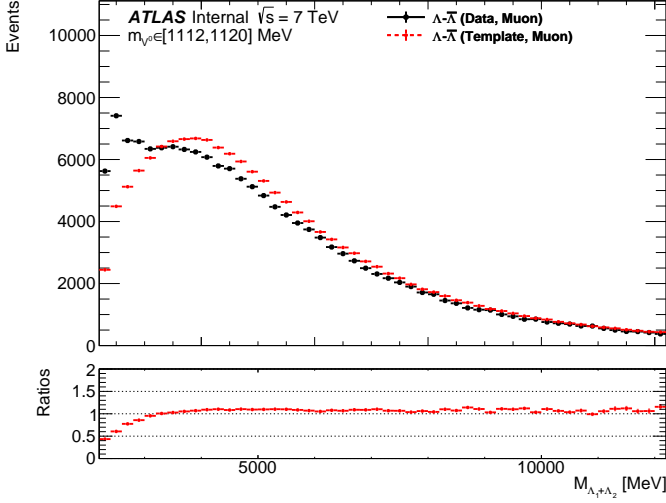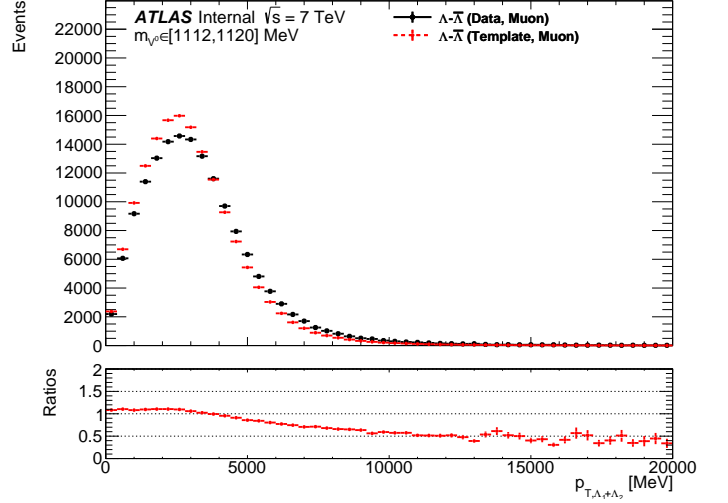
(a)

(b)

(c)

(d)

Figure 9.2.12: Distributions of $\cos\theta_1$ (left) and $\cos\theta_2$ (right) for minimum bias data sample overlaid with three templates weighted to $A$ = -1, 0, and 1 for $\Lambda^0\bar{\Lambda}^0$ (top) and $\Lambda^0\Lambda^0 + \bar{\Lambda}^0\bar{\Lambda}^0$ (bottom) events. Template-to-data ratio is shown in the ratio plot in the bottom.
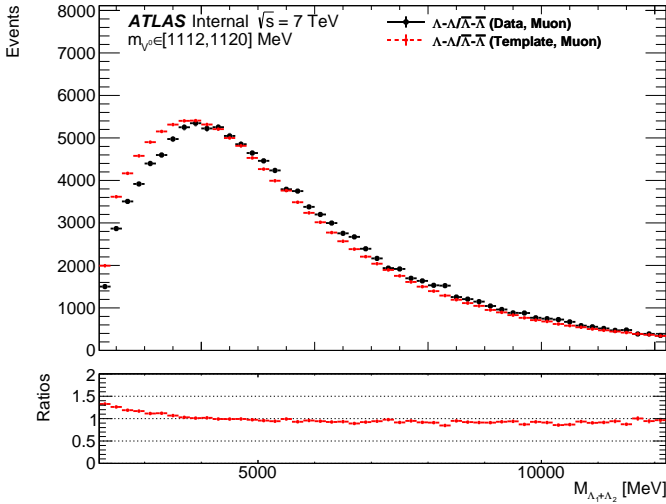
# Appendix D
# Kinematic distributions before and after weighting
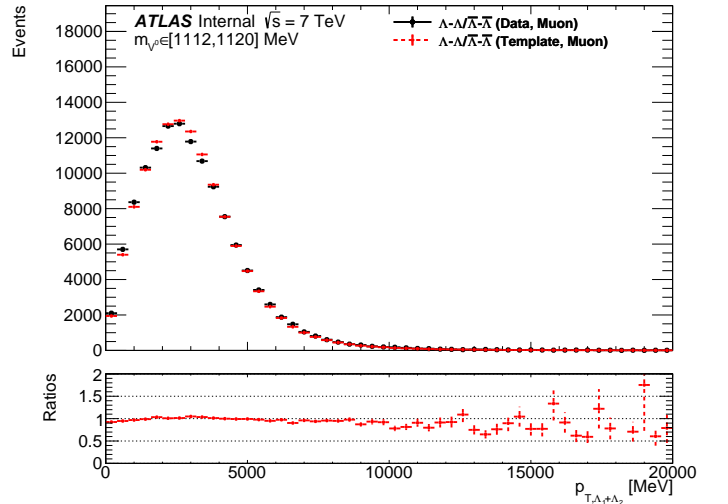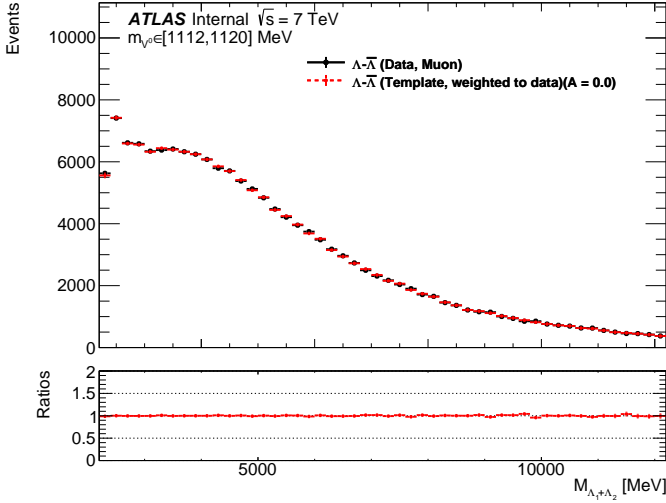
(a)　　　　　　　　　　　　　　　(b)

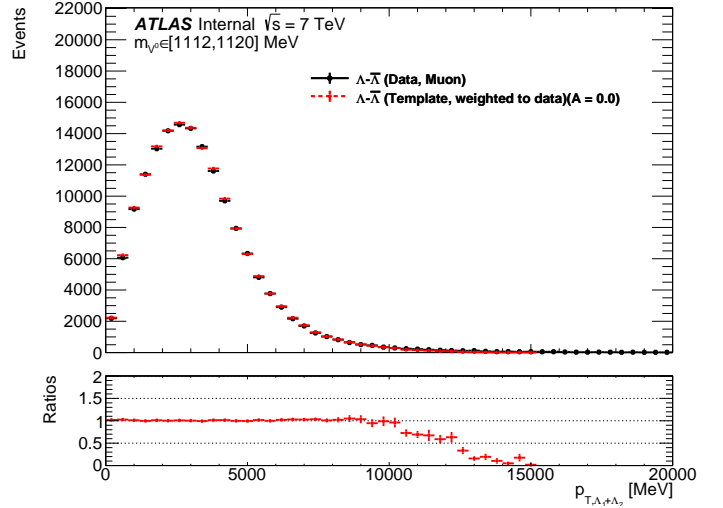(c)　　　　　　　　　　　　　　　(d)

Figure 9.3.13: Distributions of the invariant mass $m_{\Lambda\Lambda}$ (left) and transverse momentum $p_{T,\Lambda\Lambda}$ (right) for muon data sample overlaid with templates before kinematic weighting for $\Lambda^0\bar{\Lambda}^0$ (top) and $\Lambda^0\Lambda^0+\bar{\Lambda}^0\bar{\Lambda}^0$ (bottom) events. Template-to-data ratio is shown in the ratio plot in the bottom.
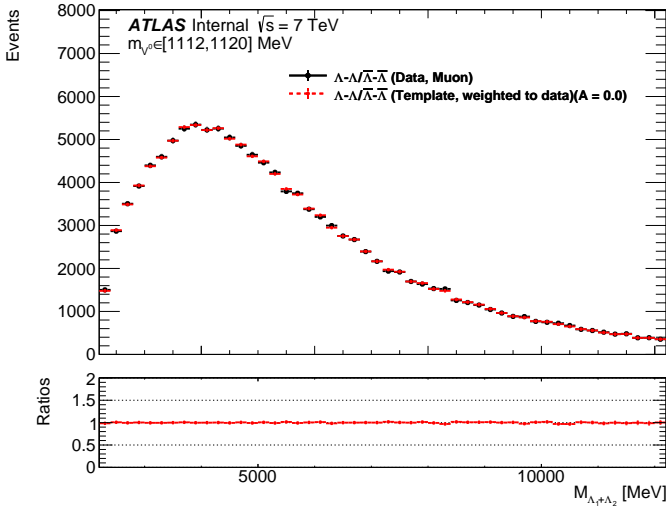
Figure 9.3.14: Distributions of the invariant mass $m_{\Lambda\Lambda}$ (left) and transverse momentum $p_{T,\Lambda\Lambda}$ (right) for muon data sample overlaid with templates after kinematic weighting for $\Lambda^0\bar{\Lambda}^0$ (top) and $\Lambda^0\Lambda^0+\bar{\Lambda}^0\bar{\Lambda}^0$ (bottom) events. Template-to-data ratio is shown in the ratio plot in the bottom.
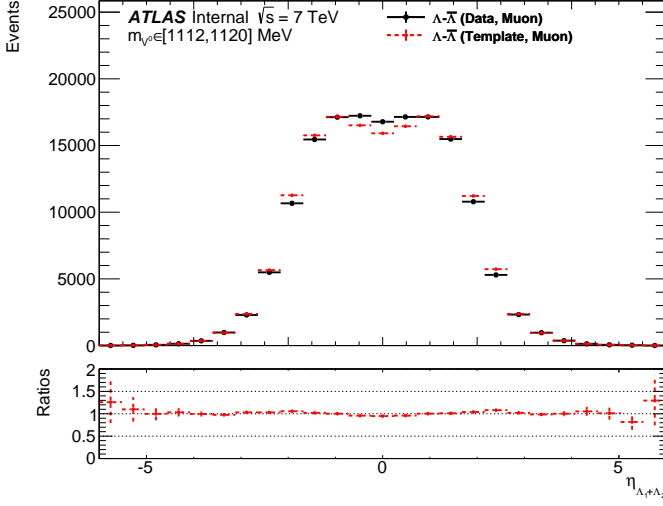
(a)
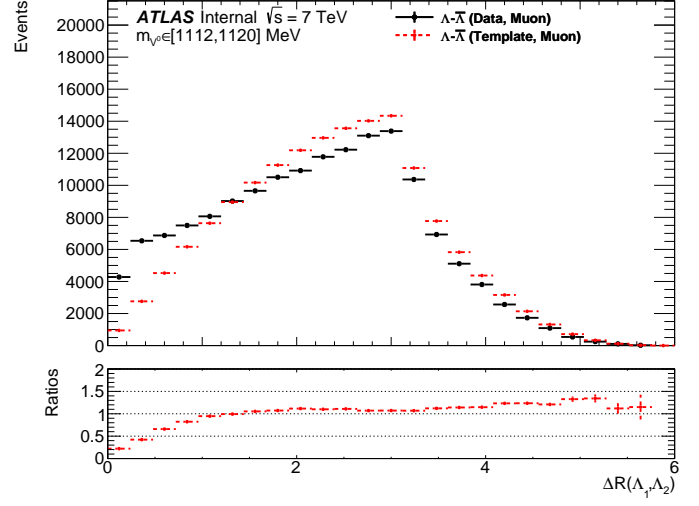
(b)
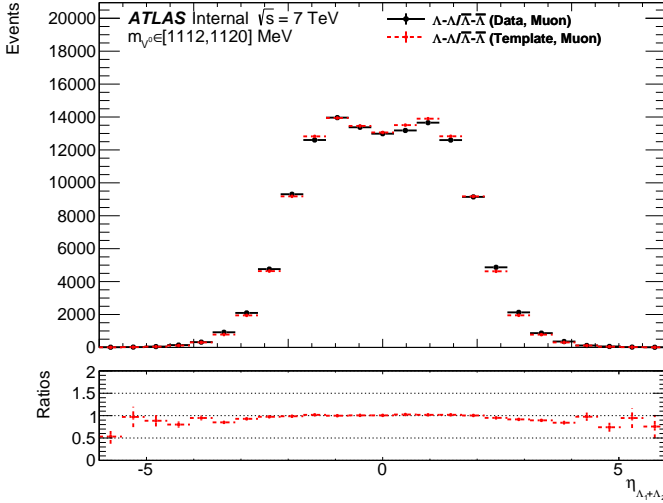
(c)
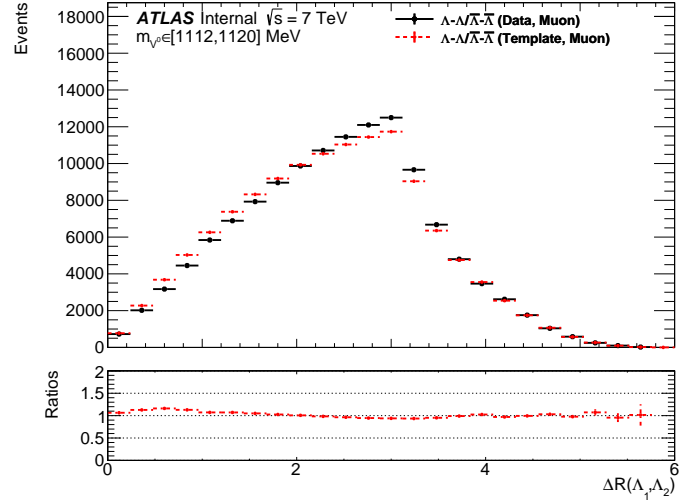
(d)

Figure 9.3.15: Distributions of the combined pseudorapidity $\eta_{\Lambda\Lambda}$ (left) and the opening angle $\Delta R$ (right) for muon data sample overlaid with templates before kinematic weighting for $\Lambda^0\bar{\Lambda}^0$ (top) and $\Lambda^0\Lambda^0 + \bar{\Lambda}^0\bar{\Lambda}^0$ (bottom) events. Template-to-data ratio is shown in the ratio plot in the bottom.
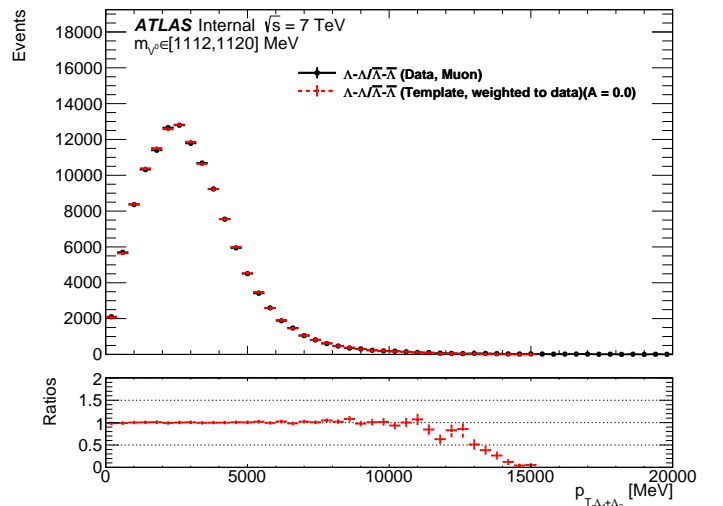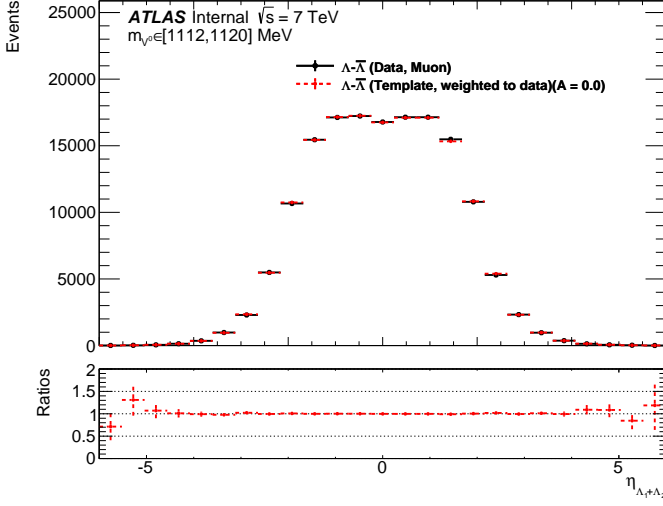
(a)
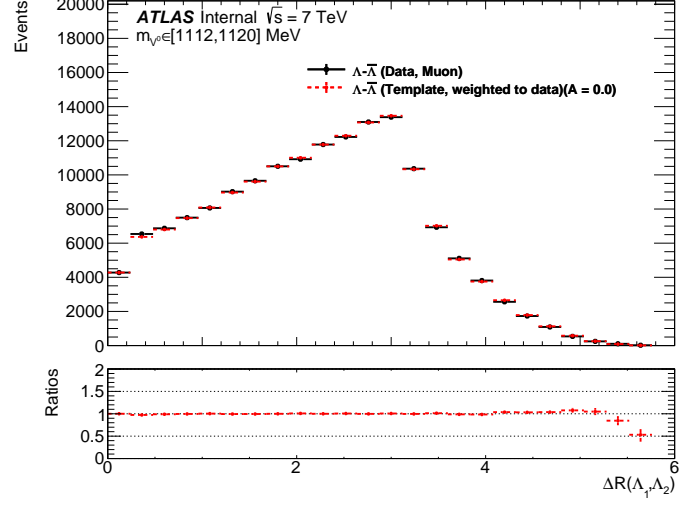
(b)
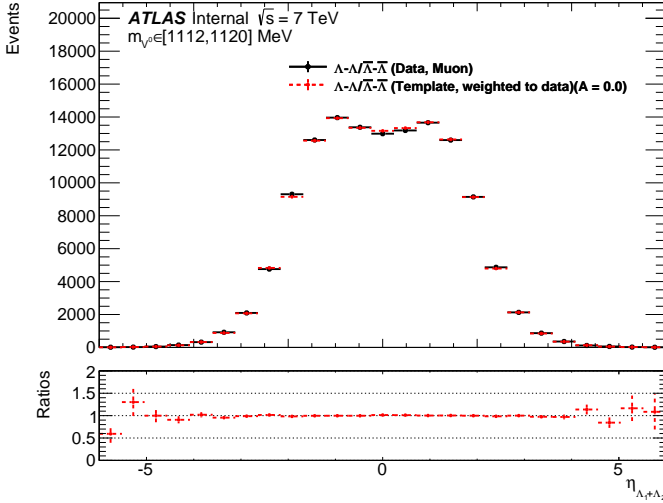
(c)
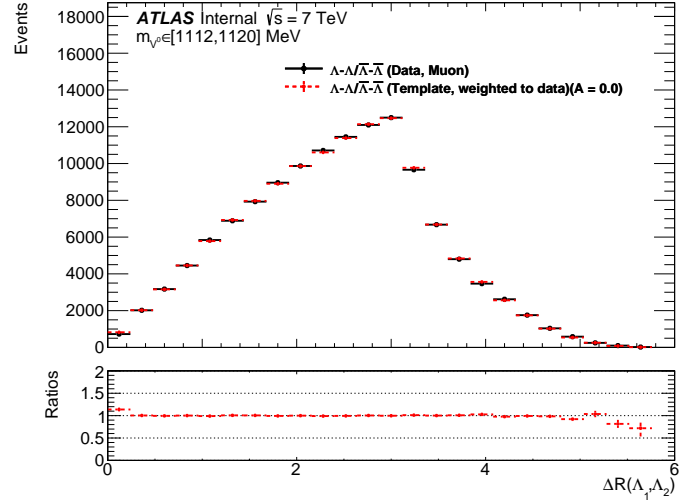
(d)

Figure 9.3.16: Distributions of the combined pseudorapidity $\eta_{\Lambda\Lambda}$ (left) and the opening angle $\Delta R$ (right) for muon data sample overlaid with templates after kinematic weighting for $\Lambda^0\bar{\Lambda}^0$ (top) and $\Lambda^0\Lambda^0+\bar{\Lambda}^0\bar{\Lambda}^0$ (bottom) events. Template-to-data ratio is shown in the ratio plot in the bottom.
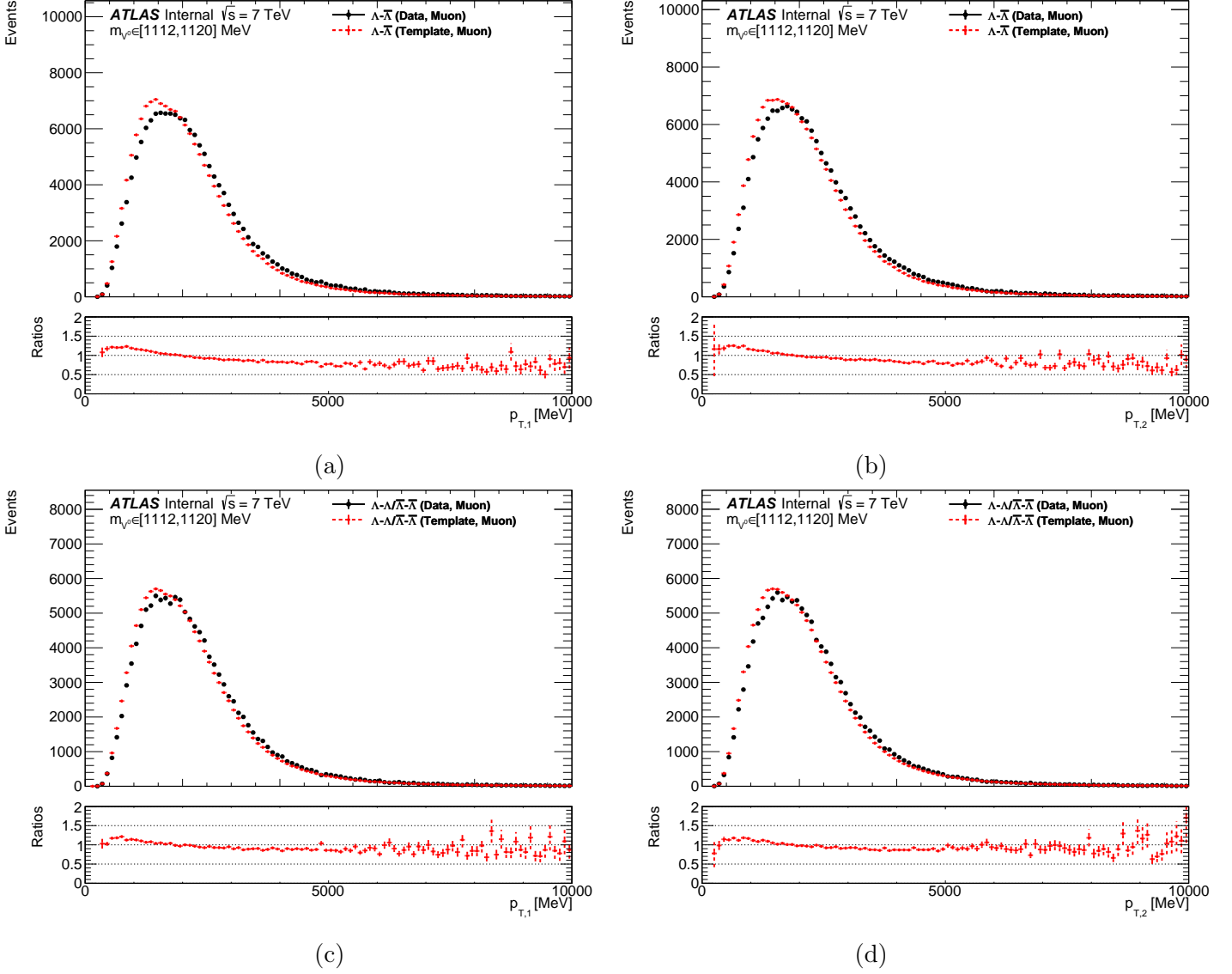
Figure 9.3.17: Distributions of the transverse momenta of the first hyperon $p_{T,1}$ (left) and the second hyperon $p_{T,2}$ (right) for muon data sample overlaid with templates before kinematic weighting for $\Lambda^0\bar{\Lambda}^0$ (top) and $\Lambda^0\Lambda^0+\bar{\Lambda}^0\bar{\Lambda}^0$ (bottom) events. Template-to-data ratio is shown in the ratio plot in the bottom.
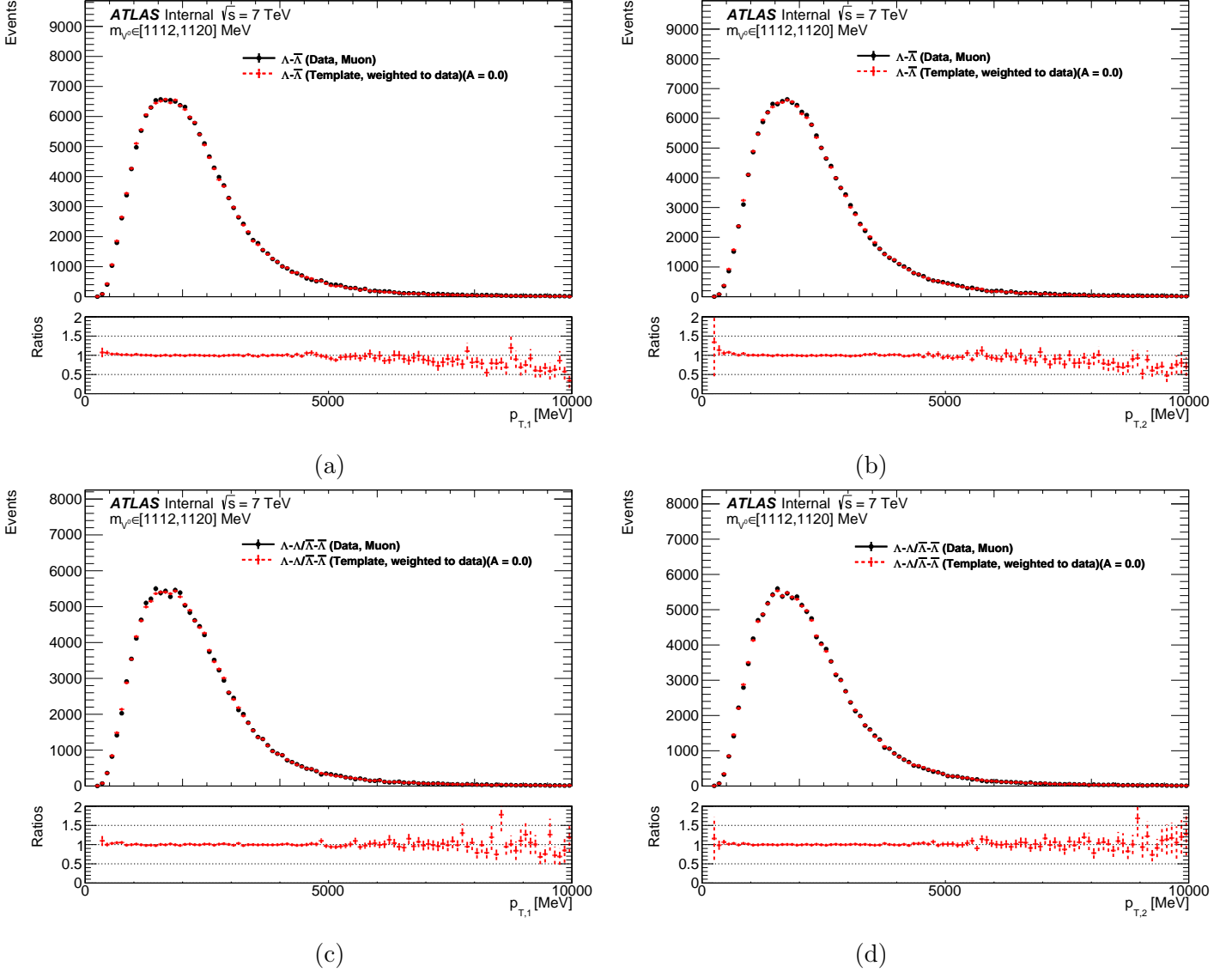
Figure 9.3.18: Distributions of the transverse momenta of the first hyperon $p_{T,1}$ (left) and the second hyperon $p_{T,2}$ (right) for muon data sample overlaid with templates after kinematic weighting for $\Lambda^0\bar{\Lambda}^0$ (top) and $\Lambda^0\Lambda^0+\bar{\Lambda}^0\bar{\Lambda}^0$ (bottom) events. Template-to-data ratio is shown in the ratio plot in the bottom.

# Appendix E
# Relating the two decay-angle bases
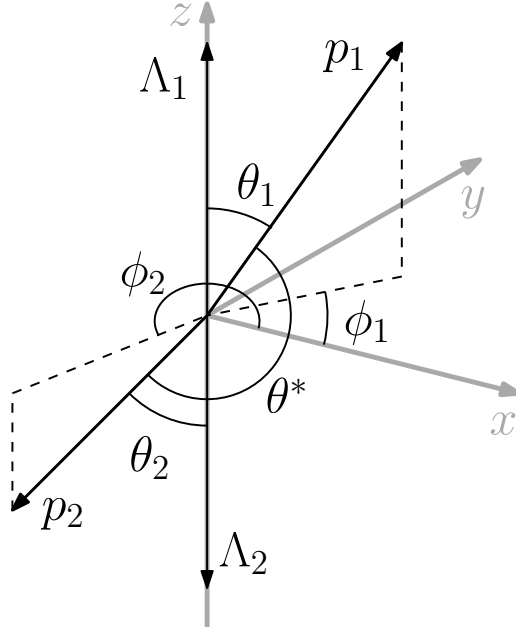


Figure 9.4.19: A diagram relating $\theta^*$ to $\theta_1$, $\theta_2$, $\phi_1$ and $\phi_2$ in the helicity frame. It can be shown that the decay angles are related by the formula $\cos\theta^* = \sin\theta_1 \sin\theta_2 \cos(\phi_1-\phi_2) - \cos\theta_1 \cos\theta_2$.

By simple 3D geometry, the two bases for the decay protons are related by a simple formula

$$\cos\theta^* = \sin\theta_1 \sin\theta_2 \cos(\phi_1 - \phi_2) - \cos\theta_1 \cos\theta_2 \qquad (9.4.14)$$

where $\theta^*$ is the angle between the two decay protons in the helicity frame and $\theta_1$, $\theta_2$, $\phi_1$ and $\phi_2$ are the polar and azimuthal angles of the decay protons with respect to their respective parent hyperon in the helicity frame as shown in Figure 9.4.19. Since the ATLAS detector is symmetric in $\phi$ direction, the first term in Eq. (9.4.15) would vanish when considering the average of the quantity on both side of the expression, that is

$$\langle \cos \theta^* \rangle = -\langle \cos \theta_1 \cos \theta_2 \rangle \qquad (9.4.15)$$

where $\langle \cos(\phi_1 - \phi_2) \rangle = 0$ using the symmetry in $\phi$ direction and $\langle V \rangle$ means the average of the variable $V$ for all the hyperon pairs in the data sample.

# Appendix F
# Cross-checks

This appendix presents several cross-checks to verify that the assumptions made in the analysis is grounded and the methodology used is self-consistent.

## Template closure test

The template is split into four independent mixed sub-samples. Without lost of generality, one sub-sample is chosen as the "pseudo-data" and another one as the template. The template is then weighted to different $A$-values and the Pearson's $\chi^2$ is calculated for each pair of "pseudo-data" and template. The extracted $A$-value of the "pseudo-data" is determined by locating the minimum value of $\chi^2$ in each $Q$ bin. Cross-checks are carried out for all four types of events independently. The mixed sub-samples are later found to have slightly different kinematics and that led to some fluctuations (less than 0.2) in the extracted $A$-values in a few $Q$ bins, particularly in the first bin for $0 < Q < 1$ GeV. After the templates are weighted to the "pseudo-data", the fluctuations become negligible when compared to the statistical uncertainty and the extracted $A$-values are consistent with zero.

## Quadrant approach

Using the convention of Ellis and Hwang [3], a one-dimensional correlation function $f(x)$ can be defined using the four quadrants of a $\cos\theta_2$ vs $\cos\theta_1$ plot as

$$\frac{\alpha^2}{4} f(x) = \frac{N(TR + BL) - N(TL + BR)}{N(TR + BL) + N(TL + BR)} \qquad (9.5.16)$$

where TR, BL, TL, and BR refer to the top-right, bottom-left, top-left and bottom-right quadrants in the $\cos\theta_2$ vs $\cos\theta_1$ distributions (Figure 9.5.23) i.e. $T = \cos\theta_2 > 0$, $B = \cos\theta_2 < 0$, $R = \cos\theta_1 > 0$ and $L = \cos\theta_1 < 0$, and $x = 2m_s/\sqrt{s}$, where $m_s$ is the strange quark mass and $\sqrt{s}$ is the center-of-mass energy, is very close to zero at $\sqrt{s} = 7$ TeV. (Figures 9.5.21 and 9.5.23)
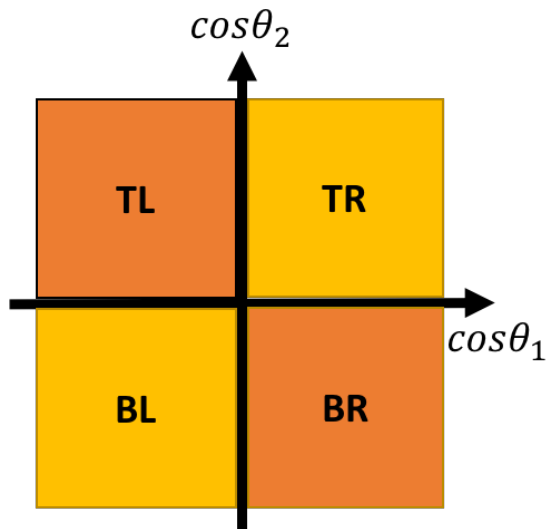


Figure 9.5.20: Figure showing the four quadrants, TL, TR, BL, and BR, in the $\cos\theta_2$ vs $\cos\theta_1$ plot.

The longitudinal polarization of the sample is constrained to be zero by parity conservation as the initial state does not change with the parity transformation [117]. Combining this with the fact that the decay angles of the mixed data sample should be uncorrelated, the $\cos\theta_2$ vs $\cos\theta_1$ distribution should therefore be flat at generator level. The detector efficiency times acceptance of the $\cos\theta_2$ vs $\cos\theta_1$ distribution can then be inferred from its reconstructed distribution as $\epsilon_{i,j} = N_{i,j}^{reco}/(N_{total}/N_{bins}) \propto N_{i,j}^{reco}$ for bin $(i, j)$, where $N_{i,j}^{reco}$ is the number of
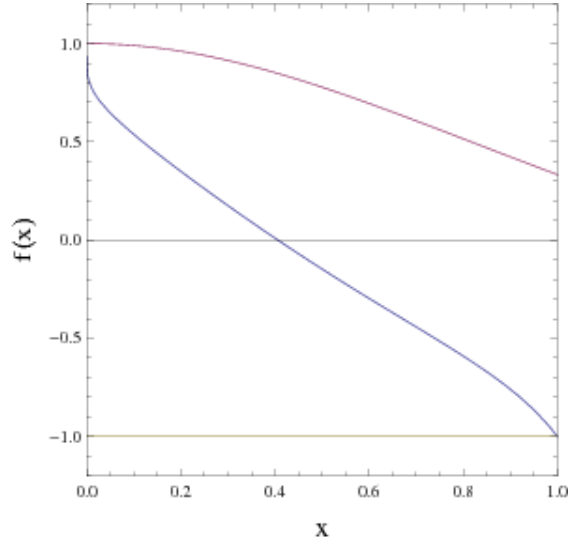
Figure 9.5.21: Graph of correlation function $f(x)$ defined in Eq. (9.5.16) from Ref. [3] as a function of $x = \frac{2m_s}{\sqrt{s}}$, where $m_s$ is the strange quark mass. The topmost line is for the vector case, the lowest line is for the scalar and pseudo-scalar cases, and the intermediate line is for the $gg \to \bar{s}s$ case.
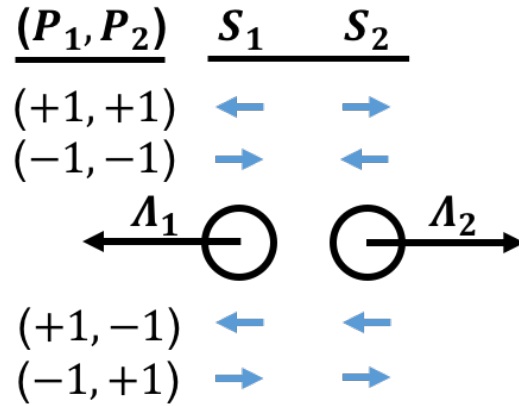


Figure 9.5.22: A schematics of the relationship between different combinations of polarizations of the hyperon pairs and the spin alignments in the helicity frame.

reconstructed events in bin $(i, j)$, $N_{total}$ is the total number of events at generator level and $N_{bins}$ is the total number of bins, assuming the contribution from bin migration is negligible.

(Figure 9.5.25) The detector effect of the data sample can then be corrected using a correction factor $R$ calculated using the mixed data sample as follow

$$\frac{N_{data}^{true}(TR+BL) - N_{data}^{true}(TL+BR)}{N_{data}^{true}(TR+BL) + N_{data}^{true}(TL+BR)} = \frac{N_{data}^{reco}(TR+BL) - R \times N_{data}^{reco}(TL+BR)}{N_{data}^{reco}(TR+BL) + R \times N_{data}^{reco}(TL+BR)},$$

(9.5.17)

where $R = \epsilon(TR+BL)/\epsilon(TL+BR) = N_{mixed}^{reco}(TR+BL)/N_{mixed}^{reco}(TL+BR)$.

$f(x)$ is calculated as a function of $Q$ for all four types of events and is shown in Figure 9.5.24. The correlation function is consistent with zero except in the large $Q$ region for the $\bar{\Lambda}^0\bar{\Lambda}^0$ events where similar deviation of $A$ from zero is also observed in the results extracted using the minimum $\chi^2$ method. (Figure 7.8.1d)



(a)                                    (b)
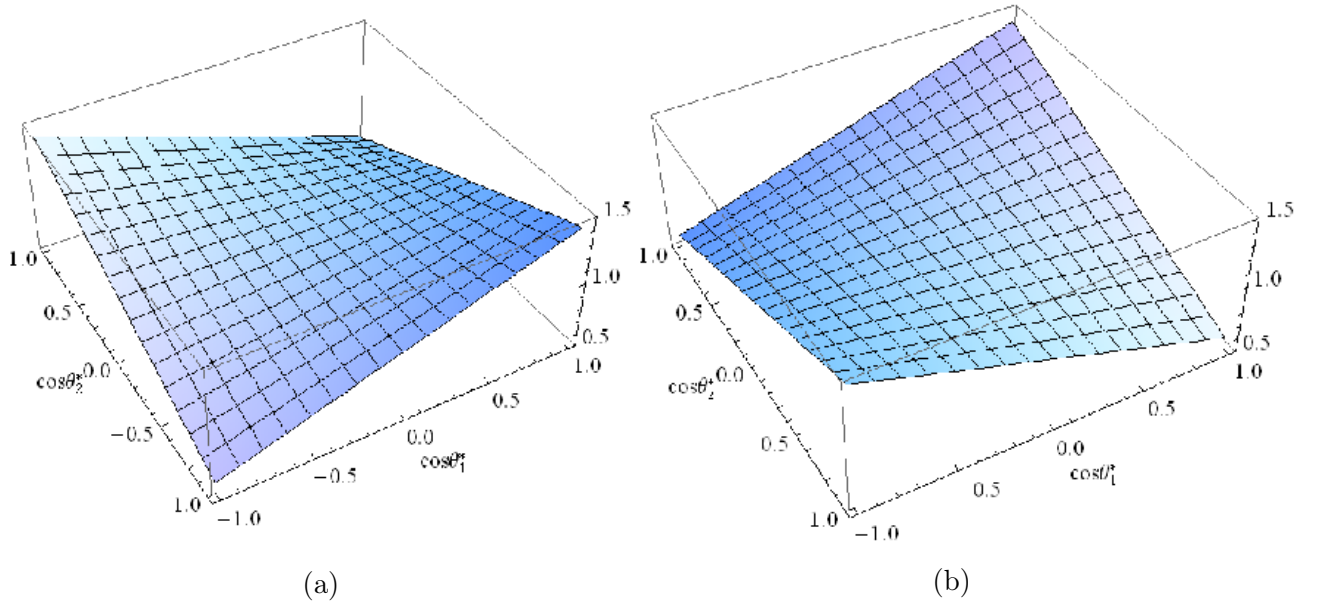
Figure 9.5.23: Distribution of $\cos\theta_2$ vs $\cos\theta_1$ for $\Lambda^0\bar{\Lambda}^0$ events produced through (a) scalar/pseudo-scalar coupling and (b) vector coupling for $m_s = 0$. [3]
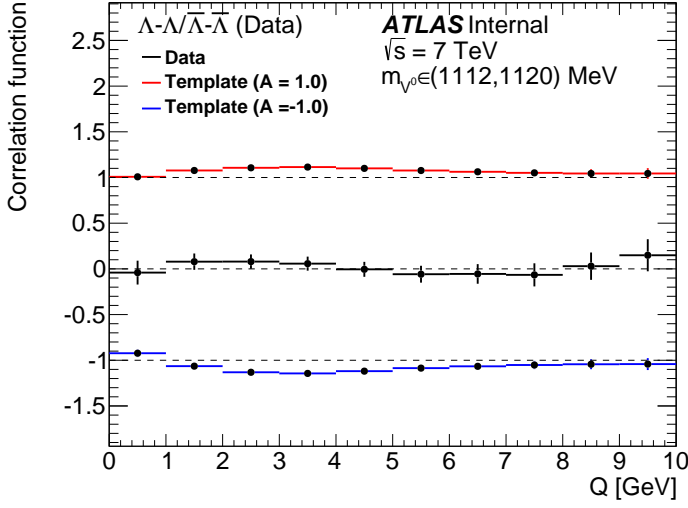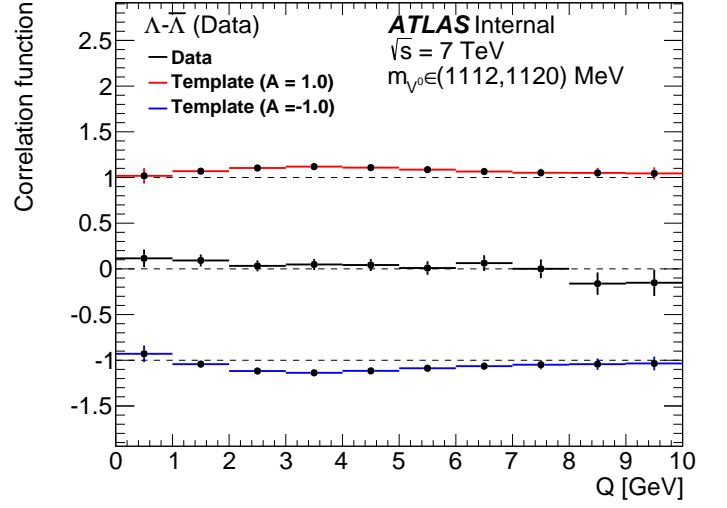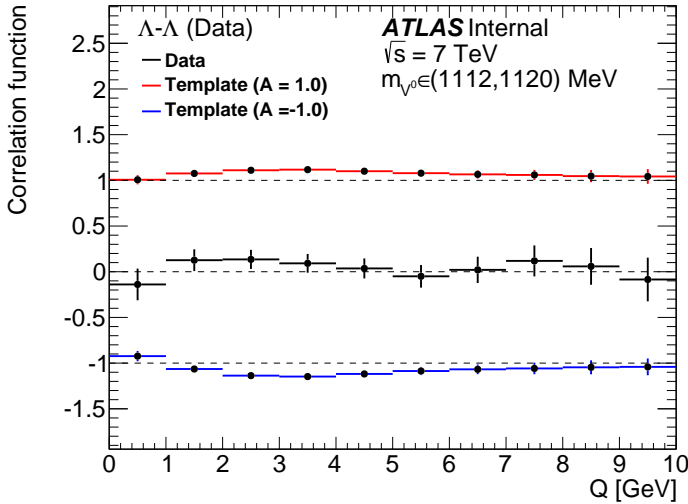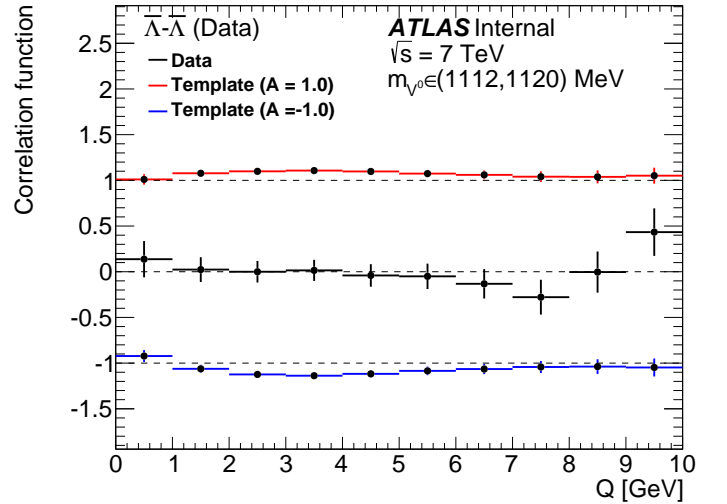
Figure 9.5.24: Correlation function $f(x)$ for (a) $\Lambda^0\bar{\Lambda}^0$, (b) $\Lambda^0\Lambda^0+\bar{\Lambda}^0\bar{\Lambda}^0$, (c) $\Lambda^0\Lambda^0$, and (d) $\bar{\Lambda}^0\bar{\Lambda}^0$ events. The red and blue curves correspond to measurements on mixed data sample weighted to $A = \pm 1$ respectively using event weight $1 - A\alpha^2\cos\theta^*$. In each case, all three samples (data and mixed samples weighted to $A = \pm 1$) are corrected using a correction factor $R$ computed using the mixed data sample with $A = 0$. The dashed lines indicate $f(x) = \pm 1$ as defined in Eq. (9.5.16). The deviation from the expected value (dashed lines) is caused by kinematic weighting, which is also the main systematic uncertainty in the minimum $\chi^2$ method. Only statistical uncertainties are shown in the figures.
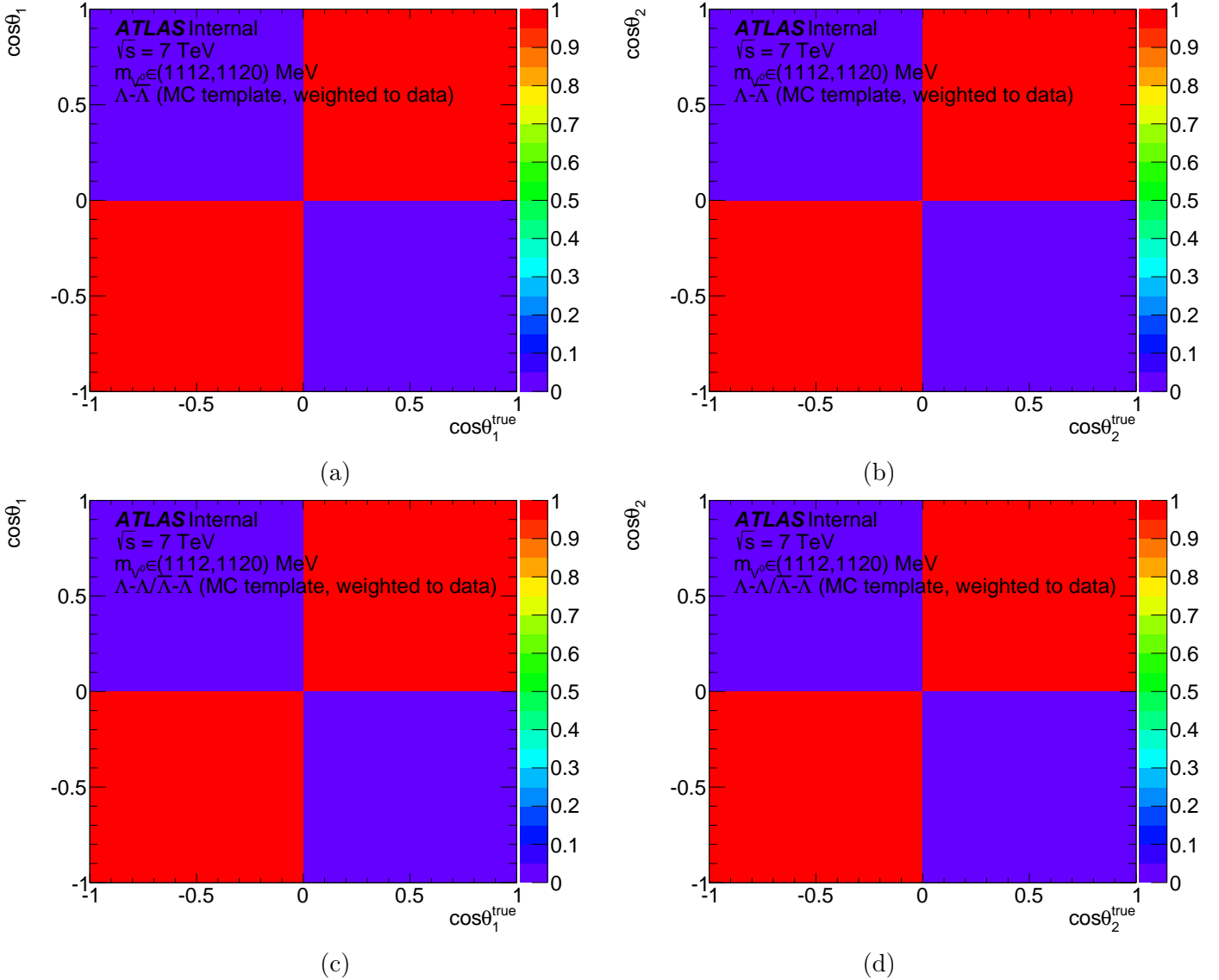
Figure 9.5.25: Migration matrices (reconstructed value versus true value) between positive and negative quadrants for $\cos\theta_1$ (a) unlike-type and (c) like-type events and $\cos\theta_2$ (b) unlike-type and (d) like-type events, computed using the mixed MC sample weighted to data and normalized in true bins. It is shown that bin migration between the positive and negative quadrants in the $\cos\theta_2$ vs $\cos\theta_1$ plot is negligible.

# Event mixing

A toy MC sample is used to generate decay angle distributions ($\cos\theta_1$, $\cos\theta_2$ and $\cos\theta^*$) at true level for different polarizations $P_1/P_2$ and spin correlation $A$ configurations. $\cos\theta_1$ from odd events and $\cos\theta_2$ from even events are then mixed to check if the spin correlation in the sample would be completely erased. A simplified naive correlation parameter defined as $C(\cos\theta_1, \cos\theta_2) = \langle\cos\theta_1\cos\theta_2\rangle - \langle\cos\theta_1\rangle\langle\cos\theta_2\rangle$ is calculated before and after the event mixing. For $A = \pm1$ (100% correlated sample), the expected value of the correlation parameter is

$$\langle C(x,y)\rangle = \frac{1}{4}\left(\int_{-1}^{1}\int_{-1}^{1} dxdy(1\pm\alpha^2xy)xy - \int_{-1}^{1}\int_{-1}^{1} dxdy(1\pm\alpha^2xy)x \int_{-1}^{1}\int_{-1}^{1} dxdy(1\pm\alpha^2xy)y\right)$$
(9.5.18)

$$= \frac{\alpha^2}{4}\left(0\pm\left.\frac{x^3}{3}\right|_{-1}^{1}\left.\frac{y^3}{3}\right|_{-1}^{1} - 0\times0\right) = \pm\frac{\alpha^2}{9} \approx \pm0.0458$$
(9.5.19)

where $\cos\theta_1$ and $\cos\theta_2$ are replaced by $x$ and $y$. For $A = 0$ (uncorrelated sample), we have

$$\langle C(x,y)\rangle = \frac{1}{4}\left(\int_{-1}^{1}\int_{-1}^{1} dxdyxy - \int_{-1}^{1}\int_{-1}^{1} dxdyx \int_{-1}^{1}\int_{-1}^{1} dxdyy\right) = 0$$
(9.5.20)

1M events of a toy MC sample are generated for each of the abovementioned spin configuration and the resulting $\cos\theta_2$ vs $\cos\theta_1$ and $\cos\theta^*$ plots are shown in Figures 9.5.26 and 9.5.27. It is shown that the values of the correlation parameter before and after the event mixing are consistent with Eqs. (9.5.18) and (9.5.20) respectively. $\cos\theta^*$ distributions also

175

show slope consistent with zero after the event mixing. This is a direct numerical proof that a reference sample free of spin correlation can be produced by event mixing. Notice that we are assuming $P_1 = P_2 = 0$ here, similar theoretical and numerical calculations can be done by putting the linear terms back into the Eqs. (9.5.18) and (9.5.20) for nonzero polarizations in the sample.
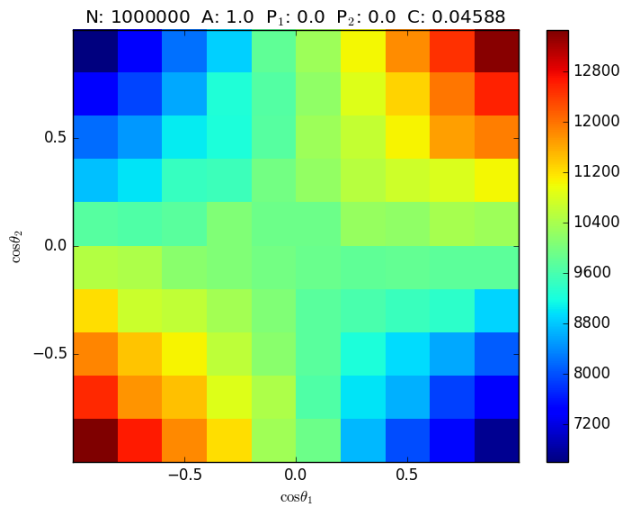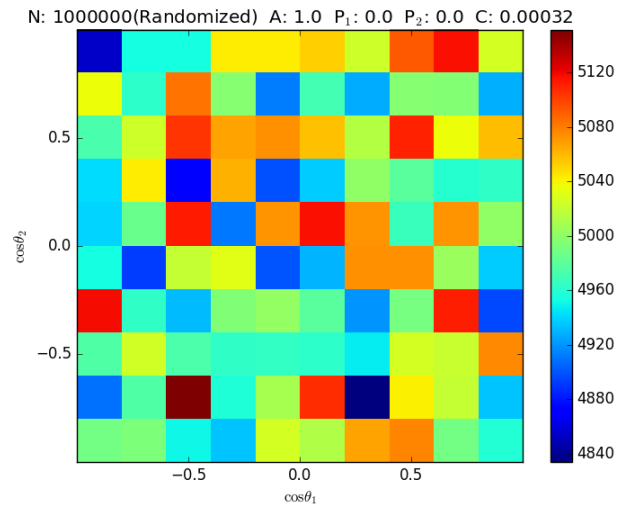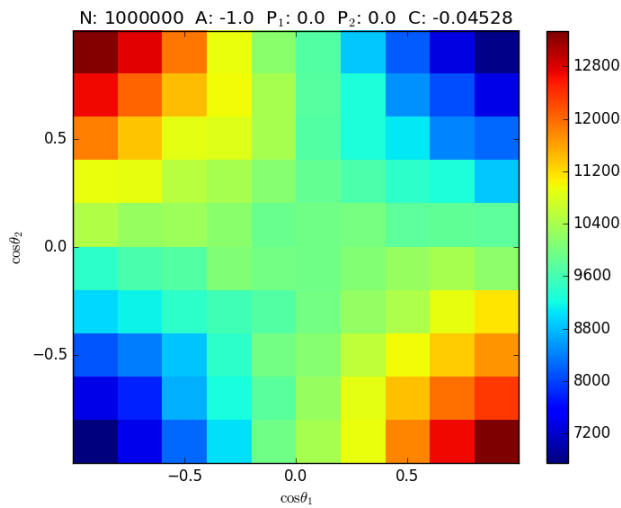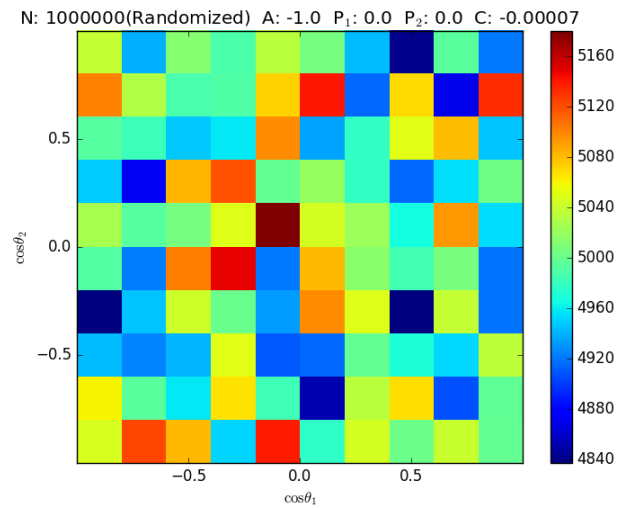
Figure 9.5.26: Distribution of $\cos\theta_2$ vs $\cos\theta_1$ of an unpolarized toy MC sample with $A = 1.0$ and $P_1 = P_2 = 0.0$ (a) before and (b) after event mixing $A = -1.0$ and $P_1 = P_2 = 0.0$ (c) before and (d) after event mixing. It is shown that for an unpolarized sample, event mixing completely erases the spin correlation in the sample at true level, reducing the value of the correlation parameter from $\sim \pm 0.0458$ to zero.
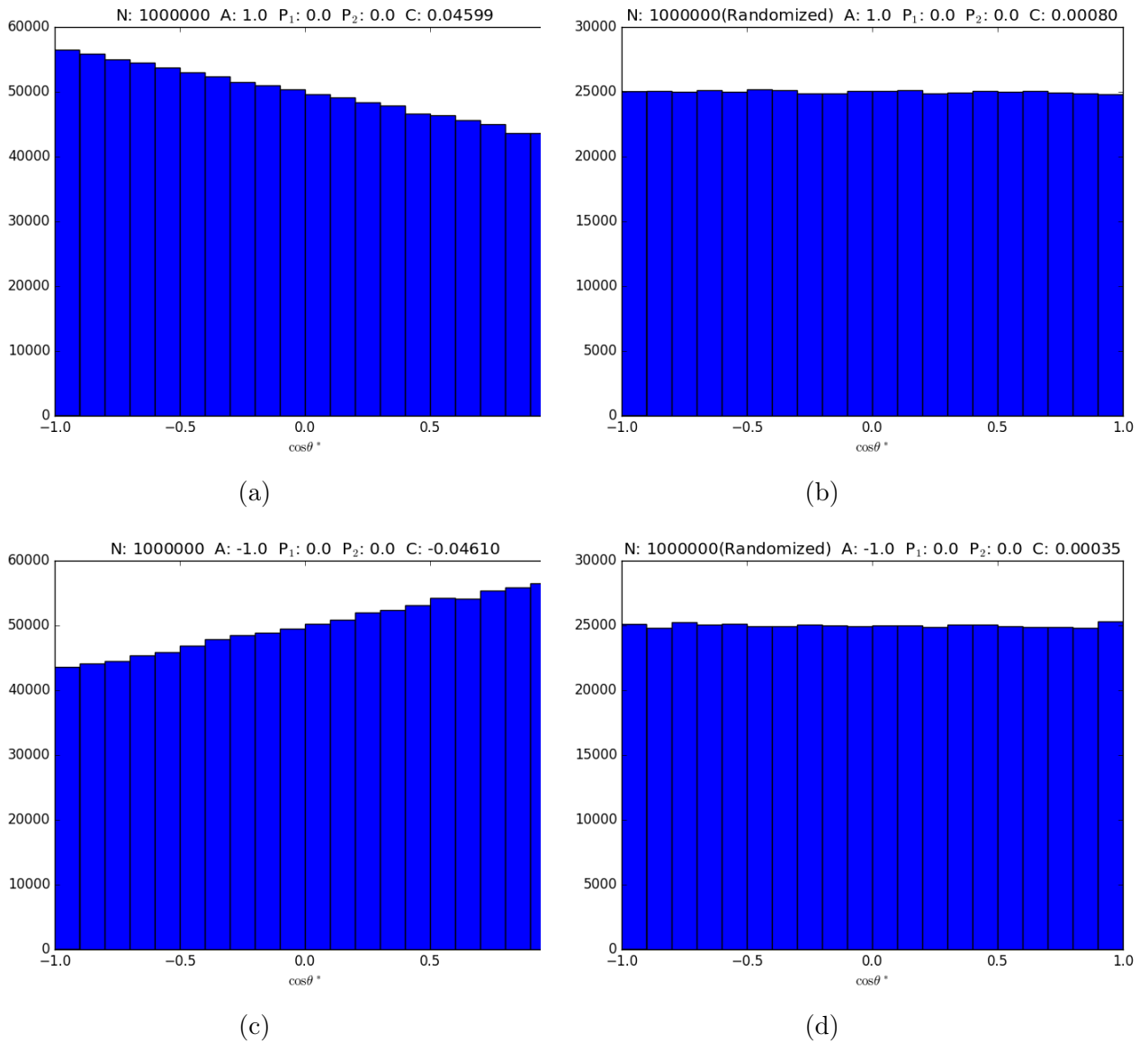
Figure 9.5.27: Distribution of $\cos\theta^*$ of an unpolarized toy MC sample with $A = 1.0$ and $P_1 = P_2 = 0.0$ (a) before and (b) after event mixing and with $A = -1.0$ and $P_1 = P_2 = 0.0$ (c) before and (d) after event mixing. It is shown that for an unpolarized sample, event mixing completely erases the spin correlation in the sample at true level, resulting in a flat $\cos\theta^*$ distribution.

# Appendix G
# Contributions

This Appendix describes the author's other contributions during the course of his graduate study.

## Overview

The analysis reported in this thesis accounts for only a fracction of the experience of the author during his graduate study. The author has worked on several other projects during his graduate study both at Michigan and at CERN.

After joining the PhD program in physics at the University of Michigan in July 2010, the author worked on several projects as a PhD pre-candidate. One project[1] is to study two available muon reconstruction algorithms, namely MUID and STACO, to understand their performances under different conditions in terms of the signal-to-background ratio of resonances, such as $\rho$, $\phi$, and $J/\Psi$, in the di-muon invariant mass spectrum. Another project is to search for the Higgs boson through the $H \rightarrow ZZ^* \rightarrow 4l$ decay channel using the early 8 TeV data set. The author summarized the preliminary results in a poster[2] presented at the 2012 US-ATLAS Physics Workshop[3] which was hosted at Ann Arbor, MI.

After moving to CERN as a PhD candidate in September 2012, the author worked on the maintenance and development of the MDT configuration database (DB)[4] as his ATLAS

---

[1]http://www-personal.umich.edu/~hccheng/talks/tomcheng_report19102011.pdf
[2]http://www-personal.umich.edu/~hccheng/talks/HZZ4lAnalysisPoster.pdf
[3]http://atlasworkshop.physics.lsa.umich.edu/
[4]https://twiki.cern.ch/twiki/bin/viewauth/Atlas/MDTConfigDB

authorship qualification requirement. The author helped developed new softwares and the DB schema to cope with the new double-readout configuration which was planned for the high luminosity runs after the first long shutdown (LS1). The modified DB schema was successfully implemented in 2015. The author also helped developed a graphical user interface (GUI)[5] for the MDT configuration DB in collaboration with another PhD student to facilitate the retrival and modification of MDT configuration parameters in the DB.

During the LS1, the author participated in the commissioning of the newly installed EE MDT chamber and gave a summary talk[6] on behalf of the commissioning team. The author also supervised a CERN REU student to work on a summer research project[78] on the selection of $\Sigma^{*\pm}$ which is described in Section 6.5.

# Contributions at ATLAS

The author gave several talks and published a proceedings on behalf of the ATLAS Collaboration in conferences at national/international level, some of which are related to the analysis reported in this thesis. Below is a list of the author's contributions.

**Talks/Conferences:**

- Measurement of Correlation between Inclusively Produced $\Lambda^0\bar{\Lambda}^0$, $\Lambda^0\Lambda^0$ and $\bar{\Lambda}^0\bar{\Lambda}^0$ Hyperon Pairs at $\sqrt{s} = 7$ TeV in the LHC ATLAS Experiment (Poster expected) - 2017-06-24 to 30, Gordon Research Conference 2017[9], Hong Kong

---

[5]https://twiki.cern.ch/twiki/bin/viewauth/Atlas/MDTConfigInterface
[6]http://www-personal.umich.edu/~hccheng/talks/20130528_muontalk_tomcheng.pdf
[7]http://cds.cern.ch/record/1748073
[8]https://indico.cern.ch/event/309212/contributions/1681322/attachments/590939/813416/thirdPresentation.pdf
[9]https://www.grc.org/programs.aspx?id=16933

- Searches for Heavy Quark States at ATLAS[10] (Talk) - 2016-06-13, XIIth International Conference on Beauty, Charm, and Hyperons in Hadronic Interactions, Fairfax, VA

- Measurement of Correlation of $\Lambda$ Pairs with the ATLAS Detector[11] (Talk) - 2015-08-05, 2015 Meeting of the APS Division of Particles and Fields, Ann Arbor, MI

- Beauty in ATLAS: New physics searches, spectroscopy and decay properties of B-hadrons[12] (Talk) - 2014-05-06, Phenomenology 2014 Symposium, Pittsburgh, PA

- Detection of the Standard Model Higgs Boson in the $H \to ZZ^* \to 4l$ channel using relaxed cuts in event selection with ATLAS Detector (Poster) - 2012-08-13, 2012 US-ATLAS Physics Workshop, Ann Arbor, MI

**Proceedings:**

- Searches for Heavy Quark States at ATLAS[13] - 2016-12-09, Proceedings of XII International Conference on Beauty, Charm, and Hyperons in Hadronic Interactions (BEACH 2016)

**ATLAS Internal Note:**

- Measurement of Correlation between Inclusively Produced $\Lambda^0 \bar{\Lambda}^0$, $\Lambda^0 \Lambda^0$ and $\bar{\Lambda}^0 \bar{\Lambda}^0$ Hyperon Pairs at $\sqrt{s} = 7$ TeV in the LHC ATLAS Experiment (ATL-COM-PHYS-2016-1798[14])

More information can be found on the author's personal website[15].

---

[10] http://www-personal.umich.edu/~hccheng/talks/BEACH2016_SearchesForHeavyQuarkStates_HokChuenCheng.pdf

[11] http://www-personal.umich.edu/~hccheng/talks/DPF2015_LamPairCorr_HokChuenCheng.pdf

[12] http://www-personal.umich.edu/~hccheng/talks/Pheno2014_Beauty_in_ATLAS_v3.pdf

[13] http://iopscience.iop.org/article/10.1088/1742-6596/770/1/012008

[14] https://cds.cern.ch/record/2239393/

[15] http://www-personal.umich.edu/~hccheng/

# Bibliography

[1] S. Belostotskii, "Topical aspects of hyperon physics," Tech. Rep. DESY-HERMES-2006-57, DESY, Hamburg, Aug 2004. 2, 23

[2] B. Andersson, G. Gustafson, G. Ingelman, and T. Sjostrand, "Parton Fragmentation and String Dynamics," *Phys. Rept.*, vol. 97, pp. 31–145, 1983. 2

[3] J. Ellis and D. S. Hwang, "Spin Correlations of $\Lambda\overline{\Lambda}$ Pairs as a Probe of Quark-Antiquark Pair Production," *Eur. Phys. J. C*, vol. 72, no. arXiv:1108.5319. KCL-PH-TH-2011-27. LCTS-2011-13. CERN-PH-TH-2011-212, p. 1877. 12 p, 2011. 2, 32, 109, 137, 169, 171, 172

[4] A. A. Savchenko, D. A. Romanov, and S. Collaboration, "Measurement of $\lambda\lambda$ spin correlations in the selex experiment," *Journal of Physics: Conference Series*, vol. 295, no. 1, p. 012089, 2011. 2, 4, 32, 36, 37

[5] OPAL Collaboration, "A First Measurement of the $\Lambda\overline{\Lambda}$ and $\Lambda\Lambda(\overline{\Lambda\Lambda})$ Spin Compositions in Hadronic $Z^0$ Decays," *Phys. Lett. B*, vol. 384, no. CERN-PPE-96-068, pp. 377–387. 16 p, 1996. 3, 32, 34

[6] DELPHI Collaboration, "Production of $\Lambda$ and $\overline{\Lambda}$ correlations in the hadronic decays of the $Z^0$," *Physics Letters B*, vol. 318, no. 1, pp. 249 – 262, 1993. 3, 32, 34

[7] ALEPH Collaboration, "Fermi-Dirac Correlations in $\Lambda$ Pairs in Hadronic Z Decays," *Phys. Lett. B*, vol. 475, no. CERN-EP-99-172. 3-4, pp. 395–406. 18 p, 1999. 3, 32, 34

[8] R. M. Duran Delgado, G. Gustafson, and L. Lonnblad, "String Effects on Fermi-Dirac Correlation Measurements," *Eur. Phys. J.*, vol. C52, pp. 113–119, 2007. 3, 23, 31, 35, 91, 109, 139, 141

[9] "Correlation femtoscopy in neutron-carbon interactions at average neutron energy of 51-GeV," *Phys. Atom. Nucl.*, vol. 68, pp. 481–487, 2005. [Yad. Fiz.68,510(2005)]. 4, 32, 39, 40, 109

[10] STAR Collaboration, "$\Lambda\Lambda$ Correlation Function in Au+Au collisions at $\sqrt{s_{NN}} = 200$ GeV," *Phys. Rev. Lett.*, vol. 114, no. 2, p. 022301, 2015. 4, 32, 37, 109

[11] E. Noether, "Invariante variationsprobleme," *Nachrichten von der Gesellschaft der Wissenschaften zu GÃ¶ttingen, Mathematisch-Physikalische Klasse*, vol. 1918, pp. 235–257, 1918. 9

[12] F. Englert and R. Brout, "Broken symmetry and the mass of gauge vector mesons," *Phys. Rev. Lett.*, vol. 13, pp. 321–323, Aug 1964. 10, 13

[13] P. W. Higgs, "Broken symmetries and the masses of gauge bosons," *Phys. Rev. Lett.*, vol. 13, pp. 508–509, Oct 1964. 10, 13

[14] G. S. Guralnik, C. R. Hagen, and T. W. B. Kibble, "Global conservation laws and massless particles," *Phys. Rev. Lett.*, vol. 13, pp. 585–587, Nov 1964. 10, 13

[15] ALTAS Collaboration, "Observation of a new particle in the search for the Standard Model Higgs boson with the ATLAS detector at the LHC," *Phys. Lett.*, vol. B716, pp. 1–29, 2012. 10

[16] CMS Collaboration, "Observation of a new boson at a mass of 125 GeV with the CMS experiment at the LHC," *Phys. Lett.*, vol. B716, pp. 30–61, 2012. 10

[17] *Phys. Lett.*, vol. 539, no. 3-4, p. 179, 2002. 11

[18] *Phys. Rev. Lett.*, vol. 89, no. 1, p. 011301, 2002. 11

[19] *Phys. Rev. Lett.*, vol. 94, p. 081801, 2004. 11

[20] *New J Phys.*, vol. 6, no. 1, p. 194, 2004. 11

[21] *Phys. Rev. Lett.*, vol. 90, no. 4, p. 041801, 2003. 11

[22] *Phys. Lett.*, vol. 67, no. 4, p. 421, 1977. 11

[23] *Phys. Rev.*, vol. 22, no. 7, p. 1694, 1980. 11

[24] *Phys. Rev.*, vol. 22, no. 9, p. 2227, 1980. 11

[25] *Phys. Rev.*, vol. 25, no. 3, p. 774, 1982. 11

[26] CDF Collaboration, "Observation of top quark production in $\bar{p}p$ collisions with the collider detector at fermilab," *Phys. Rev. Lett.*, vol. 74, pp. 2626–2631, Apr 1995. 11

[27] D0 Collaboration, "Search for high mass top quark production in $p\bar{p}$ collisions at $\sqrt{s} = 1.8$ tev," *Phys. Rev. Lett.*, vol. 74, pp. 2422–2426, Mar 1995. 11

[28] DONUT Collaboration, "Observation of tau neutrino interactions," *Physics Letters B*, vol. 504, no. 3, pp. 218 – 224, 2001. 12

[29] M. Kobayashi and T. Maskawa, "Cp-violation in the renormalizable theory of weak interaction," *Progress of Theoretical Physics*, vol. 49, no. 2, p. 652, 1973. 12

[30] M. Thomson, "Qcd and colour." `http://www.hep.phy.cam.ac.uk/~thomson/partIIIparticles/handouts/Handout_8_2011.pdf`, 2011. 15, 18

[31] D. J. Gross and F. Wilczek, "Ultraviolet behavior of non-abelian gauge theories," *Phys. Rev. Lett.*, vol. 30, pp. 1343–1346, Jun 1973. 16

[32] H. D. Politzer, "Reliable perturbative results for strong interactions?," *Phys. Rev. Lett.*, vol. 30, pp. 1346–1349, Jun 1973. 16

[33] C. Patrignani *et al.*, "Review of Particle Physics," *Chin. Phys.*, vol. C40, no. 10, p. 100001, 2016. 17

[34] T. Sjostrand, S. Mrenna, and P. Z. Skands, "PYTHIA 6.4 Physics and Manual," *JHEP*, vol. 05, p. 026, 2006. 20, 73, 96, 99, 103, 141

[35] T. Sjostrand, S. Mrenna, and P. Z. Skands, "A Brief Introduction to PYTHIA 8.1," *Comput. Phys. Commun.*, vol. 178, pp. 852–867, 2008. 20, 96, 99, 103, 141

[36] M. Bahr *et al.*, "Herwig++ Physics and Manual," *Eur. Phys. J.*, vol. C58, pp. 639–707, 2008. 20, 142

[37] T. Gleisberg, S. Hoeche, F. Krauss, M. Schonherr, S. Schumann, F. Siegert, and J. Winter, "Event generation with SHERPA 1.1," *JHEP*, vol. 02, p. 007, 2009. 20, 142

[38] C. Blanks, "Strangeness at lhcb." `http://imperialhep.blogspot.com/2011/08/strangeness-at-lhcb.html`, 2011. 20

[39] G. S. Bali and K. Schilling, "Static quark-antiquark potential: Scaling behavior and finite-size effects in su(3) lattice gauge theory," *Phys. Rev. D*, vol. 46, pp. 2636–2646, Sep 1992. 21

[40] C. S. Fordham, *Neutral Kaon and Lambda production in electron-positron annihilation at 29 GeV and the Z boson resonance*. PhD thesis, Stanford University, 1990. 21

[41] B. Andersson, S. Mohanty, and F. Soderberg, "The Lund fragmentation process for a multigluon string according to the area law," *Eur. Phys. J.*, vol. C21, pp. 631–647, 2001. 22

[42] J. A. et al., "A measurement of the spin asymmetry and determination of the structure function g1 in deep inelastic muon-proton scattering," *Physics Letters B*, vol. 206, no. 2, pp. 364 – 370, 1988. 24, 137

[43] J. T. Londergan, "Nucleon Resonances and Quark Structure," *Int. J. Mod. Phys.*, vol. E18, pp. 1135–1165, 2009. 24, 137

[44] A. W. Thomas, "Interplay of Spin and Orbital Angular Momentum in the Proton," *Phys. Rev. Lett.*, vol. 101, p. 102003, 2008. 24, 137

[45] I. e. a. Bedlinskiy, "Measurement of exclusive $\pi^0$ electroproduction structure functions and their relationship to transverse generalized parton distributions," *Phys. Rev. Lett.*, vol. 109, p. 112001, Sep 2012. 24, 137

[46] V. D. Hopper and S. Biswas, "Evidence concerning the existence of the new unstable elementary neutral particle," *Phys. Rev.*, vol. 80, pp. 1099–1100, Dec 1950. 25

[47] K. Nakamura *et al. J. Phys. G*, vol. 37, p. 075021, 2010. 25, 99, 108, 122, 136

[48] T. D. Lee and C. N. Yang, "General partial wave analysis of the decay of a hyperon of spin," *Phys. Rev.*, vol. 108, pp. 1645–1647, 1957. 25

[49] T. D. Lee, J. Steinberger, G. Feinberg, P. K. Kabir, and C. N. Yang, "Possible detection of parity nonconservation in hyperon decay," *Phys. Rev.*, vol. 106, pp. 1367–1369, 1957. 25

[50] W. G. D. Dharmaratna and G. R. Goldstein, "Single quark polarization in quantum chromodynamics subprocesses," *Phys. Rev. D*, vol. 53, pp. 1073–1086, Feb 1996. 26

[51] G. Aad *et al.*, "Measurement of the transverse polarization of $\Lambda$ and $\bar{\Lambda}$ hyperons produced in proton-proton collisions at $\sqrt{s} = 7$ TeV using the ATLAS detector," *Phys. Rev.*, vol. D91, no. 3, p. 032004, 2015. 26, 76

[52] G. Aad *et al.*, "Kshort and $\Lambda$ production in *pp* interactions at $\sqrt{s} = 0.9$ and 7 TeV measured with the ATLAS detector at the LHC," *Phys. Rev.*, vol. D85, p. 012001, 2012. 26

[53] K. Heller in *Proceedings of 9th International Symposium on High Energy Spin Physics. Springer-Verlag, Bonn, Germany*, p. 97, 1990. 26

[54] ALICE Collaboration, "Insight into particle production mechanisms via angular correlations of identified particles in pp collisions at $\sqrt{s} = 7$ TeV," 2016. 29, 31, 32, 33, 34

[55] T. Kress, "Particle correlations at LEP," in *High-energy physics. Proceedings, 1st International Conference, HEP-MAD'01, Antananarivo, Madagascar, September 27-October 5, 2001*, pp. 223–231, 2002. 30

[56] STAR Collaboration, "Proton-$\Lambda$ correlations in central au+au collisions at $\sqrt{s_{NN}} = 200$ gev," *Phys. Rev. C*, vol. 74, p. 064906, Dec 2006. 31, 32, 37, 38

[57] G. Goldhaber, S. Goldhaber, W. Lee, and A. Pais, "Influence of bose-einstein statistics on the antiproton-proton annihilation process," *Phys. Rev.*, vol. 120, pp. 300–312, 1960. 31

[58] G. Alexander and I. Cohen, "Measure of pi's and Lambda's emitter radius via Bose-Einstein and Fermi-Dirac statistics," in *Hadron structure '98. Proceedings, International Conference, HS'98, Stara Lesna, Slovakia, September 7-13, 1998*, 1998. 32, 36

[59] "Results on correlations and fluctuations from NA49," *Nucl. Phys. A*, vol. 715, no. nucl-ex/0208020, pp. 55–64. 10 p, 2002. 32, 38, 39

[60] L. R. Evans and P. Bryant, "LHC Machine," *J. Instrum.*, vol. 3, p. S08001. 164 p, 2008. 42

[61] O. S. Bruning, P. Collier, P. Lebrun, S. Myers, R. Ostojic, J. Poole, and P. Proudlock, "LHC Design Report Vol.1: The LHC Main Ring," 2004. 42

[62] O. Buning, P. Collier, P. Lebrun, S. Myers, R. Ostojic, J. Poole, and P. Proudlock, "LHC Design Report. 2. The LHC infrastructure and general services," 2004. 42

[63] M. Benedikt, P. Collier, V. Mertens, J. Poole, and K. Schindl, *LHC Design Report*. Geneva: CERN, 2004. 42

[64] ATLAS Collaboration, "The atlas experiment at the cern large hadron collider," *JINST*, vol. 3, p. S08003, 2008. 42, 48, 49, 51, 52, 54, 56, 57, 61

[65] ATLAS Collaboration, *ATLAS detector and physics performance: Technical Design Report, 1*. Technical Design Report ATLAS, Geneva: CERN, 1999. 42

[66] ATLAS Collaboration, *ATLAS detector and physics performance: Technical Design Report, 2*. Technical Design Report ATLAS, Geneva: CERN, 1999. 42

[67] LEP Collaboration, *LEP design report*. Geneva: CERN, 1984. 42

[68] R. Cid and X. Cid-Vidal, "Taking a closer look at lhc." 43, 45

[69] M. Bajko, F. Bertinelli, N. Catalan-Lasheras, S. Claudet, P. Cruikshank, K. Dahlerup-Petersen, R. Denz, P. Fessia, C. Garion, J. Jimenez, G. Kirby, P. Lebrun, S. Le Naour, K.-H. Mess, M. Modena, V. Montabonnet, R. Nunes, V. Parma, A. Perin, G. de Rijk, A. Rijllart, L. Rossi, R. Schmidt, A. Siemko, P. Strubin, L. Tavian, H. Thiesen, J. Tock, E. Todesco, R. Veness, A. Verweij, L. Walckiers, R. Van Weelderen, R. Wolf, S. FehÃ©r, R. Flora, M. Koratzinos, P. Limon, and J. Strait, "Report of the Task Force on the Incident of 19th September 2008 at the LHC," Tech. Rep. LHC-PROJECT-Report-1168. CERN-LHC-PROJECT-Report-1168, CERN, Geneva, Mar 2009. 44

[70] G. Apollinari, O. BrÃŒening, and L. Rossi, "High Luminosity LHC Project Description," Tech. Rep. CERN-ACC-2014-0321, CERN, Geneva, Dec 2014. 44, 45

[71] CERN, "Lhc performance reaches new highs," Jul 2016. 44, 45

[72] C. Lefevre, "LHC: the guide." Jan 2008. 45

[73] C. De Melis, "The CERN accelerator complex. Complexe des accelerateurs du CERN," Jul 2016. General Photo. 47

[74] ALICE Collaboration, "The ALICE experiment at the CERN LHC. A Large Ion Collider Experiment," *J. Instrum.*, vol. 3, p. S08002. 259 p, 2008. 47

[75] CMS Collaboration, "The CMS experiment at the CERN LHC. The Compact Muon Solenoid experiment," *J. Instrum.*, vol. 3, p. S08004. 361 p, 2008. 48

[76] LHCb Collaboration, "The LHCb Detector at the LHC," *J. Instrum.*, vol. 3, no. LHCb-DP-2008-001. CERN-LHCb-DP-2008-001, p. S08005, 2008. 48

[77] TOTEM Collaboration, *Total cross-section, elastic scattering and diffraction dissociation at the Large Hadron Collider at CERN: TOTEM Technical Design Report.* Technical Design Report TOTEM, Geneva: CERN, 2004. 48

[78] MoEDAL Collaboration, "Technical Design Report of the MoEDAL Experiment," Tech. Rep. CERN-LHCC-2009-006. MoEDAL-TDR-001, Jun 2009. 48

[79] LHCf Collaboration, *LHCf experiment: Technical Design Report.* Technical Design Report LHCf, Geneva: CERN, 2006. 48

[80] FlightGlobal, "Airbus to offer higher-weight a380 from 2013," Feb 2012. 48

[81] ATLAS Collaboration, *ATLAS inner detector: Technical Design Report, 1.* Technical Design Report ATLAS, Geneva: CERN, 1997. 51

[82] ATLAS Collaboration, *ATLAS inner detector: Technical Design Report, 2*. Technical Design Report ATLAS, Geneva: CERN, 1997. 51

[83] ATLAS Collaboration, *ATLAS pixel detector: Technical Design Report*. Technical Design Report ATLAS, Geneva: CERN, 1998. 52

[84] ATLAS Collaboration, "ATLAS pixel detector electronics and sensors," *J. Instrum.*, vol. 3, p. P07007, 2008. 52

[85] ATLAS Collaboration, "The Silicon Microstrip Sensors of the ATLAS SemiConductor Tracker," Tech. Rep. ATL-INDET-PUB-2007-007. ATL-COM-INDET-2007-008. CERN-ATL-COM-INDET-2007-008. 1, CERN, Geneva, Mar 2007. 53

[86] ATLAS TRT Collaboration, "The ATLAS Transition Radiation Tracker (TRT) proportional drift tube: design and performance," *J. Instrum.*, vol. 3, p. P02013, 2008. 53

[87] ATLAS Collaboration, *ATLAS calorimeter performance: Technical Design Report*. Technical Design Report ATLAS, Geneva: CERN, 1996. 54

[88] ATLAS Collaboration, *ATLAS liquid-argon calorimeter: Technical Design Report*. Technical Design Report ATLAS, Geneva: CERN, 1996. 54

[89] ATLAS Collaboration, *ATLAS tile calorimeter: Technical Design Report*. Technical Design Report ATLAS, Geneva: CERN, 1996. 54

[90] ATLAS Collaboration, *ATLAS muon spectrometer: Technical Design Report*. Technical Design Report ATLAS, Geneva: CERN, 1997. 56

[91] ATLAS Collaboration, *ATLAS magnet system: Technical Design Report, 1*. Technical Design Report ATLAS, Geneva: CERN, 1997. 59

[92] ATLAS Collaboration, *ATLAS central solenoid: Technical Design Report*. Technical Design Report ATLAS, Geneva: CERN, 1997. 60

[93] ATLAS Collaboration, *ATLAS end-cap toroids: Technical Design Report*. Technical Design Report ATLAS, Geneva: CERN, 1997. 60

[94] ATLAS Collaboration, *ATLAS barrel toroid: Technical Design Report*. Technical Design Report ATLAS, Geneva: CERN, 1997. 60

[95] ATLAS Collaboration, "Performance of the ATLAS Trigger System in 2010," *Eur. Phys. J.*, vol. C72, p. 1849, 2012. 62

[96] ATLAS Collaboration, "Technical Design Report for the Phase-I Upgrade of the AT-LAS TDAQ System," Tech. Rep. CERN-LHCC-2013-018. ATLAS-TDR-023, Sep 2013. Final version presented to December 2013 LHCC. 62

[97] ATLAS Collaboration, *ATLAS level-1 trigger: Technical Design Report.* Technical Design Report ATLAS, Geneva: CERN, 1998. 63

[98] "Performance of the ATLAS Trigger System in 2010," *Eur. Phys. J.*, vol. C72, p. 1849, 2012. 64, 65, 67, 70, 72

[99] "Performance of the ATLAS Muon Trigger in p-p collisions at $\sqrt{s} = 7TeV$," Tech. Rep. ATLAS-CONF-2010-095, CERN, Geneva, Oct 2010. 71

[100] W. H. Bell, "Minimum Bias Physics at the LHC with the ATLAS Detector," Tech. Rep. ATL-PHYS-PROC-2009-051. ATL-COM-PHYS-2009-156, CERN, Geneva, Mar 2009. Requesting PROC approval such that the proceedings might be submitted. 71

[101] "Performance of the Minimum Bias Trigger in p-p Collisions at Sqrt(S) = 7 TeV," Tech. Rep. ATLAS-CONF-2010-068, CERN, Geneva, Jul 2010. 71

[102] "Performance of the ATLAS Minimum Bias and Forward Detector Triggers in pPb collisions," Tech. Rep. ATLAS-CONF-2013-104, CERN, Geneva, Nov 2013. 73

[103] P. Jenni and M. Nessi, "ATLAS Forward Detectors for Luminosity Measurement and Monitoring," Tech. Rep. CERN-LHCC-2004-010. LHCC-I-014, CERN, Geneva, Mar 2004. revised version number 1 submitted on 2004-03-22 14:56:11. 73

[104] M. Bruschi, "The ATLAS luminosity monitor," *Nucl. Instrum. Methods Phys. Res., A*, vol. 623, pp. 371–373. 3 p, Apr 2009. Deadline: April 20th 2009. 73

[105] P. Jenni, M. Nessi, and M. Nordberg, "Zero Degree Calorimeters for ATLAS," Tech. Rep. LHCC-I-016. CERN-LHCC-2007-001, CERN, Geneva, Jan 2007. 73

[106] S. Ask, "Simulation of Luminosity Monitoring in ATLAS," Tech. Rep. ATL-LUM-PUB-2006-001. ATL-COM-LUM-2005-002, CERN, Geneva, Sep 2005. 73

[107] "New ATLAS event generator tunes to 2010 data," Tech. Rep. ATL-PHYS-PUB-2011-008, CERN, Geneva, Apr 2011. 73

[108] A. Sherstnev and R. S. Thorne, "Parton Distributions for LO Generators," *Eur. Phys. J.*, vol. C55, pp. 553–575, 2008. 73

[109] S. Agostinelli *et al.*, "Geant4: A simulation toolkit," *Nucl. Instrum. Meth. A*, vol. 506 no. 3, pp. 250 – 303, 2003. 74

[110] G. Aad *et al.*, "The ATLAS Simulation Infrastructure," *Eur. Phys. J.*, vol. C70, pp. 823–874, 2010. 74

[111] D. Scheirich, *Measurements of $\Lambda^0$ and $\Lambda_B^0$ Baryon Properties in the Atlas Experiment.* PhD thesis, University of Michigan, Ann Arbor, 2013. 76, 79, 80, 145

[112] W. Verkerke and D. Kirkby, "Roofit users manual v2. 07," 82, 83

[113] J. Smit, V. Lyuboshitz, and V. Lyuboshitz, "Strong and Electroweak Matter Spin Correlations in the $\Lambda\Lambda$ and $\Lambda\bar{\Lambda}$ Pairs Produced in Relativistic Heavy Ion Collisions," *Nuclear Physics A*, vol. 820, no. 1, pp. 311c–314c, 2009. 109

[114] N. D. Gagunashvili, "Comparison of weighted and unweighted histograms." PoS(ACAT)054, 2007, 2006. 112

[115] B. Andersson, G. Gustafson, and G. Ingelman, "A semiclassical model for the polarization on inclusively produced $\lambda^0$-particles at high energies," *Physics Letters B*, vol. 85, no. 4, pp. 417 – 420, 1979. 136, 137

[116] G. Aad *et al.*, "Charged-particle multiplicities in pp interactions measured with the ATLAS detector at the LHC," *New J. Phys.*, vol. 13, p. 053033, 2011. 153

[117] D. Scheirich, H. A. Neal, and J. Zhu, "Measurement of $\Lambda^0$ polarization in ATLAS (internal documentation)," Tech. Rep. ATL-COM-PHYS-2011-1672, CERN, Geneva, Dec 2011. 170